

# PERMEABILITY EVOLUTION IN VOLCANIC SYSTEMS

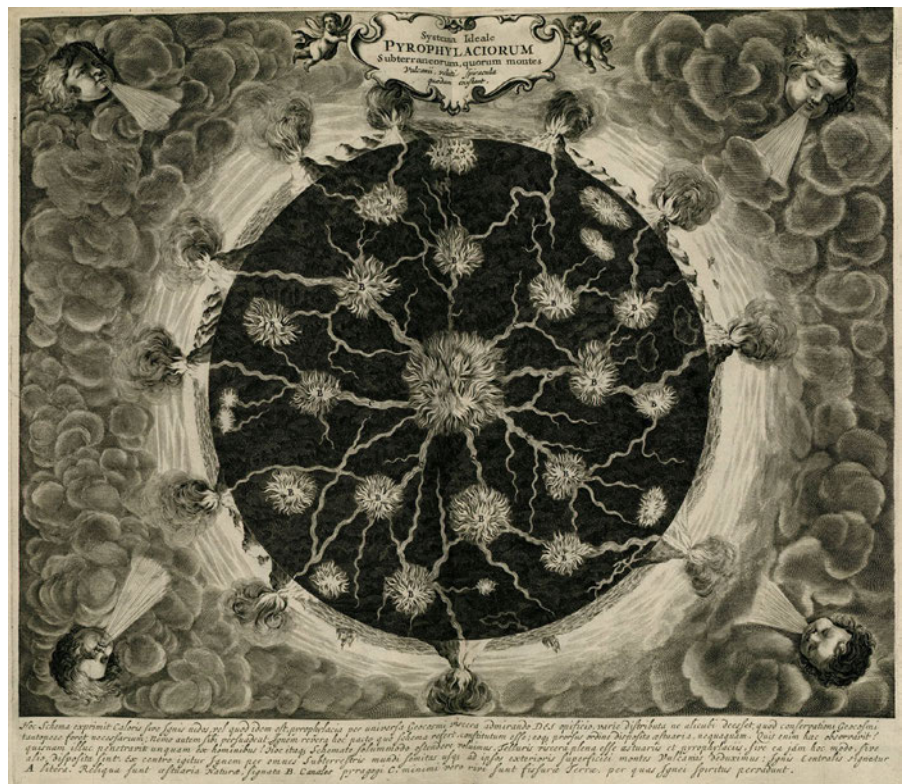
*Field, Laboratory, and Numerical Investigations*

JAMES FARQUHARSON



September 2016

Illustration of  
underground fire  
canals and the  
interior of Earth  
from Athanasius  
Kircher's  
Mundus  
Subterraneus,  
1664.



# James Farquharson: Permeability evolution in volcanic systems: *Field, Laboratory, and Numerical Investigations*

September 2016

For Hannah, who will never read this.



## FOREWORD

---

In the seventeenth century, Athanasius Kircher, in his excellently-titled *The Vulcano's or, Burning and Fire-vomiting Mountains Famous in the World; With their Remarkables*, remarked the following:

*These Vulcano's therefore are nothing but the vent-holes or breath-pipes of Nature, to give vent to the superfluous choaking fumes and smoaky vapours, which fly upward, and make way and free passage for the vehemency of the within-conceived burnings...<sup>1</sup>*

While much of Kircher's scientific work is now known to be wrong, the premise still rings true that, beneath the surface, a volcano contains a complex and interweaving system of passageways. Indeed, these passageways—networks of fissures, fractures, and pores—are now generally understood to exert an important influence on how volcanoes behave: will they erupt, or not? If so, will it be through the emission of riverine flows or mountainous domes of lava, or in the form of a catastrophic explosion? This largely depends on whether gases and other fluids derived from the magma can escape from a volcanic system (think of a tea kettle) or will build up (think of a champagne bottle).

Over two hundred years after Kircher, in a study that epitomises the advent of modern volcanology at the turn of the twentieth century, Alfred Lacroix was to write:

*L'éruption actuelle a été essentiellement caractérisée par ce fait que les dégagements gazeux et l'émission de matériaux solides se sont produits par une ouverture unique ... on verra plus loin que ce dôme n'a pas présenté d'ouverture béante permanente, pendant tout le temps où je l'ai étudié; s'il en a possédé une ou plusieurs pendant les paroxysmes, ce qui est vraisemblable, elles ont été de durée éphémère.<sup>2</sup>*

[The current eruption was essentially characterised by the fact that gaseous emissions and lava extrusion occurred through a single opening ... we shall see later that the dome did not contain a permanent gaping opening throughout the time when I studied it; if it possessed one or more during the paroxysms, which is likely, they were ephemeral.]

---

<sup>1</sup> Kircher, A., 1669. *The Vulcano's or, Burning and Fire-Vomiting Mountains Famous in the World; with their Remarkables*.

<sup>2</sup> Lacroix, A., 1904. *La Montagne Pelée et ses éruptions* (Vol. 1). Masson et Cie.

Clearly then, these networks through which fluids can travel evolve in space and time. Since the work of Lacroix and his contemporaries, hundreds of peer-reviewed studies have explored—directly or indirectly—how the escape of volatiles helps govern the style and frequency of volcanic activity. Surely then, there is nothing left to explore? This thesis occupies some of the no man’s land between volcanology and rock mechanics, while hopefully remaining faithful to both disciplines. Titled *Permeability Evolution in Volcanic Systems: Field, Laboratory, and Numerical Investigations*, this is a predominantly experimental study, and its role is to attempt to pin down some of the underlying mechanics that regulate volcanic processes on a much larger-scale. This work would not have been possible without the assistance, direction and inspiration of many people, who are listed overleaf (I apologise if I’ve forgotten anyone).

## ACKNOWLEDGEMENTS

---

This PhD was funded through an Initiative d'Excellence (IDEX) "Contrats Doctoraux" grant provided by the French state. Fieldwork was funded in part by the Laboratoire d'Excellence (LABEX) grant ANR-11-LABX-0050\_G-EAU-THERMIE-PROFONDE and so benefits from state funding managed by the Agence National de la Recherche (ANR) as part of the "Investissements d'avenir" program. This work was carried out between 2013 and 2016 at the École et Observatoire des Sciences de la Terre, Université de Strasbourg. Fieldwork was primarily carried out at Volcán de Colima (Mexico), during April and June of 2014.

First of all, I would like to express my very great appreciation to Patrick Baud and Mike Heap, who provided sagacious and dynamic guidance throughout the course of this PhD, and who afforded this project the freedom to evolve in its own manner. Along with Patrick and Mike, my thesis jury was composed of Caroline Martel, Philip Meredith, Marie Edmonds, Alexandre Schubnel, and Renaud Tous-saint, to each of whom I wish to express my sincere gratitude.

I extend warm thanks to Thierry Reuschlé, without whose expert knowledge of measuring permeability and deformation this thesis would have been a great deal shorter (or taken a great deal longer). I am particularly grateful also to both Alexandra Kushnir and Luke Griffiths, who provided inspiring discussions and timely distractions in equal measure over the course of the last three years. Most of the experiments would not have been possible were it not for Bertrand Renaudié, who has churned out scores of samples for me in the last three years, and the microstructural analysis would have been impossible without Ulf Zinkernagel, who prepared all the thin sections, and Gilles Morvan, who spent many an hour alongside me on the SEM.

Parts of this thesis have been published or are submitted for publication, and I owe a debt of gratitude to each and all of my co-authors: Mike, Patrick, Yan Lavallée, Nick Varley, Fabian Wadsworth. As well as generously providing field data, Nick greatly facilitated fieldwork in Mexico, offering transport, equipment, and a base of operations during my time there. I also thank all the people with whom I have worked in different projects not presented herein, including Kelly Russell and Stephan Kolzenburg. During fieldwork in Mexico I was assisted, in one way or another, by Oliver Lamb, Graeme Alexander

William Sinclair, Josh Greenwood, Tom McLaughlin, Elinor Meredith, and Esther Adelstein, for which they have my thanks. Thanks are also extended to Bec Fitzgerald, Staś Mordensky, Stephanie Santos and Ravi Tej, who shared their hut with me in New Zealand.

This work has greatly benefitted from discussions with several people, each of whom provided some fresh perspective or idea that has percolated into the study, and—I think—enriched it as a result. Thanks then are due to Hugh Tuffen, Jackie Kendrick, Paul Siratovich, Ben Kennedy, Dan Faulkner, Phil Meredith, Nicolas Brantut, Irving Munigua, Jérémie Vasseur, Klaus Mayer, Bastien Wild, Anthony Lamur, Sebastian Müller, Mathieu Colombier, John Browning, Jon Hanson and Gian Marco Marmoni. Je remercie Olivier, Zacharie, et Dimitri, qui ont fourni à la fois de la bière et de la perspective, quand il fallait.

Phil Meredith kindly provided basalt from Mount Etna, and Yoshi Nara provided a block of Kumamoto andesite, for which I thank them both. One of the andesitic sample sets came from a block collected in 2004 by Oliver Spieler and Sebastian Müller (a different one) from Volcán de Colima, for which they are also acknowledged. Thanks must also be extended to Ulrich Küppers, Katharine Cashman, Agust Gudmundsson, Hugh Tuffen, and a number of anonymous researchers who lent their time and expertise to reviewing some of the chapters herein.

## ABSTRACT

---

Terrestrial volcanism is the surface expression of buoyancy-driven ascent of magma through the Earth's crust. During ascent, magmatic volatiles exsolve from the magma to form a separate gas phase as a result of decompression or thermal vesiculation, and it is the expansion—and attendant bubble pressure increase—of this gas phase that provides the driving force for magma fragmentation and explosive volcanic eruptions. However, this pressurisation may be avoided if the volcanic system can bleed off these volatiles: a process called "outgassing". The underlying parameter governing a volcano's capacity to outgas is its permeability, and the genesis and longevity of permeable pathways are thus critical factors governing the dynamics of a volcanic system. This thesis addresses the evolution of permeability of a volcanic edifice as a function of various thermal and mechanical processes, using a combination of field, laboratory, and numerical modelling techniques, presented as five standalone studies in Chapter 3 – 7. Chapter 1 describes the formation of porosity and permeability in volcanoes, and presents some of the most relevant literature and concepts which are referred to throughout the thesis. Chapter 2 describes the experimental methods employed throughout the thesis.

Chapter 3 explores the underlying microstructural characteristics that govern permeability in edifice-forming rocks. Density and permeability field measurements are presented from 572 samples of andesite from Volcán de Colima (Mexico). For any given porosity, up to four orders of magnitude in permeability can be observed, a range which is little affected by meso-scale textural differences, oxidation, or alteration. Laboratory and microstructural analyses reveal that the andesites collected are microstructurally diverse and complex. The ratio of total and unconnected porosity  $\Gamma$  is defined here and comprises a useful proxy for determining the overall connectivity of a sample. Statistical analysis yields a threshold in connected porosity where the dominant microstructural element controlling fluid flow changes, i.e. from crack- to pore-dominated flowpath geometries. Systematic analysis of microstructures indicates that the fluid flow in low porosity andesites (here  $<0.14$ ) is controlled by tortuous microcracks, whereas in the more porous samples ( $> 0.14$ ) flow mainly occurs in a network of large interconnected pores.

Chapter 4 presents a series of triaxial deformation experiments, designed to explore the response of variably-porous volcanic rock

to stress and strain under different volcano-relevant pressure conditions. At low initial porosities, samples exhibit exclusively dilatant behaviour (macroscopic fracture generation), associated with large increases in permeability. With increasing strain, dilation continues as the sample slides on its fault. At high porosities, failure is predominantly compactant irrespective of the effective pressure applied to the sample (i.e. the difference between the confining and pore fluid pressures), and permeability tends to decrease. Intermediate porosity andesites exhibit relatively little porosity change, regardless of their mode of failure. In this range, failure mode is strongly dependent on the effective pressure conditions, and permeability evolution is much more intricate. Complex deformation behaviours are notable at intermediate porosities, including transitions from compactant to dilatant behaviour, or from dilatant to compactant (which is here termed  $C''$ ). This highlights that the transition from dilatant to compactant behaviour and vice versa is not only controlled by physical properties of a rock—most importantly, its porosity—and the effective pressure (or depth) at which it is deformed, but may also be governed by the post-failure strain to which the rock is subjected.

[Chapter 4](#) highlights that the effective pressure imposed on a rock is critical in dictating its strength and the manner in which it fails. [Chapter 5](#) investigates the potential for failure to be brought about by adjusting the pore pressure only, analogous to fluid migration in a volcanic edifice. Experimental data show that brittle failure can be caused by increasing pore pressure over periods between 1 min to 1 day, a process termed "embrittlement". Furthermore, oscillating pore fluid pressures can cause iterative and cumulative damage, ultimately resulting in brittle failure under stress regimes where the rock would otherwise be intact. This suggests that macroscopic failure occurs after the accumulation of a threshold amount of damage, and that only small fluctuations in pore pressure in the edifice may be required to trigger failure previously-damaged rock. Finally, it is shown that inelastic compaction of volcanic rock (as we may expect in much of the deep edifice) can be overprinted by shear fractures due to this mechanism of embrittlement. Embrittlement at depth may create transient outgassing pathways by linking fracture networks near the edifice to larger-scale regional fault systems. These data affirm that pore pressure fluctuations associated with volcanic unrest may play a crucial role in dictating the evolution of permeability in a volcanic system.

Discontinuities can form in volcanic rock through a host of interrelated magmatic processes, and provide volcanologists with preserved snapshots of these mechanisms. Several discontinuity-bearing blocks were collected from Volcán de Colima, and an examination of their

microstructure and a systematic laboratory study of their physical properties is presented in [Chapter 6](#). These features are relics of both dilatant processes, for example inhomogeneous bubble expansion, cavitation, and magma fracturing, and compactant process, such as pore infill by transported ash or fracture healing. Depending on their genesis and extent, these features can act as pathways for or barriers to fluid flow. In short, if a feature acts as a conduit for fluid flow, then orientation of the feature parallel to fluid flow typically has a markedly greater influence on permeability than when the feature is normal to fluid flow. On the other hand, a feature acting as a barrier for fluid flow will exert its maximum influence when oriented perpendicular to fluid flow. Further, dilatant mechanism operative in low-porosity magma will have a marked influence on permeability, but tend not to increase porosity significantly. In contrast, dilatant processes in high-porosity material tend to have only a marginal influence on permeability, regardless of the overall porosity increase.

[Chapter 7](#) explores the relation between permeability evolution in volcanic systems and the timescales and mechanisms of pore pressure increase, by integrating a series of experimentally-derived equations into a multi-step algorithm. Significantly, a critical permeability threshold is defined—determined using fracture geometry and effective viscosity parameters—dictating whether or not pore pressure will increase in a given volcanic system. Case studies are employed to show that this model can not only predict timescales over which permeability will evolve, but also—crucially—highlights fundamental differences in the propensity for pore pressure build-up at different volcanoes. In low-permeability systems, fracturing will act as a highly efficient outgassing mechanism. However, pore pressure will increase as the decreasing fracture permeability intersects the critical permeability. This means that either a) the system will not achieve its pre-fracture permeability or b) the system will be driven inexorably towards explosive failure. Literature data is used to determine the ranges of this threshold for six silicic volcanoes; notably, the wide span of their critical values reflects the spectrum of eruptive activity observed at these systems.

Finally, [Chapter 8](#) provides a concise summary of the preceding chapters, and offers some personal perspectives for future research integrating experimental data into multi-discipline studies of the evolution of the gas fraction in active volcanic systems.



## CONTENTS

---

<b>I</b>	<b>THESIS</b>	<b>1</b>
<b>1</b>	<b>INTRODUCTION</b>	<b>3</b>
1.1	Volcanic eruptions explosive or effusive? . . . . .	3
1.2	Fluid flow in porous media . . . . .	4
1.3	Development of porosity in volcanic systems . . . . .	4
1.4	Permeability in volcanic systems . . . . .	5
1.5	Mechanical deformation of volcanic materials . . . . .	9
1.6	Deformation and strain in a volcano . . . . .	13
1.7	Structure of the thesis . . . . .	13
<b>2</b>	<b>METHODS</b>	<b>17</b>
2.1	Sample preparation . . . . .	17
2.2	Sample characterisation . . . . .	17
2.2.1	Porosity . . . . .	17
2.2.2	Permeability . . . . .	18
2.2.3	Non-laminar flow 1: Turbulence . . . . .	20
2.2.4	Non-laminar flow 2: Gas slippage . . . . .	20
2.3	Triaxial deformation . . . . .	22
2.3.1	Sample loading . . . . .	22
2.3.2	Porosity change . . . . .	24
2.3.3	Effective pressure . . . . .	24
2.3.4	Sample drainage . . . . .	26
2.3.5	A note on temperature . . . . .	28
<b>3</b>	<b>MICROSTRUCTURAL CONTROLS ON VOLCANIC ROCK PERMEABILITY</b>	<b>31</b>
3.1	Introduction . . . . .	31
3.2	Case study: Volcán de Colima . . . . .	33
3.3	Methods . . . . .	33
3.3.1	Field methods . . . . .	33
3.3.2	Laboratory methods . . . . .	39
3.4	Results and discussion . . . . .	40
3.4.1	Density distribution from the vent . . . . .	40
3.4.2	Porosity and permeability relationship . . . . .	42
3.4.3	Volcán de Colima: microstructurally complex . . . . .	44
3.4.4	A critical porosity: microstructural change . . . . .	48
3.5	Chapter summary . . . . .	55
<b>4</b>	<b>STRAIN-DEPENDENT PERMEABILITY</b>	<b>57</b>
4.1	Introduction . . . . .	58
4.1.1	Deformation and strain in volcanic environments . . . . .	58
4.1.2	Fracture and compaction in the field . . . . .	58
4.1.3	Deformation and permeability . . . . .	61
4.2	Materials and methods . . . . .	62

4.2.1	Deformation conditions . . . . .	64
4.2.2	Post-deformation permeability . . . . .	64
4.3	Results . . . . .	67
4.3.1	Deformation behaviour . . . . .	69
4.3.2	Porosity evolution . . . . .	69
4.3.3	Permeability evolution . . . . .	73
4.3.4	Porosity and permeability evolution with strain	73
4.4	Discussion . . . . .	74
4.4.1	Fracture and compaction of volcanic rock . . . . .	74
4.4.2	Post-failure behaviour . . . . .	79
4.4.3	Permeability–porosity evolution summary . . . . .	84
4.5	Implications for volcanology . . . . .	86
4.5.1	Distribution of fracture and compaction throughout the edifice: implications for outgassing . . . . .	88
4.5.2	Shear faulting, gouge formation, and permeability evolution . . . . .	89
4.5.3	Evolving edifice permeability: an indicator of changing eruptive styles? . . . . .	91
4.6	Chapter summary . . . . .	92
5	PORE FLUID-INDUCED EMBRITTLEMENT	95
5.1	Introduction . . . . .	95
5.2	Evidence for deviations in pore fluid pressure . . . . .	97
5.3	Materials and methods . . . . .	100
5.4	Results . . . . .	103
5.4.1	Constant strain rate with constant pore pressure	103
5.4.2	Increasing pore pressure under constant differential stress . . . . .	105
5.4.3	Pore pressure oscillation under constant differential stress . . . . .	106
5.4.4	Pore pressure increase during constant strain rate deformation . . . . .	107
5.5	Discussion . . . . .	108
5.5.1	The road to failure: stress paths and failure modes of edifice-forming andesite . . . . .	108
5.6	Volcanic edifice embrittlement . . . . .	113
5.6.1	Outgassing and eruptive behaviour . . . . .	113
5.6.2	Edifice stability and seismicity . . . . .	115
5.7	Chapter summary . . . . .	118
6	THE DEVELOPMENT OF PERMEABILITY ANISOTROPY	121
6.1	Introduction . . . . .	121
6.2	Materials and methods . . . . .	123
6.3	Microstructural observations . . . . .	127
6.4	Microstructural interpretations . . . . .	132
6.4.1	Banding in pumiceous samples . . . . .	136
6.4.2	Shear strain-induced flow banding . . . . .	137
6.4.3	Magma fracture and sintering . . . . .	138

6.4.4	Evidence for gas transport . . . . .	141
6.5	Permeability anisotropy . . . . .	146
6.6	Outgassing and volcanic activity . . . . .	152
6.7	Considerations for scaling and modelling . . . . .	156
6.8	Field interpretations . . . . .	158
6.9	Chapter summary . . . . .	159
7	SINTERING-DRIVEN EQUIVALENT PERMEABILITY EVOLUTION	167
7.1	Introduction . . . . .	167
7.2	General porosity reduction model . . . . .	168
7.3	Extension to a permeability reduction model . . . . .	171
7.4	Scaling physical regimes . . . . .	171
7.4.1	Assessing the calibrated range of the sintering model . . . . .	171
7.4.2	A critical permeability threshold for explosive volcanism . . . . .	172
7.5	A computational tool for volcanologists . . . . .	182
7.5.1	Case studies: Mount Unzen and Chaitén . . . . .	182
7.6	Perspectives . . . . .	185
7.7	Chapter summary . . . . .	186
8	CONCLUSIONS AND PERSPECTIVES	187
8.1	Conclusions . . . . .	187
8.1.1	Microstructural controls on volcanic rock permeability . . . . .	187
8.1.2	Exploring the mechanical behaviour of volcanic rock . . . . .	188
8.1.3	Permeability anisotropy: not all outgassing routes are created equal . . . . .	190
8.1.4	Permeability, outgassing, pore pressure and explosive fragmentation . . . . .	191
8.2	Perspectives . . . . .	192
8.2.1	Towards a universal model of permeability and porosity . . . . .	192
8.2.2	Other mechanisms of permeability evolution . . . . .	194
8.2.3	Integrating experimental rock deformation with other data . . . . .	194
II	APPENDICES	197
A	APPENDIX TO CHAPTER 2: INERTIAL EFFECTS	199
B	APPENDIX TO CHAPTER 3: TINYPERM II: AN ASSESSMENT	201
C	APPENDIX TO CHAPTER 3: TRANSFORMING FIELD DENSITY DATA	211
D	APPENDIX TO CHAPTER 4: IS ROCK STRENGTH COMPOSITION-DEPENDENT?	213
E	APPENDIX TO CHAPTER 7: fractured conduit permeability ( $k$ ) reduction	215

E.1	Model functions . . . . .	215
E.2	MATLAB® script . . . . .	216
<b>III</b>	<b>ANNEXES</b>	<b>229</b>
<b>F</b>	<b>FRACTURE AND COMPACTION OF ANDESITE IN A VOLCANIC EDIFICE</b>	<b>231</b>
<b>G</b>	<b>RÉSUMÉ DÉTAILLÉ EN FRANÇAIS</b>	<b>251</b>
G.1	Chapitre 1: Introduction . . . . .	251
G.2	Chapitre 2: Méthodes . . . . .	254
G.3	Chapitre 3: Impact de la microstructure sur la perméabilité des roches volcaniques de Colima (Mexique) . .	254
G.4	Chapitre 4: Impact de la déformation sur la perméabilité des roches volcaniques . . . . .	256
G.5	Chapitre 5: Endommagement des roches sous l'effet de variations de la pression de pore . . . . .	258
G.6	Chapitre 6: L'anisotropie de la perméabilité dans les dômes de lave et les conduits volcaniques . . . . .	260
G.7	Chapitre 7: L'évolution de la perméabilité équivalente autour d'un conduit volcanique: densification des cendres volcaniques chaudes dans les fractures . . . . .	261
G.8	Chapitre 8: Conclusions . . . . .	264
<b>IV</b>	<b>BIBLIOGRAPHY</b>	<b>267</b>
	<b>BIBLIOGRAPHY</b>	<b>269</b>

## LIST OF FIGURES

---

Figure 1.1	To flow or blow? . . . . .	4
Figure 1.2	Selected permeability – porosity data . . . . .	7
Figure 1.3	Viscous densification and permeability . . . . .	9
Figure 1.4	Fracture and compaction: microstructure . . . . .	11
Figure 1.5	Effective pressure and axial strain vs. permeability . . . . .	12
Figure 2.1	Permeameter schematic . . . . .	22
Figure 2.2	Schematic of triaxial deformation apparatus . .	23
Figure 2.3	Schematic of the setup used to test sample drainage . . . . .	27
Figure 2.4	Sample drainage . . . . .	29
Figure 3.1	Sampling sites at Volcán de Colima . . . . .	34
Figure 3.2	Volcán de Colima: Field photographsl . . . . .	36
Figure 3.3	Density measurement field setup . . . . .	37
Figure 3.4	Rock classification scheme . . . . .	38
Figure 3.5	Density distribution of collected samples . . .	41
Figure 3.6	Permeability – porosity data for 542 samples .	43
Figure 3.7	Permeability – porosity data sorted by sample classification . . . . .	46
Figure 3.8	Physical property data of laboratory samples .	49
Figure 3.9	Volcán de Colima andesites: Microstructure .	52
Figure 3.10	Piecewise regression curves . . . . .	54
Figure 4.1	Strain and outgassing in volcanic environments	60
Figure 4.2	Sampling locations . . . . .	63
Figure 4.3	Example mechanical data . . . . .	65
Figure 4.4	Samples deformed in compression: dilation and compaction . . . . .	66
Figure 4.5	Mechanical data for all samples of this study .	70
Figure 4.6	Porosity change vs. inelastic strain . . . . .	71
Figure 4.7	Incremental porosity change . . . . .	72
Figure 4.8	Post-deformation permeability . . . . .	74
Figure 4.9	Permeability and porosity evolution with strain	75
Figure 4.10	Dilation and compaction: Microstructure . . .	77
Figure 4.11	Porosity change vs. effective mean stress . . .	80
Figure 4.12	$C^{*'}:$ Microstructure . . . . .	82
Figure 4.13	$C^{''}:$ Microstructure . . . . .	83
Figure 4.14	$\lambda\phi$ vs. $\lambda k$ . . . . .	85
Figure 4.15	Summarised porosity–permeability evolutions	87
Figure 5.1	Thermal imaging of Volcán de Colima . . . . .	99
Figure 5.2	Mechanical data: constant strain rate tests . .	104
Figure 5.3	Mechanical data: pore pressure increase test .	105

Figure 5.4	Inelastic strain vs. time-to-failure . . . . .	106
Figure 5.5	Pore pressure and AE rate vs. time . . . . .	107
Figure 5.6	Mechanical data: constant strain rate and pore pressure increase . . . . .	109
Figure 5.7	Stress paths of deformation experiments . . . .	110
Figure 5.8	Cumulative acoustic energy vs. time . . . . .	112
Figure 5.9	Embrittlement in the edifice . . . . .	116
Figure 6.1	Volcán de Colima sample sites . . . . .	124
Figure 6.2	Discontinuity-bearing blocks . . . . .	125
Figure 6.3	Discontinuity-bearing core samples . . . . .	128
Figure 6.4	Microstructure . . . . .	133
Figure 6.5	Evidence of shear-induced transtension . . . .	139
Figure 6.6	The evolution of sintering . . . . .	142
Figure 6.7	Progressive pore occlusion . . . . .	144
Figure 6.8	Textural evidence for silica polymorphs . . . .	161
Figure 6.9	Porosity–permeability data . . . . .	162
Figure 6.10	The development of permeability . . . . .	163
Figure 6.11	Scale-dependent permeability anisotropy . . .	164
Figure 6.12	Taupō Volcanic Zone: strain localisation . . .	165
Figure 7.1	Ash-filled fractures . . . . .	169
Figure 7.2	Dimensional analysis . . . . .	175
Figure 7.3	Permeability evolution . . . . .	184
Figure 8.1	Permeability – porosity data for three Ruapehu andesites . . . . .	193
Figure 8.2	Cerro Evermann fissure . . . . .	196
Figure A.1	Flow and pressure data . . . . .	200
Figure B.1	Box-and-whisker distribution . . . . .	202
Figure B.2	Field vs. Laboratory measurements . . . . .	203
Figure C.1	Density–porosity transformation . . . . .	212
Figure D.1	Compiled strength data . . . . .	213

## LIST OF TABLES

---

Table 2.1	Porosity and experimental conditions for porous andesites . . . . .	26
Table 3.1	Physical properties of a suite of Volcán de Colima andesites . . . . .	45
Table 4.1	Physical properties for rocks examined in this chapter . . . . .	65
Table 4.2	Physical property data and deformation conditions for samples of this chapter. . . . .	67
Table 5.1	Experimental conditions and results: summary	102
Table 6.1	Block (hand-sample) descriptions . . . . .	126
Table 6.2	Band and host-rock porosities . . . . .	130
Table 6.3	Porosity–permeability data . . . . .	146
Table 6.4	Calculation parameters . . . . .	150
Table 7.1	Notation used . . . . .	177
Table B.1	Laboratory vs. TinyPerm permeability data . .	203
Table B.2	Full table of (transformed) sedimentary permeability data . . . . .	205



Part I  
THESIS



# 1

## INTRODUCTION

---

*We must take off the cover of all Subterraneous places and deep Caverns, to see the inside of the Earth; and lay bare the roots of Mountains, to look into those holes and Vaults that are under them, fill'd sometimes with Fire, sometimes with Water, and sometimes with thick Air and Vapours.*

— Thomas Burnet, *Tellurius Theoria Sacra*, 1684

### 1.1 VOLCANIC ERUPTIONS EXPLOSIVE OR EFFUSIVE?

Terrestrial volcanism is the surface expression of buoyancy-driven ascent of magma through the Earth's crust. At depth, dissolved volatiles—gases such as H<sub>2</sub>O, CO<sub>2</sub>, SO<sub>2</sub> and lesser amounts of other species—make up a significant proportion of the magma (e.g. Liu et al., 2005). Throughout its journey to the surface, this upwardly-mobile magma will undergo exsolution (vesiculation) of its volatile cargo due to processes such as decompression (e.g. Proussevitch and Sahagian, 1998; Massol et al., 2001; Cashman 2004; Gonnermann and Manga, 2013) and thermal vesiculation (Lavallée et al., 2015), whereby these volatiles separate into a discrete gas fraction in the form of bubbles. The rapid expansion of these bubbles as they approach the surface can generate overpressures in the magma, the kinetic engine that typically drives explosive fragmentation (e.g. Sparks, 1978). However, this pressure build-up can be precluded—promoting effusive or quiescent behaviour—if magmatic volatiles can bleed off, or "outgas", from the magma.

As such, magmas which cannot outgas sufficiently will be oversaturated in volatiles, potentially resulting in the build-up of pressure and explosive eruptions (e.g. Melnik et al., 2005; Diller et al., 2006). By contrast, efficiently outgassed magmas are typically erupted in effusive events—lava flows, domes, or spines—which, despite their ability to cause substantial and permanent infrastructural and property damage, are generally non-fatal (e.g. Auker et al., 2013), notwithstanding post-emplacement collapse (e.g. Abdurachman et al., 2000). So it is that the potential for outgassing is a crucial consideration with respect to the volatile budget of a volcano, and the attendant implications for eruptive behaviour. This concept is illustrated in [Figure 1.1](#).

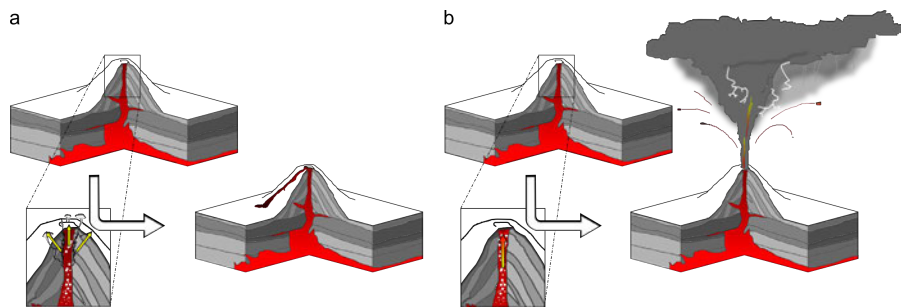


**Figure 1.1:** *To flow or blow?* Volcanoes can exhibit drastically different eruptive behaviour (or none at all), depending on the volume and evolution of magmatic volatiles. a) Outgassing through connected, fracture networks, or laterally through the edifice should reduce the explosive potential of a volcano, promoting non-explosive behaviour. b) Contrastingly, the build-up of pressure due to bubble growth in a low-permeability system may result in violent, explosive eruptions.

## 1.2 FLUID FLOW IN POROUS MEDIA

In order to discuss fluid transport through a volcanic system, we must first define two concepts (both of which are physical properties of a medium): porosity and permeability. Porosity  $\phi$  is the fraction of a given medium, such as rock, that is occupied by void space. In rocks and magma, porosity may be comprised of pores (vesicles), fractures, or—commonly—some combination of both. Permeability  $k$  is the capacity for fluid flow through solid material by way of its (connected) porosity, and can vary over twelve orders of magnitude in natural rocks (Guéguen and Palciauskas, 1994).

## 1.3 DEVELOPMENT OF POROSITY IN VOLCANIC SYSTEMS

The development of porosity in volcanoes begins in the ascending magma. Volatile saturation of the magma depends primarily on the processes of crystal fractionation, crustal contamination, and magma mixing, in turn largely reliant on its origin. The total amount of dissolved volatiles that can be retained in a silicate melt is a function of its composition as well as the pressure and temperature conditions (e.g. Liu et al., 2005). If this volume is exceeded, the melt becomes supersaturated, and the law of thermodynamic equilibrium dictates that a discrete vapour phase must form. The growth of bubbles is then a function of the interplay between the saturation equilibrium (volume energy) and surface tension (surface energy): bubbles smaller than a critical radius will collapse due to capillary forces; bubbles greater than a critical radius will be stable and can expand (Navon and Lyakhovsky, 1998; Cashman et al., 2000). Once established, bubble growth is assisted by volatile diffusion and hindered by the melt viscosity,

both of which are functions of the melt composition.

As long as volatile oversaturation exists, exsolution continues, and bubbles can continue to nucleate, grow (as a consequence of diffusion or decompression-induced expansion: Sparks, 1978), and coalesce (e.g. Martel and Iacono-Marziano, 2015) until the system achieves mechanical and chemical equilibrium (Lensky et al., 2004). Magma fracture is also possible, through one of two processes: fragmentation resulting from a pore pressure that exceeds the tensile strength of the magma (i.e. a fragmentation threshold: e.g. Alidibirov and Dingwell, 1996; Zhang, 1999; Koyaguchi et al., 2008), or by magma failure due to rapid shearing surpassing a critical strain rate in areas of strain localisation (e.g. Woods and Koyaguchi, 1994; Martí et al., 1999; Papale, 1999; Gonnermann and Manga, 2003; Melnik et al., 2005; Lavallée et al., 2008; 2013). In either scenario, failure occurs at the glass transition  $T_g$  because the accumulated strain exceeds the elastic limit of the material and cannot be relaxed viscously (Dingwell, 1996). Reduction of porosity may also occur, through sintering-driven densification (e.g. Quane et al., 2009; Vasseur et al., 2013; Heap et al., 2014a; Kolzenburg and Russell, 2014; Wadsworth et al., 2014; Heap et al., 2015b), viscous compaction and foam collapse (Ashwell and Kendrick et al., 2015; Martel and Iacono-Marziano, 2015) or vapour phase precipitation (Wright et al., 2011; Kushnir et al., 2016).

Upon cooling, the geometry of the porosity is frozen in place, providing a snapshot of the high temperature mechanisms at work in the conduit or dyke cluster beneath the surface. However, during and after emplacement other processes come into play: new fractures can arise due to thermal, mechanical, or chemical stresses, for example (e.g. Le Pennec et al., 2001; Vinciguerra et al., 2005; Platz et al., 2007; Gaunt et al., 2016). Comminution—the gradual reduction of the mean clast or particle size by progressive fracturing, abrasion, collision, and/or fluvial reworking—is often associated with transport and remobilisation of volcanic materials (e.g. Manga et al., 2011; Kueppers et al., 2012). Alternatively, porosity can be reduced, for example, by hydrothermal circulation and mineral precipitation (e.g. Edmonds et al., 2003; Ball et al., 2015), by the deposition of volcanic debris inside pores and cracks (e.g. Tuffen et al., 2003; Kendrick et al., 2016), or by mechanical compaction (e.g. Stanchits et al., 2006; Zhu et al., 2011; Loaiza et al., 2012; Heap et al., 2015a).

#### 1.4 PERMEABILITY IN VOLCANIC SYSTEMS

A typical stratovolcano is composed of a central magmatic conduit or cluster of dykes encompassed by indiscriminately emplaced layers

of lava, explosive ejecta, and other volcaniclastic deposits (e.g. Biggs et al., 2010; Gudmundsson, 2012). Iterative accumulation of these products creates an edifice with spatially-variable physical properties, often exhibiting pervasive differences in porosity and permeability down to the intra-clast scale. While this model does not describe all terrestrial volcanism, the majority of the conclusions of this thesis are more widely applicable to volcanic systems in general.

Fundamentally, a full understanding of the potential hazard posed by any volcanic system relies on determining whether outgassing can occur, and how this may happen. Processes which have been inferred or assumed from field, laboratory, and numerical studies include gas transport through interconnected bubble chains in the magma (e.g. Eichelberger et al., 1986; Okumura et al., 2009), lateral outgassing from the conduit margin into the edifice and thence through the edifice rock (e.g. Jaupart and Allègre, 1991; Jaupart, 1998; Collombet, 2009), or fluid flow through fracture networks in magma, edifice rock, and lava domes (e.g. Stasiuk et al., 1996; Gonnermann and Manga, 2003; Rust et al., 2004; Edmonds and Herd, 2007; Castro et al., 2012; Cabrera et al., 2011; Lavallée et al., 2013; Pallister et al., 2013; Gaunt et al., 2014), each of which depend on the permeability of a particular portion of the volcano. Thus transport networks for magmatic volatiles are dependant not only on large-scale fault systems (which may not necessarily provide a direct pathway for volcanic gas species: see Varley and Taran, 2003), but also on the fluid transport properties of the constituent edifice-forming rocks and the generation of fracture systems through which gases can travel.

Over the last three decades, permeability of volcanic rocks has become an increasingly prevalent metric with which to discuss mechanisms of outgassing and thus eruption dynamics. Since the seminal work of Eichelberger et al. (1986), a great many studies have examined the relationship between the permeability and porosity of volcanic rocks. Eichelberger et al. (1986) measured a suite of rhyolites from the Inyo Domes chain (California, USA) and outlined a permeable foam model to explain non-explosive silicic volcanism, work that was built on by Westrich and Eichelberger (1994). Klug and Cashman (1996) measured the porosity and permeability of a range of airfall deposits and tuffs from Crater Lake and Mount St Helens (USA), proposing a simple power law relation between the two properties.

Another notable contribution is that of Mueller et al. (2005), who measured porous rocks of explosive origin and less-porous extrusive lavas and adopted a combination of a capillary tube model (for effusive materials) and a percolation model based on a system of fully penetrable spheres (for explosive products). Mueller et al. (2005) infer

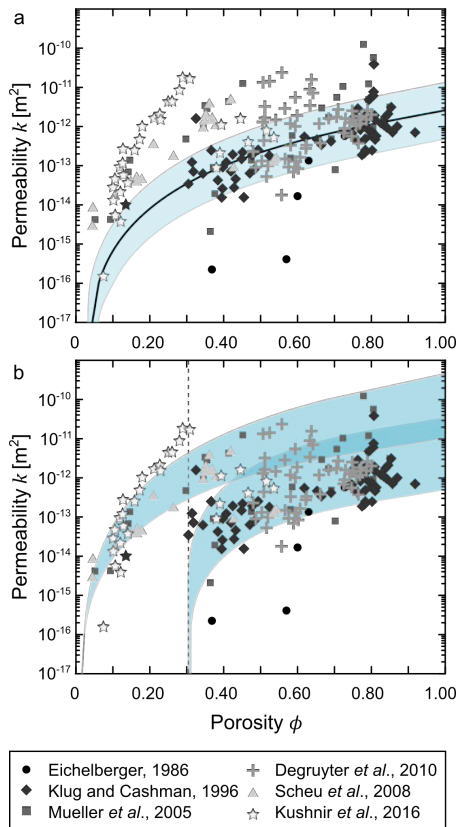


Figure 1.2: A compilation of selected permeability – (connected) porosity data. a) Black curve shows the power law approximation proposed by Klug and Cashman (1996). b) Mueller et al. (2005) proposed two overlapping models: a capillary tube model (low porosity/effusive origin) and a percolation model (high porosity/ explosive origin). Dashed grey line indicates the percolation threshold.

a significant influence on permeability not only from the pore volume, but also on pore size, shape, and distribution. Select permeability – porosity data are shown in Figure 1.2, reproduced from Eichelberger et al. (1986), Klug and Cashman (1994), Mueller et al. (2005), Scheu et al. (2008), Degruyter et al. (2010) and Kushnir et al. (2016). This plot encompasses the majority of the range of permeability and porosity that has been measured for volcanic rocks, and emphasises the fact that the permeability of these materials cannot be modelled simply as a function of the connected porosity (Mueller et al., 2005; Degruyter et al., 2010). Rather, there must be other governing factors that are equally as important as the volume of connected pore space.

Several researchers have essayed to determine the underlying microstructural processes governing permeability (e.g. Saar and Manga, 1999; Jouniaux et al., 2000; Blower, 2001; Rust and Cashman, 2004; Wright et al., 2006; Bernard et al., 2007; Wright et al., 2009; Yokoyama and Takeuchi, 2009; Rust and Cashman, 2011; Heap et al., 2014a).

These studies emphasise the importance of connectivity of pore space which, given the complex and interrelated methods of formation, is not necessarily described well by established permeability models, many of which were constructed based on sedimentary materials or granular media (e.g. Costa, 2006).

Moreover, a number of authors have focussed on the development of bubble anisotropy and the attendant influence on permeability; for example, Tait et al. (1998) measured porosity and permeability of Santorini pumice, noting significant anisotropy depending on the sample orientation. Similarly, Wright et al. (2006) measured a range of rhyolitic pumice from Ramadas caldera (Argentina), Monte Pilato (Lipari, Italy), Tumalo Tuff (USA) and Toya Tuff (Japan), Bernard et al., 2007 characterised suites of samples from Montagne Pelée (Martinique), and Degruyter et al. (2010) examined pumice from the Kos Plateau Tuff (Argentina). Each of these authors measure permeability differences of an order of magnitude or greater, arising from preferential vesicle elongation. Recent works have also sought to characterise the physical properties of strain localisation features such as frictional melts (Kendrick et al., 2014) and ash-filled fractures (Kolzenburg et al., 2012; Kendrick et al., 2016).

These and other studies (e.g. Melnik and Sparks, 1999; Klug et al., 2002; Melnik and Sparks, 2002; Dobson et al., 2003; Gonnermann and Manga, 2007; Platz et al., 2007; Nakamura et al., 2008; Yokoyama and Takeuchi, 2009; Bouvet de Maisonneuve et al., 2009; Ball et al., 2013; Heap et al., 2014b, 2015; Mayer et al., 2015) illustrate the variations in physical rock properties that echo the wide range of magmatic compositions and eruptive styles (e.g. Spieler et al., 2004; Burgisser and Gardner, 2005; Mueller et al., 2008). In turn, such studies typically aim to relate these parameters to the migration of gas through the volcanic system—governing fragmentation mechanisms (e.g. Dingwell, 1998; Papale, 2001), pressurisation of lava domes and spines (Sparks, 1997), and the transitions between violent and nonviolent eruptive activity (Eichelberger et al., 1986; Dingwell, 1996; Gonnermann and Manga, 2003, 2005)—or to provide forensic insight into historical eruptive activity (Kueppers et al., 2005; Gonnermann and Manga, 2007; Mueller et al., 2011). These data can subsequently inform predictive numerical models that estimate the evolution of the gas fraction in volcanic systems (e.g. Jaupart, 1998; Collombet, 2009; Collinson and Neuberg, 2012).

Taken together, these studies paint a broad and complex picture of permeability in volcanic materials. However, post-mortem porosity and permeability measurements provide only snapshots of dynamic processes. Heap et al. (2015b) measured permeability and porosity of

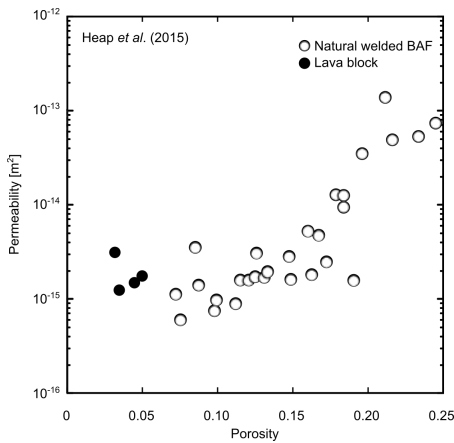


Figure 1.3: Permeability and porosity data reproduced after Heap et al. (2015b), illustrating the impact of viscous densification on permeability.

variably welded (but compositionally identical) block-and-ash deposits flows from Mount Meager volcano (Canada). Their results emphasise that physical properties can evolve during and after emplacement of volcanic products. Figure 1.3 presents data from that study, indicating the clear trend of lower permeability associated with less porous (i.e. more welded) samples. Experimentally, Ashwell and Kendrick et al. (2015) demonstrated a similar phenomenon: with viscous compaction, both permeability and porosity of rhyolitic samples (from the Taupō Volcanic Zone, New Zealand) were observed to decrease significantly. Furthermore, research that addresses the response of permeability to hydrostatic loading (e.g. Vinciguerra et al., 2005; Watanabe et al., 2008; Fortin et al., 2011; Faoro et al., 2013) or triaxial compression (Alam et al., 2014) highlight that its evolution depends on a range of parameters, including pore geometry and confining pressure. This shall be discussed further in the next section.

## 1.5 MECHANICAL DEFORMATION OF VOLCANIC MATERIALS

Although experimental rock deformation research has been historically focused primarily on sedimentary and intrusive igneous rocks (e.g. Brace and Jones, 1971; Wong et al., 1997; Wong and Baud, 2012), recent studies have begun to explore the phenomenological behaviour of relatively more heterogeneous volcanic materials under hydrostatic (e.g. Balme et al., 2004; Vinciguerra et al., 2005; Fortin et al., 2011; Nara et al., 2011), uniaxial (Jeong et al., 2007; Heap et al., 2012; Scaefer et al., 2015; Heap and Kennedy, 2016; Zhu et al., 2016), and triaxial (Shimada et al., 1989; Benson et al., 2008; Tuffen et al., 2008; Smith et al., 2008; Heap et al., 2011; Loaiza et al. 2012; Adelinet et al. 2013; Heap et al., 2014c, 2015a; Violay et al., 2015; Heap and Wadsworth, 2016; Zhu

et al., 2016) conditions.

These studies highlight the broad range of strength and different failure modes observed in porous volcanic rock. Volcanic rocks—indeed all porous rocks—may either dilate or compact in response to an applied differential stress or a change in the pore pressure. Dilatant brittle failure comprises an increase in porosity through the formation, growth, and coalescence of stress-induced fractures. In compression, this culminates in an axial or shear fracture. Contrastingly, shear-enhanced compaction involves (by definition) a loss of porosity. In Alban Hills tuff, deformed under triaxial conditions, this mode of failure was shown to be a manifestation of a mechanism of cataclastic pore collapse (Zhu et al., 2011). This process involves intense micro-cracking developing in a concentric damage zone around a pore. As cataclasis (progressive fracturing and comminution) continues, comminuted fragments can spall into the void space, thus reducing porosity (Zhu et al., 2010). Examples of the microstructure accompanying these failure modes is shown in [Figure 1.4](#), from Fortin et al. (2011) and Zhu et al. (2016), respectively.

Shear-enhanced compaction is ductile behaviour. However, volcanic materials are often subject to thermal stresses as well as mechanical stresses. In this case, the material may deform viscously, whereby molecules diffuse within amorphous material that is above its glass transition (which is to say it flows): a process wherein the material is often referred to as "ductile" in volcanology literature. The terms dilatant and compactant are used herein in order to avoid any potential misunderstanding that could arise. (Note that dilatant and compactant are both valid characterisations for materials in a viscoelastic regime.)

Dilatant and compactant behaviour of volcanic rock has been investigated by numerous authors, often in concert with changes in other physical properties such as permeability. For example, Vinciguerra et al. (2005), Fortin et al. (2011), and Nara et al. (2011) examined permeability change as a function of different confining pressures in Sel-jadur and Etna basalts in order to study the influence of dilatant thermal and mechanical cracking. Heap and Kennedy (2016) fractured andesites from Mount Ruapehu (New Zealand) in tension (under uniaxial conditions), in order to investigate the influence of a through-running tensile fracture on sample permeability. Faoro et al. (2013) investigated the evolution of permeability of Etna basalt at low strain in the dilatant regime, while Alam et al. (2014) examined permeability change in Shikotsu welded tuff in both the dilatant and compactant regimes.

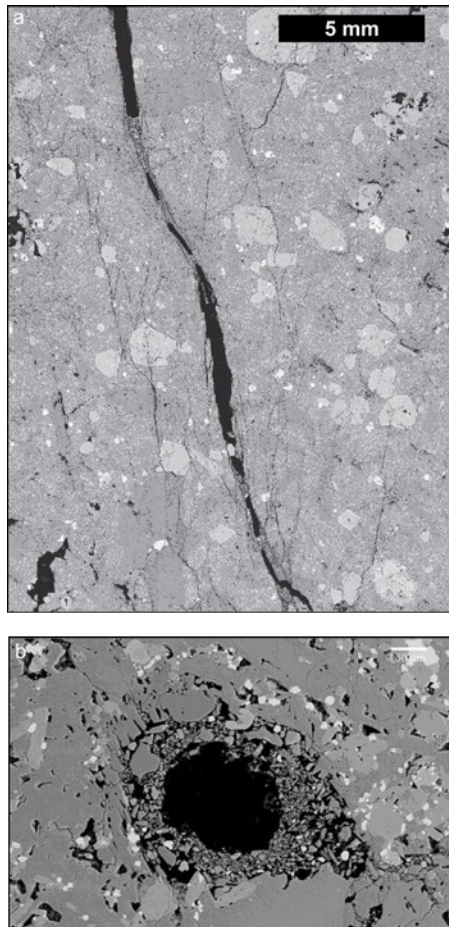


Figure 1.4: Example microstructure of dilatant fracturing and cataclastic pore collapse. a) Field Emission Gun-Scanning Electron Microscope (FESEM) map of fracture Etna basalt (cropped image from Fortin et al. 2011). b) Also a sample of Etna basalt, this time having failed through cataclastic pore collapse. Scanning Electron Microscope (SEM) shows macropore with a radius on the order of  $100 \mu\text{m}$  surrounded by a halo of cataclastic damage. From Zhu et al. (2016). Porosity is black in either case.

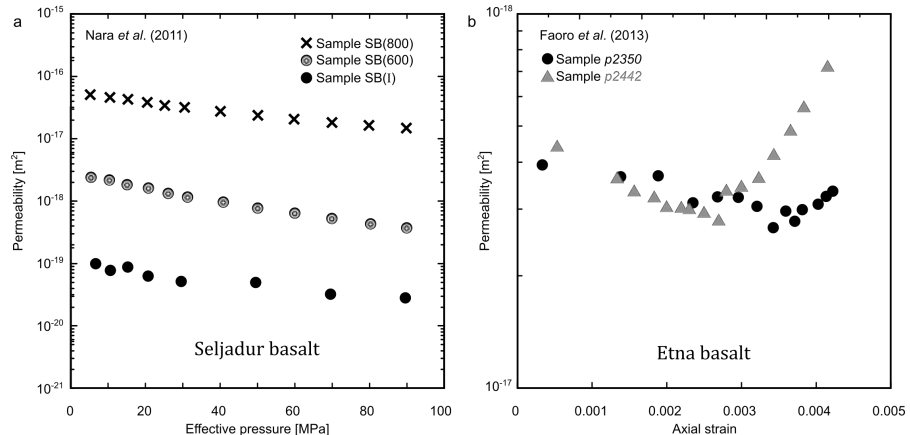


Figure 1.5: The influence of a) effective pressure and b) axial strain on permeability of two basalts, reproduced from Nara et al. (2011) and Faoro et al. (2013). a) Data show that permeability tends to decrease in samples of Seljadur basalt with increasing effective pressure. Samples are intact (I) and heat treated at 600 and 800 °C. b) Evolution of permeability as a function of axial strain for each loading cycle on samples of Etna basalt (samples p2350 and p2442). Refer to Nara et al. (2011) and Faoro et al. (2013) for discussion.

Example data from Nara et al. (2011) is reproduced in Figure 1.5a. The figure shows that as effective pressure was increased in a pressure vessel (the difference between the pore and confining pressures, discussed in Chapter 2), the permeability of samples of Seljadur basalt decreased monotonously. Further, data from Faoro et al. (2013) are presented in Figure 1.5b, showing the evolution of permeability of two basalt samples with increasing axial strain during cyclic loading tests. Both these studies show that permeability of volcanic materials can be influenced by mechanical deformation.

Additional rock physics studies have sought to tie volcanic rock deformation to volcanic geophysical signals: Benson et al. (2008) and Burlini and Di Toro (2008) related laboratory measurements of acoustic emissions in Etna basalt—an indicator of fracturing on the micro-scale—to seismic signals monitored at active volcanoes. Moreover, the transition between brittle failure to shear enhanced compaction has been explored by, for example, Shimada et al. (1989), who deformed Yakuno basalt (Kyoto prefecture, Japan) at very high confining pressures (3 GPa), Zhu et al. (2011) for Alban Hills tuff (Italy), Heap et al. (2015a) for variably porous Volcán de Colima (Mexico) andesite, and Zhu et al. (2016) for Etna basalt. Further explorations of compaction were carried out by Loaiza et al. (2012) and Adelinet et al. (2013), who studied compaction in trachyandesite from the Açores (Portugal) and basalt from Rejkjanes (Iceland), highlighting the tendency for compaction localisation in these materials at high confining pressures.

## 1.6 DEFORMATION AND STRAIN IN A VOLCANO

Studies of ground deformation around active volcanoes highlight that they are high-strain environments (e.g. Ōmori, 1920; Mogi, 1958; Dzurisin, 2003), often characterised by periodic inflation and deflation of the edifice (e.g. Elsworth et al., 1996; Voight and Elsworth, 1997; Watson et al., 2000; Hooper et al., 2004; Wadge et al., 2006), indicative of pressurisation of shallow conduits or dykes due to volatile loss and crystallisation (Voight et al., 1998; Denlinger and Hoblitt, 1999; Clarke et al., 2007), or deep-seated magma chamber deformation (Melnik and Sparks, 1999; Melnik and Sparks, 2005; Wadge et al., 2006). Migration of magma and fluids is expected to impart significant mechanical strain on the edifice during periods of major unrest (e.g. Elsworth and Voight, 1992; Elsworth et al., 1996; Voight and Elsworth, 1997; Roman et al., 2004; Gerst and Savage, 2004), and also during eruptive quiescence (e.g. Dvorak et al., 1986; Bonafede, 1991; Reid, 2004). Moreover, the continued loading of the edifice due to iterative emplacement of erupted material will serve to increase the overlying stress (i.e. the confining stress) in any given region of the edifice (e.g. Heap et al., 2015a). It is generally understood that all volcanoes deform under their own weight to some extent (Shteynberg and Solov'yev, 1976; Dieterich, 1988; van Wyk de Vries and Borgia, 1996), driven largely by gravitational spreading and substratum flexure (van Wyk de Vries and Matela, 1998). Further, the overlying stress may be influenced by loading and unloading of volcanoes by ice, either seasonally or due to longer-scale climatic variations (e.g. Sigmundsson et al., 2010).

## 1.7 STRUCTURE OF THE THESIS

It has been well established that permeability and porosity are important constraints regarding the eruptive style of a volcano. Moreover, laboratory studies of the physical and mechanical properties of volcanic rocks have shown that permeability can evolve under different stress or strain conditions, and numerous remote-sensing and analogue studies show that volcanoes are inherently high-strain environments.

Building on the work outlined above, this thesis sets out to explore how the permeability of a volcanic system may evolve in space and time as a function of various thermo-mechanical processes. While the migration of bubbles through magma is an area of exciting and active research—and undoubtedly contributes to what may be considered as the overall permeability of a volcano—the following chapters primarily focus on the permeability of the edifice and edifice rocks, factors that are often simplified or neglected in models of gas evolution in

volcanic systems, due in large part to the paucity of available data.

The ultimate goal of this research is to help constrain the mechanisms underpinning the style and dynamics of volcanic eruptions by interrogating volcanic systems through the lenses of rock deformation and fluid transport. Nevertheless, numerous other environmental and industrial applications exist where the permeability of volcanic materials—and their response to induced stress and strain—is of prime importance. For example, the performance of geothermal reservoirs (e.g. Siratovich et al., 2014; Stimac et al., 2014; Grant 2015) and nuclear waste repositories (e.g. Smyth 1982) are both determined by the capacity for fluid migration in those systems: high permeability is often desirable in the first instance, whereas an impermeable rock mass is sought after for the latter case. Similarly, hydrocarbon reservoirs are typically composed of a relatively permeable rock mass overlain by an impermeable cap rock which serves to trap oil and gas. While volcanic rocks cannot produce hydrocarbons, much recent work has been focused on the propensity for volcanic and plutonic formations to act as effective stores of hydrocarbons (e.g. Sruoga et al., 2004; see Zou, 2013 for a review).

Given the preamble above, this thesis seeks to address the following overarching questions:

1. Can we relate the permeability of edifice material to its physical properties, such as porosity?
2. How do porosity and permeability evolve as a consequence of mechanical deformation under volcano-relevant conditions?
3. How do conduit processes influence permeability and permeability anisotropy, and what is the influence of small-scale processes on a volcanic system as a whole?

In order to explore these topics, this thesis has been conducted as a series of studies, each with the purpose of tackling a specific facet of porosity or permeability change in volcanic systems. Complemented by field measurements (performed during a month-long field campaign at Volcán de Colima, Mexico), microstructural observation, and numerical modelling, these studies are built on a foundation of triaxial rock deformation experiments and laboratory characterisation of rock physical properties. [Chapter 2](#) summarises the main experimental methods used throughout.

[Chapter 3](#) presents a suite of density and permeability measurements made in the field on hundreds of edifice-forming rocks from Volcán de Colima (Mexico). The interpretation of these data is aided by a complementary laboratory-based examination of andesites col-

lected during this field campaign. Using Scanning Electron Microscope (SEM) analysis, this chapter explores the microstructural complexity inherent in volcanic materials, and examines the relationship between porosity and permeability in these rocks. The results and discussion are presented in:

Farquharson, J. I., M. J. Heap, N. Varley, P. Baud, and T. Reuschlé, 2015. *Permeability and porosity relationships of edifice-forming andesites: A combined field and laboratory study*. Journal of Volcanology and Geothermal Research, 297, 52-68.

[Chapter 4](#) investigates how the porosity and permeability of variably porous volcanic rocks evolve when subjected to mechanical deformation at different effective pressures and to different degrees of inelastic strain, concepts which are defined fully in [Chapter 2](#). SEM analysis allows the study of microstructural evolution arising from different deformation behaviours: porosity-increasing (dilatant) and porosity-decreasing (compactant). In turn these microstructural characteristics largely dictate the evolution of permeability. In part, this chapter is published as:

Farquharson, J. I., M. J. Heap, and P. Baud. *Strain-induced permeability increase in volcanic rock*. Geophysical Research Letters.

and:

Farquharson, J. I., P. Baud, and M.J. Heap. *Inelastic compaction and permeability evolution in volcanic rock*. Solid Earth Discussions.

[Chapter 5](#) addresses the potential for porosity to be created through an alternative deformation mechanism, involving induced fluid movement through samples of edifice-forming andesite. By means of a targeted triaxial deformation campaign, this chapter highlights a potentially important fracture-generation mechanism that has been largely overlooked in volcanology and related disciplines, and outlines possible consequences of its occurrence in volcanic systems. It is published as:

Farquharson, J. I., M. J. Heap, P. Baud, T. Reuschlé, and N. R. Varley. *Pore pressure embrittlement in a volcanic edifice*. Bulletin of Volcanology, 78(6).

[Chapter 6](#) examines a suite of heterogeneous rocks collected from Volcán de Colima. These discontinuity-bearing samples provide snapshots of strain localisation processes that occur during magma ascent and extrusion. Alongside a systematic porosity and permeabil-

ity study, the genetic processes of the discontinuities are interpreted through detailed microstructural examination. The results and discussions appear in full in the following publication:

Farquharson, J. I., M. J. Heap, Y. Lavallée, N. R. Varley, and P. Baud. *Evidence for the development of permeability anisotropy in lava domes and volcanic conduits.* Journal of Volcanology and Geothermal Research, 323, pp.163-185.

[Chapter 7](#) combines a sequence of numerical models in order to investigate the influence of generating and healing fractures on the permeability around a volcanic conduit, over a range of scales.

Finally, [Chapter 8](#) collates the conclusions of the five preceding chapters, and outlines some perspectives for future research.

Parts of this work ([Chapter 4](#) and [5](#) in particular) are based on the results and conclusions of a previous article:

Heap, M.J., Farquharson, J.I., Baud, P., Lavallée, Y. and Reuschlé, T., 2015. *Fracture and compaction of andesite in a volcanic edifice.* Bulletin of Volcanology, 77(6), pp.1-19.

For completeness and convenience, this article is included as an annex to the thesis.

# 2

## METHODS

---

*He'd argue with rocks and the rocks would win.*

— Neil Gaiman, *American Gods*, 2011

*Throughout the subsequent chapters, a range of experimental methods are mentioned, several of which techniques are employed more than once. To avoid redundancy therefore, methods are summarised in this chapter. Where the methods employed in subsequent chapters differ from those outlined below, this will be stated explicitly. Where methods employed were particular to a single study, they are outlined in the corresponding chapter.*

### 2.1 SAMPLE PREPARATION

Materials used to study permeability and deformation were collected or quarried from a range of active and historically active volcanic environments (The majority were collected during a month-long field campaign at Volcán de Colima, Mexico, in May and June 2014), often in the form of a cuboidal block or hand samples, and occasionally significantly larger irregular blocks. In order to carry out laboratory characterisation and experimentation, this larger source material was sawn and drilled into cylindrical cores with a nominal diameter of 20 mm. Cores were then precision-ground so that their faces were flat and parallel, typically to a length of  $40 \pm 1$  mm. Bertrand Renaudié is thanked for the majority of sample preparation at Université de Strasbourg.

### 2.2 SAMPLE CHARACTERISATION

#### 2.2.1 Porosity

In rock of given volume  $V$ , porosity is given by  $(\phi = (V - V_s))/V$ , where  $V_s$  is the volume of solid material. Prior to characterising their physical properties, all samples were dried at  $40^\circ\text{C}$  under a vacuum for a minimum of 48 hours. The solid volume  $V_s$  of each sample was determined using helium pycnometry (AccuPyc II 1340 from Micromeritics), which subsequently allows the calculation of the connected gas porosity  $\phi$  if the sample mass and dimensions (and hence its geometric volume  $V$ ) are known. Automated measurements of  $V_s$  were performed iteratively until five consecutive measurements yielded results within a range of 0.01% of the sample volume, so precision of the pycnometer measurements was high (generally  $<0.005$

$\text{cm}^3$ ). A greater degree of error arises when manually measuring the sample dimensions. Repeat measurements allowed an estimation of error in the length and diameter, which typically amounted to  $<0.05 \text{ cm}^3$  in terms of volume. Adopting the notation that  $\epsilon_\phi$  is the error on the porosity calculation and that  $\epsilon_x$  and  $\epsilon_y$  are the independently calculated errors for measurements of  $V_s$  and  $V$ , then the propagated error can be approximated by:

$$\epsilon_\phi = \phi \cdot \sqrt{\left(\frac{\epsilon_z}{V - V_s}\right)^2 + \left(\frac{\epsilon_y}{V}\right)^2}; \quad \epsilon_z = \sqrt{\epsilon_x^2 + \epsilon_y^2} \quad (2.1)$$

Values for  $\epsilon_\phi$  are generally  $<0.005$  for the range of porosities measured using this method throughout the thesis. As such, probable error on connected gas porosity measurements is low, and always contained within the symbol size when plotted graphically.

Dry mass and sample dimensions were determined using a precision balance and digital callipers, respectively. Connected water porosity was also measured for some samples, employing the Archimedes principle of displacement (a.k.a. the triple-weight porosity). In this case, the weight of a dry sample  $W_d$  was measured in air, before the sample was saturated with distilled water. The water-saturated weight  $W_s$  was measured in air, and the immersed weight  $W_i$  of the saturated sample was measured by suspending the sample in distilled water by means of a cradle attached to the underside of the balance. Connected water porosity is given thus:

$$\phi_w = \frac{W_s - W_d}{W_s - W_i} \quad (2.2)$$

In this case, the error is a function of the precision of the balance ( $0.001 \text{ g}$ ) and the escape of water from surface porosity, which is not readily quantifiable. This problem is amplified for very porous volcanic samples, as such this method is often inappropriate for measuring these volcanic materials. Errors are undoubtedly greater than those obtained for gas measurements, but presumably still smaller than the symbol size. Often it is useful to compare the connected porosity  $\phi$  with the total porosity  $\phi_t$ , which also includes any unconnected pore space. This is determined by measuring the mass and volume of powdered rock and calculating  $\rho_s$ , the powder density (a.k.a. particle or skeletal density):  $\phi_t = 1 - (\rho_b / \rho_s)$ .

### 2.2.2 Permeability

The constitutive equation governing fluid transport in porous and granular media was originally derived from experiments performed by Henry Darcy in the 1850s on the flow of water at different levels

through sand. Since Darcy's work, the theoretical framework of fluid transport—which is based on Newton's second law—has been well established and expanded, such that flow of gas through a porous medium may be given thus:

$$Q_v = \frac{-kA}{\nu} \frac{(p_b - p_a)}{\ell} \quad (2.3)$$

where  $\nu$  is the fluid viscosity,  $Q_v$  is the volumetric flow rate,  $A$  is the cross-sectional area available for flow and  $\ell$  is the distance over which fluid flow occurs (i.e. the sample length). In a fluid transport system, flow is driven towards the region of lowest potential energy: in the special case of horizontal flow, this may be described by a differential between a region of relatively high pressure  $p_b$  to one of relatively lower pressure  $p_a$ : a pressure differential or pressure drop  $\nabla p$ . [Equation 2.3](#) is valid for all porous media as long as flow is laminar (two cases of non-laminar flow are discussed hereafter).

While this expression is sufficient for the case of laminar (or "streamline") flow, when considering an ideal compressible gas measured under atmospheric conditions, it becomes convenient to present gas permeability  $k_{gas}$  in the following manner (Klinkenberg, 1941; McPhee and Arthur, 1991):

$$k_{gas} = \frac{Q_v \nu \ell \cdot p_{atm}}{A \cdot \nabla p \bar{p}} \quad (2.4)$$

where  $p_{atm}$  is the atmospheric pressure at which  $Q_v$  is measured, and the driving pressure is given as a product of the differential pressure  $\nabla p$  and the mean pressure over the sample  $\bar{p}$ . The mean pressure  $\bar{p}$  is determined by the upstream and downstream pressures  $p_b$  and  $p_a$  such that  $\bar{p} = (p_b + p_a)/2$ . Under ambient conditions,  $p_a$  is equal to the atmospheric pressure  $p_{atm}$ , and  $p_b$  is equal to  $\nabla p + p_{atm}$ . The mean pressure therefore simplifies to  $\bar{p} = (\nabla p + 2p_{atm})/2$ .

In the following chapters, gas permeability was measured using a steady-state permeameter for all but a few samples (a selection of samples had too low a permeability to measure in this method, see [Chapter 3](#)). The apparatus is a commercial benchtop permeameter from Vinci Technologies which was modified for the purposes of this thesis by incorporating interchangeable El-Flow volumetric mass flowmeters (from Bronkhorst) to measure the volumetric flow rate of gas at the downstream end of experimental samples. A schematic of the modified setup is shown in [Figure 2.1](#). The off-the-shelf permeameter accommodates samples that are 25.4 mm in diameter. In order to be compatible with core samples with a 20 mm diameter (required for other experimental methods such as triaxial deformation), samples were inserted into impermeable rubber tubing (nitrile, viton, or silicone) with appropriate inner and outer diameters before being

loaded into the permeameter.

Gas permeability was measured using either nitrogen or argon as the permeant (pore fluid). A confining pressure of 1 MPa was applied radially to the sample, in order to ensure that no leakage can occur along its margins during measurement. The sample was then left under this confining pressure for 1 hour, to allow for any necessary microstructural equilibrium. As shown in [Figure 2.1](#), gas would then flow through the sample, whilst the volumetric flow rate  $Q_v$  and the pressure differential  $\nabla p$  across the sample were continuously monitored by means of customised data acquisition system and a LabVIEW program written for this purpose.

The pressure of gas entering the sample could be adjusted using a regulator attached to the permeant gas bottle. By altering the flow of gas, a range of different values of  $\nabla p$  was imposed across the samples (typically between 0.001 and 0.2 MPa). Once steady-state flow was achieved, the volumetric flow rate was noted. Thus with knowledge of the gas viscosity and sample dimensions, permeability could be calculated using [Equation 2.4](#). However, two scenarios can necessitate that post-measurement corrections need to be applied to the calculated values due to inertial effects: flow turbulence or gas slippage.

### 2.2.3 Non-laminar flow 1: Turbulence

Forchheimer (1901) conducted fluid flow experiments through porous media, noting that the relationship between the pressure differential  $\nabla p$  and the volumetric flow rate  $Q_v$  becomes nonlinear at high fluid velocities due to flow no longer being laminar. To account for this turbulence, an inertial term  $\iota$  must be introduced, such that:

$$\frac{1}{k_{fo}} = \frac{1}{k_{gas}} - \iota \cdot Q_v \quad (2.5)$$

where  $k_{fo}$  is the Forchheimer-corrected permeability value, and  $k_{gas}$  is the as-measured value. In this scenario, the measured gas permeability would be lower than the true (corrected) permeability, as turbulence induces resistance to fluid flow.

### 2.2.4 Non-laminar flow 2: Gas slippage

In his seminal 1941 paper, Klinkenberg showed that as the characteristic pore size or aperture approaches the mean free path of the permeant gas—the distance travelled between consecutive molecular collisions—interactions between the gas molecules and the pore (or crack) walls serve to reduce resistance to flow. Simply put, during liquid laminar flow, the layer of molecules adjacent to the pore (or

crack) walls is static. However, for gases this molecule layer has a nonzero velocity due to molecular diffusion ("slip"). This slippage results in a higher flow rate at any given pressure differential for a gas than a liquid. Accordingly, the permeability measured using a gas would be artificially higher than if determined using a liquid.

The relationship of Klinkenberg (1941) is incorporated thus:

$$k_{fo} = k_{kl} \left( 1 + \frac{1}{\bar{p}} \right) \quad (2.6)$$

where  $k_{fo}$  is the Forchheimer-corrected permeability calculated from gas flow experiments,  $\bar{p}$  is the mean flow pressure of gas in the system,  $b$  is the Klinkenberg parameter (which depends on both the gas used but also the pore structure), and  $k_{kl}$  is the Klinkenberg-corrected permeability value.

In the absence of inertial effects, plotting  $Q_v$  against the driving pressure (i.e.  $\nabla p \bar{p}$ ) yields a linear relationship. Deviations from linear behaviour indicate that one or both of the inertial phenomena described above are influencing the calculated permeability. In practice, the corrected permeability can be calculated using the slope and intercept of graphs of  $Q_v$  against  $k_{gas}^{-1}$ , and  $\bar{p}^{-1}$  against  $k_{fo}$ . Hereafter, measured permeability, corrected for turbulence and/or gas slippage when necessary, is always presented as  $k$ . Appendix 2A shows exemplary data from volcanic rocks which exhibit laminar flow, turbulence, and gas slippage. The effects of inertial flow, especially in the case of gas slippage tends to be slight, although non-negligible.

Sources of error in the permeability measurements include the sample dimensions, and the resolution of the pressure transducer and flow-meters. As mentioned, permeability is determined as a function of the  $Q_v - \nabla p \bar{p}$  curve, which is a series of points fit by a simple linear regression (when flow is laminar). The respective precision of the transducer and flowmeter is thus encompassed by the coefficient of determination of the regression line (i.e. its  $r^2$  value). If the data are unaffected by turbulence or gas slippage, then  $r^2$  is generally greater than 0.99. If flow is nonlaminar,  $r^2$  tends to be appreciably lower, and the permeability is determined using Equation 2.5 or 2.6 as appropriate. Repeat measurements suggest that experimental error is engirdled by the symbol size when plotted graphically.

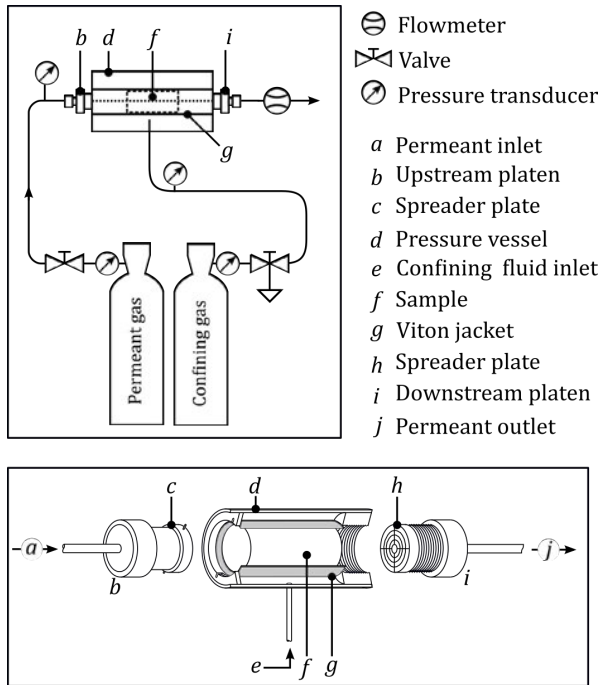


Figure 2.1: Schematic of steady-state permeameter used throughout this thesis. Arrows indicate direction of gas flow through sample. Lower panel shows sample assemblage in detail.

### 2.3 TRIAXIAL DEFORMATION

#### 2.3.1 Sample loading

After their initial characterisation, samples which were to undergo triaxial deformation were soldered into copper foil (in order that deformed samples could retain their structure upon unloading) and saturated with distilled water. A jacketed sample would then be inserted into a nitrile tube before being mounted inside the pressure vessel of the triaxial rig at Université de Strasbourg (as used by, for example, Klein and Reuschlé, 2003; Heap et al., 2014c; Baud et al., 2015) [Figure 2.2](#) shows a schematic of the deformation apparatus. The nitrile sheath ensured that the sample was isolated from the pressure chamber, which was filled with oil (the confining fluid) during deformation. However, the sample could still be subjected to changes in the imposed confining pressure  $p_c$  by injecting or withdrawing oil by means of a servo-controlled actuator (pressure intensifier). Similarly, the pressure of pore fluid (water) inside the sample  $p_p$  was controlled with a second intensifier. Confined samples were deformed by an axial loading ram controlled by a third actuator.

Samples were deformed either under a constant stress (where the force applied to the sample by the loading ram remained constant throughout all or part of the test), or at a constant strain rate. Strain

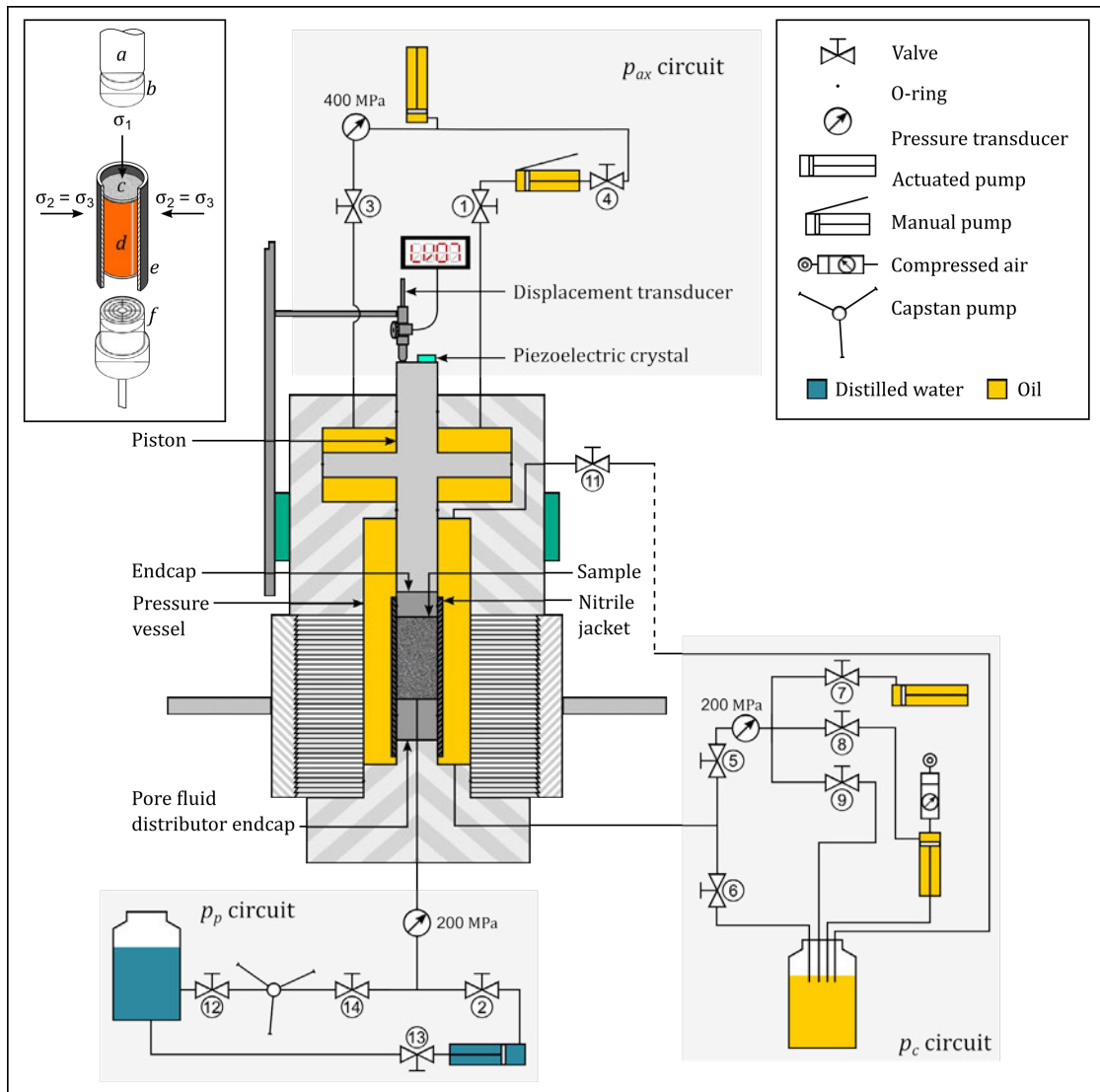


Figure 2.2: Schematic of triaxial deformation apparatus, including confining pressure ( $p_c$ ), pore pressure ( $p_p$ ), and axial pressure ( $p_{ax}$ ) circuits. Detail of sample assemblage is shown inset. a) axial piston; b) "blank" endcap; c) sample; d) copper foil jacket; e) nitrile jacket; f) pore fluid distributor endcap. Directions of major  $\sigma_1$  and minor  $\sigma_3$  principal stresses are as shown, such that  $\sigma_1 > \sigma_2 = \sigma_3$ . Not to scale. Numbered valves allow various parts of each circuit to be used at any given time.

$\varepsilon$  is a measure of sample deformation given as the fractional shortening of a sample  $\delta\ell/\ell$ , where  $\delta\ell$  is the change in length of a sample initially of length  $\ell$ . Axial strain is measured using a linear variable displacement transducer (LVDT) mounted to the top of the axial piston, and stress is monitored by a load cell.

The strain rate  $\dot{\varepsilon}$  adopted throughout is  $10^{-5} \text{ s}^{-1}$ . While strain rates encountered throughout any active volcanic system will undoubtedly vary in space and time, this value is comparable to shear rates inferred by Rust et al. (2003) to occur along volcanic conduit margins. Moreover, this strain rate assures that samples remain drained throughout deformation (sample deformation proceeds slower than the response of the pore pressure and the sample stays fully saturated during the experiment, discussed in a later section). The chosen rate is congruent with the international standard in rock mechanics (Kovari et al. 1983; see also Ulusay and Hudson 2007), meaning that the results displayed herein can be compared to the profusion of triaxial deformation data in the rock mechanics literature.

Throughout these chapters, the convention is adopted that stress and strain in compression are positive. Typically, mechanical data is presented as the differential stress, denoted as  $Q$ , against axial strain  $\varepsilon$ . Differential stress is defined as the difference between the major and minor principal stresses:  $Q = \sigma_1 - \sigma_3$  where  $\sigma_1$  and  $\sigma_3$  are the axial and confining pressures, respectively.

### 2.3.2 Porosity change

During deformation, the recorded movement of the pore pressure pore pressure actuator yields the change in pore volume during non-hydrostatic deformation and unloading of the sample, which is normalised to give the porosity change  $\delta\phi$ , related to the volumetric strain undergone by a sample.

### 2.3.3 Effective pressure

Any loading of a saturated porous medium is defined by the stress components  $\sigma_{ij}$  and the pore fluid pressure  $p_p$ . Moreover, if the poromechanical response of said medium to an applied stress coincides with that of the stress difference  $\sigma_{ij} - \alpha \cdot p_p \delta_{ij}$  then the latter quantity is referred to as the effective stress  $\langle \sigma_{ij} \rangle$ . In particular, if the coefficient  $\alpha$  is unity, then the quantity  $\sigma_{ij} - \alpha \cdot p_p \delta_{ij}$  corresponds to Terzaghi's formulation (a.k.a. Terzaghi's effective stress or Terzaghi's principle: Terzaghi, 1923; Baud et al., 2015). For elastic deformation, the effective stress law can be derived from the linear theory of poroelasticity (Berryman, 1992; Wang, 2000) with the effective stress coefficient given by

the Biot–Willis coefficient  $\alpha$ , whereby  $0 \leq \alpha \leq 1$  (e.g. Paterson and Wong, 2005). For inelastic deformation and failure,  $\alpha$  can be determined experimentally.

In conventional triaxial deformation experiments, this simple effective stress law is defined in terms of an effective pressure, whereby  $p_{eff} = p_c - \alpha \cdot p_p$ , with  $p_{eff}$  and  $p_c$  being the effective and confining pressures, respectively. Simply put, in the case where  $\alpha = 1$ , the stress regime on a sample deformed at respective confining and pore pressures of 10 and 15 MPa would be identical to that imposed with confining and pore pressures of 100 and 105 MPa, respectively (the effective pressure would be 5 MPa in both cases). In contrast, if the volumetric response of the fluid and solid constituents are unequal and  $\alpha < 1$ , then the stress regimes in the two scenarios will differ. In essence, this means that the measured failure stress of a sample would be different in each scenario, all other parameters being equal. There exists a paucity of data on this coefficient for the failure of porous rocks, largely due to the natural variability between samples, which makes its determination often challenging and sometimes quite impossible (a recent contribution by Baud et al., 2016 determined values of  $\alpha$  of 0.95 and 0.96 for sandstone deformed over a wide range of effective pressures in the dilatant and compactant regimes, respectively).

Since the subsequent chapters of this thesis present triaxial experiments at different pressures, it is important to verify that the effective pressure coefficient does not differ significantly from unity in porous volcanic rocks. As a pilot study, a series of constant strain rate tests were performed at the same nominal effective pressure according to Terzaghi's principle (i.e.  $p_{eff}$  if  $\alpha = 1$ ), but imposing different confining and pore pressures. In an attempt to minimise sample variability, samples of andesite (from Volcán de Colima, Mexico) were selected with the same connected porosity. The experimental conditions and differential stress at failure are given in [Table 2.1](#).

Here,  $\alpha$  is calculated as the value that equalises the ratio of the minimum and maximum peak stresses ( $\sigma_{p_a}$  and  $\sigma_{p_b}$ ) and the ratio of the corresponding effective pressures ( $p_{eff_a}$  and  $p_{eff_b}$ ):

$$\frac{\sigma_{p_a}}{\sigma_{p_b}} = \frac{p_{eff_a}}{p_{eff_b}} \approx 0.73 \quad (2.7)$$

which occurs when  $\alpha \approx 0.98$ , a value comparable to that determined recently by Baud et al. (2015) for Bleuerswiller sandstone. However, the natural variability in strength of these andesites is high: samples A5-09 and A5-11 were deformed under identical experimental conditions, yet there is a discrepancy of 18.68 MPa between their differential stresses at failure.

Table 2.1: Porosity, pressure conditions and differential stress at failure for porous andesite.  $p_p$ ,  $p_c$ , and  $p_{eff}$  correspond respectively to the pore, confining, and effective pressures. Along with the peak differential stress  $\sigma_p$ , all are given in MPa.

Sample	$\phi$	$p_p$	$p_c$	$p_{eff} = p_c - \alpha \cdot p_p$		
				$\alpha = 1$	$\alpha = 0.98$	$\sigma_p$
A5-09	0.09	55	60	5	6.13	138.87
A5-11	0.09	55	60	5	6.13	157.55
A5-13	0.09	105	110	5	7.16	177.61
A5-17	0.09	10	15	5	5.21	128.83

Given the level of natural heterogeneity in these Volcán de Colima andesites (a result of their complex and variable microstructure)—and indeed, in other intrusive and extrusive igneous rocks—it seems that these data are not sufficient to state conclusively that the effective pressure coefficient differs significantly from unity in these materials. For example, further tests would be required to ascertain whether  $\alpha$  is significantly influenced by physical or chemical properties of the rock (e.g. porosity, pore size distribution, mineralogical assemblage). Nevertheless, although the exact value of the Biot–Willis coefficient cannot be constrained in these andesites, this pilot study does confirm that the true value is not likely to differ significantly from unity. As such, the use of Terzaghi's principle of effective pressure in the presented tests has been considered a valid assumption.

### 2.3.4 Sample drainage

If the deformation of a sample proceeds at a rate faster than the response time of the pore pressure intensifier, the experiment is considered "undrained". In such a scenario, the tips of fast growing dilatant microcracks would not be fluid-saturated; this not only provides an underestimate of the porosity change during deformation, but can also influence the mechanical behaviour of the rock. Sample drainage was an important consideration in the experiments presented herein. If the experiments were undrained, there would be a discrepancy between the pore pressure expected in the rock (i.e. the measured/imposed value), and the actual pore pressure within the rock. This would further complicate matters by creating a heterogeneous pore pressure distribution within the sample. In order to assess whether samples were drained (i.e. fully saturated) during all the experiments, the setup shown in [Figure 2.3](#) was used. This experimental setup allowed the increase or decrease of pore pressure using an intensifier whilst monitoring both up- and downstream pressure. When the downstream valve ( $h$  in [Figure 2.3](#)) is closed, any pressure deviation

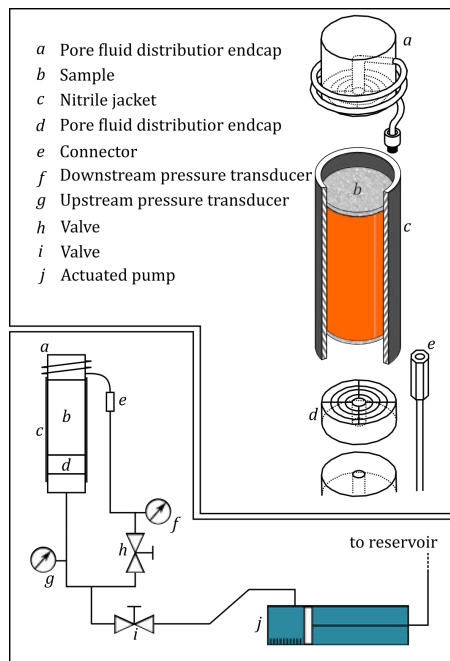


Figure 2.3: Schematic of the setup used to test sample drainage. When the upstream valve is open, pore pressure within the sample can be increased or decreased by the intensifier (*j*). If the downstream valve is open, then the pore pressure circuit is fully connected. However, when (*i*) is open and (*h*) closed, the pressure response measured at (*g*) depends on whether or not the sample is fully saturated.

measured by the downstream transducer (*f* in Figure 2.3) must first have flowed through the sample. By servo-controlling the upstream pore fluid pressure and monitoring the downstream pressure, it can be determined whether the sample is drained at different pressure increase rates.

Using a sample of porous andesite, pore pressure was oscillated between 10 and 20 MPa, whilst confining pressure was maintained at 40 MPa. Pressure was cycled at incrementally faster rates, from an initial value of  $5.0 \times 10^{-2}$  MPa s $^{-1}$ , to a final rate of  $5.0 \times 10^{-1}$  MPa s $^{-1}$ . Were the sample undrained, one would expect to see a delay in the response of the downstream pressure relative to the upstream pressure. However, as shown in Figure 2.4, no delay can be seen. This indicates that the permeability of these porous andesites is sufficiently high to preclude sample desaturation, even at significantly high rates of pore pressure increase (much higher than those imposed during any of the tests).

### 2.3.5 *A note on temperature*

Other than in extreme proximity to the conduit, host rock in a volcano will rarely be above the glass transition temperature of its melt phase  $T_g$  (the distance to which heat can propagate from the conduit into the edifice over time  $t$  is proportional to  $\sqrt{\kappa t}$ , where  $\kappa$  is the thermal conductivity of the edifice rock). All triaxial tests presented throughout this thesis were carried out at room temperature, though it is acknowledged that some chemical and mechanical processes may be enhanced even at temperatures below this threshold. Mechanically,  $K_{Ic}$ —the critical stress intensity factor—may be lowered at increased temperature (Meredith and Atkinson, 1985), allowing cracks to grow at lower stresses. Chemically, the rate of stress-corrosion cracking has been shown to increase with increasing temperature (see Brantut et al., 2013, for a review).

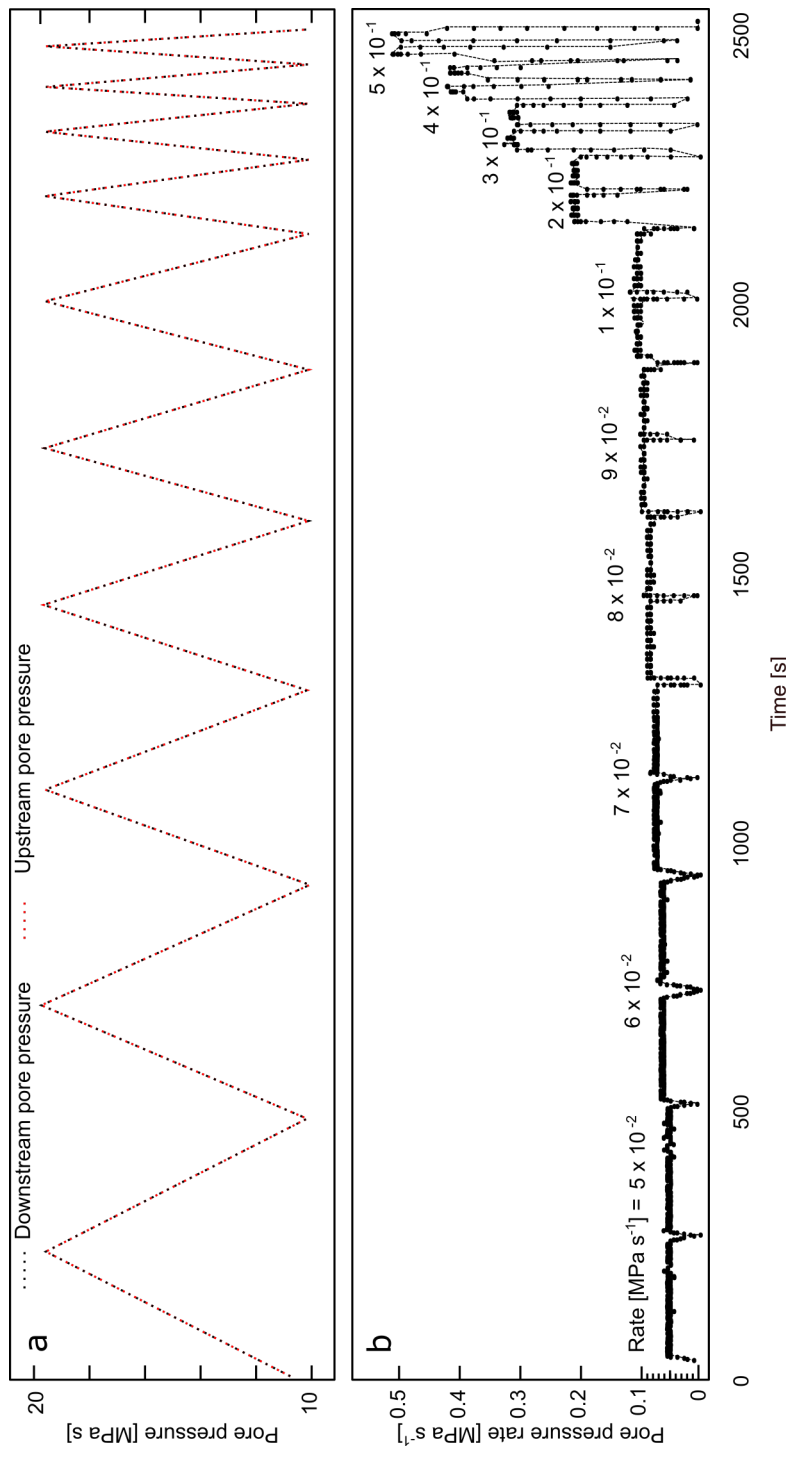


Figure 2.4: Mechanical data from a triaxial experiment designed to examine sample drainage in porous andesitic rock (sample C8). a) Pore pressure against time showing the monitored upstream (red dotted curve) pressure as a function of changing downstream (black dotted curve) pressure. b) Pore pressure rate against time showing the (absolute) rate of pore pressure change during the experiment.



# 3

## MICROSTRUCTURAL CONTROLS ON VOLCANIC ROCK PERMEABILITY

---

... they are wholly marred,  
so mightily hath passed upon them the vapour of fire.

— Homer, *The Odyssey*, c. 850 BCE

*The permeability of a volcanic edifice, amongst other parameters, is of great importance in governing eruptive style, magnitude, and frequency of active stratovolcanoes. In order to investigate how permeability (and other properties) may evolve in a volcanic system, it is important to first examine the range of values expected in a natural volcanic environment. Moreover, in order to establish a foundation upon which to base discussions of volcanic rock permeability and its effect on volcanic systems, it is important to understand the underlying properties that govern permeability itself. This chapter comprises a combined field and laboratory study of andesites from Volcán de Colima, a volcano whose geology, geometry, and eruptive activity are generally representative of intermediate stratovolcanoes. The study involves an assessment of density and permeability measurements performed in the field, bolstered by laboratory measurements and Scanning Electron Microscope analysis.*

These data and conclusions are published as: **Farquharson, J. I., M. J. Heap, N. Varley, P. Baud, and T. Reuschlé, 2015. Permeability and porosity relationships of edifice-forming andesites: A combined field and laboratory study. Journal of Volcanology and Geothermal Research. 297, 52-68.**

### 3.1 INTRODUCTION

Models of volcanic processes must be built on a foundation of observed or experimentally derived parameters; however, as we often wish to understand fluid flow in regions of the edifice that are difficult or indeed impossible to access, permeability cannot necessarily be determined *in situ*. It is thus of importance to relate transport properties of porous volcanic rocks to the governing physical properties, such as porosity.

Though it is evident that the capacity for fluid transport through a porous rock is somewhat dependent on its connected pore space  $\phi$ , it is nontrivial to define a precise relationship due to the microstructural complexity of the medium involved (e.g. Zhu and Wong, 1996;

Bernabé et al., 2003). Generally, permeability  $k$  is estimated as some function of connected porosity, such that  $k = f(\phi)$ , where  $f$  may include further parameters such as tortuosity  $\tau$  or pore aperture radius. This relation then forms the basis of permeability modelling reliant on empirical or semi-empirical Kozeny–Carman equations (geometrical models), or network modelling (statistical models) (see Guéguen and Palciauskas, 1994 for a review).

It is recognised that no all-encompassing theory exists to describe this relationship in all media, due primarily to the fact that some pore geometries may be more effective than others at transporting fluid (e.g. Bernabé et al., 2003). Nevertheless, models such as the Kozeny–Carman (see Kozeny, 1927; Carman, 1937), or percolation theory (Sahimi, 1994) have been employed and modified in order to describe the behaviour of volcanic rocks (e.g. Klug and Cashman, 1996; Klug et al., 2002; Mueller et al., 2005; Costa et al., 2006). In turn, estimates of permeability can be included in numerical simulations of various volcanic processes, with the ultimate aim of predicting the behaviour of a given volcanic system (e.g. Lacey et al., 1981; Day, 1996; Clarke et al., 2002a, b; Reid, 2004; Collinson and Neuberg, 2012; Lavallée et al., 2013).

Previous experimental studies concerning the permeability and porosity of volcanic rocks (e.g. Eichelberger et al., 1986; Klug and Cashman, 1996; Tait et al., 1998; Saar and Manga, 1999; Klug et al., 2002; Melnik and Sparks, 2002; Sruoga et al., 2004; Mueller et al., 2005; Wright et al., 2006; Bernard et al., 2007; Bouvet de Maisonneuve et al., 2009; Yokoyama and Takeuchi, 2009; Heap et al., 2014a, b; Gaunt et al., 2014; Okomura and Sasaki, 2014; Kushnir et al., 2016) have highlighted a vast range of measured values.

Porosity of the various volcanic materials—as determined in these laboratory-based studies—has been shown to range from essentially nonporous glasses to scoracious ejecta with porosity of 0.90, while permeabilities in the range of  $10^{-17} – 10^{-8}$  m<sup>2</sup> have been measured. The spatiotemporal variations of the physical properties of volcanic rocks necessitate the sampling of a statistically robust dataset (Kueppers et al., 2005; Bernard et al., 2015). In light of these factors, the research herein comprises a systematic field campaign assessing the permeability of edifice-forming rocks representative of a typical andesitic volcano. Combined with field-based density measurements and a complementary laboratory-based study, the microstructural processes governing permeability in volcanic rocks are explored.

### 3.2 CASE STUDY: VOLCÁN DE COLIMA

Volcán de Colima is situated at  $19^{\circ}30'45.82''\text{N}$ ,  $103^{\circ}37'2.07''\text{W}$  on the Colima–Jalisco border at the south-western margin of the Trans-Mexican Volcanic Belt (Figure 3.1). Along with the extinct Nevado edifice, the volcano comprises the Colima Volcanic Complex, marking the conjunction of the Colima rift zone and the Tamazula fault (Rodríguez-Ellizarrás, 1995; Norini et al., 2010). Overlying a Cretaceous basement consisting of deformed volcanic and sedimentary rocks (Rodríguez-Ellizarrás, 1995), Volcán de Colima forms a typical stratocone, with eruptive products varying little in bulk composition: crystal-rich andesites with  $\text{SiO}_2$  contents typically between 58 - 61 wt.% (Luhr et al., 2002; Mora et al., 2002; Valdez-Moreno et al., 2006; Reubi and Blundy, 2008; Savov et al., 2008). Historic volcanism has been characterised by periods of effusive activity (dome formation and lava flows, determined by magma ascent rates), punctuated by frequent Vulcanian explosions and commonly culminating in voluminous Plinian eruptions (e.g. Luhr, 2002; Varley et al., 2010; James and Varley, 2012; Lavallée et al., 2012).

Volcán de Colima exhibits many characteristics common to convergent margin volcanoes, such as Santa María (Guatemala), Ruapehu (New Zealand), Lascar (Chile), Mount Merapi (Indonesia), Citlaltépetl (Mexico), or Egmont Volcano (New Zealand): the steep conical edifice structure overlying a sedimentary basement (e.g. Carrasco-Nuñez, 2000; Smyth et al., 2005; Gaylord and Neall, 2012) fosters frequent collapse events (e.g. Rose Jr et al., 1977; Gardeweg et al., 1997; Gamble et al., 1999; Camus et al., 2000; Carrasco-Nuñez, 2000), with cyclic eruptive behaviour interspersing periods of dome effusion (e.g. Rose Jr et al. 1977; Houghton et al., 1987; Gardeweg et al., 1997; Gamble et al., 1999; Camus et al., 2000; Carrasco-Nuñez, 2000; Gaylord and Neall, 2012). Combined with its consistently intermediate composition, it is reasonable to propose Volcán de Colima as generally representative of andesitic stratovolcanoes worldwide.

### 3.3 METHODS

#### 3.3.1 Field methods

A total of 572 hand samples were collected from sites around the volcano (shown in Figure 3.1), comprising over half a metric ton of andesitic edifice rock. The sites are debris-flow tracks, locally termed barrancas: La Lumbre, Montegrande, and El Zarco; as well as a site at El Playón, the area between the summit cone and the ancient caldera wall (Figure 3.1). Each barranca is a potent vestige of where pyroclastic currents and lahars have coursed down the mountainside,

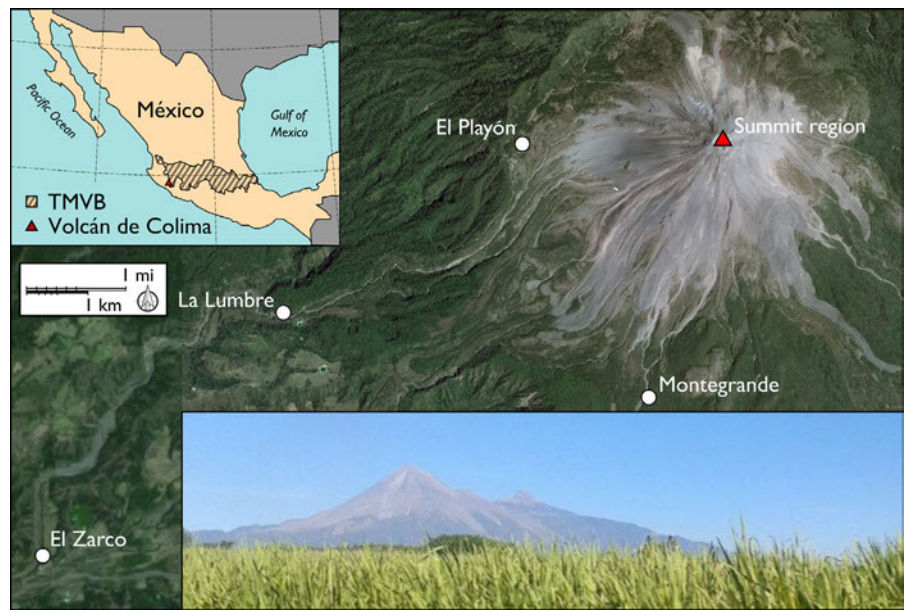


Figure 3.1: Sampling sites at Volcán de Colima: El Playón (PLY), Montegrande (MG), La Lumbre (LL), and El Zarco (EZ). Inset map gives the location of Volcán de Colima within the Trans-Mexican Volcanic Belt (TMVB). Map is a composite of Google Earth™ imagery ( $19^{\circ}30'45.82''\text{N}$ ,  $103^{\circ}37'2.07''\text{W}$ ).

scarring the landscape with a series of steep debris-ridden gullies radiating away from the summit. These flow phenomena are an ever-present threat during periods of unrest at Volcán de Colima (as shown in the photo of Figure 3.2, taken from one of the base camps during fieldwork).

These sites were chosen due to their accessibility and the fact that they all include exposed areas with abundant suitably-sized material for the purposes of the following methods (i.e. approximately fist-sized: Figure 3.2a, c,d,f). From a random starting location at each site, loose surface rocks were collected from the immediate vicinity. The collected samples comprise a range of variably remobilised and re-worked explosive and effusive products, representative of the edifice-forming materials. A portable air permeameter (Vindum Engineering TinyPerm II) was used to measure the permeability of each hand sample. By evacuating air from a rock, the TinyPerm II unit calculates a value based on the monitored response function of the transient vacuum at the nozzle-rock interface, which corresponds to the sample permeability. The relation between the given TinyPerm value and Darcian permeability is discussed in Appendix B.

The ability to make autonomous and rapid measurements is extremely useful when working in the field; as such these permeameters have seen increasing use in volcanology and related geoscience disciplines (e.g. Possemiers et al., 2012; Invernizzi et al., 2014; Vign-

aroli et al., 2014; Schaefer et al., 2015; Kendrick et al., 2016). For this reason, [Appendix B](#) also includes systematic assessment (comprising 400 measurements) of the capabilities, accuracy, and repeatability of a TinyPerm unit.

Permeability anisotropy in volcanic rocks has been discussed by several authors (e.g. Clavaud et al., 2008; Wright et al., 2009; Gaunt et al., 2014), resulting as a function of anisotropic bubble growth and crack propagation during ascent, eruption, and emplacement of volcanic materials. In laboratory measurements, the pathway for fluid flow can be approximated as a cylindrical sample is peripherally confined the rate of flow through the sample is controlled ([Chapter 2](#)). The field process, on the other hand, involves the evacuation of irregularly shaped, unconfined samples, meaning that measurement is nominally isotropic, even if the actual permeability of the sample is not. As the edifice is constructed of rocks chaotically oriented with respect to any existing anisotropy, field permeability was measured on an average of three faces for each sample (where this was possible: given the heterogeneous shape and size of the hand samples, this procedure was not always feasible).

Bulk rock density was also determined for each sample using an Archimedean weighting method similar to that employed by Kueppers et al. (2005). The method described herein differs in that it accounts for imbibition in the post-processing stage, rather than during the measurement itself: specifically, Kueppers et al. (2005) vacuum-seal rocks in plastic bags to avoid this process. The setup consisted of a balance mounted on a tripod, with a water-filled bag suspended underneath ([Figure 3.3](#)). A windbreak was used in the field in order to minimise the effects of wind on the balance (see inset in [Figure 3.3](#)). The balance, with a precision of 0.1 g and a load limit of 5000 g, was used to measure the weight of the rock in air (point *a* in [Figure 3.3](#)), and the apparent immersed weight taken in a sample basket (point *b*). Assuming the fluid (water) density to be 1000 kg m<sup>-3</sup> (1 g cm<sup>-3</sup>), then bulk rock density  $\rho$  can be determined from the Archimedes principle, such that:

$$\rho = \frac{W}{W - W_I} \quad (3.1)$$

where  $W$  is weight in air,  $W_I$  is the apparent immersed weight, and the denominator is hence equal to the weight of displaced fluid. Measurements of density were subsequently transformed into porosity data; full details are presented in [Appendix C](#). A limit to this method arises in the measurement of some highly pumiceous samples: highly porous pyroclasts with a specific gravity < 1 could not be immersed in water due to their buoyancy. While samples could be weighed down with an object of known calibration mass, this method was not em-



Figure 3.2: Photographs from field campaign at Volcán de Colima. a) Montegrande, a barranca where much of the fieldwork was carried out. Oliver Lamb for scale. b) Pyroclastic density current generated through the collapse of relatively small eruption column. Photo taken from the base camp at El Playón, another of the sample sites. c - d) Base camp at El Playón. Measured rocks were assigned an alphanumeric identifier, labelled, and stored under a tarpaulin sheet during fieldwork. e) Density and TinyPerm measurements being carried out in the field (Montegrande). f) All samples were transported to the Centro de Intercambio e Investigación en Vulcanología (CIIV) at Universidad de Colima, in order to be photographed and repeat measurements made. g) Repeat measurements being performed. h) One of numerous Vulcanian explosions observed while collecting samples. Photo taken from the northern flank of the volcano, approximately 800 m from the active summit region.

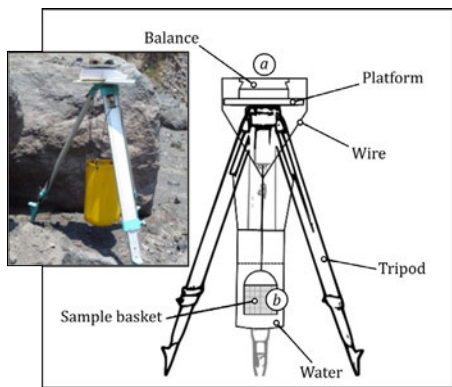


Figure 3.3: Schematic of the field setup for measuring sample density (inset shows a photograph), based on the method employed by Kueppers et al. (2005). Weight measurements are performed at points *a* and *b* (see text for discussion). Bag provided by Landjoff Ltd.

ployed in this study, mainly due to the fact that relatively few (7) of these highly pumiceous samples were collected.

In addition to quantitative measurements, each hand sample was also categorised in terms of visible alteration or structure, or differences in colour; examples of each of these categories are given in Figure 3.4. In order to be of practical use in the field, classifications are based on differences readily discernible in hand samples, as such none of the following descriptors are used with a compositional or genetic connotation. "Pumiceous" samples are defined by their high vesicularity, low density, and pale grey colour (Figure 3.4c). Samples containing an abundance of large pores and being dark grey to black in colour are referred to as "scoracious", although these textures can extend to lower porosities as well, and occasionally exhibit additional comagmatic features (Figure 3.4d). Volcanic material that cannot be texturally described as pumiceous or scoracious is simply referred to hereafter as "lava" (Figure 3.4b). "Lava" is generally grey aphanitic to porphyritic juvenile andesite; however rocks in these three categories could also display a variable degree of alteration, including oxidation (examples of which are given in Figure 3.4e – h). Alteration is also manifest in general weathering of the rocks (e.g., due to rainfall, fluvial reworking, and other transport processes), as well as mineral phase replacement resulting from hydrothermal processes (John et al., 2008; Lavallée et al., 2012). The strong correlation of connected porosity and density determined in the following section attests to there being very little variation in bulk composition across the range of samples (see Appendix C).

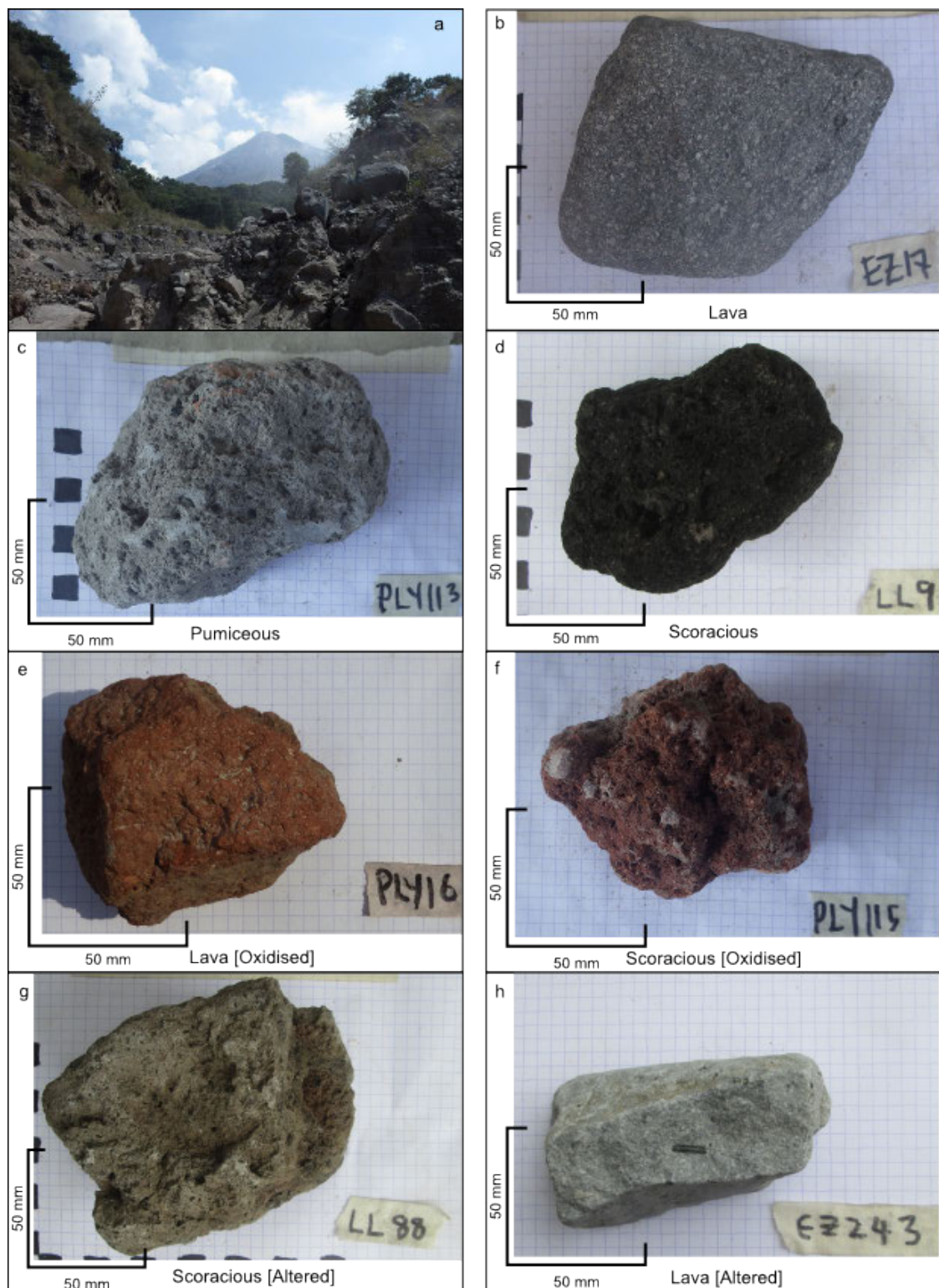


Figure 3.4: Rock classification scheme. a) Barranca Montegrande, a representative debris-flow-track from which samples were collected. Summit of Volcán de Colima can be seen in the background. b) Pristine porphyritic lava. c) pumiceous pyroclast. d) Scoracious sample, characterised by large, variably elongated pores (vesicles), and typically dark in colour. e) and f) show oxidised samples, as evidenced by their brick red colour. Texturally f) is described as scoracious, respectively. g) and h) both show examples of altered clasts: in g) significant post-emplacement weathering can be observed; in h) evidence of hydrothermal vapour-phase alteration can be seen.

### 3.3.2 Laboratory methods

To complement the field study, a selection of samples was collected to be analysed in the Experimental Geophysics laboratory at Université de Strasbourg. Not only does this afford a more robust exploration of their physical properties and the opportunity to image their microstructure, but also allows access to permeability data in a range below that measurable by the TinyPerm unit. Based solely on their density, eleven rocks were sub-sampled from the entire dataset, to represent the range of porosities observed in the field. Variations in texture or permeability were not considered at this point (the selection process was thus a stratified-random sampling method). Seventeen cylindrical cores, 20 mm in diameter, were obtained from the sample set and precision ground to a nominal length of 40 mm.

Connected water porosity, connected gas porosity, and powder density were measured using the methods described in [Chapter 2](#). The permeability of samples at the extremes of the porosity range (i.e.  $\phi \leq 0.05$  or  $\geq 0.55$ ) could not be measured accurately in the benchtop permeameter at that time, so these were measured independently by Thierry Reuschlé at Université de Strasbourg using the pulse decay method. Total porosity  $\phi_t$  was determined as  $1 - (\rho_b / \rho_s)$ , i.e. the ratio of bulk and power densities for each sample, allowing unconnected porosity  $\phi_u$  to be calculated as  $\phi_t - \phi$ . The double-weight field method was also tested in the laboratory by performing an equivalent set of measurements (i.e. dry mass and apparent immersed dry weight), shown in [Appendix C](#) ([Figure C.1](#)). Gas permeability of each core was measured as outlined in [Chapter 2](#). It should be noted that cores were obtained in only one direction from each of the 11 hand samples; consequently, subsequent analyses and discussion do not account for potential anisotropy in these rocks. Hydraulic radii of samples were determined with Brunauer, Emmett, and Teller krypton adsorption (BET) by Thierry Reuschlé, in order to use the modified Kozeny–Carman relation (after Heap et al., 2014b) to assess microstructural controls on the permeability of these rocks. The revised Kozeny–Carman equation can be shown as (Yokoyama and Takeuchi, 2009; Heap et al., 2014b):

$$k_{KC} = \frac{\phi^3}{b \cdot \tau^2 \rho_b^2 S_{BET}^2} \quad (3.2)$$

where  $k_{KC}$  is the predicted permeability,  $S_{BET}$  is the specific surface area, and  $b$  is a geometric constant. Assuming that porosity is either crack-controlled ( $b = 12$ ), or a pore-controlled ( $b = 8$ ) (Bernabé et al., 2010) the equation can thus be solved for tortuosity  $\tau$  by substituting  $k_{KC}$  with the measured permeability of each sample.

### 3.4 RESULTS AND DISCUSSION

#### 3.4.1 Density distribution from the vent

Of the 572 collected samples, density could not be determined for a number of samples which were too buoyant for the field density method. [Figure 3.5](#) shows the density of the remaining samples collected at each of the sampling sites shown in [Figure 3.1](#). The data are here plotted in accordance with the weighted abundance analysis presented in [Bernard et al. \(2015\)](#). Relatively uniform or bimodal distributions in density and porosity are seen at the site closest to the active summit region (i.e. El Playón), while the distribution becomes unimodal and notably skewed towards high densities (low porosities) as one moves to sites increasingly more distal: Montegrande, La Lumbre, and El Zarco, respectively. This phenomenon has been noted in previous field studies (e.g. [Kueppers et al., 2005](#)), and can be attributed to the increased transport distance and associated degradation of more friable, porous materials. As volcanic deposits are remobilised away from the vent, higher-porosity rocks will be preferentially comminuted into smaller size classes by processes such as abrasion, collision, and fluvial reworking (as shown experimentally by [Manga et al., 2011; Kueppers et al., 2012](#)). As such, the proportion of relatively dense rocks should increase with distance from the vent, as observed in these data.

The array of porous media collected and measured in the course of this study indicates that edifice material (and hence, the edifice of Volcán de Colima) exhibits extraordinary heterogeneity in terms of its physical properties. A wide range of densities can be observed in the dataset, from 1142.40 to 2813.79 kg m<sup>-3</sup>, indicating a correspondingly broad variance in porosities (0.025 - 0.73).

The porosity within volcanic materials can either be in the form of cracks (due to thermal, mechanical, or chemical stresses) or pores, the frozen-in relicts of bubble formation, growth, and coalescence. As the volatile content in magma comprises one of the fundamental driving forces of explosive activity, the post-eruptive porosity allows insight into the eruption dynamics and pre- and syn-eruptive conditions within the conduit (e.g. [Kueppers et al., 2005; Gonnermann and Manga, 2007; Mueller et al., 2011](#)). A tendency towards relatively high porosity values (e.g. as observed at El Playón: [Figure 3.5](#)) is indicative of deposits of predominantly explosive origin, while low-porosity data is associated with predominantly extrusive material ([Mueller et al., 2011](#)); the range of measured porosities thus attests to the array of observed eruption styles at Volcán de Colima (e.g. [González et al., 2002; Mueller et al., 2011](#)). Variability of host-rock porosity also exerts

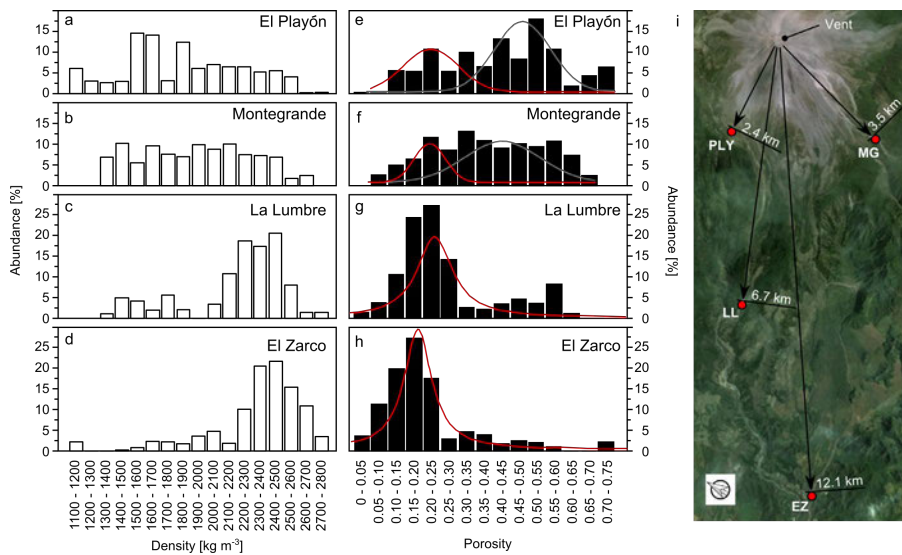


Figure 3.5: a) - d) show the density distribution of collected samples for each of the collection sites. e) - h) shows the porosity distribution across the sample sites. Data are shown in terms of their weighted abundance, after Bernard et al. (2015). The map (i) indicates the relative distance of each site from the active vent. Note that distance indicated is the minimum transport distance (i.e. straight-line distance). PLY = El Playón; MG = Montegrande; LL = La Lumbre; EZ = El Zarco. Peaks in the high-end of the density distributions are described by the red curves. Low-density peaks are shown by grey curves. For El Playón and Montegrande, the distribution is bimodal; La Lumbre and El Zarco show increasingly skewed distributions. Curves fitted using Origin data analysis software. Data comprises 118, 94, 97, and 232 samples respectively at each study site.

a significant influence over strength and deformation modes within the edifice, in turn affecting outgassing through the edifice and flank stability (Heap et al., 2015a). As such, it is imperative that future models of volcanic processes—such as conduit outgassing or mechanical stressing of the edifice—account for the potential diversity of the physical rock properties which underpin these processes.

The density distribution of the erupted material at Volcán de Colima over time is best approximated by that of samples measured at El Playón, closest to the active summit crater: Figure 3.5 shows that this distribution is bimodal. If the initial volatile content of magma is assumed to be roughly equivalent through time, we can surmise that—in general—dense rocks result from efficiently outgassed magma, likely to have erupted effusively. On the other hand, the lower density peak represents inefficient outgassing of magma and the retention of explosive potential energy. The low porosity and permeability of dense lavas will consequently limit outgassing, resulting in the eruption of less dense material. In turn, this material will increase the per-

meability of the edifice, fostering extrusion of dense products, and so the cycle continues. Thus, explosive decompression and fragmentation serves to facilitate outgassing in future eruptive cycles (e.g. Gonnermann and Manga, 2003). It is probable that the range of porosities is therefore linked to the frequency and cyclicity of highly explosive eruptions at Volcán de Colima (e.g. Robin et al., 1991; Luhr, 2002), and at least partially dictates the observed transition between explosive and effusive behaviours.

Further, previous works have shown that porosity has a significant influence on the strength and failure mode of volcanic rocks (e.g. Zhu et al., 2011; Heap et al., 2014b). The increased proportion of high-porosity material near the vent and proximal flanks of the volcano will consequently decrease stability in this region, leading to more frequent, local slope failure than observed distal to the vent.

### 3.4.2 Porosity and permeability relationship

The initial dataset of 572 hand samples contained 30 samples which were either too buoyant or of too low a permeability to determine porosity or permeability in the field (the lower limit of the field permeameter did not permit measurements of permeability for some of the very low porosity samples). Samples for which a value for either porosity or permeability could not be obtained are not included in any further analysis. Transformed field data are displayed in [Figure 3.6](#): these data show that there is a general trend of increasing permeability with increasing porosity. Porosity values range from 0.025 to 0.73, while permeabilities lie between  $7.6 \times 10^{-16}$  and  $6.5 \times 10^{-11} \text{ m}^2$ .

For rocks of comparable porosity, a difference in permeability of up to four orders of magnitude can be observed, as has been noted in previous studies of volcanic materials (e.g. Saar and Manga, 1999; Klug et al., 2002; Mueller et al., 2005; Bouvet de Maisonneuve et al., 2009; Wright et al., 2009; Yokoyama and Takeuchi, 2009). Moreover, comparable values of permeability can also be associated with rocks with very different porosities. While part of this distribution may be explained by permeability anisotropy (as discussed previously; see e.g. Clavaud et al., 2008; Wright et al., 2009; Gaunt et al., 2014), microstructural attributes such pore geometry will contribute significantly to permeability. For instance, a rock with a single through-running crack could have a very low porosity, whilst providing an effective fluid conduit. On the other hand, a rock structure consisting of many large pores connected by tortuous microcracks could be poor at transmitting fluids, despite having a relatively high porosity. It is important to note that the edifice is haphazardly constructed of variably

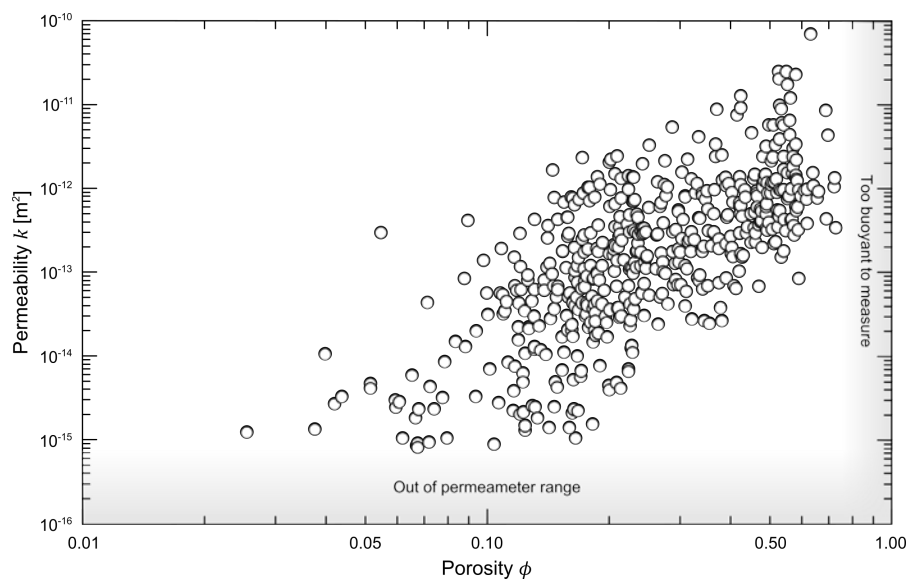


Figure 3.6: Permeability – porosity data for 542 samples across all sample sites and all classifications, as measured in the field. Shaded areas indicate regions where the field methods were ineffective, either because sample permeability was below the limit of the permeameter, or because samples were too buoyant to measure using the double-weight method outlined in the text; in the cases where a measurement for either porosity or permeability could not be obtained, the data are not shown. Each point is a mean value from multiple measurements, as discussed in the text.

porous material with differing eruptive and emplacement histories: in reality, a representative suite of edifice-forming rocks is bound to contain both these end-members and a range of more or less effective pore geometries in between (discussed in detail below). Due to this inherent natural variability, it is therefore unsurprising that a large degree of scatter is evident in these field data.

[Figure 3.7](#) displays the field permeability data grouped by the rock classification scheme described previously (lava, scoracious, pumiceous, altered and oxidised). Notably, the degree of scatter observed in [Figure 3.7](#) appears to be largely unaffected by meso-scale textural differences, or by syn- or post-eruption alteration. Juvenile lava ([Figure 3.4b](#), [3.7a](#)) comprises the majority of field samples ( $n = 378$ ), and encompasses the range of measured permeabilities and porosities. For any given porosity, permeability may differ by up to four orders of magnitude, a phenomenon which is consistent for the oxidised and altered rocks (denoted by the red and black filled symbols, respectively). Scoracious samples ([Figure 3.4d](#), [3.7b](#)) display a similar range of permeability for a given porosity, with porosities of around 0.60 yielding permeability values from  $7.8 \times 10^{-14}$  to  $6.5 \times 10^{-11} \text{ m}^2$ . It is possible that the elongation of vesicles associated with scoracious deposits gives rise to a significant degree of permeability anisotropy, as discussed by Wright et al. (2009). Pumiceous samples ([Figure 3.4c](#)) exhibit a narrower extent of permeabilities, from  $6.3 \times 10^{-14}$  to  $1.4 \times 10^{-12} \text{ m}^2$  ([Figure 3.7c](#)), however this is presumably a product of their low sample number ( $n = 16$ ) relative to the other classes. While hydrothermal alteration, weathering, or oxidation will influence the porosity and permeability of an individual sample, following the subdivision of the data into these categories, the general permeability–porosity trend (as observed in [Figure 3.6](#)) is unaffected, as shown in the synopsis plot of [Figure 3.7d](#).

### 3.4.3 Volcán de Colima: microstructurally complex

To provide deeper insight into the observed variability of the field samples, laboratory measurements of physical rock properties (including permeability) were performed on select rocks, and an assessment of the micro-scale complexities in andesites representative of the observed porosity range of edifice-forming rocks. Measuring permeabilities in the laboratory allows the inclusion of samples that would otherwise fall below the measurable limit imposed by the field method. Given that meso-scale textural differences have been shown to explain little of the variation in the field data ([Figure 3.7](#)), the sample set is comprised of juvenile lava, scoracious, and pumiceous material in order to maximise the porosity range (from 0.04 to 0.59,

Table 3.1: Physical properties of a suite of Volcán de Colima andesites, including porosity, bulk density, specific surface area, permeability, tortuosity, and connectivity. Tortuosity has been calculated according to [Equation 3.2](#), assuming  $b = 8$  or  $12$  (see text for discussion). Letter in brackets refers to sample classification: L = lava; S = scoriaous; P = pumiceous.  $\phi$  and  $\phi_u$  are connected and unconnected porosity, respectively.  $\Gamma$  = connectivity;  $\rho_b$  = bulk density;  $S_{BET}$  = specific surface area;  $k$  = gas permeability;  $\tau$  = tortuosity.

Sample	$\phi$	$\phi_u$	$\Gamma$	$\rho_b$ [kg m <sup>-3</sup> ]	$S_{BET}$ [m <sup>2</sup> kg <sup>-3</sup> ]	$k$ [m <sup>2</sup> ]	$\tau$
EZ_120 (L)	0.19	0.017	0.91	2139.32	28	$2.72 \times 10^{-13}$	0.90
EZ_121 (L)	0.10	0.003	0.97	2454.39	18	$6.05 \times 10^{-14}$	0.79
EZ_69 (L)	0.05	0.011	0.76	2670.47	522	$1.62 \times 10^{-17}$	0.50
EZ_94 (L)	0.04	0.006	0.82	2658.23	546	$9.47 \times 10^{-17}$	0.13
LL_43a (S)	0.47	0.008	0.98	1422.23	96	$4.17 \times 10^{-13}$	1.29
LL_43b (S)	0.48	0.009	0.98	1386.71	82	$4.48 \times 10^{-13}$	1.55
LL_74a (L)	0.11	0.007	0.93	2396.42	59	$5.29 \times 10^{-14}$	0.31
LL_74b (L)	0.09	0.009	0.90	2448.07	47	$1.25 \times 10^{-15}$	1.76
LL_96 (S)	0.45	0.017	0.96	1450.14	212	$4.37 \times 10^{-13}$	0.52
MG_02 (L)	0.23	0.008	0.97	2054.79	36	$4.37 \times 10^{-13}$	0.82
MG_22a (L)	0.27	<0.001	1.00	1943.45	42	$4.39 \times 10^{-13}$	0.94
MG_22b (L)	0.25	<0.001	1.00	2024.24	36	$4.39 \times 10^{-13}$	0.89
MG_28 (S)	0.47	0.010	0.98	1436.68	53	$4.67 \times 10^{-13}$	2.16
PLY_116a (P)	0.58	0.020	0.96	1094.30	56	$3.94 \times 10^{-12}$	1.27
PLY_116b (P)	0.58	0.021	0.96	1081.20	70	$1.75 \times 10^{-12}$	1.56
PLY_116c (P)	0.59	0.020	0.97	1042.74	63	$1.40 \times 10^{-12}$	2.08
PLY_116d (P)	0.59	0.022	0.96	1060.52	61	$1.77 \times 10^{-12}$	1.84

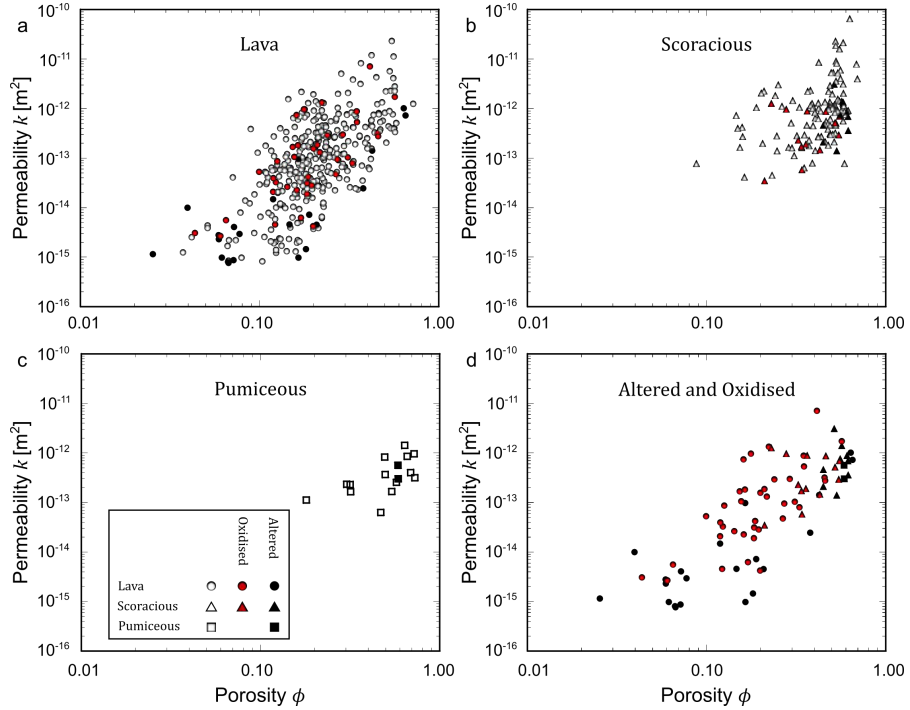


Figure 3.7: Permeability – porosity data sorted by sample classification; a) lava ( $n = 390$ ); b) scoracious material ( $n = 136$ ); c) pumiceous material ( $n = 16$ ); and d) altered (including oxidised) samples ( $n = 95$ ). By definition, scoracious and pumiceous rocks (b, c) occupy only the higher-porosity domain. Lava, altered, and oxidised samples (a, d), on the other hand, encompass the whole range of porosities and permeabilities.

in 17 cylindrical cores; see [Table 3.1](#)).

[Figure 3.8](#) displays the laboratory-determined values for permeability and connected gas porosity against other measured or calculated physical properties: specific surface area, tortuosity ([Equation 3.2](#)), and overall connectivity. As a proxy for overall pore connectivity within these andesites, a dimensionless parameter  $\Gamma$  is defined such that  $\Gamma = 1 - (\phi_u / \phi)$ . Physical property data for each sample are also given in [Table 3.1](#).

As observed in the field data ([Figure 3.6](#)), permeability increases with increasing connected porosity ([Figure 3.8a](#)). The increase is non-linear (in log–log space); indeed, the data appears to describe a dogleg or kink. This phenomenon is discussed in detail in the following section. Specific surface area of these andesites appears to fall into two distinct families ([Figure 3.8b](#)), with the majority of samples containing a specific surface area of less than  $100 \text{ m}^2 \text{ kg}^{-1}$ , and showing an increasing trend with increasing porosity. However, for the two samples containing the lowest porosities, higher surface areas (in excess of  $500 \text{ m}^2 \text{ kg}^{-1}$ : [Table 3.1](#)) are measured. For perspective, the surface area within a cylindrical sample (EZ-94: length = 41.11 mm; diameter = 19.91 mm) is greater than the area between the goalposts in a football (soccer) goal. Notably, Scanning Electron Microscope (SEM) analysis<sup>1</sup> has shown that the high surface area data are associated with a pilotaxitic groundmass containing abundant high aspect ratio microlites, attributed to syn- and post-eruptive differentiation. Micro-scale pore space (microporosity) between these microlites, which can be observed in the SEM photomicrographs of [Figure 3.9a – c](#), serves to greatly increase the internal surface area whilst contributing little to overall porosity and fluid transport. Samples with only microporosity (e.g. EZ-69; EZ-94) have very low permeabilities ([Figure 3.8a](#); [Table 3.1](#)), thus one may infer that micropores do not contribute significantly to fluid transport in the samples with higher permeabilities (see also Saar and Manga, 1999). The fact that a large proportion of the internal surface does not contribute to fluid flow highlights that the permeability of these samples are poorly approximated by the Kozeny–Carman relation ([Equation 3.2](#)). In contrast, the specific surface area within sandstone, a rock with a much simpler microstructure, has been shown to correspond strongly with both porosity and permeability (e.g. Rabbani and Jamshidi, 2014).

Calculated tortuosities of all samples were low ( $0 < \tau < 2.2$ ), with the majority  $< 1$  ([Figure 3.8c](#); [Table 3.1](#)). In reality a tortuosity less than one is impossible (this representing a perfectly straight flow

---

<sup>1</sup> All microscopy presented in this thesis was undertaken on carbon-coated thin sections using a Tescan®VEGA-II Scanning Electron Microscope.

path); however, values in this range have been predicted previously for volcanic rocks, such as highly-porous andesite (Heap et al., 2014b), and rhyolitic pumice (Degruyter et al., 2009; Wright et al., 2009). In contrast to Heap et al. (2014a) however, high tortuosities are not observed at values of low connect porosity. It is a peculiarity of these data that the anomalously high surface areas cancel out the effects of low connected porosity when using [Equation 3.2](#), yielding low tortuosity values. Even disregarding these two values, it is clear that internal surface area alone does not appear to exert a dominant control on permeability and is thus is a poor predictor of permeability in the volcanic rocks of this study ([Figure 3.8d](#)).

Overall connectivity  $\Gamma$  lies between zero and one, where zero represents a pore network completely isolated from the outside of the sample, and one corresponds to a sample where all of the porosity is connected. [Figure 3.8e](#) shows the relation of this parameter to connected porosity (on linear axes), while [Figure 3.8f](#) illustrates the approximately exponential increase in permeability with pore connectivity. While this parameter affords insight into the degree of connectivity to the outside of the sample, it does not indicate the relative efficiency of each pore interconnection. Ostensibly, measuring properties such as connected porosity or surface area makes use of all available pore space. On the other hand, pathways perpendicular to flow, excessively tortuous, or involve very narrow pore apertures may be redundant to flow, and thus not included in measurements of permeability. The physical meaning of the increase of *Gamma* at low porosities is presumably linked to the percolation threshold of interconnecting cracks.

#### 3.4.4 A critical porosity: microstructural change

When describing permeability as proportional to integer powers of geometrical parameters (i.e.  $\phi$ ,  $\tau$ ,  $S$ ), as in [Equation 3.2](#), is it generally given that these parameters are similarly correlated by power-law relations (Bernabé et al., 2003). One can thus infer that the slope  $m$  of a fitted curve is the exponent of the relation  $k = f(\phi^m)$ . However, and as seen in [Figure 3.8a](#), the assumption that permeability can be simply described by porosity to a single power law exponent  $m$  is false, at least in the case of the andesites of this study. In previous laboratory studies involving physical properties of volcanic rocks (andesites from Volcán de Colima: Heap et al., 2014b; welded block-and-ash flow deposits from Mount Meager, Canada: Heap et al., 2014a), a critical "crossover" porosity, at which the value of  $m$  changes significantly, was observed. A crossover porosity has similarly been observed in sandstone (Bourbié and Zinszner, 1985). In each case, the crossover porosity was interpreted as the result of a distinct change

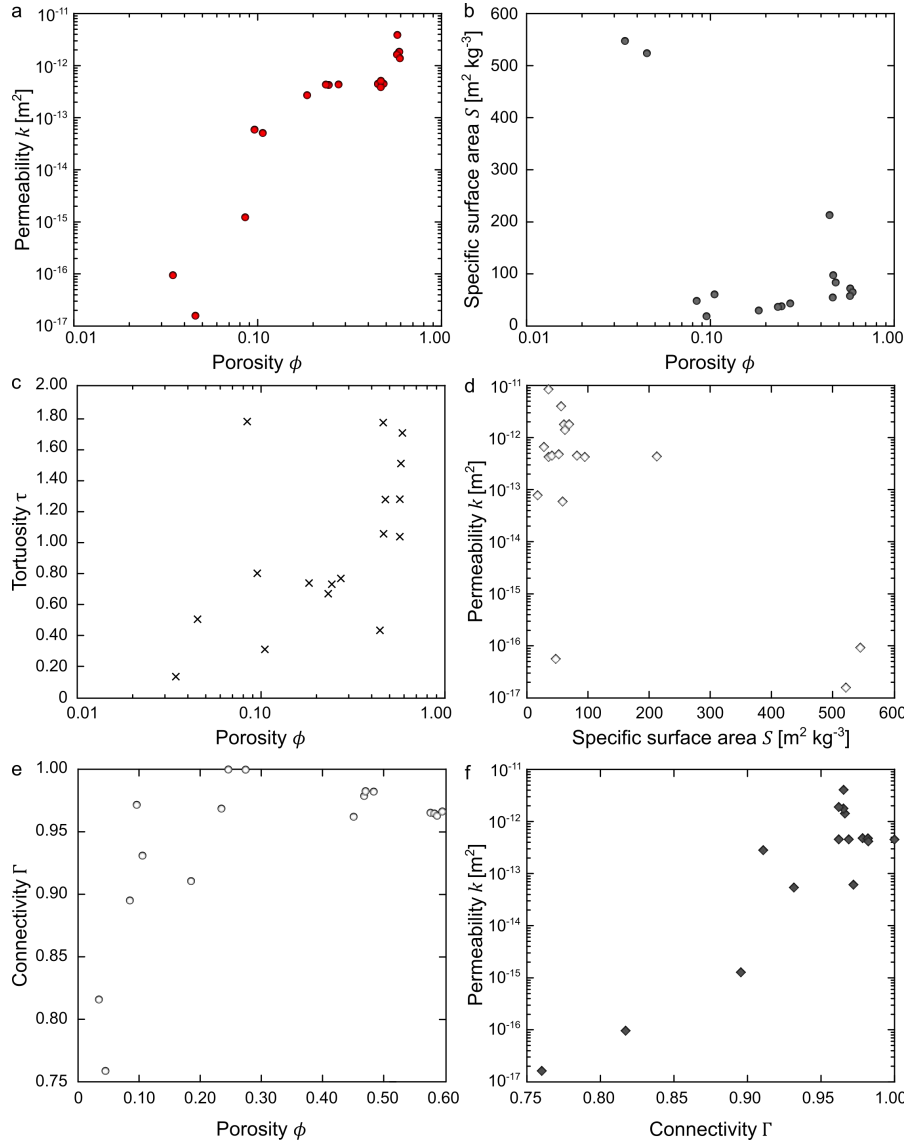


Figure 3.8: Physical property data of laboratory samples. a) shows connected gas porosity against gas permeability on log–log axes. Gas porosity versus specific surface area is given in b), and tortuosities calculated according to Equation 3.2 in panel c). d) shows specific surface area against gas permeability. e) shows pore connectivity, plotted against connected porosity (note that porosity is here shown on a linear axis, in contrast to the other panels. See text for discussion). Finally, f) displays gas permeability against connectivity in semi-log space.

in rock microstructure. These studies by Heap and co-workers (2014a, b) on volcanic materials estimate the threshold value of porosity to exist between 0.12 and 0.15, though this value is assigned on a best-estimate basis.

When plotted in log–log space this threshold resembles a piecewise linear model, as has been applied in other geoscientific studies, notably that of Hatton et al. (1994). The piecewise linear model assumes that log transformed data are described by one linear relationship until a defined changepoint (crossover), whereafter data are described by a linear relation with a different slope (correspondingly, the original data may be described by two distinct power-law relations). The existence of such a changepoint in the field data cannot be definitively argued, the reasons for which are twofold: firstly, data obtained in the field does not extend to lower permeabilities ( $< 10^{-16} \text{ m}^2$ ). Secondly, any fitted curve is influenced by the porosity distribution of the sample set, which causes the paired permeability–porosity data to cluster between 0.10 and 0.25. However, laboratory-derived data (and that of Heap et al., 2014b) are not hindered by either issue: it can therefore be determined whether a statistically justifiable crossover value exists.

Although increasing the complexity of a model can yield curves that better fit the data (in the sense that the residual sum of squares  $S_R^2$  is minimised), arbitrarily increasing model complexity without accounting for the increased number of model parameters can yield false relationships or models which cannot be generally applied. With this in mind, the modified Bayesian Information Criterion approach outlined by Main et al. (1999) is adopted, which imposes a penalty for each additional parameter introduced into the model. The cases of a one- and two-slope model are compared below.

Herein,  $y_i = \gamma(x_i) + \epsilon_i$ , for  $i = 1, \dots, n$ , where  $y_i$  is the  $i$ th iteration of the variable to be predicted (in this case,  $\log_{10} k$ ),  $\gamma(x_i)$  is the predicted value of  $y_i$  and a function of  $x_i$ , the explanatory variable (in this case  $\log_{10} \phi$ ), and  $\epsilon_i$  is an error term. The residual sum of squares is defined as:

$$S_R^2 = \sum_{i=1}^n [y_i - \gamma(x_i)]^2 \quad (3.3)$$

where  $n$  is the sample size. The independent  $(x_i, y_i)$  data pairs are resampled using a bootstrapping procedure, and the position of a potential changepoint  $x^*$  is determined by piecewise linear regression. The two cases for determining  $\gamma(x_i)$  are as follows:

$$\gamma(x_i) = a_0 + b_0(x_i); \varphi = 3 \quad (3.4)$$

and

$$\gamma(x_i) = a_1 + \{b_1 x_i [\forall x_i < x^*]\} + \{x^*(b_1 - b_2) + b_2 x_i [\forall x_i \geq x^*]\}; \varphi = 5 \quad (3.5)$$

The simple linear case ([Equation 3.4](#)) is described by intercept  $a_0$  and slope  $b_0$ , while [Equation 3.5](#) comprises an intercept  $a_1$ , a slope term  $b_1$  for all values below the changepoint  $x^*$ , and a slope  $b_2$ , corresponding to the slope for all values equal to or greater than  $x^*$ . For each model,  $\varphi$  is the number of unknown parameters (including the error term).

As in Main et al., (1999), the information criteria for the linear and changepoint models are given by

$$BIC_R = L(y) - \frac{1}{2}\varphi \ln\left(\frac{n}{2\pi}\right) \quad (3.6)$$

and

$$BIC_{x^*} = L(y, x^*) - \frac{1}{2}\varphi \ln\left(\frac{n}{2\pi}\right) \quad (3.7)$$

respectively, where  $L(y)$  is the maximised log-likelihood function, given by  $-n/2 \ln(S_R^2)$ . For the data of this study,  $BIC(x^*)$  is greater than  $BIC_R$  for values of  $x^*$  around 1.14, corresponding to a porosity of approximately 0.14 and a permeability of around  $1.8 \times 10^{-13} \text{ m}^2$ . For these laboratory data, the difference between [Equation 3.6](#) and [3.7](#) is greater than 3; typically this analysis is considered robust if  $BIC(x^*) - BIC_R \geq 1$ .

A re-examination of compiled literature data (Mueller, 2006; Kolzenburg et al., 2012; Kendrick et al., 2013; Richard et al., 2013; Heap et al., 2014b) using the information criterion analysis described above supports the prediction of a changepoint or crossover, despite the fact that these laboratory data were collected using different permeants, under different pressures, and with different experimental setups and methods. Specifically,  $BIC(x^*) > BIC_R$  when  $x^*$  is close to 1.18 (corresponding to 0.14 porosity). [Figure 3.10a](#) and [3.10b](#) display the laboratory data of this study and that of other authors, respectively, indicating the model exponents and changepoint locations. The high-porosity exponent for each dataset is remarkably similar (1.7 and 1.5; [Figure 3.10](#)). While the lower exponents differ somewhat, this difference is greatly exaggerated by the logged  $x$ -axis and the fact that low-porosity data are relatively more scarce in the literature. Importantly, this comparison indicates that a changepoint in the permeability–porosity data is not merely an artefact of the selected laboratory

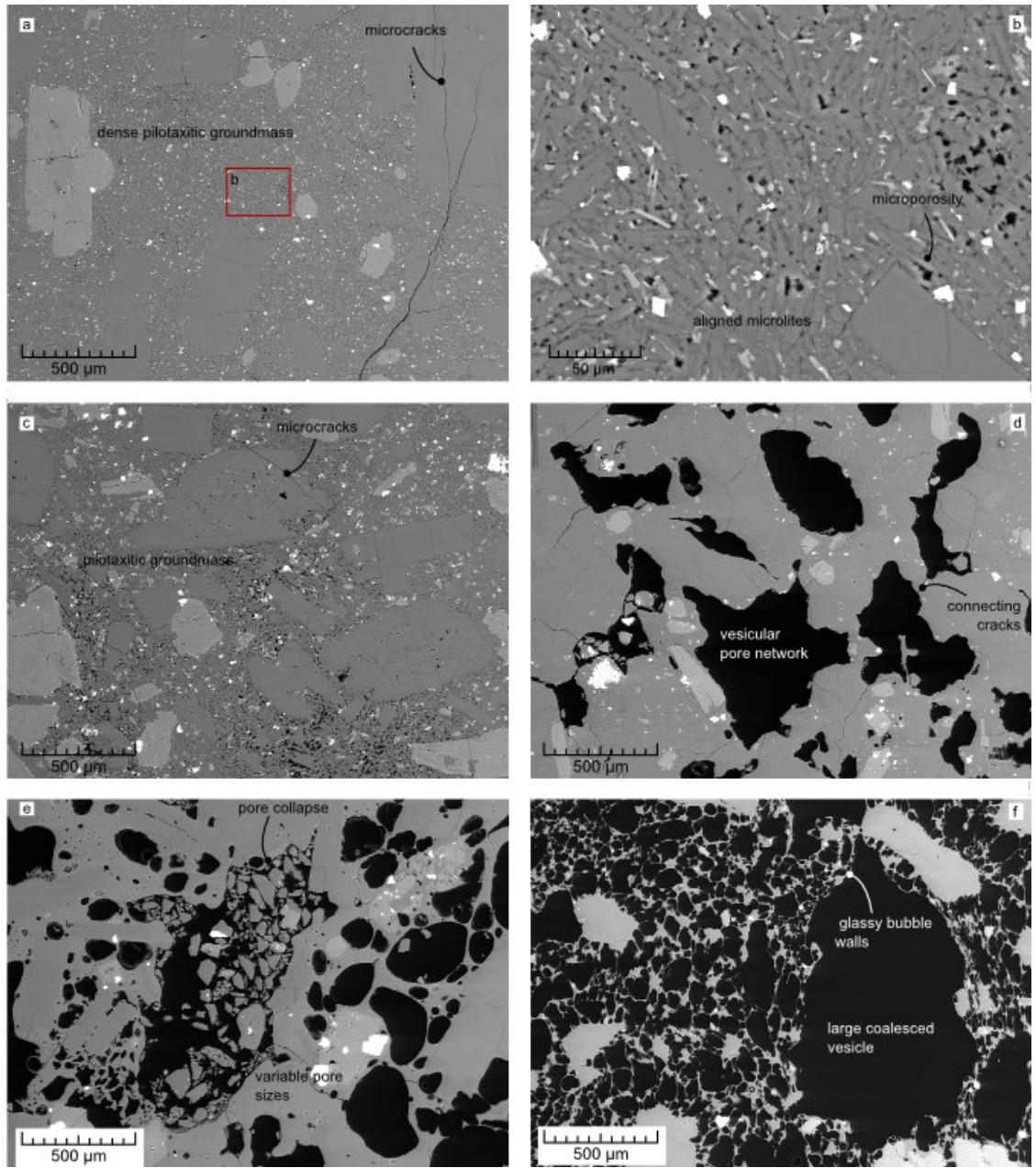


Figure 3.9: Scanning electron microscope (SEM) backscatter photomicrographs of an array of andesites from Volcán de Colima. a) is from sample EZ-94, with a porosity  $< 0.04$ . The sample has a highly dense pilotaxitic groundmass containing thin and tortuous microcracks. b) shows a close-up view of the abundant microlites in a), highlighting their flow-alignment and intercrystalline microporosity. Similar textures can be observed in c), sample EZ-69 (porosity  $\sim 0.05$ ). The pilotaxitic textures observed in these samples corresponds to anomalously high surface area measurements. d), a more porous rock (MG-22:  $\sim 0.25$ ) shows large subspherical pores, variably well connected with cracks. e) shows connected vesicles in a glassy groundmass (sample LL96:  $\sim 0.45$ ). Finally, f) shows a pumiceous sample (PLY116:  $\sim 0.58$ ), with characteristically large pores and thin glassy bubble walls. The sequence of images shows a transition between crack- and pore-dominated geometries (as discussed in text).

samples of this study.

The preceding analysis is useful as it identifies the porosity (and permeability) where one can expect to observe a significant change in microstructure. The differences discernible between the SEM photomicrographs in [Figure 3.9a – c](#) (below the changepoint) and [Figure 3.9d – f](#) (above the changepoint), are congruent with this conclusion: in the former, pathways available for fluid flow consist primarily of microcracks and microporosity. The latter show relatively large sub-spherical to spherical pores, which could provide relatively less constricted and tortuous pathways for flow. By extension, rocks in the field should largely follow one power law trend below a porosity around 0.14 (where fluid flow is crack-controlled), and another trend above this threshold (where fluid flow is pore-controlled).

Despite lacking SEM images at or close to the assumed changepoint, it is reasonable to suppose that a discrete changepoint is an over-simplification of the evolution from a low to a high exponent (rather, it is presumably a transitional "changezone"). As discussed by Heap et al. (2014b), the changepoint is likely to represent a critical porosity threshold beneath which fluid transport is dominated by tortuous microcracks. Although the genesis of porosity is initially pre- or syn-eruptive (i.e. formation porosity: see [Chapter 1](#)), microcracks are ubiquitous across the range of collected porosities (porosity likely formed during emplacement and transport; [Figure 3.9a, c, d](#)). As a result, the values of permeability measured on edifice-forming rocks will inevitably be than their pre- or syn-eruptive permeabilities. In samples with low initial porosity ([Figure 3.9a - c](#)), fluid flow is restricted largely to these tortuous microcracks. Where the initial porosity is higher ([Figure 3.9d–f](#)), the cracks serve to link existing porosity. If effective fluid pathways exist, then additional porosity (formed by bubble growth, thermal cracking, or transport processes) has a marginal impact on permeability, explaining why the power law exponent is lower above the changepoint porosity.

Overall pore connectivity  $\Gamma$  can be seen to follow two distinct patterns ([Figure 3.8e](#)) as porosity increases: connectivity increases linearly until the predicted changepoint, after which it plateaus around  $\Gamma = 1$ . This indicates that any additional porosity below the changepoint serves to connect a correspondingly larger fraction of the pore space. Above around 0.14 porosity, essentially all porosity is connected to the outside of the sample, and thus constitutes a potential fluid pathway. The permeability is thus little influenced by additional porosity; rather, the effectiveness of pore connections—determined largely by pore apertures—must govern the flow of fluid through the

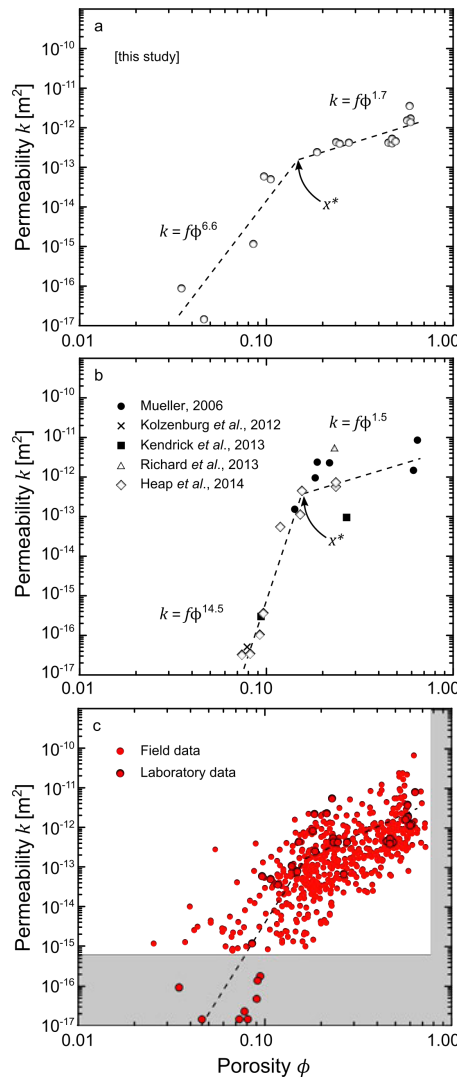


Figure 3.10: Piecewise regression curves fit through a) the data of this study, and b) compiled laboratory data. c) displays the field data overlain with the piecewise model derived from all the laboratory data. Refer to text for discussion.

rock.

Figure 3.10c shows the field data overlain with a relation derived from all of the compiled Volcán de Colima laboratory data ( $x^*$  corresponds to a porosity of 0.16): it can be seen that despite the scatter observed in the field data, the permeability–porosity trend is congruent with a changepoint model. While a discrete changepoint  $x^*$  is probably a simplification, these data strongly suggest that this model captures a significant component of the microstructural complexity displayed by edifice-forming volcanic rocks.

### 3.5 CHAPTER SUMMARY

The goal of this combined field and laboratory study was to explore the relationship between porosity and permeability of edifice-forming andesitic rocks at Volcán de Colima, and to identify the likely microstructural controls governing this relationship (given its structural and eruptive characteristics, Volcán de Colima is typical of many andesitic stratovolcanoes). This chapter highlights a wide range of bulk density of samples at Volcán de Colima, suggesting of a wide range of eruptive styles. With increasing distance from the active vent, the measured samples tend towards a skewed density distribution, as dense, low-porosity rocks typically survive comminution during remobilisation more so than less indurate rocks. The measured densities (between 1142.40 to 2813.79 kg m<sup>-3</sup>) correspond to porosity values between 0.03 and 0.73. Measured field permeabilities are in the range of 10<sup>-16</sup> to 10<sup>-11</sup> m<sup>2</sup>, encompassing values significantly greater than those generally assumed for fluid transport in magma, and thus emphasising the importance of host-rock permeability in facilitating outgassing of volatiles and, in turn, governing eruption dynamics.

For any given porosity a permeability range of up to four orders of magnitude is observed, which can be partially explained by natural variability in microstructural attributes (pore geometries and pore connectivity). This range of stochasticity is little affected by meso-scale textural differences, oxidation, or alteration, although the bubble elongation associated with scoracious deposits fosters the largest degree of scatter. In the laboratory, permeabilities as low as 9.5 × 10<sup>-17</sup> m<sup>2</sup> were measured, corresponding to low porosities ( $\leq 0.05$ ) and high internal surface areas.

Microstructural analysis reveals that high surface areas are associated with an inter-microlite microporosity, which does not appear to significantly increase porosity or pore connectivity, resulting in underestimation of fluid pathway tortuosities. Low porosity samples are dominated by tortuous microcracks, whereas highly-porous samples contain large interconnected pores. Consistently low calculated tortuosity values highlight that the Kozeny–Carman relation is a poor predictor of connectivity and cannot adequately capture the microstructural complexity of volcanic rocks.

The ratio of total and unconnected porosity  $\Gamma$  comprises a useful proxy for determining the overall connectivity of a sample, although it does not describe the efficiency of fluid flow through pore networks. The relationship of permeability to connected porosity was observed to follow two distinct power-law trends: a threshold in connected porosity was identified at approximately 0.14 using piecewise regres-

sion and Bayesian Information Criterion analyses. At this changepoint, the permeable network of these volcanic rocks presumably becomes pore-dominated rather than microcrack-dominated. The changepoint is congruent with a change in the relation between  $\Gamma$  and connected porosity. The improved connectivity of fluid pathways above  $\sim 0.14$  is manifest in a reduced exponent in the power-law relation between permeability and porosity. While the supposition that this exponent changes at a distinct changepoint is a simplification, it describes well the permeability data presented in this chapter. A firmer understanding of the microstructural attributes and physical properties controlling permeability is important for the long-term goal of understanding volcanic outgassing and the attendant controls on the frequent transition between effusive and explosive behaviour characteristic of many active andesitic volcanoes.

# 4

## STRAIN-DEPENDENT PERMEABILITY

---

*For without void, naught can be crushed, it seems ... Nor can it take  
The damp, or seeping cold or piercing fire, those old destroyers three;  
But the more void within a thing,  
The more entirely it totters at their sure assault.*

— Lucretius, *On the Nature of Things*, 50 BCE<sup>1</sup>

*Volcanic edifice permeability plays an important role in outgassing and eruptive behaviour and as shown in the previous chapter, can vary significantly as a function of physical properties of the edifice rock. Active volcanoes are high-strain environments, and as such it is important to consider how permeability evolves when volcanic materials are subject to progressive inelastic strain. Notably, previous experimental studies have highlighted that volcanic rock can deform in one of two ways when subjected to a compressive stress: dilatant or compactant. This chapter employs a series of triaxial deformation experiments to investigate the influence of both types of failure on volcanic rock, as well as exploring the factors which govern the propensity for dilation over compaction and vice versa, as well as the potential for volcanic rock to transition from one predominant deformation behaviour to the other. The chapter closes with an investigation of the implications results for outgassing in volcanic environments and the transition from explosive to effusive eruptive styles.*

In part, data from this chapter are published as two separate papers:  
**Farquharson, J. I., M. J. Heap, P. Baud.** 2016 *Strain-induced permeability increase in volcanic rock*. Geophysical Research Letters.  
and  
**Farquharson, J. I., P. Baud, and M.J. Heap.** 2016 *Inelastic compaction and permeability evolution in volcanic rock*. Solid Earth Discussions.

Much of this chapter is based on the work and conclusions of a previous article: Heap, M.J., **Farquharson, J.I.**, Baud, P., Lavallée, Y. and Reuschlé, T., 2015. *Fracture and compaction of andesite in a volcanic edifice*. Bulletin of Volcanology, 77(6), pp.1-19. For convenience, this article is included as an annex to the thesis.

---

<sup>1</sup> Translated by William Ellery Leonard

#### 4.1 INTRODUCTION

##### 4.1.1 *Deformation and strain in volcanic environments*

The propensity for lateral outgassing is governed by the permeability of the volcanic edifice, a medley of effused lavas, explosive ejecta, and other volcaniclastic deposits (e.g. Gudmundsson, 2012). In turn, edifice permeability is dependent on physical properties of these rocks (such as their porosity) and their mechanical response to stress and strain.

As highlighted in the introductory chapter, active volcanoes are high-strain systems (e.g. Ōmori, 1920; Mogi, 1958; Dzurisin, 2003) as result of their volumetric evolution over time. Magma is a constantly evolving multi-phase medium, and as it migrates through the crust, vesiculating and crystallising along the way, it can impart significant mechanical stress on the surrounding edifice rock (e.g. Voight et al., 1998; Denlinger and Hoblitt, 1999; Clarke et al., 2007; Heimisson et al., 2015). Deeper in the crust, magma chamber deformation is also thought to pressurise conduit and dyke systems above, in turn resulting in periodic displacement of the edifice (e.g. Melnik and Sparks, 1999; Melnik and Sparks, 2005; Wadge et al., 2006). Moreover, much of the edifice is likely to be fluid-saturated (e.g. Day, 1996), in turn a function of permeability, permeability anisotropy, and heat flux (Hurwitz et al., 2003): migration of fluids can serve to adjust the *in situ* stress conditions and influence the short-term failure strength of edifice-forming rocks. The *in situ* stress conditions are also a function of depth (i.e. the overburden or confining stress), which can vary over time at any given point. For example, iterative emplacement of lavas or airfall deposits with consecutive eruptions will tend to increase the confining stress acting on the buried material of former eruptions, whereas gravitational flank collapse would serve to decrease it.

Given the importance of fluid movement through volcanic systems, this chapter seeks to address two fundamental questions:

1. How do volcanic rocks respond to strain under volcano-relevant conditions?
2. How may their permeability be affected as a result?

##### 4.1.2 *Fracture and compaction in the field*

Field studies show that shallow volcanic environments are riddled with fractures on different scales, highlighting that edifice-forming material is often prone to dilatant fracture. For example, Tuffen and Dingwell (2005) describe exposed conduits in the Rauðufossafjöll vol-

canic complex (south-central Iceland), noting complex networks of anastomosed and cross-cutting shear fractures. Indeed, fractures in volcanic rock have been described ranging from the micro-scale (e.g. Kushnir et al., 2016), to macrofractures visible to the naked eye (Cruz and Chouet, 1997; Kolzenburg et al., 2012; Gaunt et al., 2014; Lavallée et al., 2016) and large-scale faults and fissures (e.g. Varley and Taran, 2003; Walter et al., 2015).

Spectacular evidence for shear fracturing in volcanic environments has been observed during the extrusion of lava spines and domes: monolithic or blocky structures of dense, well-outgassed lava which extrude along extensive conduit-parallel faults. Eruptive activity at Mount St Helens (Washington, USA) between 2004 and 2008 saw the growth of a massive "whaleback" dome, accompanied by substantial shear zones at its margins, a testament to the high strains concentrated during extrusion (e.g. Rust et al., 2004; Iverson et al., 2006; Cashman et al., 2008; Kennedy and Russell, 2012). Images are shown in [Figure 4.1a](#) and [4.1b](#). The 1990 -1995 eruption of Mount Unzen (Kyūshū, Japan) culminated in the emplacement of a spine over 40 m in height (Nakada et al., 1999) which exhibits substantial damage and evidence of large-scale cataclasis at its margins (Smith et al., 2001). Other evidence, such as cavitation, crystal shearing, and frictional melting textures highlight the high strains encountered in and around the margins of the conduit (Smith et al., 2001; Hornby et al., 2015).

Manifestations of compaction in volcanic environments tend to be less immediately obvious in the field, not least due to the fact that compaction is enhanced in relatively deep regions of the edifice. However, bulk rock density (and reciprocally, rock porosity) has been estimated during scientific drilling projects—in concert with gravimetric and other geophysical data—at, for example, Campi Flegrei, Italy (Barberi et al., 1991) and Mount Unzen (Sakuma et al., 2008). These studies highlight a predictable decrease in porosity with increasing depth, supported in either case by a general increase in ultrasonic wave velocities with increasing depth, indicative of a reduction in porosity with increasing lithostatic pressure. This observation is borne out by experimental deformation studies, which show that the propensity for compactant—rather than dilatant—behaviour of volcanic rock is intrinsically linked to the confining pressure under which the rock is deformed (e.g. Shimada et al., 1989; Heap et al., 2015a; Zhu et al., 2016), amongst other factors (e.g. temperature: Viloy et al., 2012).

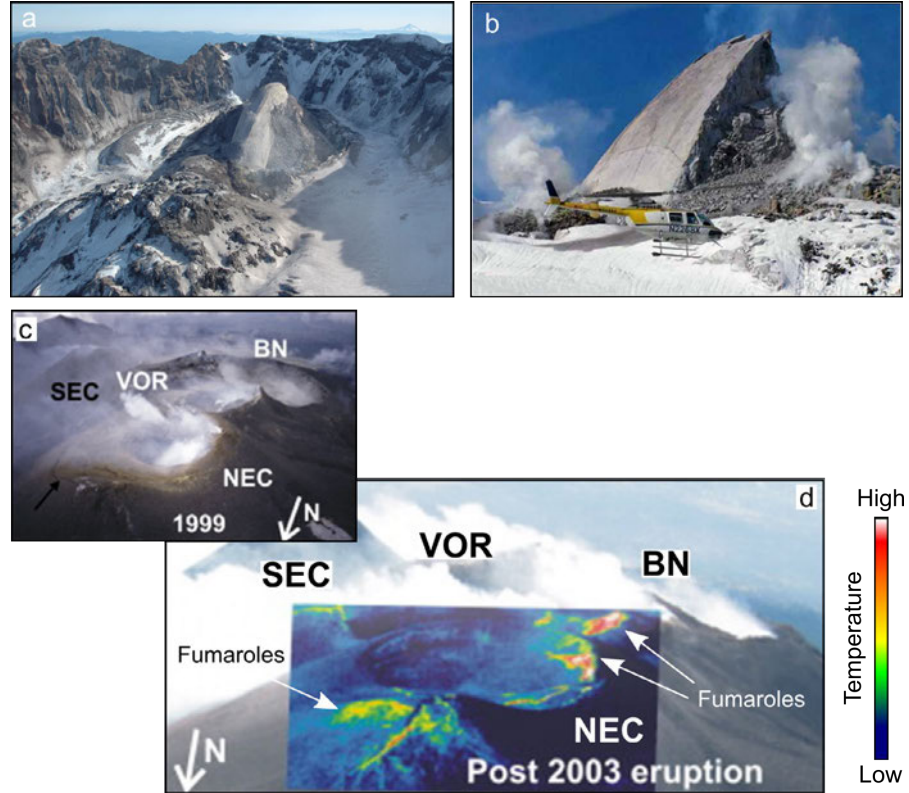


Figure 4.1: Strain and outgassing in volcanic environments. a) The "whale-back" lava dome that grew at Mount St Helens between 2004 and 2008 (photograph by USGS, 22 February 2005). Note the extensive mantle of talus and gouge covering the relatively smooth dome carapace. b) Another view of the Mount St Helens dome (photograph by Daniel Dzurisin, USGS, 28 April 2006). Steam can be seen emitting from the heavily comminuted shear margin. c) True colour photograph (modified after Spampinato et al., 2011) of the summit craters of Mount Etna. NEC, SEC, VOR, and BN are the North-East crater, the South-East crater, Voragine, and Bocca Nuova, respectively. d) Photograph from a similar vantage, overlain with infrared image (modified after Spampinato et al., 2011). Colourbar highlights the relative thermal emission around the North-East crater. Active fumarole areas are indicated by arrows.

#### 4.1.3 Deformation and permeability

A few previous studies have explored pre-failure permeability change in plutonic (Zoback and Byerlee, 1975; Kiyama et al., 1996; Mitchell and Faulkner, 2008) and volcanic (Faoro et al., 2013) rocks. In each case, the authors report a general increase in permeability in the lead up to dilatant failure. Studies of post-failure permeability change are mostly limited to investigations on sedimentary and synthetic materials. In sandstones, dilatant failure in triaxial compression has been observed to increase (Mordecai and Morris, 1970; Keaney et al., 1998; Heiland, 2003; Xiaochun et al., 2003) or decrease (Gatto, 1984; Zhu and Wong 1997; Vajdova et al. 2004) permeability. Similarly, post-failure compaction of sandstone has yielded both decreases (Zhu and Wong, 1997; Baud et al., 2012) and increases (Xiaochun et al., 2003) in permeability. Alam et al. (2014) investigated permeability evolution of Shikotsu welded tuff, finding that permeability decreased monotonously with triaxial compression (both in dilation and compaction) and that the rate of permeability decrease was tied to the effective pressure under which deformation was performed. These studies show that the development of permeability in deforming media is often not straightforward.

Due to the critical influence of volatile outgassing in actively evolving volcanic environments, it is important to understand if and how permeability may change during dilation or compaction of volcanic rock. In the field, observations of extruding domes highlight the common occurrence of volatile outgassing through faults and fumaroles at their margins. For example, observations of steam and sulphur venting around the base of a dome were reported by Heilprin (1903) during eruptive activity in the early 1900s at Montagne Pelée, Martinique (the so-called "Tower of Pelée"). Sparks et al. (2000) describe the appearance of gas and ash venting at the interface of the base of the dome and the neighbouring wallrock at Soufrière Hills Volcano, Montserrat. Similarly, after persistent extrusion of a dense dacitic plug at Mount St Helens, steaming fumaroles were recorded originating from around its base (Pallister et al., 2012; see also [Figure 4.1b](#)). This field evidence suggests that the ubiquity of fracture and gouge formation during the ascent and extrusion of dense, viscous lava may in fact facilitate outgassing around the conduit.

Nevertheless, such obvious point-source outgassing is not ubiquitous at active volcanoes; rather, one may observe fumarole "fields", in portions of the edifice where outgassing—and by extension, permeability—is evidently enhanced relative to other parts (e.g. Oppenheimer et al., 1993; Bukumirovic et al., 1997). Individual fumaroles, or fields thereof, have been observed to become active or inactive during dif-

ferent phases of volcanic activity (e.g. Harris and Maciejewski, 2000; Vaselli et al., 2003). Moreover, their lateral extent and distribution may evolve and migrate as the edifice responds to subsurface strain (e.g. Harris and Maciejewski, 2000). Often, thermal monitoring of fumarole fields is employed to indirectly detect subsurface changes in outgassing routes and gas flux (Spampinato et al., 2011: see [Figure 4.1c, d](#); see Ramsey and Harris, 2013 for a review). Clearly then, the distribution and spatio-temporal evolution of actively emitting fumaroles must indicate a difference in—and evolution of—overall permeability of edifice regions.

With this preamble in mind, this chapter investigates the permeability of a suite of volcanic rocks as a function of stress states spanning the transition between dilatant and compactant behaviour. Given the high and variable strains anticipated in natural volcanic environments, this chapter addresses the evolution of both porosity and permeability with sustained axial strain and continued post-failure deformation.

#### 4.2 MATERIALS AND METHODS

Based on a previous study of the mechanical behaviour of andesite from Volcán de Colima (Heap et al., 2015a), a suite of volcanic rock samples was selected with porosities between 0.05 and 0.22. This range assures that both dilatant and compactant behaviour can be obtained under volcano-relevant pressure conditions and, more generally, encompasses modal porosities previously measured for edifice material (e.g. Heap et al., 2015a; Lavallée et al., 2016; see also [Chapter 3](#)). Chemical composition of magma influences its rheology, and thus the formation of porosity while magma or lava is above its glass transition temperature  $T_g$  (see [Chapter 1](#)); in this study, however, only the mechanical response of cooled, variably-porous rocks is investigated; as such materials of varying composition are used indiscriminately. While mechanical behaviour may be influenced by the mineralogy of sample suites with varying origins, it is presumed that any consequent variation will be insignificant compared to that caused by the range of porosities studied. Compiled strength data from Heap et al. (2015a) and Zhu et al. (2016) are shown in [Appendix D](#), affirming this assumption.

The samples chosen for this study comprise basalt from Mount Etna (Sicily, Etna), andesite quarried from the Kumamoto Prefecture (Kyūshū, Japan), andesite collected from Mt Ruapehu in the Taupō Volcanic Zone (New Zealand), and andesites collected from a debris-flow track (La Lumbre) and a riverbed (El Zarco) on the flanks of Volcán de Colima (Mexico): see [Figure 4.2](#). For comparison, data are

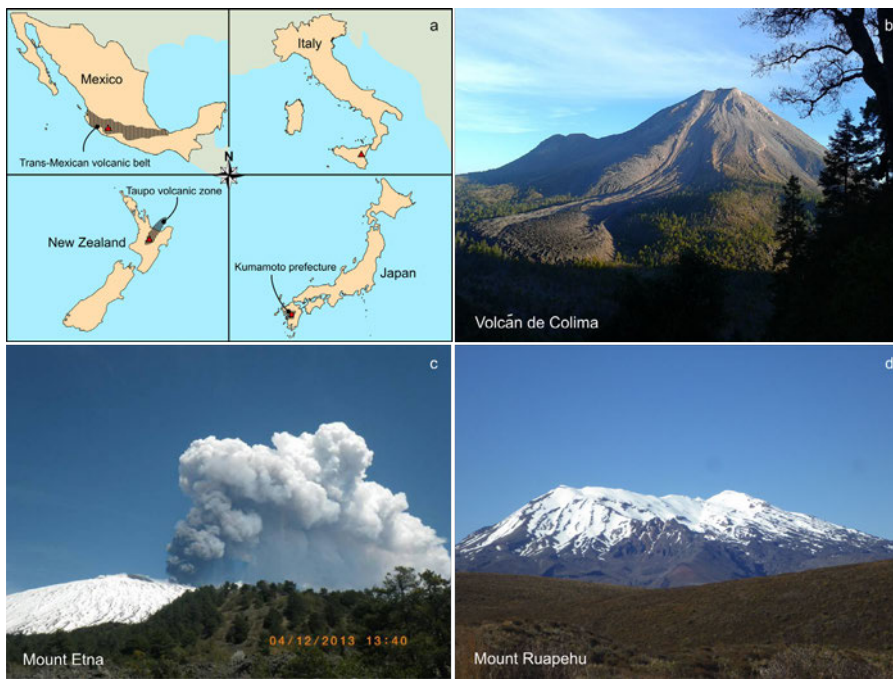


**Figure 4.2:** Sampling locations for volcanic materials used throughout this study. a) Location maps highlighting Volcán de Colima, Mount Etna, and Mount Ruapehu (marked as triangles), and the Kumamoto quarry (collection site of KA samples; marked as a square). b) Volcán de Colima, Mexico (EZ, LLB, and C8 samples). c) Mount Etna, Italy (EB samples). d) Mount Ruapehu, New Zealand (R10 samples).

included from a block-and-ash flow deposit from the San Antonio ravine on the southern slope of Volcán de Colima (published in Heap et al. 2014b; 2015a) Typical porosity and permeability values for these rock types are given in [Table 4.1](#). To assess the impact of dilatant or compactant deformation on the permeability of volcanic rocks, the following three steps were followed for each rock type:

1. suites of samples were prepared and their permeability measured,
2. samples were deformed under set effective pressures to a given degree of axial strain,
3. the permeability of the deformed samples was re-measured.

The above steps are described in more detail hereafter.

Samples were prepared and characterised (connected gas porosity, gas permeability) as described in [Chapter 2](#). Where necessary, corrections were applied to the measured permeability values to account for turbulent flow (see Forchheimer, 1901) or the gas slippage effect (see Klinkenberg, 1941), which become non-negligible at the extremes of the porosity range studied here.

#### 4.2.1 Deformation conditions

Next, samples were loaded into the triaxial rig (see [Chapter 2](#)), and pore and confining pressures were increased to a target effective pressure. As touched on in [Chapter 2](#), it is generally assumed that a simple law of effective pressure  $p_{eff}$  holds for any physical property, whereby  $p_{eff} = p_c - \alpha \cdot p_p$ , with  $p_c$  and  $p_p$  being the applied confining and pore pressures, respectively. During mechanical deformation, the poroelastic constant  $\alpha$  is the Biot–Willis coefficient (e.g. Paterson and Wong 2005), and the experiments referred to in [Chapter 2](#) suggest that its value does not differ significantly from unity in andesitic rock when considering its failure strength.

Confining pressure  $p_c$  is proportional to depth  $z$ , approximated by  $p_c = \rho_b \cdot g z$ , where  $g$  is acceleration due to gravity, and  $\rho_b$  is the bulk density of the overlying material (with  $p_c$  being given in Pa). To explore mechanical behaviour of volcanic rocks under relevant pressure conditions, effective pressures between 10 and 70 MPa are imposed during these tests, representing depths in the edifice from < 500 m down to a maximum of 3200 – 4000 m, assuming bulk rock densities between around 2000 and 2500 kg m<sup>-3</sup>. Importantly, this pressure range spans the expected transition between dilatant and compactant behaviour for many of the porosities studied herein.

Each sample was deformed until a targeted axial strain was achieved, up to a maximum of approximately 0.24 (i.e. a 24% reduction in sample length along the loading axis), irrespective of mode of failure. Examples of two sample suites are shown in [Figure 4.3](#). Once the desired axial strain had been attained, the sample was unloaded, vacuum-dried, and its permeability measured once more. [Table 4.2](#) gives the experimental conditions for each sample, including the target effective pressure and axial strain. In order to examine inelastic strain  $\varepsilon_i$ , the elastic strain  $\varepsilon_e$  (which is recovered during the unloading of the sample) is subtracted from the targeted strain accumulated throughout the experiment (an example is shown in [Figure 4.3](#)). Similarly, in order to study the inelastic porosity change  $\delta\phi_i$ , the elastic porosity change—recovered during unloading—is subtracted from the total porosity change measured throughout triaxial deformation ([Figure 4.3](#)).

#### 4.2.2 Post-deformation permeability

Investigations towards determining  $\alpha$  for properties (including permeability) other than rock strength indicate that this coefficient may differ as a function of porosity, pore geometry, and other factors,

Table 4.1: Representative physical property data for rocks used throughout this chapter.  $\phi$  = connected porosity;  $k$  = permeability.

Rock type	Prefix	$\phi$	$k$ [m <sup>2</sup> ]
Etna basalt	EB	0.05	$7.29 \times 10^{-17}$
Colima andesite (El Zarco)	EZ	0.08	$2.95 \times 10^{-16}$
Kumamoto andesite	KA	0.14	$9.57 \times 10^{-17}$
Ruapehu andesite	R10	0.16	$9.16 \times 10^{-16}$
Colima andesite (La Lumbre)	LLB	0.22	$4.70 \times 10^{-13}$
Colima andesite (San Antonio)	C8	0.18 <sup>a</sup>	$1.08 \times 10^{-12}$ <sup>b</sup>

<sup>a</sup> Water porosity measured using the triple-weight method (Heap et al., 2015).

<sup>b</sup> Water permeability measured under 2 MPa of confining pressure (Heap et al., 2015).

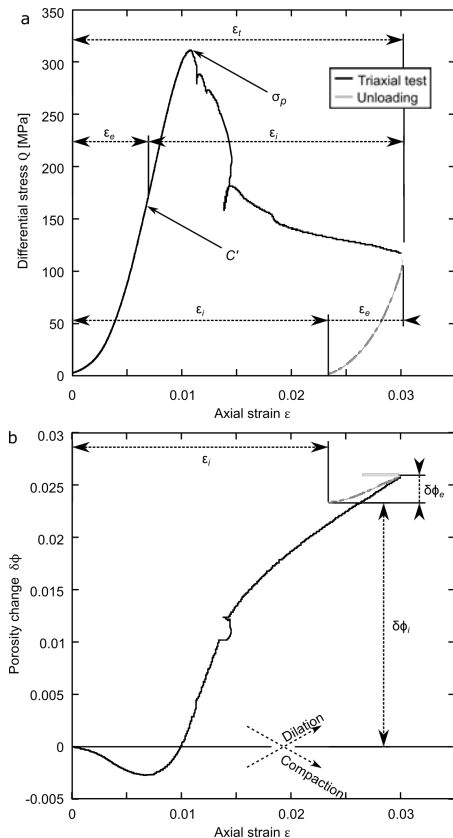


Figure 4.3: Example mechanical data highlighting the total (solid black line) and inelastic (solid grey line) strain components. a) Differential stress–strain versus axial strain for sample EB-11. The initial portion of the stress–strain curve is convex, becoming approximately linear prior to failure. This initial stage represents elastic (recoverable) strain  $\varepsilon_e$ . Inelastic strain is determined as the difference between total and elastic strain ( $\varepsilon_i = \varepsilon_t - \varepsilon_e$ ). Refer to discussion for detailed explanation of mechanical data. b) Porosity change versus axial strain during triaxial deformation. Inelastic porosity change  $\delta\phi_i$  is taken as the total porosity change minus that recovered during unloading ( $\delta\phi_i = \delta\phi_t - \delta\phi_e$ ).

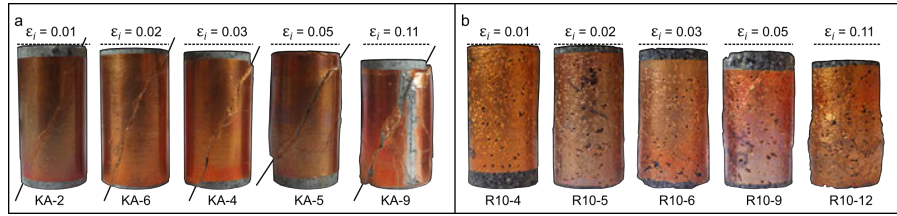


Figure 4.4: Samples deformed to differing degrees of axial strain. a) Kumamoto andesite (KA;  $\phi = 0.14$ ) deformed under 10 MPa effective pressure. Solid lines highlight shear fractures generated through the samples. b) Ruapehu andesite (R10;  $\phi = 0.16$ ) deformed under 50 MPa effective pressure. In either case, dashed lines highlight shortening of the samples due to compaction. Samples underwent inelastic strain of 0.01, 0.02, 0.03, 0.05, and 0.11.

which is to say that  $\alpha$  for one property may not be the same as  $\alpha$  for a second property (Bernabé, 1986). Given the lack of constraint on  $\alpha$  for the permeability of volcanic rocks, permeability is measured at the lowest possible confining pressure (1 MPa, rather than at "in situ" pressures) in order to allow comparison within and between sample sets. This method also avoids the potential for creep—a mechanism of deformation whereby sub-critical crack growth induces damage and possibly even failure at stresses below the short-term strength of the rock (e.g. Brantut et al., 2013; Heap et al., 2015e)—as well as precluding other phenomena such as stress relaxation that may arise when measuring permeability under triaxial conditions.

Measuring permeability requires that the sample dimensions, specifically length and area, are be well constrained (see [Chapter 1](#) and [2](#)). Prior to initial measurements of permeability, sample dimensions are measured accurately using digital callipers. After mechanical deformation, however, samples are often non-cylindrical—being barreled and/or extensively fractured (see [Figure 4.4](#))—making their mean radii nontrivial to determine. Assuming that the solid volume remains constant throughout deformation, then the post-deformation volume is equal to the sum of solid volume, the initial porosity, and the pore volume change after deformation. As described in [Chapter 2](#), the pore volume change is monitored during triaxial deformation. This differential  $\delta\phi$  normalised to the initial sample dimensions is shown as positive during dilation and negative during compaction. Summing  $\delta\phi$  and the initial porosity  $\phi$  thus allows the determination of the mean post-deformation area  $A_{post}$  of the sample thus:

$$A_{post} = \left[ \frac{V_s}{1 - (\phi + \delta\phi)} \right] \cdot \ell_{post}^{-1} \quad (4.1)$$

where  $\ell_{post}$  is the mean post-deformation length of the sample.

## 4.3 RESULTS

Pre- and post-deformation permeability,  $k_0$  and  $k_e$  respectively, are shown in [Table 4.2](#) for all samples, alongside initial porosity, porosity change, and the experimental conditions (inelastic strain and effective pressure).

**Table 4.2:** Physical property data and deformation conditions for each sample. EB = Etna Basalt; EZ = El Zarco andesite (Colima) ; KA = Kumamoto andesite; R10 = Ruapehu andesite; LLB = La Lumbre andesite (Colima); C8 = San Antonio andesite (Colima) . Initial porosity and permeability are given as  $\phi$  and  $k_0$ , respectively.  $\delta\phi_i$  = inelastic porosity change;  $\phi + \delta\phi_i$  = post-deformation porosity;  $k_e$  = post-deformation permeability. Samples were deformed under an effective pressure  $p_{eff}$  until a total target strain  $\varepsilon_t$ , then unloaded to determine the inelastic strain  $\varepsilon_i$ .

Sample	$\phi$	$p_{eff}$ [MPa]	$\varepsilon_t$	$\varepsilon_i$	$\delta\phi_i$	$\phi + \delta\phi_i$	$k_0$ [ $m^2$ ]	$k_e$ [ $m^2$ ]
EB-8	0.05	10	0.020	0.007	0.011	0.06	$7.31 \times 10^{-17}$	$5.10 \times 10^{-16}$
EB-11	0.05	10	0.030	0.019	0.023	0.07	$8.02 \times 10^{-17}$	$3.32 \times 10^{-15}$
EB-10	0.05	10	0.060	0.049	0.028	0.08	$7.08 \times 10^{-17}$	$8.20 \times 10^{-15}$
EB-12	0.05	10	0.100	0.090	0.036	0.08	$5.70 \times 10^{-17}$	$8.09 \times 10^{-15}$
EB-13	0.05	10	0.100	0.090	0.030	0.08	$7.47 \times 10^{-17}$	$6.13 \times 10^{-14}$
EB-9	0.05	10	0.120	0.109	0.038	0.09	$8.14 \times 10^{-17}$	$3.66 \times 10^{-15}$
EZ-13	0.08	10	0.007 c	0.002	0.000	0.08	$1.95 \times 10^{-16}$	$2.07 \times 10^{-16}$
EZ-2	0.08	10	0.010	0.003	0.002	0.08	$2.98 \times 10^{-16}$	$2.23 \times 10^{-15}$
EZ-5	0.08	10	0.020	0.014	0.009	0.09	$2.05 \times 10^{-16}$	$2.55 \times 10^{-14}$
EZ-11	0.07	10	0.040	0.035	0.016	0.09	$3.08 \times 10^{-16}$	$4.29 \times 10^{-14}$
EZ-6	0.08	10	0.060	0.055	0.016	0.09	$3.86 \times 10^{-16}$	$2.24 \times 10^{-14}$
EZ-7	0.09	10	0.080	0.075	0.018	0.11	$5.22 \times 10^{-16}$	$9.19 \times 10^{-14}$
EZ-12	0.09	10	0.100	0.092	0.035	0.12	$3.95 \times 10^{-16}$	$9.91 \times 10^{-14}$
EZ-3	0.07	10	0.120	0.114	0.026	0.10	$2.97 \times 10^{-16}$	$3.36 \times 10^{-13}$
EZ-9	0.08	30	0.020	0.012	0.001	0.08	$4.05 \times 10^{-16}$	$2.58 \times 10^{-15}$
KA-2	0.13	10	0.020	0.012	0.005	0.14	$1.12 \times 10^{-16}$	$4.27 \times 10^{-17}$
KA-6	0.15	10	0.030	0.024	0.007	0.16	$1.11 \times 10^{-16}$	$1.21 \times 10^{-15}$
KA-4	0.14	10	0.040	0.035	0.007	0.15	$1.35 \times 10^{-16}$	$5.21 \times 10^{-15}$
KA-5	0.15	10	0.060	0.053	0.015	0.16	$1.32 \times 10^{-16}$	$7.25 \times 10^{-17}$
KA-9	0.13	10	0.120	0.114	0.018	0.14	$7.76 \times 10^{-17}$	$9.11 \times 10^{-14}$

Table 4.2: Continued

Sample	$\phi$	$p_{eff}$ [MPa]	$\varepsilon_t$	$\varepsilon_i$	$\delta\phi_i$	$\phi + \delta\phi_i$	$k_0$ [ $m^2$ ]	$k_e$ [ $m^2$ ]
KA-12	0.12	30	0.060	0.052	0.003	0.12	$5.35 \times 10^{-17}$	$5.57 \times 10^{-14}$
KA-3	0.14	50	0.060	0.049	0.001	0.14	$1.35 \times 10^{-16}$	$6.16 \times 10^{-16}$
KA-7	0.12	70	0.060	0.046	-0.003	0.12	$1.14 \times 10^{-16}$	$7.39 \times 10^{-15}$
R10-3	0.16	10	0.020	0.016	0.001	0.16	$2.16 \times 10^{-15}$	$2.89 \times 10^{-15}$
R10-10	0.16	10	0.030	0.025	0.002	0.16	$7.79 \times 10^{-16}$	$6.35 \times 10^{-16}$
R10-11	0.16	10	0.040	0.035	0.001	0.16	$8.69 \times 10^{-16}$	$1.40 \times 10^{-15}$
R10-7	0.14	10	0.060	0.055	0.007	0.15	$1.82 \times 10^{-15}$	$1.97 \times 10^{-15}$
R10-13	0.17	10	0.120	0.115	0.005	0.18	$8.40 \times 10^{-16}$	$1.55 \times 10^{-13}$
R10-15	0.17	30	0.020	0.015	-0.004	0.17	$1.61 \times 10^{-16}$	$3.01 \times 10^{-14}$
R10-4	0.15	50	0.020	0.015	-0.007	0.14	$1.47 \times 10^{-15}$	$3.06 \times 10^{-16}$
R10-5	0.14	50	0.030	0.024	-0.008	0.13	$1.26 \times 10^{-15}$	$2.21 \times 10^{-16}$
R10-6	0.15	50	0.040	0.034	-0.012	0.14	$1.39 \times 10^{-15}$	$1.90 \times 10^{-16}$
R10-9	0.15	50	0.060	0.053	-0.014	0.13	$1.23 \times 10^{-15}$	$4.90 \times 10^{-17}$
R10-12	0.18	50	0.120	0.112	-0.028	0.15	$1.72 \times 10^{-15}$	$8.05 \times 10^{-16}$
R10-16	0.21	70	0.020	0.014	-0.007	0.20	$2.94 \times 10^{-16}$	$4.15 \times 10^{-15}$
R10-17	0.17	70	0.060	0.052	-0.024	0.15	$8.46 \times 10^{-17}$	$1.90 \times 10^{-14}$
LLB-6	0.21	10	0.010	0.006	-0.005	0.21	$3.80 \times 10^{-13}$	$4.38 \times 10^{-13}$
LLB-7	0.23	10	0.030	0.026	-0.017	0.21	$4.83 \times 10^{-13}$	$3.71 \times 10^{-12}$
LLB-1	0.21	10	0.060	0.055	-0.020	0.19	$5.01 \times 10^{-13}$	$3.37 \times 10^{-13}$
LLB-10	0.22	30	0.030	0.025	-0.021	0.20	$5.24 \times 10^{-13}$	$3.56 \times 10^{-12}$
LLB-9	0.22	30	0.060	0.054	-0.040	0.18	$4.97 \times 10^{-13}$	$1.62 \times 10^{-13}$
LLB-13	0.22	30	0.240	0.233	-0.055	0.16	$4.84 \times 10^{-12}$	$5.51 \times 10^{-14}$
LLB-3	0.19	50	0.030	0.024	-0.019	0.18	$5.31 \times 10^{-13}$	$5.20 \times 10^{-13}$
LLB-11	0.22	50	0.060	0.054	-0.045	0.18	$5.03 \times 10^{-13}$	$1.29 \times 10^{-12}$
LLB-5	0.21	50	0.180	0.174	-0.074	0.13	$4.32 \times 10^{-13}$	$3.44 \times 10^{-14}$
LLB-14	0.23	70	0.060	0.054	-0.048	0.18	$4.70 \times 10^{-13}$	$1.27 \times 10^{-12}$
C8-26	0.17	50	0.015	0.010	-0.011	0.16	$6.22 \times 10^{-12}$	$2.55 \times 10^{-12}$
C8-25	0.17	50	0.045	0.038	-0.027	0.15	$3.24 \times 10^{-12}$	$3.10 \times 10^{-13}$

### 4.3.1 Deformation behaviour

Mechanical data for all samples are shown in [Figure 4.5](#), plotted as differential stress applied to the sample versus axial strain (note that the solid symbols in each case represent the inelastic strain undergone by the sample). One can observe five symptomatic stages of dilatant failure under compression (e.g. Brace et al. 1966; Hoek and Bieniawski 1965; Scholz 1968) in [Figure 4.5a - c](#): 1) the stress–strain curve is concave upwards, a consequence of the closure of microcracks aligned perpendicular to the maximum principal stress; 2) the stress–strain curve is approximately linear in the poroelastic phase; 3) the curve deviates from linear behaviour as the stress is sufficient to generate new dilatant microcracks (the onset of inelastic deformation:  $C'$ ); 4) the material achieves a peak stress ( $\sigma_p$ )—its compressive strength—after which failure is marked by a significant stress drop; 5) with ongoing strain, the samples exhibit a more or less constant residual stress characterised by a flattening of the respective stress–strain curves.

Samples which undergo compaction exhibit the same initial concave upwards slope followed by linear elastic behaviour. In the ductile regime, deviation from linear behaviour is termed  $C^*$  (Wong et al., 1997), representing the onset of inelastic deformation. Thereafter, the material may continue to accommodate approximately the same amount of stress, or accumulate additional stress (a phenomenon known as strain-hardening), which can be observed in samples R10 and LLB, respectively ([Figure 4.5d, e](#)) where the stress–strain curve tends upwards post-failure and the sample strengthens with increasing strain. In many of the compactant samples, the stress–strain curve is variably interposed by stress drops.

### 4.3.2 Porosity evolution

Inelastic change in sample porosity is shown in [Figure 4.6](#), as a function of the inelastic strain accumulated by each sample. [Figure 4.6](#) highlights that contrasting behaviour can be observed for different samples: some show an increase in porosity (dilatancy) whereas the porosity of others decreases with increasing strain (compaction). It can be seen that samples with relatively low initial porosity display the greatest relative increase in porosity: the porosity of Etna basalt (EB) increases from 0.05 to 0.09 when taken to a strain of around 0.12 at 10 MPa effective pressure ( $\delta\phi_i = 0.04$ ). However, a more porous sample—El Zarco andesite (EZ)—increases from 0.07 to 0.10 for a comparable amount of strain and at the same effective pressure ( $\delta\phi_i = 0.03$ ). At initial porosities that are higher still, behaviour is compactant under the same conditions: for samples of La Lumbre andesite (LLB) deformed up to an inelastic strain of 0.06, the porosity

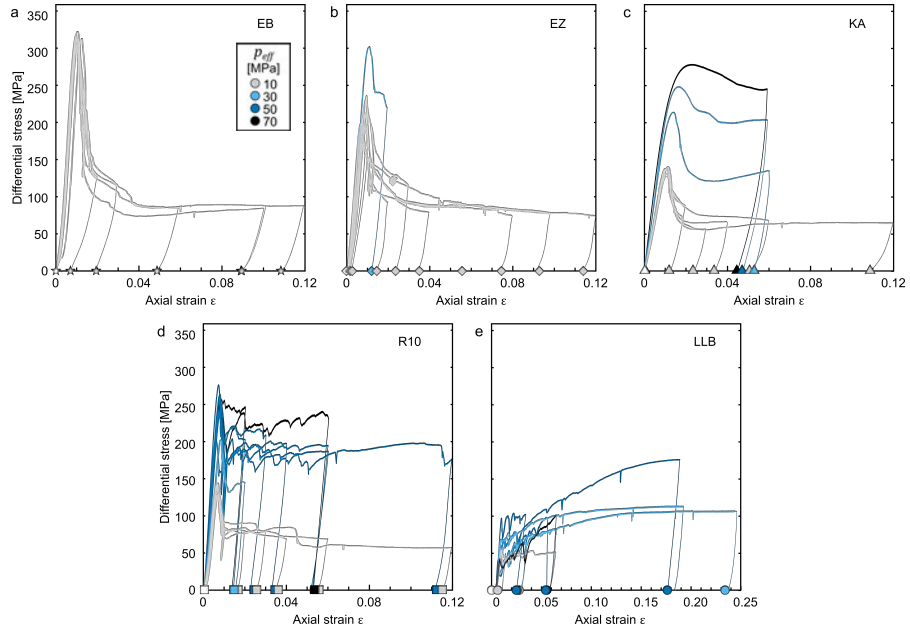


Figure 4.5: Mechanical data for all samples of this study. Solid symbols represent the inelastic strain accumulated (strain after unloading).  
 a) Etna basalt, deformed at 10 MPa effective pressure to varying degrees of strain. At higher effective pressures, the low-porosity basalt could not be broken in the experimental apparatus. b) El Zarco andesite, deformed at 10 and 30 MPa effective pressure. c) Kumamoto andesite, deformed at 10, 30, 50, and 70 MPa effective pressure. Each of the tests in a) to c) failed in a dilatant (brittle) fashion. At the highest effective pressure tested—70 MPa—the sample of Kumamoto andesite showed transitional behaviour but was still predominantly dilatant. d) Ruapehu andesite shows a transition between dilatant and compactant behaviour depending on the effective pressure: below 30 MPa, failure is dilatant, whereas at 50 and 70 MPa effective pressure, the samples yielded in a compactant manner. e) La Lumbre andesite exhibits compactant (ductile) behaviour even at the lowest effective pressure tested (10 MPa). Note difference in  $x$ -axis relative to the other panels.

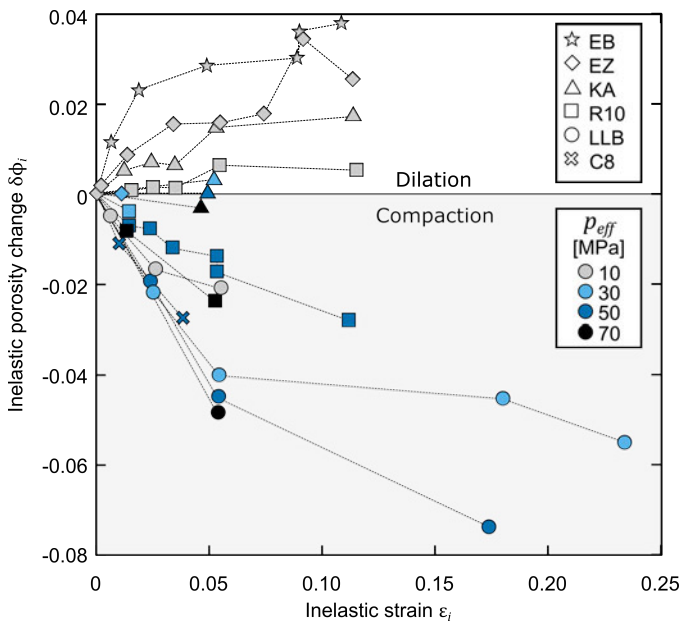


Figure 4.6: Inelastic change in porosity against the inelastic strain undergone by each sample. Positive numbers indicate dilation (porosity creation), whereas negative values represent inelastic compaction (porosity loss). Samples are distinguished by different symbols, with different effective pressures being shown by symbol colour.

decreased from 0.21 to 0.19 ( $\delta\phi_i = -0.02$ ). Another key feature of these data is that with increasing effective pressure, samples from the same suite may exhibit either dilatant or compactant behaviour.

Figure 4.7 shows the incremental change in porosity per unit strain  $\delta\phi_i/\varepsilon_i$  as a function of the initial sample porosity for all samples, including San Antonio (C8) andesite from Heap et al. (2015a). Simply put, the further from zero on the  $y$ -axis, the greater the change in porosity for a given increment of strain, hence the greater the rate of porosity increase or decrease. The sign of this ratio defines whether the porosity change is dilatant ( $\delta\phi_i/\varepsilon_i > 0$ ) or compactant ( $\delta\phi_i/\varepsilon_i < 0$ ). If  $\delta\phi_i/\varepsilon_i = 0$ , then imparting additional inelastic strain to the sample will not influence its porosity. At low initial porosities (i.e.  $\phi \lesssim 0.12$ ), the data typically lie above this line, whereas at greater porosities (i.e.  $\phi \gtrsim 0.18$ ), data are below this line. A transitional intermediate samples from the same suite may be above or below this zone can be discerned ( $0.12 \lesssim \phi \lesssim 0.18$ ) wherein line, depending on the mode of failure (in turn reliant on the effective pressure: Figure 4.7a).

All samples tend to approach  $\delta\phi_i/\varepsilon_i = 0$  with progressive accumulation of strain. Significantly, this indicates that there exists a limit to both dilation and compaction, which shall be discussed in a later section. At the extremes of the porosity range studied herein (i.e. EB:  $\phi =$

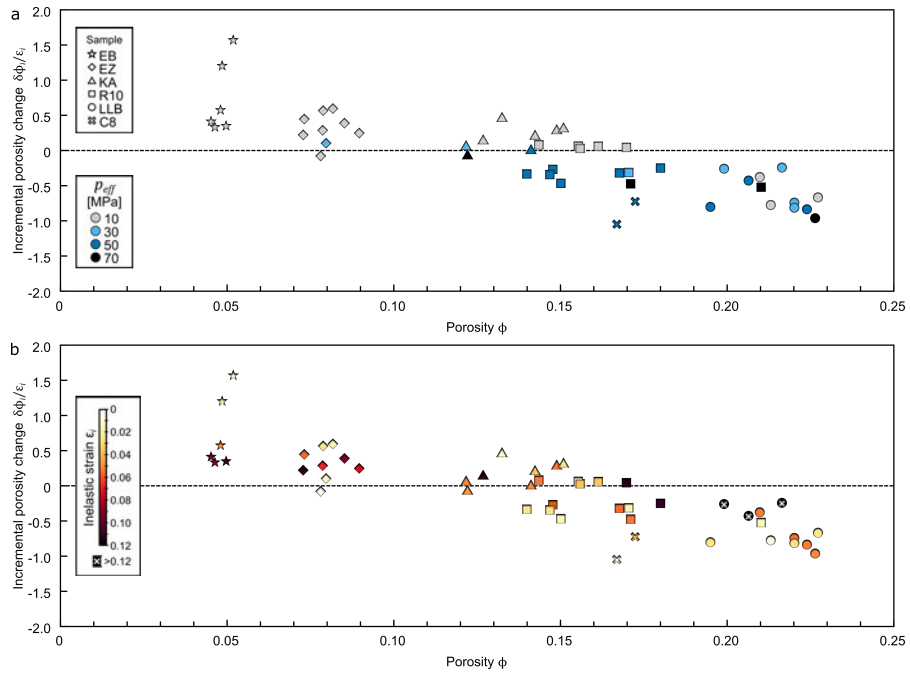


Figure 4.7: Incremental change in porosity with strain accumulation for all volcanic rocks studied. a) At low porosities, data tend to lie above  $\delta\phi_i/\epsilon_i = 0$ , indicating that porosity change is dilatant. Conversely, samples with relatively higher porosities are typically below this line, signifying porosity loss with strain. At intermediate porosities, data are clustered about the line of  $\delta\phi_i/\epsilon_i = 0$ , meaning that porosity change with strain (either dilatant or compactant) is less pronounced. Note the importance of effective pressure for determining dilation or compaction, especially at intermediate porosities ( $0.10 \lesssim \phi \lesssim 0.16$ ). b) With progressive accumulation of strain, samples tend towards the centre line, irrespective of the initial porosity.

0.05; LLB:  $\phi = 0.22$ ), a great amount of strain (in excess of 12% change in the sample volume) is required in order to approach this threshold. However, at intermediate porosities, the limit of dilation or compaction—where strain no longer influences porosity change—may be attained by accumulating much lower amounts of strain.

#### 4.3.3 Permeability evolution

Post-deformation sample permeability  $k_e$  is displayed in Figure 4.8, for all samples. For the lowest porosity sample suites, EB and EZ, we observe that permeability is essentially always higher than the initial value after inelastically accumulating strain (Figure 4.8a, b). In detail, EB increases from around  $7.29 \times 10^{-17} \text{ m}^2$  (the mean initial value of the sample suite) to a maximum of  $6.13 \times 10^{-14} \text{ m}^2$ . The mean starting permeability of EZ andesite was  $3.23 \times 10^{-16} \text{ m}^2$ , which increased to  $3.36 \times 10^{-13} \text{ m}^2$  after being strained to 0.12. An intermediate porosity andesite, KA (see Figure 4.8c), exhibits complex behaviour: both moderate decreases in permeability during some experiments, and an overarching trend of increasing permeability with increasing strain. Ruapehu andesite (Figure 4.8d) shows increases or decreases in permeability of one to two orders of magnitude, depending on the effective pressure (in turn governing the failure mode). The most porous andesite, LLB, is correspondingly that with the highest initial permeability (on average,  $8.34 \times 10^{-13} \text{ m}^2$ ). With increased strain, samples exhibit a general decrease in permeability mostly of the effective pressure at which they were deformed.

#### 4.3.4 Porosity and permeability evolution with strain

Figure 4.9 illustrates the three changing properties—permeability, porosity, and strain—for all samples (including San Antonio (C8) andesite: Heap et al., 2015a). It can be seen that at low initial porosities (EB: Figure 4.9a, EZ: Figure 4.9b) the evolution of permeability and porosity with increasing strain is fairly well constrained. Notably, for relatively small increases in porosity as a result of high strains, permeability can increase by over three orders of magnitude. In the most porous sample (LLB: Figure 4.9e), decreases in permeability of around two orders of magnitude are associated with relatively much larger changes in sample porosity. This is in agreement with the C8 data (Figure 4.9f), which follows a similar trend.

In the intermediate porosity range—KA and R10 (Figure 4.9c, d)—the behaviour is less clear-cut. KA typically exhibits an increase in permeability with negligible amounts of inelastic porosity change. How-

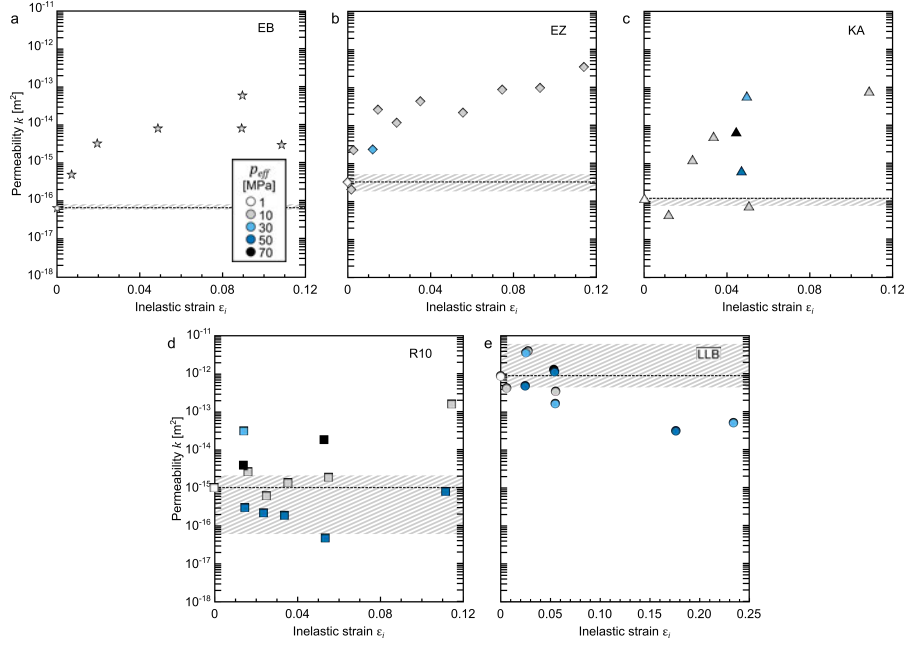


Figure 4.8: Post-deformation permeability of all samples. Shaded area shows range of initial permeabilities, with mean permeability for each sample suite shown by the dashed line. a) EB = Etna basalt. b) EZ = El Zarco andesite. c) KA = Kumamoto andesite. d) R10 = Ruapehu andesite. e) LLB = La Lumbre andesite. Refer to text for discussion.

ever, some samples become marginally less permeable, despite porosity remaining the same, or indeed increasing. R10 generally exhibits moderate decreases in permeability for small decreases in porosity (compaction) or relatively large (two orders of magnitude) increases for approximately the same amount of porosity increase (dilation). The propensity to increase or decrease in permeability is seemingly tied to the effective pressure and failure mode.

#### 4.4 DISCUSSION

##### 4.4.1 Fracture and compaction of volcanic rock

Figure 4.5 shows that there is a notable influence on mechanical behaviour exerted not only by the initial sample porosity—relatively low porosity samples are stronger than their more porous counterparts—but also by the effective pressure  $p_{eff}$ . In detail, samples are more likely to exhibit compactant behaviour at high effective pressures (as observed by, for example, Shimada et al., 1989).

In porous volcanic rock, dilatant failure is the result of propagation and coalescence of microcracks, which culminate in the generation of a macroscopic fracture through the sample and render it

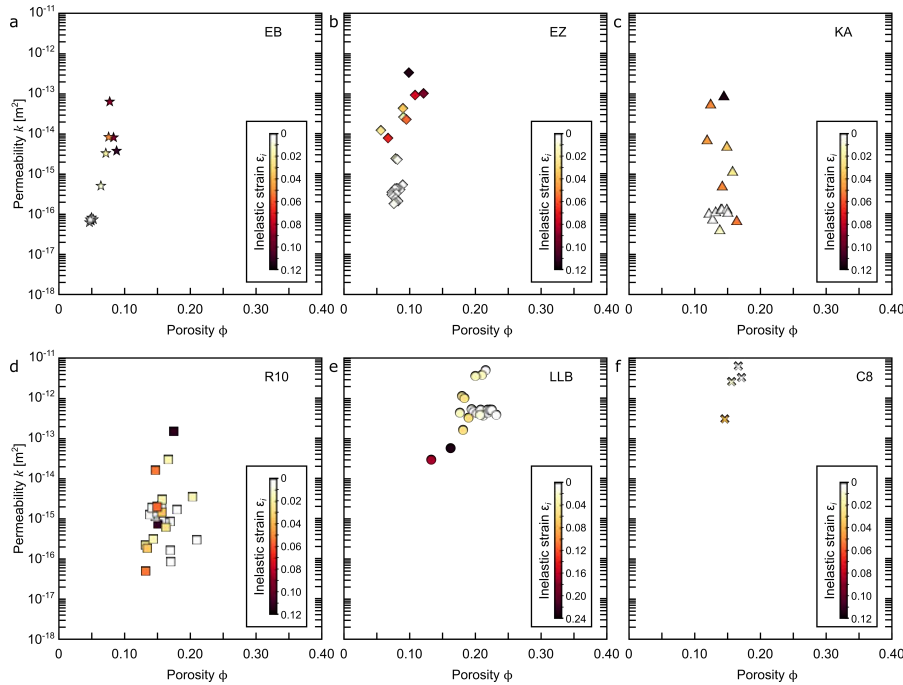


Figure 4.9: Permeability and porosity evolution with strain. The degree of inelastic strain accumulated by the each sample is represented by the colourbar. Note that the colourbar scale for panel e) differs from the others. a) Etna basalt. b) El Zarco andesite. c) Kumamoto andesite. d) Ruapehu andesite. e) La Lumbre andesite. f) San Antonio C8 andesite (Heap et al., 2015a). Refer to text for discussion.

unable to accommodate significant amounts of stress relative to its pre-failure state (e.g. Lockner et al., 1991). Compactional yield in volcanic rock has been attributed to distributed (Zhu et al., 2011; Heap et al., 2015c) or localised (Loaiza et al., 2012; Adelinet et al., 2013; Heap et al. 2015a) cataclastic pore collapse. [Figure 4.10](#) illustrates the progression of damage in these samples Kumamoto andesite (deformed under 10 MPa effective pressure to 0.01 and 0.11 strain) and Ruapehu andesite (deformed under 50 MPa effective pressure to 0.01 and 0.11 strain). In the former samples, the mechanical (and porosity change) data ([Figure 4.5c](#)) suggests dilatant brittle failure, which is supported by the attendant microtextures.

[Figure 4.10a](#) shows shear fractures oriented obliquely to the maximum principal stress. Relatively little damage can be observed elsewhere in the sample. In more detail, [Figure 4.10b](#) highlights the coalescence of two neighbouring fractures. After a greater accumulation of strain ([Figure 4.10c, d](#)), more complex structures can be observed. As well as the development of macroscopic shear faults in these andesites, increased strain promotes conjugate faulting, manifest in secondary fractures which intersect the primary fault at angles of around  $60^\circ$  and  $120^\circ$  ([Figure 4.10c](#)). Moreover, the primary fault zone is itself relatively much wider than its low-strain counterpart (typically around a factor of 5 between the two examples KA-2 and KA-9). When subject to higher strains, a simple shear fracture evolves into a zone of damage, comprising pulverised material originating from either fracture plane ([Figure 4.9d](#)). The degree of shear is evident in the occurrence of crystal fragments entrained within the shear band, which provide natural strain markers.

[Figure 4.10e, f, and 4.10g, h](#) (Ruapehu andesites R10-4 and R10-12, respectively), exemplify a different failure mode. In agreement with the mechanical data ([Figure 4.5d](#)), variably distributed pore collapse can be observed throughout these samples. Notably, the mechanical data exhibit post-failure stress drops, which is inferred to signal compaction localisation. Heap et al. (2015a) describe the same phenomenon in San Antonio (C8) andesite, and their microstructural campaign shows that these intermittent stress drops are associated with the formation of compaction bands (i.e. compaction localisation: Wong et al. 2001; Baud et al. 2004).

At a relatively low strain (0.01), clear evidence of the destruction of crystals and groundmass infilling former void space can be made out. The existence of relatively undamaged groundmass and unfilled pores ([Figure 4.10e](#)) underlines the tendency for compaction to localise. This predisposition has been suggested to be a function of stress nucleation, around poorly connected equant porosity (Adelinet et al., 2013), due to preferential alignment of pores (Loaiza et al., 2013),

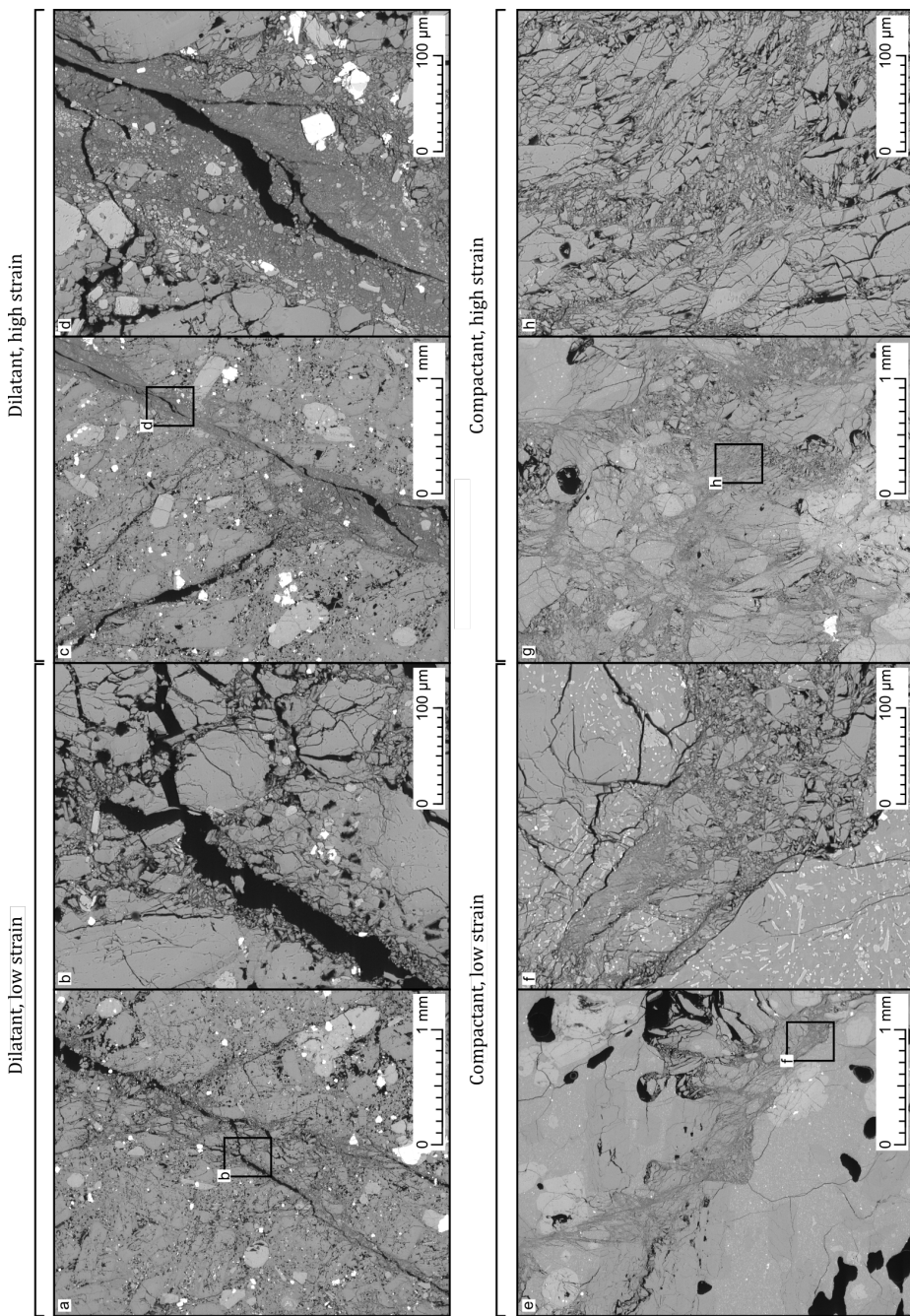


Figure 4.10: Dilation and compaction: Microstructure.  
(Caption overleaf)

Figure 4.10: Microstructural evolution of damage with strain in dilatancy and compaction. a) Kumamoto andesite (KA-2) deformed at an effective pressure of 10 MPa to an inelastic strain of 0.01. Coalesced cracks can be observed cutting across the sample as a macroscopic fracture (porosity is black). Note that macroscopic fracture appears to have evolved stepwise, with smaller fractures being progressively interlinked by connecting cracks. b) Detailed view of fracture shown in a). Note jigsaw-fit geometry of fracture planes, approximately 20  $\mu\text{m}$  apart. Occasional granular material can also be seen on the fracture margins. c) Kumamoto andesite (KA-9) deformed at an effective pressure of 10 MPa to an inelastic strain of 0.11. As with KA-2, a macroscopic fracture can be seen through the sample. However, higher strain promotes the development of a conjugate fracture system. d) Detailed image of the interior of the fracture shown in c). Width is typically greater than 100  $\mu\text{m}$ . Comminuted granular material is abundant within the fracture, with pulverised phenocrysts highlighting substantial shear on the fault. e) Ruapehu andesite (R10-4) deformed at an effective pressure of 50 MPa to an inelastic strain of 0.01. Compaction of the sample is manifest in zones of collapsed pores where crushed material fills in former void space. Bands of crushed pores proximal to undamaged porosity highlights the tendency for compaction localisation in porous andesite at relatively low strain. f) Detailed image of a compaction band, approximately 100 - 300  $\mu\text{m}$  thick and traversing the sample. Jigsaw-fit geometry of granular material indicates that it is essentially in situ. g) Ruapehu andesite (R10-12) deformed under the same conditions as R10-4, but having accumulated a strain of 0.11. In this case, distinct bands of compaction cannot be distinguished; rather, a zone of intensely crushed groundmass comprises approximately half of the sample. Within the substantially deformed regions, the only relatively unscathed porosity tends to be spherical or subspherical. h) As in f), the fragmental material exhibits little or no evidence of transport. Note that samples KA and R10 have different porosities and compositions; this figure is simply to illustrate how damage evolves in the dilatant and compactant regimes.

or along pre-existing planes of weakness such as zones of amoeboid pores or microfractures (Heap et al., 2015a).

[Figure 4.9f](#) shows that there often exists a sharp boundary between a compaction band and the surrounding host rock. Jigsaw-fit configurations of fragments within these bands indicates that the material is for the most part in situ. Once strain has progressed to a greater degree (0.11: [Figure 4.9f, g](#)), discrete compaction bands cannot be readily distinguished. Rather, regions of compaction can be observed that encompass greater than half of the sample. In these heavily deformed zones, the only surviving pores appear to have notably high rounded-

ness and sphericity. As evident in the low-strain example ([Figure 4.9e](#), [f](#)), the fragmental material remains more-or-less in situ ([Figure 4.9h](#)).

#### 4.4.2 Post-failure behaviour

Dependent on the initial physical properties of our samples and the conditions under which they are deformed, one may observe a range of failure modes and post-failure behaviours, as hinted at previously. [Figure 4.11](#) plots the porosity change during deformation against the effective mean stress for selected samples of Volcán de Colima and Ruapehu andesites. Effective mean stress  $P$  is a function of all mechanical stresses acting on a sample, determined by  $\sigma_1 + \sigma_2/3 - p_p$ , where  $\sigma_1$  is the axial pressure, and  $\sigma_3 \equiv p_c$  (the confining pressure). The dashed lines in [Figure 4.11a](#) and [4.11b](#) indicate hydrostatic deformation of the samples in the absence of an applied axial load (i.e. deformation solely as a function of increasing confining pressure). Inelastic porosity change is achieved when the porosity evolution of a sample deviates from the hydrostatic path.

In the compactant case, the porosity evolution during deformation deviates to the right of the hydrostatic curve at the onset of shear-enhanced compaction  $C^*$  (Wong et al., 1997). [Figure 4.11a](#) shows data from porous La Lumbre andesite (Volcán de Colima;  $\phi \simeq 0.22$ ), all of which exhibit a compactant failure mode, irrespective of the effective pressure at which they were deformed. Post-failure, the samples continue to compact under the continued application of an axial load. However, beyond a threshold stress-strain accumulation, sample LLB-13 ([Figure 4.11a](#)) exhibits a transition from compactant deformation to dilatant behaviour. This transition has been previously described in sedimentary (e.g. Schock et al., 1973; Baud et al., 2000; Vajdova et al., 2004; Baud et al., 2006) and volcanic rock (Heap et al., 2015a) and is termed  $C^{*\prime}$ .

[Figure 4.11b](#) shows comparable data for samples of Ruapehu andesite ( $\phi \simeq 0.16$ ). At high effective pressure ( $p_{eff}=70$  MPa), deformation behaviour is much the same as observed for the La Lumbre samples ([Figure 4.11a](#)). At lower effective pressure, however, dilatancy is observed. In the dilatant case, the effective mean stress–porosity change curve deviates to the left of the hydrostatic curve at the onset of dilatant microcracking  $C'$  with failure defined by a peak stress  $\sigma_p$ . Post failure, a stress drop is typically observed, followed by continued dilation at a residual stress level (for example, the sample deformed at an effective pressure of 10 MPa). However, transitional behaviour also occurs in these andesites at intermediate effective pressures. In the samples shown deformed under 30 and 50 MPa of effective pressure, failure is dilatant but succeeded by compaction which continues

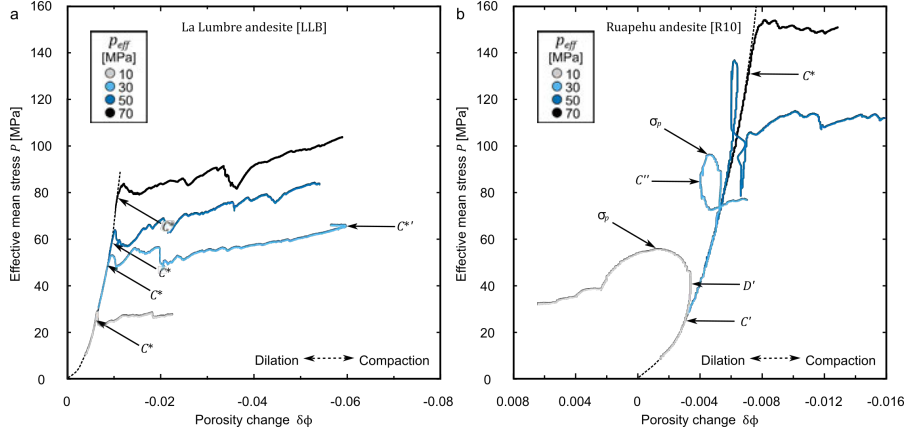


Figure 4.11: Porosity change during deformation against the effective mean stress of two sample sets. a) La Lumbre andesite exhibits typical compactant behaviour, deviating from the hydrostatic (dashed) curve at the onset of shear-enhanced compaction  $C^*$ , under a range of effective pressures. After a threshold stress-strain accumulation, the behaviour can transition from compactant to dilatant, as highlighted by an arrow, at a point termed  $C^{*\prime}$ . b) Ruapehu andesite deformed under effective pressures from 10 to 70 MPa. At relatively low effective pressure, failure mode is dilatant, characterised by the onset of dilatant cracking  $C'$  and a peak stress  $\sigma_p$ . At 70 MPa effective pressure, the failure mode and post-failure deformation is compactant, characterised by a deviation from the hydrostatic (dashed) curve towards the right-hand-side of the panel. At intermediate effective pressures we observe that the initial failure is dilatant, again defined by the points  $C'$  and  $\sigma_p$ . However, post-failure behaviour switches to compaction at a point indicated here as  $C''$ .

for as long as the experiments lasted. This switch in deformation behaviour is hereafter referred to as  $C''$ , signifying a post-failure strain-dependent dilatant–compactant transition.

[Figure 4.12](#) and [4.13](#) show microstructure accompanying these strain-dependent transitions in deformation behaviour. As described by Heap et al. (2015a), the transition from compaction to dilation in volcanic rock is characterised by significant shortening and barrelling of the sample [Figure 4.12a](#))—a consequence of the relatively high strain required to exceed the threshold  $C^{*'}\prime$ —and the generation of a dilatant shear band. Zones of intense compaction and shear can be observed in [Figure 4.12a](#), a composite image of a sample (LLB-13) which has surpassed  $C^{*'}\prime$ . The overall geometry of these zones is reminiscent of an extensive conjugate fault system (e.g. [Figure 4.10c, d](#)), with relatively less damage in wedges on either end of the sample ([Figure 4.12b](#)). Throughout much of the sample, the original porosity cannot be discerned due to infilling by comminuted fragments of groundmass and crystals: the process of cataclastic pore collapse (e.g. Zhu et al., 2010). As shown in [Figure 4.12c, d](#), in regions where cataclasis is most developed—and thus where the degree of porosity loss is greatest—local stress fields have allowed dilatant shear fractures to propagate and coalesce. As indicated in [Figure 4.7](#) and the attendant discussion, the development of macroscopic fractures in thoroughly compacted samples indicates a limit to the degree of possible compaction of volcanic rock. However, the fact that compaction exhibits a tendency to localise ([Figure 4.12a, b](#); see also [Figure 4.10e - h](#)) means that the transition from compaction to dilation may be dependent on local porosity loss rather than the "global" inelastic porosity loss of the entire sample. This may well prove to be a function of pore size and shape distribution, parameters which are typically more heterogeneous in volcanic rock than sedimentary or plutonic materials, for example.

The transition to compactant behaviour after dilatant failure ( $C''$ : [Figure 4.13a – d](#)) appears to be more closely linked to the effective pressure under which deformation occurs which, along with initial sample porosity, is a key determinant of the initial failure mode in these volcanic rocks ([Figure 4.6](#)). [Figure 4.13b](#) shows that the cataclasis associated with compaction in volcanic rocks is almost exclusively located around the shear fault imparted during macroscopic sample failure: the majority of the rest of the sample shows little or no evidence of cataclastic pore collapse.

Typically, cataclasis in fractured environments is manifest in the generation of fault gouge, a mechanism driven by friction, involving both fracturing and the movement and rotation of rigid fragments

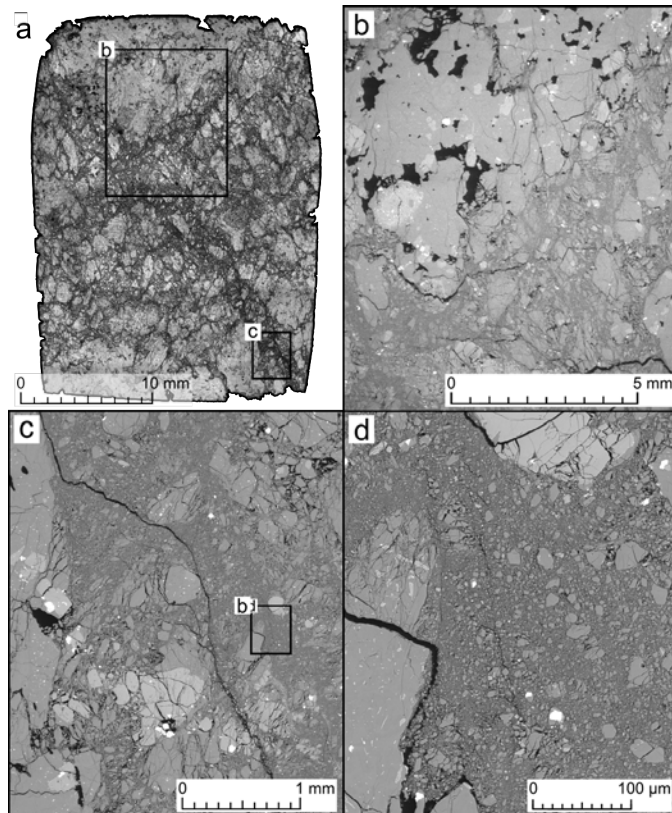


Figure 4.12: Microstructural evidence of transition in deformation behaviour  $C^{*!}$ . a) Stitched composite image of 78 optical micrographs of La Lumbre andesite (sample LLB-13), deformed at 30 MPa effective pressure to an inelastic strain of 0.24. Darker regions indicate densely fractured zones. Note the barrelled shape of the sample and the localisation of intensely damaged zones into shear bands. b) Back-scattered scanning electron microscope (SEM) image showing contrast between zones of cataclasis and relatively less damaged rock. Note that, while the latter regions are intensely fractured, remnant porosity can be discerned throughout (porosity is black). Large fractures can be seen snaking through the shear bands. c) SEM image of part of a pronounced shear band. The interior of the shear zone is composed of comminuted granular material overprinted by through-running dilatant fractures. d) Detailed view of intensely pulverised groundmass and crystals within the shear band. Fragments are typically  $<10 \mu\text{m}$  in diameter.

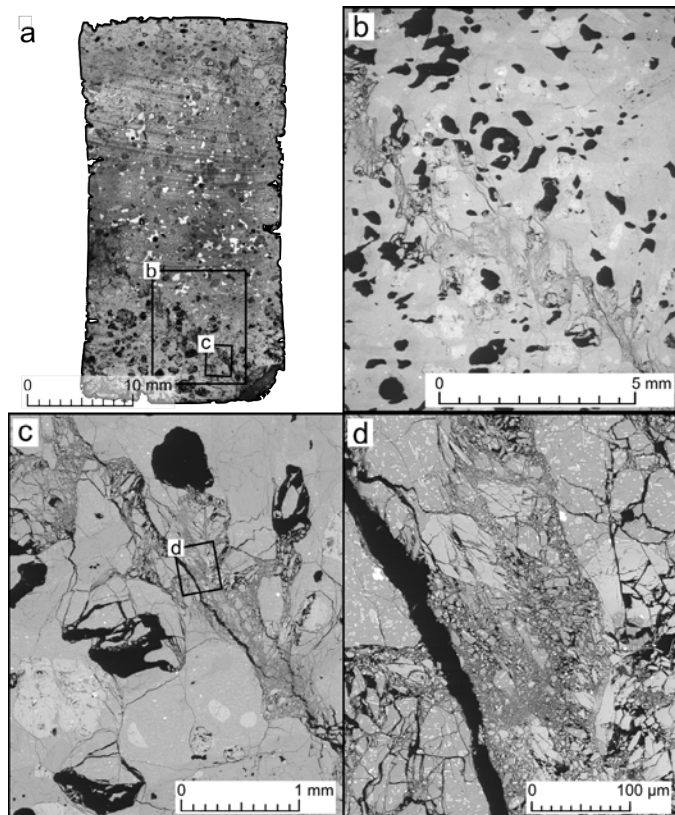


Figure 4.13: Microstructural evidence of transition in deformation behaviour  $C''$ . a) Stitched composite image of 88 optical micrographs of Ruapehu andesite (sample R10-15), deformed under 30 MPa effective pressure to an inelastic strain of 0.01. b) SEM image of part of prominent shear fracture. Proximal to the shear fracture is evidence of abundant cataclasis. Further afield, porosity is relatively undamaged. c) Fracture zone subperpendicular to maximum principle stress (i.e. the direction of loading), characterised by a macroscopic fracture surrounded by a damage zone approximately 200 - 500  $\mu\text{m}$  in thickness comprising crushed fracture plane material. Note that pores adjacent to the fracture zone exhibit incipient cataclastic pore collapse, whereby damage propagates at pore margins and promotes comminuted fragments to spall into the void space. d) Detailed image of fracture. Note that there is little evidence of shear along the primary fracture (approximately 20  $\mu\text{m}$  in width); rather, the jigsaw-fit geometries of the crushed groundmass and crystals indicates that compaction occurred mostly in situ.

(e.g. Engelder, 1974). During compaction, cataclasis tends to localise more-or-less concentrically around pores, causing granular fragments to spall into the void space (Zhu et al., 2010; 2011). In detail ([Figure 4.13c](#)) evidence can be observed of both friction-induced cataclasis (along the primary fracture planes) and cataclastic pore collapse which progresses in a cascading fashion away from the through-running shear fault. ([Figure 4.13d](#) highlights the fine gouge created along the fault plane (10s of  $\mu\text{m}$  and less in diameter).

#### 4.4.3 Permeability–porosity evolution summary

A summary plot of porosity and permeability change from this study is presented in ([Figure 4.14a](#), using the fractional change in porosity with respect to the initial porosity such that  $\lambda\phi = \delta\phi_i/\phi_0$ . Similarly, the fractional change in permeability is given by:

$$\lambda k = \frac{\log_{10} k_e - \log_{10} k_0}{\log_{10} k_0} \quad (4.2)$$

Mapping  $\lambda k$  and  $\lambda\phi$  defines a domain with four quadrants (I - IV), which indicate whether porosity and permeability increase or decrease with increasing strain. As shown in [Figure 4.14a](#), the deformed samples predominantly fall within II and III, corresponding to concomitant porosity and permeability increase, or concomitant porosity and permeability decrease respectively.

Each of the sample suites EB, EZ, KA, R10, and LLB are shown in detail in [Figure 4.14b - f](#), indicating the degree of inelastic strain accumulated. Comparing [Figure 4.14b](#) and [4.14c](#), for example, it can be seen that with an increase in initial porosity, the change in porosity with additional strain is less pronounced (i.e. there is a decreasing propensity for dilation with increasing initial porosity). Generally, with increasing effective pressure, the  $\lambda\phi$  versus  $\lambda k$  trajectory for these samples tends to rotate anti-clockwise around the origin (e.g. [Figure 4.14d, e](#)).

Notably, the permeability of each sample was measured after unloading, at the same confining pressure (1 MPa). The fact that there is a measurable difference between samples deformed at different effective pressures in the same deformation regime (i.e. dilatant or compactant) is presumably testament to the fact that grain size distribution is highly sensitive to the confining pressure at which it forms (Engelder, 1974; Kennedy and Russell, 2012). One may expect pore infill through cataclasis to be more efficient when the fractured granular material is relatively small, suggesting that permeability reduction via compaction may be more efficient under higher effective pressures, which was also noted by Alam et al. (2014). Samples which

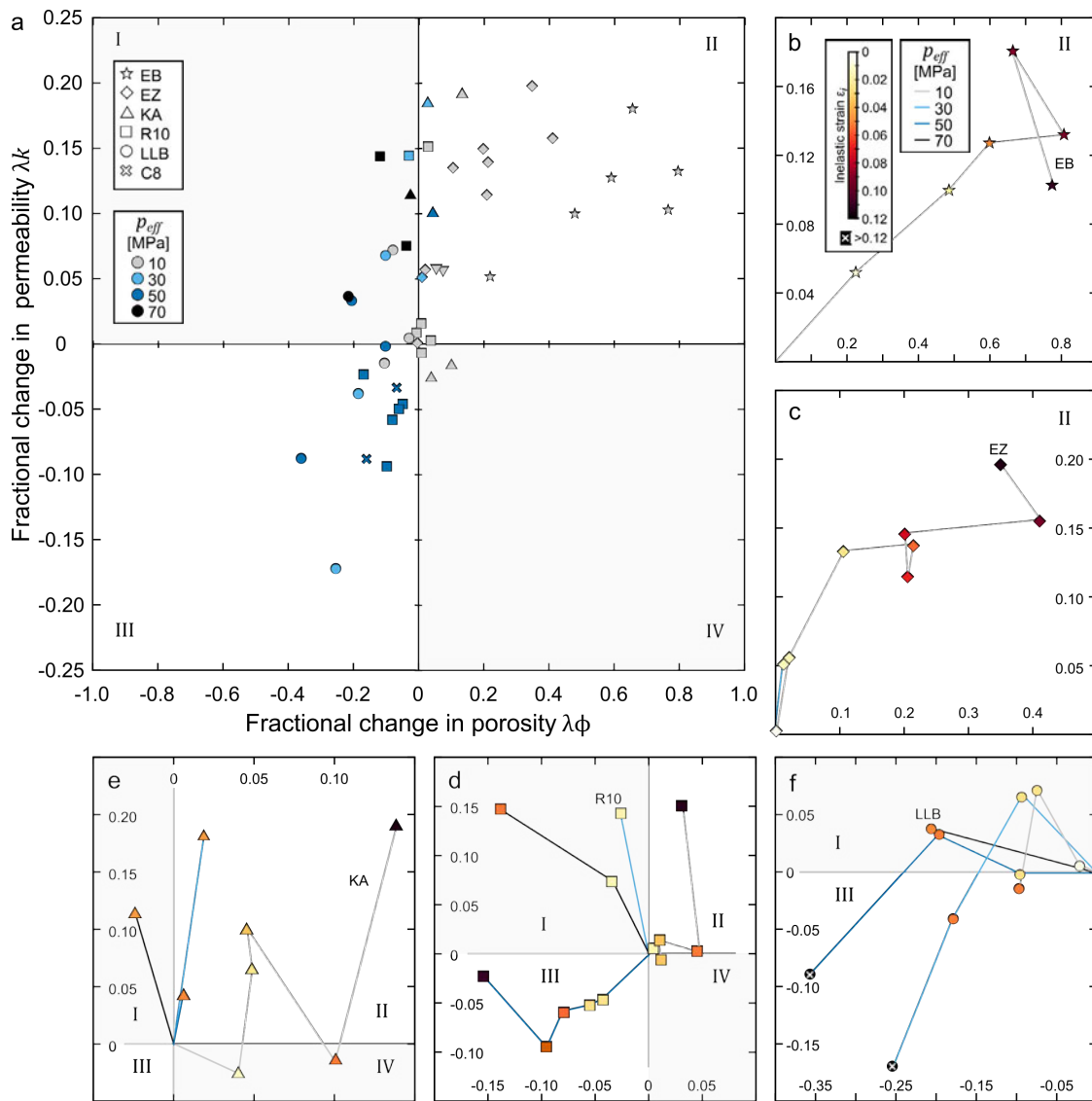


Figure 4.14: Fractional change in permeability and porosity for the rocks studied herein. a) Sample suites are defined by symbols as shown, and effective pressure is given by the symbol color. EB: Etna basalt; EZ: El Zarco (Colima) andesite; KA: Kumamoto andesite; R10: Ruapehu andesite; LLB: La Lumbre (Colima) andesite; C8: San Antonio (Colima) andesite. Quadrants I - IV signify permeability increase associated with porosity decrease (I), concomitant permeability and porosity increase (II), concomitant permeability and porosity decrease (III), and permeability decrease associated with porosity increase (IV), respectively. c) to f) show the detailed progression of  $\lambda \phi$  and  $\lambda k$  with strain (indicated by the colourbar). b) EB: Etna basalt. c) EZ: El Zarco (Colima) andesite. d) KA: Kumamoto andesite. e) R10: Ruapehu andesite. f) LLB: La Lumbre (Colima) andesite.

could be deformed at effective pressures higher than 10 MPa tend to be situated in I and IV, emphasising the increased propensity for net compactant behavior at high effective pressures and high porosities. Commonly, the greater the degree of strain experienced by the sample, the further it lies from the origin. These general trends are summarised in [Figure 4.15](#); nevertheless, it is clear that these three parameters—porosity, effective pressure, and inelastic strain—cannot fully determine the relative changes in permeability observed.

For example, the trends for Etna basalt ([Figure 4.14b](#)) and El Zanco andesite ([Figure 4.14c](#)) are nonlinear with increasing strain, most likely due to heterogeneity between individual samples. While shear faults in individual samples look macroscopically similar, it is possible that small variations in fault angle relative to the sample axis may influence the efficiency of a fracture as a fluid pathway. Samples of Kumamoto and Ruapehu andesite at low effective pressure (10 MPa) exhibit complex behaviour whereby porosity increases at low strain without significant changes in permeability (at higher strains, both porosity and permeability are relatively greater than the initial values). This characteristic is only apparent in the intermediate-porosity andesites (i.e. 0.14 - 0.16), which display the greatest variation in deformation behaviour, occasionally contrasting porosity evolution with deformation, and the highest propensity to exhibit net compaction despite failing in the brittle regime (samples of R10 deformed at 30 - 50 MPa effective pressure often exhibit the transitional dilatant-compactant switch  $C''$ , whereby the sample contains a discrete fracture but has undergone post-failure compaction). Moreover, samples of Ruapehu andesite deformed at an effective pressure of 70 MPa plot unexpectedly in quadrant I: permeability increase associated with porosity decrease. While samples of La Lumbre andesite show a decrease in both porosity and permeability at high strains, permeability appears to increase at low strains, yielding a parabolic  $\lambda\phi-\lambda k$  trajectory.

#### 4.5 IMPLICATIONS FOR VOLCANOLOGY

The results and discussion above illustrate the range of mechanical responses of volcanic rock to imposed strain under volcano-relevant conditions. Moreover, these data reveal that permeability evolution as a function of deformation is remarkably complex. The next section examines these results in a broader context: if we can expect permeability of edifice-forming rocks to vary due to porosity, effective pressure and strain, then what influence does this have on volcanic activity?

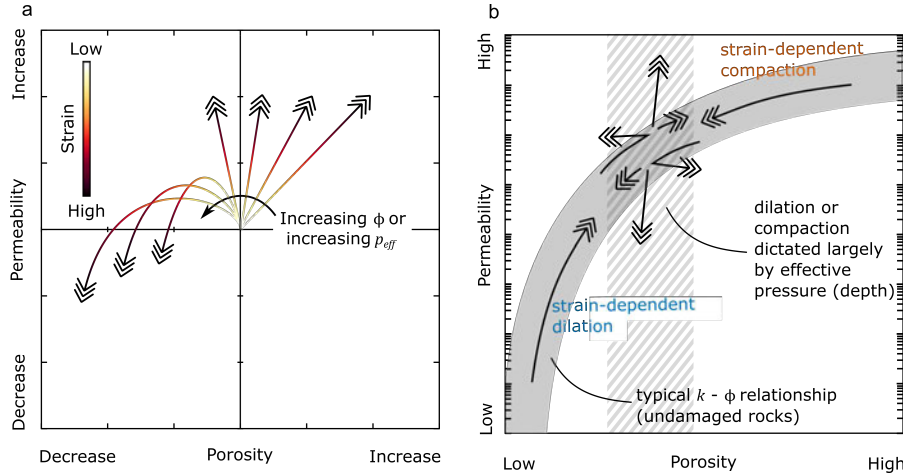


Figure 4.15: Summarised porosity–permeability evolutions guided by the data presented in this chapter. a) At low initial porosities  $\phi$  and low effective pressures  $p_{eff}$ , dilatant behavior is expected, accompanied by an increase in permeability. As initial porosity or effective pressure increase, porosity increase is less pronounced. Eventually, samples may exhibit porosity loss associated with permeability increase (especially at intermediate porosities or in the case of samples having surpassed  $C''$ ). At high initial porosities or high effective pressures, compaction is expected to result in significant permeability reduction. With increasing effective pressure in the compactant regime, increasingly efficient cataclasis results in relatively lower porosity and permeability than an equivalent sample at a lower effective pressure. b) At low or high initial porosities, strain-induced permeability evolution serves to move samples along the typical porosity–permeability path anticipated for undamaged volcanic rocks (as shown in Chapter 3). However, in an intermediate range of porosities, more complex behavior may be observed, as indicated. Refer to text for discussion.

#### 4.5.1 *Distribution of fracture and compaction throughout the edifice: implications for outgassing*

Due to different histories of degassing, ascent, and eruption processes for different volcanic ejecta and effusive products (e.g. Mueller et al., 2011), anisotropic edifice porosity may arise over time. Volcán Rincon de la Vieja (Costa Rica), for example, exhibits contrasting flank compositions as tephra is predominantly deposited on the western side due to the prevailing trade winds, whereas flow phenomena have been historically concentrated to the north and south (Kemper et al., 1996). Similarly, Volcán Casita (Nicaragua) is composed primarily of pyroclastic units on the southwest (again a consequence of the prevailing wind direction), whilst the majority of relatively denser lava flows extend to the east because of an asymmetric crater morphology (van Wyk de Vries et al., 2000). Geophysical surveys of active and historic volcanoes indicate that significant variations in density (and hence, porosity) may be a common feature of stratovolcanic edifices. For example, Tiede et al. (2005) use gravimetric inversion to explore edifice density at Gunung Merapi (Java, Indonesia), identifying a relatively low-density unit on the western flank. These authors calculate an average porosity of 0.21 for this unit: a high value compared to the average edifice porosity of around 0.15 determined by Setiawan (2002) and the range of 0.05 - 0.10 estimated by Commer et al. (2005) for the region directly below the Merapi summit. These values are generally consistent with measured laboratory values of porosity (Le Pennec et al., 2001; Kushnir et al., 2016). Similar contrasts in density have been inferred from gravimetric studies of several other volcanic regions such as Mauna Loa, Hawai'i (Zucca et al., 1982), Campi Flegrei, Italy (Cubellis et al., 1995), Cordón Caulle, Chile (Sepúlveda et al., 2005), and at in the Central Volcanic Complex of Tenerife, Spain (Gottsmann et al., 2008).

The experimental data presented here show that relatively porous edifice rock is prone to compact, even under low effective pressure (i.e. at shallow depths), whereas rocks with a low initial porosity will preferentially dilate when subject to strain. Thus one or other of these two processes will be dominant in different regions of a volcanic edifice: for the example of Gunung Merapi, the relatively porous western flank should compact under its own weight in the shallow edifice; on the other hand, the denser regions will fracture near the surface but facilitate compaction at depth by increasing the overlying lithostatic pressure (i.e. the confining pressure  $p_c$ ). Accordingly, permeability reduction should occur over time and with increased strain in the western portion of the edifice, whereas permeability of the other flanks should generally increase. This is in agreement with the broad trend of outgassing observed at Gunung Merapi: quiescent outgassing oc-

curs through and around the central vent, as well as through fumarole fields located to the east, southeast, and south of the main crater (Le Cloarec and Gauthier, 2003), while fumarole fields are absent to the west of the crater.

#### 4.5.2 *Shear faulting, gouge formation, and permeability evolution*

From the experimental data in the dilatant regime it can be inferred that in shallow volcanic environments, one should often expect to observe ongoing dilatancy and permeability increase of several orders of magnitude with strain. Indeed, gas flux data from well-monitored dome eruptions at volcanoes such as Mount St Helens, Mount Unzen, Soufrière Hills Volcano (Montserrat), or Santiaguito (Guatemala), offer tantalising hints of such a phenomenon. Using surface gas flux measurements to assess the permeability of a volcanic system requires numerous assumptions: foremost, one must assume that the emission of a given gas species—such as SO<sub>2</sub>—is solely derived from the magma and is representative of the emission of the gas phase as a whole. A second presumption is that the total gas budget is equivalent through time (for example, by constant replenishment of the gas fraction from depth). Without post-hoc analysis of melt inclusions or quenched melts (Edmonds, 2008, and references therein), it can be difficult if not impossible to decouple the influences of evolving system permeability and non-constant magma flux on any measured change in gas emission.

Nevertheless, with caution changing rates of gas discharged at the surface of a volcano may be viewed as a reflection of the changing permeability of its upper system. For example, SO<sub>2</sub> emission data from Santiaguito, Guatemala, shows that the volcano passively outgasses during periods of repose (Holland et al., 2011). Notable peaks in the emitted volume of SO<sub>2</sub> are associated with explosive events which involve the development of networks of shear fractures around the conduit and the generation of unconsolidated fault gouge in the shallow edifice (Lavallée et al., 2013).

This following section outlines eruptive sequences associated with dome-building phases at three different volcanoes: Mount Unzen, Popocatépetl (Mexico), and Soufrière Hills Volcano. In each case, a brief description of the period of activity precedes suggestions of how the process of strain-induced dilation and permeability increase may have been a contributing factor.

At Mount Unzen, the emergence of a lava dome in 1991 coincided with the commencement of detectable SO<sub>2</sub> emission (Hirabayashi et al., 1995). Despite the generally decreasing rate of lava extrusion

between 1991 and 1994, Hirabayashi et al. (1995) show that the discharge rate of SO<sub>2</sub> over the same time period remained high (hundreds of tons per day). These authors estimate that around 80% of the potential sulphur inventory was outgassed over the time period: this suggests that the generation of extensive zones of cataclasis associated with dome and spine extrusion at Mount Unzen (Smith et al., 2001) constituted a highly efficient outgassing mechanism, which we suggest may have contributed to the gradual cessation of activity by 1995.

In December 1994, volcanic activity re-awakened at Popocatépetl after 67 years of slumber (e.g. De la Cruz Reyna et al., 2008). After a period of Vulcanian activity, eruptive behaviour throughout 1995 and early 1996 was characterised by intermittent explosions with progressively longer repose times and with the erupted plumes becoming increasingly ash-poor over this time (Delgado-Granados et al., 2001). In August 1995, ash eruptions ceased entirely and the volcano re-entered a state of quiescence until March 1996. The subsequent two years saw the emplacement of a new lava dome, and new cycles of effusive and explosive activity with a trend of increasing repose timescales echoing the activity of 1995 - 1996. Despite a decrease in the lava extrusion rate, vigorous outgassing activity was monitored over this time and for a few months after the cessation of dome extrusion in September of 1998; indeed, SO<sub>2</sub> emissions remained high throughout the active period (a discharge tens of thousands of tons of SO<sub>2</sub> per day: Delgado-Granados et al., 2001).

Finally, Herd et al. (2005) describe a sequence of five Vulcanian explosions at Soufrière Hills Volcano in 2003, and emphasise that the repose time between eruptions becomes progressively longer. Ultimately, this eruptive sequence culminated in a non-explosive outgassing event (Edmonds and Herd, 2007). It is generally understood that an efficient outgassing mechanism may preclude pressure build-up and facilitate effusive behaviour or quiescence: as such, Edmonds and Herd (2007) propose that continued gas loss through a developing shear fracture network surrounding the conduit led to an eventual release of overpressure in the conduit magma and provoked a transition from explosive to effusive activity.

The three case studies described above share four main points in common: 1) each was associated with repeated cycles of explosive activity, interposed by relative quiescence or effusion of lava domes; 2) in each case, the repose periods between successive explosive eruptions became gradually longer with time; 3) in each case, explosivity petered out over time, culminating in a transition from generally explosive to effusive behaviour, or indeed a cessation of activity al-

together; 4) in each case, the onset of significant SO<sub>2</sub> emissions were concomitant with the beginning of the period of unrest. However, despite generally decreasing trends of lava extrusion rate, monitored gas emissions remained high.

This field evidence supports the conclusion that the mechanisms of shear fracturing and friction-driven gouge generation results in increased permeability in shallow volcanic environments (i.e. under low confining pressures). The eruptive sequences each comprised at least one protracted period of dome extrusion, where one would expect the development of progressively thick zones of cataclasis (e.g. [Figure 4.10a - d](#)) and highly permeable fault zones around the dome margins and in the shallow edifice ([Figure 4.8](#)). The measurement of voluminous discharges of SO<sub>2</sub> after the onset of extrusive activity suggests that networks of shear fractures allowed efficient outgassing to occur.

Explosive activity is generally driven by rapid bubble expansion near the surface, which provides the kinetic energy necessary for explosive fragmentation. If expansion occurs faster than the relaxation timescale of the magma—a product, amongst other factors, of its viscosity—then pore pressures are liable to increase (e.g. Dingwell, 1996); in turn, this promotes explosive fragmentation of magma. In the case studies above, lengthening repose times between eruptions indicates that the threshold pressure required for explosive failure (e.g. Melnik and Sparks, 2002; Koyaguchi et al., 2008) was becoming progressively more difficult to attain (Edmonds and Herd, 2007). Based on the experimental data and the case studies above, it is probable that strain-induced dilation accompanied the ascent and/or extrusion of dense, viscous magma. As zones of fractures evolved as a function of increasing strain, the permeability of the shallow conduit margins increased, potentially by several orders of magnitude as suggested by the experimental data presented above. As a result, magmatic volatiles were efficiently siphoned from the system, prolonging—and eventually precluding—the generation of pore overpressures.

#### *4.5.3 Evolving edifice permeability: an indicator of changing eruptive styles?*

Taken together, the field evidence outlined in [Section 4.5.1](#) and [Section 4.5.2](#) underscores the importance of the spatial distribution of edifice rock with differing physical and mechanical properties in terms of the development of permeability and outgassing routes in volcanic systems. Moreover, it supports the conclusion that the mechanisms of shear fracturing and friction-driven gouge generation results in increased permeability in shallow volcanic environments (i.e. under low confining pressures). Gas loss from magma through increasingly

permeable shear fracture zones may well dictate, at least in some systems, the transition from explosive to effusive activity, as appears to have been the case at Soufrière Hills Volcano (Edmonds and Herd, 2007) for example, or from effusive activity to quiescence (such as observed at Mount Unzen).

The experimental data of this chapter highlight the tendency for dense rock to become more permeable, and for porous rock to compact, with increasing strain. Thus, whereas low-porosity regions of the edifice may generally be poor at passive outgassing during periods of eruptive quiescence, when subject to strain, for example as a result of shallow fluid migration (e.g. Denlinger and Hoblitt 1999; Clarke et al. 2007) or deep-seated magma chamber deformation (e.g. Melnik and Sparks 2005; Wadge et al., 2006), the increased propensity for shear fracture generation may forge effective pathways for gas release. On the other hand, highly porous edifice rock may constitute an effective means of passive outgassing, but its permeability will tend to decrease with the accumulation of strain. This implies that the spatial and temporal distribution of fumaroles and the vigor with which they outgas may contain information regarding subsurface strain accumulation: in a quiescent system, a reduction of passive outgassing of magmatic gas species may suggest, therefore, strain-induced permeability reduction, portending a build-up of pressure and potential explosive activity.

#### 4.6 CHAPTER SUMMARY

During triaxial compression, dilatant failure is observed via macroscopic fault generation in volcanic rocks with low initial porosities when deformed under low effective pressures. With increasing strain, dilation tends to continue as a consequence of fault sliding. Correspondingly, an increase in permeability is typically associated with dilatant behaviour. Inelastic compaction—manifest by cataclastic pore collapse—was observed in volcanic rocks that were relatively more porous or that were deformed under higher effective pressures. With increasing strain, compaction tends to localise. However, under very high strains, samples were so damaged that individual compaction localisation features cannot be discerned; rather, large portions of the sample were entirely pulverised. In these compactant cases, permeability increase or decrease appears to correspond to both the amount of strain accumulated and the effective pressure at which deformation was performed. While cataclastic pore collapse is governed by the pore size (e.g. Zhu et al., 2010; 2011), the grain size of comminuted fragments is thought to be a function of the effective pressure at which it is formed (Engelder, 1974; Kennedy and Russell, 2012). As such, permeability reduction through this mechanism is presumably

more efficient when it occurs under high effective pressures (a finer distribution of fragments will more readily occlude the pores around which they develop through cataclasis).

An analysis of the ratio of inelastic porosity change and inelastic strain shows that at extreme porosities, a great deal of porosity change (dilation or compaction) may be associated with increasing strain. However, samples in an intermediate porosity range ( $0.12 \lesssim \phi \lesssim 0.18$ ) lie close to the threshold whereat  $\delta\phi_i/\varepsilon_i = 0$ . This implies that with increased strain, these samples will undergo little porosity change. Indeed, this is what is observed: irrespective of the mode of failure (which is strongly dependent on the effective pressure) large changes in permeability can be observed as fault structures or compaction bands increase in size and complexity, but porosity evolution tends to be negligible. Complex deformation behaviours are also notable at intermediate porosities, including transitions from compactant to dilatant behaviour (a threshold known as  $C^{*I}$ ), or from dilatant to compactant (which is here termed  $C^{*II}$ ). Significantly, this highlights that the transition from dilatant to compactant (i.e. brittle to ductile) behaviour is not only dictated by the initial physical properties of a rock—most importantly, its porosity—and the effective pressure (or depth) at which it is deformed, but can also be a phenomenon governed by the degree of post-failure strain to which the rock is subjected. Combined with the tendency for damage to localise in volcanic materials, it is clear that global variables such as inelastic porosity change or inelastic strain fail to entirely indicate how permeability may evolve in volcanic systems.

Spatial differences in edifice density are likely common, and could give rise to anisotropy in edifice permeability, manifest in—amongst other things—an uneven distribution of actively outgassing fumaroles. It is further highlighted that changing patterns of gas emission at active volcanoes may reflect strain-induced evolution of permeability in the shallow edifice, especially around the margins of extruding lava domes and spines. While in an unstrained volcanic environment, regions of the edifice composed of dense rock will typically be poor at passive outgassing, dilation-induced permeability increase should facilitate volatile outgassing through dense rock when subject to high strains. On the other hand, porous rock will be more effective at outgassing during periods of inactivity, but will preferentially compact and thus become less efficient at outgassing when accumulating strain. These observations suggest that changes in distribution or intensity of fumarole outgassing across the flanks and summit of a volcano, for example, may reflect subsurface strain and renewed volcanic activity.



# 5

## PORE FLUID-INDUCED EMBRITTLEMENT

---

*Therefore a time would come when the elastic and explosive forces of the imprisoned gases would upheave this ponderous cover and drive out for themselves openings through tall chimneys.*

— Jules Verne, *Journey to the Center of the Earth*, 1864

*Chapter 4* investigated how mechanical deformation can influence porosity and permeability evolution in volcanic rocks. Importantly, the results showed that changes in confining pressure at which deformation was performed had a strong influence on the failure mode—dilation or compaction—as well as the post-failure behaviour. However, as hinted at in *Chapter 1*, there are many roads to Rome: effective pressure is controlled by the pore pressure as well as the confining pressure. In a volcano, pore pressures are prone to fluctuations (during periods of unrest, for example). This chapter explores the effect of altering pore fluid pressures within intact and deforming rock. In detail, the phenomenon of fluid-induced embrittlement is studied, and the attendant implications for volcano outgassing are discussed.

This chapter is published as: Farquharson, J. I., M. J. Heap, P. Baud, T. Reuschlé, N. R. Varley. *Pore pressure embrittlement in a volcanic edifice*. Bulletin of Volcanology, 78(6).

### 5.1 INTRODUCTION

It has long been acknowledged that pore fluids and pore fluid pressure have a significant function in faulting processes (Hubbert and Rubey, 1959; Rubey and Hubbert, 1959; Johnson and McEvilly, 1995; Baud et al., 2000; Faulkner and Rutter, 2001; Vinciguerra et al., 2004; Paterson and Wong, 2005; Ougier-Simonin and Zhu, 2013) and slope stability, usually in the context of mass movement and slope failure (e.g. Day, 1996; Voight and Elsworth, 1997; Jousset et al., 2013). The mechanical behaviour and failure mode of rocks are governed by their physical properties (such as porosity and pore size) and the local effective pressure  $p_{eff}$  (e.g. Wong and Baud, 2012). The effective pressure acting on a rock is a function of the confining pressure (equivalent to the lithostatic pressure) surrounding it, and the pore fluid pressure within it ( $p_c$  and  $p_p$ , respectively). Inelastic strain accumulation at low effective pressure often results in dilatant failure (macroscopically "brittle" behaviour i.e. fracture generation), whereas a compactant failure mode—where the deforming material experiences inelastic porosity loss during deformation—is typically observed at

high effective pressures ([Chapter 4](#)). Both of these failure modes have been observed in previous experimental studies on volcanic rocks in which the pore fluid pressure was kept constant and experiments were performed at different confining pressures (e.g. Kennedy et al., 2009; Zhu et al., 2011; Loaiza et al., 2012; Adelinet et al., 2013; Heap et al., 2014b; 2015a, c; see also [Chapter 4](#)). However, the effective pressure will decrease if pore pressure increases and therefore rock embrittlement—the transition from an elastic or compactant regime to dilatant (i.e. macroscopically brittle) failure—can occur if the pore pressure is increased sufficiently.

In a volcanological context, deviations from the equilibrium pore pressure have been thought responsible for the mechanical deformation of volcanic edifices (e.g. Nishi et al., 1996; Caricchi et al., 2011; Jousset et al., 2013; Sisson and Power, 2013). Within a volcanic system, edifice rocks are typically fluid-saturated (Day, 1996). This multiphase medium is often subject to significant thermal and mechanical stresses (e.g. Roman et al., 2004; Costa et al., 2007) which offer a range of processes by which pore fluid pressure may increase. For example, source vents of explosive eruptions are often plugged by variably fractured lava domes or choked conduits (e.g. Voight et al., 1999; Johnson and Lees, 2000; Diller et al., 2006). As long as volatile disequilibrium exists, a gas phase will continue to exsolve from the magma, allowing pore pressure to build beneath the plug (Lensky et al., 2004). Further, solidification or crystallisation of conduit magma, thermal expansion of fluids, and hydrothermal circulation can all affect edifice pore fluid volume in an open system (e.g. Voight and Elsworth, 1997; Sisson and Bacon, 1999); as such, sustained increases in pore pressure are probably a common occurrence within the edifice of a volcanic system.

The cyclic or episodic nature of many volcanic processes is similarly well documented: cycles in outgassing, seismicity, and explosive eruptions have been detected at numerous volcanic systems, often reflected in contemporaneous geophysical data, highlighting the inflation and deflation of the edifice (Denlinger and Hoblitt, 1999; Watson et al., 2000; Michaut et al., 2013; Yokoo et al., 2013; Anderson et al., 2015; Heimisson et al., 2015). This fact is significant, as it suggests that cyclic processes in the conduit, such as the movement of gas aggregates or "slugs" (James et al., 2004; De Lauro et al., 2012), the ascent of vesicularity-stratified magma (Voight et al., 1999), or transient plugging events (Johnson and Lees, 2000), may bring about oscillatory volumetric deformation of the edifice. Correspondingly we may expect oscillation of pore fluid pressures in the edifice over a range of timescales.

## 5.2 EVIDENCE FOR DEVIATIONS IN PORE FLUID PRESSURE

Direct field evidence for magmagenic fluctuations in pore fluid pressure is rare, but does exist. For example, two magma intrusion events at Krafla, Iceland (September 1977 and July 1978) were associated with transient increases in country rock pore pressure measured at a proximal geothermal well. During the first event, an increase of 0.76 MPa was recorded (4300 m from the intrusion); during the latter, an increase of 0.36 MPa was recorded approximately 9300 m from the intrusion (Sigurdsson, 1982; Elsworth and Voight, 1992; Elsworth et al., 1996). Shibata and Akita (2001) report water level changes in wells proximal to Usu volcano, Japan, interpreted as a direct result of volumetric expansion of the magma chamber, and subsequent intrusion of magma into the edificial fracture network. A similar interpretation is used to explain water pressure changes measured near Kīlauea, Hawai'i (Hurwitz and Johnson, 2003). Hydraulic head changes of a few centimetres in these latter examples reflect transient pore pressure increases on the order of 0.001 MPa (hydraulic head is directly related to the pressure head  $\psi$ , which in a confined well can be described by  $\psi = p_p / \rho_f \cdot g$ , where  $\rho_f$  and  $g$  are the fluid density and acceleration due to gravity, respectively).

Further quantitative and qualitative examples are highlighted by Newhall et al. (2001), who estimate that pore fluid pressures in confined volcanic systems may rise by as much as several tens of MPa as a result of magmagenic thermo-mechanical pressurisation. Moreover, hydrofractures—where the pore fluid pressure exceeds the confining pressure and results in brittle failure of rock—have also been inferred in volcanic systems from field observations and chemical analysis (e.g. Heiken et al., 1988; Gudmundsson et al., 2008), a testament to the high pore fluid pressures that can accumulate in rock adjacent to the conduit and intrusions.

As magmatic intrusions and ascent comprise the predominant source of thermal and mechanical stresses within a volcanic structure, thus the rates and magnitudes of increases in pore pressure, and their impact on rock mechanical behaviour and failure mode, may be expected to be correspondingly highest near to the conduit and intrusive magmatic bodies (for example, pore fluid pressure has been estimated to increase with temperature at a rate of around  $1 - 2 \text{ MPa } ^\circ\text{C}^{-1}$ ; Knapp and Knight, 1977). Indeed, recent work (e.g. Rust et al., 2004; Lavallée et al., 2013; Gaunt et al., 2014) has argued the existence of a "halo" surrounding the conduit that comprises intensely fractured magma or edifice rock, through which magmatic gases—primarily steam—can readily outgas. Strain modelling (Young and Gottsmann, 2015) indicates that this assumption is necessary to explain recent syn-

eruptive volumetric strain data recorded at Soufrière Hills Volcano (Montserrat). Further, a recent study by Strehlow et al. (2015) employs Finite Element Analysis to model the poroelastic responses of a saturated volcanic edifice system to subsurface magmagenic strain. These studies emphasise the importance of understanding the hydro-mechanical interactions between the porous edifice and magma chambers, conduits, and intrusions.

Field evidence from Volcán de Colima illustrates that subsurface magmagenic strain is reflected in the degree of fumarolic outgassing from the upper flanks of the edifice. [Figure 5.1](#) shows thermal emission data along a transect on the upper edifice of the volcano, for three dates with varying volcanic activity. Airborne thermal surveillance has previously proved to be a useful tool to establish variations in the emplacement of domes at Volcán de Colima, as well as variations in fumarole temperature and heat flux (Hutchison et al. 2013), while the monitoring of fumarole temperatures from fixed ground vantage points has also contributed in the understanding of the evolution of eruptive activity (Stevenson and Varley, 2008). In [Figure 5.1](#), peaks above the background temperature (in the range of 0 – 20 °C) are inferred to represent fumarole emission. Notably, during a period of minimal eruptive activity—July 2012—just one active emitting fumarole was registered in the transect. In January 2013, effusive activity was occurring, but extruding at a low rate and confined within a deep crater. The increase in activity relative to July 2012 is evident in the appearance of a second fumarole, at a greater distance from the crater rim. Finally, the high-temperature fumaroles observed in February 2015 reflect higher rates of extrusion and correspondingly more vigorous outgassing from the flanks of the volcano. There is thus a correlation between the ascent of strain-inducing bodies (gas or magma) with increases in gas flux from the edifice (e.g. Harris and Maciejewski, 2000), in turn associated with increases in pore fluid pressure.

Distal from volcanic conduits, larger-scale regional fault systems have also been observed to vent magmatic gases (e.g. Heiligmann et al., 1997; Giamanco et al., 1998). A study by Varley and Taran (2003), showed that fault architecture near Volcán de Colima did not comprise a constant pathway for magmatic gas species. However, anomalous radon (Varley and Taran, 2003) and boron (Taran et al., 2000) measurements around the edifice could suggest that transient pathways are formed at some depth, temporarily allowing gases to escape from the volcanic system. Further, long-period (LP) seismic events, characterised by transient seismic signals lasting tens of seconds with periods less than or equal to two seconds (Lahr et al., 1994; Chouet, 1996; Neuberg, 2000), have been recorded in abundance in many vol-

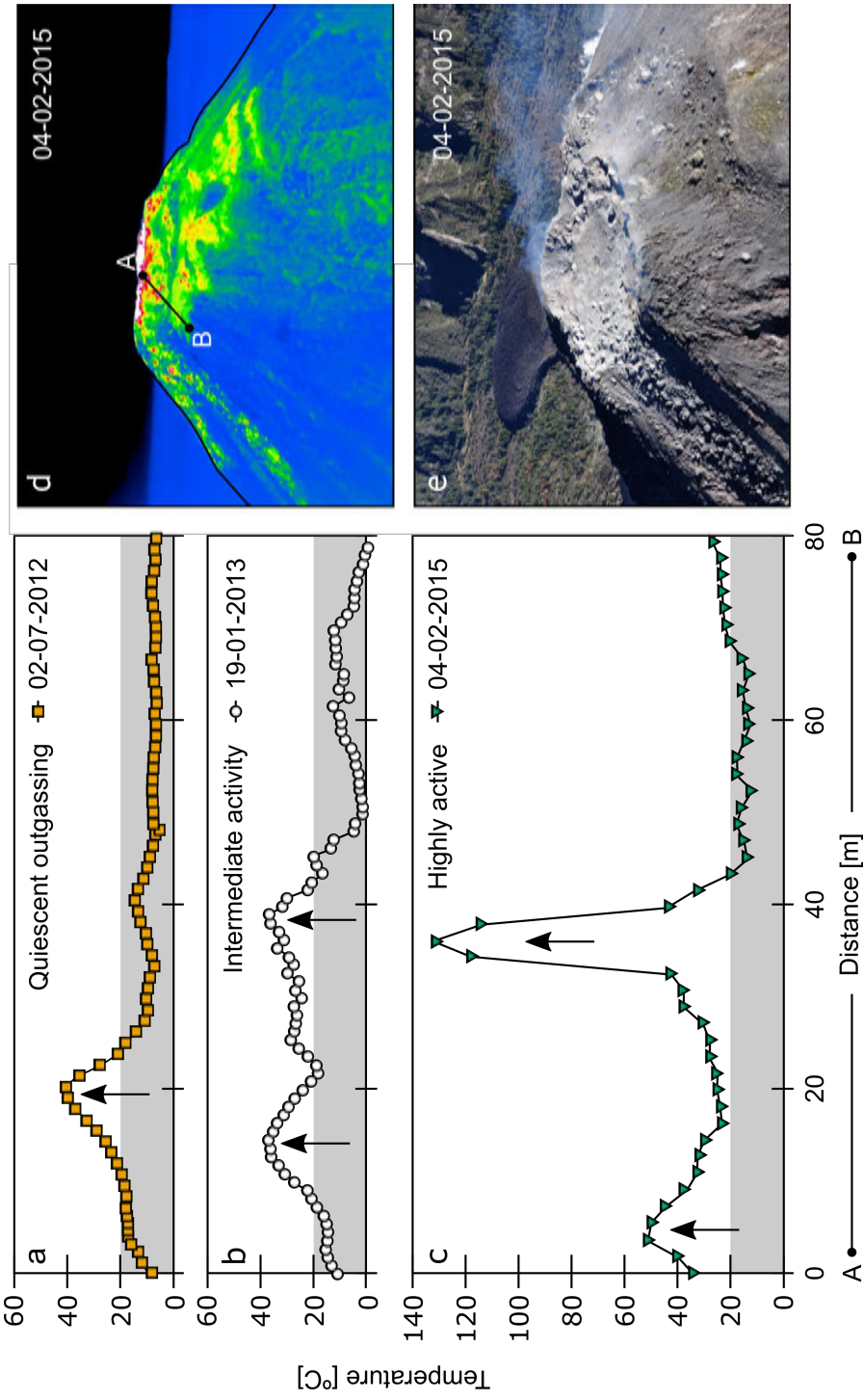


Figure 5.1: Temperature recorded along a transect from the crater rim of Volcán de Colima down the uppermost part of the edifice (i.e. parallel to the principal slope direction) using a Jenoptik VarioCam with  $640 \times 480$  pixel resolution (sensitive in the  $7.5 - 14 \mu\text{m}$  wavelength band). Data were acquired from light aircraft overflights of the volcano on three dates: a) 02 July 2013, b) 19 January 2013, and c) 04 February 2015, as part of the CHIV (Centro de Intercambio e Investigación en Vulcanología) volunteer program. Data were provided by Dr Nick Varley, and initial analysis was performed by Amy Sharp. Flights were in the early morning in each case, in order to avoid the effects of solar heating, and surface features were used in order to ensure consistency of viewing geometry, pixel size, and field of view. Each time period corresponds to a different level of effusive activity. Arrows highlight peaks above the average background temperature range, indicating the presence of fumaroles. Panel d) shows the transect on a typical thermal image, and e) is a true-colour photograph from approximately the same vantage.

canic environments, such as Volcán de Colima, Mexico (e.g. De Lauro et al., 2012; Boué et al., 2015), and Merapi, Indonesia (e.g. Jousset et al., 2013). LP events have been interpreted as shear fracture events (e.g. Neuberg et al., 2006; Varley et al., 2010; Thomas and Neuberg, 2012), slow-rupture failure of edifice-forming material (e.g. Harrington and Brodsky, 2007; Bean et al., 2014), or the resonance of fluid-filled fractures (Lahr et al., 1994; De Lauro et al., 2012).

Despite the evidence described above, there is a paucity of experimental studies on the impact of fluctuating pore fluid pressures on the mechanical behaviour and failure mode of volcanic rocks, and the attendant implications for outgassing and volcanic edifice stability. For example, the potential for the existence of fractures in deeper parts of the edifice—where predominantly compactant behaviour is expected (Heap et al., 2015a; see also [Chapter 4](#))—means that there must be a mechanism of embrittlement which can occur under stress conditions which would otherwise preclude brittle behaviour. Accordingly, the following outlines an experimental study designed to investigate the process of pore fluid-induced embrittlement in porous volcanic rocks.

### 5.3 MATERIALS AND METHODS

Samples were cored from a block of porous andesite (block C8, as described in Heap et al. 2014b; 2015a) collected from the 1998 block-and-ash flow deposits of Volcán de Colima. Although the material was collected from Volcán de Colima, the attendant discussions and conclusions are more widely applicable to stratovolcanoes with comparable eruption styles and cycles, such as Soufrière Hills Volcano, Montserrat, Lascar (Chile), Ruapehu (New Zealand), or Merapi (Indonesia). Sample preparation was carried out as described in [Chapter 2](#), and a subsample of nine cores selected in order to minimise variations in connected (water) porosity  $\phi_w$ . While it may be that  $\alpha$  (the Biot–Willis coefficient) is slightly  $<1$  for andesites (see [Chapter 2](#)), for the relatively small range of pressures imposed in this study the effect of  $\alpha \neq 1$  is negligible and inconsequential in terms of the discussion. As such, the effective pressure convention  $p_{eff} = p_c - \alpha \cdot p_p$  is adopted.

Experiments were performed at confining pressures between 0 and 40 MPa ([Table 5.1](#)). The bulk density  $\rho_b$  of volcanic rock at Volcán de Colima has been observed to vary significantly (e.g. Mueller et al., 2011; Farquharson et al., 2015; Lavallée et al., 2016), the majority of erupted products falling in a density range between around 2000 and 2500 kg m<sup>-3</sup> (Heap et al., 2015a; Lavallée et al., 2016). Approximating the lithostatic pressure as previously ( $\rho_b \cdot gz$ ; e.g. Jaeger et al., 2009), the imposed pressures represent depths in the edifice from 0 m down

to around 1600 – 2000 m.

Acoustic emissions (AE) during sample deformation are associated with microcracking (Lockner, 1993). In order to assess microstructural damage, AE was monitored throughout the experiments with a piezoelectric transducer attached to the top of the upper piston, and the signal processed by AEwin software. AE energy is displayed herein in arbitrary units: AE hits were recorded if signal amplitude was greater than 40 decibels; "energy" simply represents the root-mean-square of the received waveform. Note that these data are presented in arbitrary units (root-mean-square of the waveform divided by  $10^6$ ) as the values are not directly comparable with those recorded using different experimental or field setups: AE is used here as a tool to understand the onset and extent of microcracking during our experiments. Confining and pore pressures were measured and regulated using servo-controlled actuators. Refer to [Chapter 2](#) for full details.

Two types of test were performed: constant strain rate and constant differential stress experiments. For both types of experiment, the initial target confining and pore pressures were first applied to the sample (except in the case of a uniaxial experiment which was deformed in a water bath at atmospheric pressure using a Schenck uniaxial deformation apparatus). During the constant strain rate experiments, an axial load was applied at a constant strain rate of  $10^{-5}$   $s^{-1}$  (i.e. in the same manner as the tests of the previous chapter) until the sample failed.

During the constant differential stress experiments, differential stress  $Q$  and confining pressure were kept stable: following microstructural equilibration at the chosen effective pressure, the axial load was increased at a constant rate of  $10^{-5}$   $s^{-1}$  until the differential stress was equal to 60 MPa (a value within the poroelastic domain, as guided by previous constant strain rate tests). Samples were left overnight (for a minimum of 16 hours) under constant differential stress. Since the rock is within the poroelastic domain, zero axial and volumetric deformation of the sample was recorded during this time. Pore pressures were then increased at servo-controlled rates ( $5.0 \times 10^{-1}$ ,  $5.0 \times 10^{-2}$ ,  $5.0 \times 10^{-3}$ , or  $5.0 \times 10^{-4}$  MPa  $s^{-1}$ ) from a starting value of 10 MPa. A further test was performed where a sample was held under a constant confining pressure and differential stress and the pore pressure was oscillated at regular intervals. In a final test, pore pressure was increased in a sample undergoing constant strain rate deformation in the compactant regime. All of the experiments reported in this study are summarised in [Table 5.1](#).

Table 5.1: Summary of experimental conditions and results.  $\phi$  is connected porosity.  $p_c$ ,  $p_p$ , and  $p_{eff}$ , are confining, pore, and effective pressures, respectively, and  $\dot{p}_p$  is the pore pressure increase rate.  $\sigma_p$  is the peak stress of brittle-failure samples;  $C'$  is the onset of dilatant microcracking;  $C^*$  is the onset of shear-enhanced compaction.

Sample	$\phi$	Initial $p_p$ [MPa]	$\dot{p}_p$ [MPa s <sup>-1</sup> ]	$p_{eff}$ at failure [MPa]	$\sigma_p$ [MPa]	$C'$ [MPa]	$C^*$
C8-29	0.16	0	0	-	0	35.7	18.1
C8-14	0.16	15	10	-	5	73.5	29.8
C8-13	0.16	20	10	-	10	91.1	44.2
C8-32	0.16	40	10	-	30	-	-
C8-12	0.17	40	10	$5.0 \times 10^{-1}$	0.4	60.0	-
C8-03	0.16	40	10	$5.0 \times 10^{-2}$	1.0	60.0 <sup>a</sup>	-
C8-27	0.16	40	10	$5.0 \times 10^{-3}$	1.3	60.0 <sup>b</sup>	-
C8-28	0.16	40	10	$5.0 \times 10^{-4}$	4.9	60.0 <sup>c</sup>	-
C8-31	0.18	40	10	$5.0 \times 10^{-3}$	12.4	60.0 <sup>d</sup>	-
C8-34	0.16	40	10	$5.0 \times 10^{-2}$	30	-	92.1

<sup>a</sup> Experiments were performed under load-control; differential stress  $Q$  is maintained at 60 MPa throughout.

<sup>b</sup> See footnote [a](#)

<sup>c</sup> See footnote [a](#)

<sup>d</sup> See footnote [a](#)

## 5.4 RESULTS

### 5.4.1 Constant strain rate with constant pore pressure

[Figure 5.2a](#) shows the stress–strain curves for each of the constant strain rate tests. Dilatant/brittle behaviour can be observed for the samples deformed at effective pressures of 0, 5, and 10 MPa, whereas compactant deformation is evident at an effective pressure of 30 MPa. This distinction is further highlighted in the curves of porosity against axial strain, shown in [Figure 5.2b](#).

[Figure 5.2c](#) shows an example of the first type of failure mode (brittle/dilatant), showing differential stress and cumulative acoustic emission energy as a function of axial strain (both curves are independent proxies for damage in the sample). In each of the brittle experiments (i.e.  $p_{eff} = 0, 5$ , or  $10$  MPa), an initially convex slope can be observed in the stress–strain curves, typical of the closure of pre-existing microcracks aligned approximately perpendicular to the direction of loading. As can be observed in [Figure 5.2b](#), this corresponds to an initial decrease in porosity with the initial closure of microcracks.  $C'$  (shown in [Figure 5.2c](#)) defines the onset of dilatant microcracking (Wong et al., 1997), after which point the rate of compaction decreases. Samples subsequently underwent axial splitting ( $p_{eff} = 0$  MPa), or shear fracturing ( $p_{eff} = 5, 10$  MPa), following peak stresses ( $\sigma_p$ ) of 35.7, 73.5, and 91.1 MPa, respectively ([Table 5.1](#)). The rate of acoustic emissions accelerates significantly prior to sample failure, indicating an increase in the rate of microcracking events as brittle failure is approached ([Figure 5.2c](#)).

When deformed at an effective pressure of 30 MPa, a different failure mode is observed: compaction, as discussed in the previous chapter. The sample responds in a purely compactant manner, associated with monotonously decreasing porosity with increasing strain ([Figure 5.2b](#)), and the capacity of the material to deform to a substantial strain without failing ([Figure 5.2d](#)). The onset of inelastic deformation (shear-enhanced compaction) is termed  $C^*$  (Wong et al., 1997; Wong and Baud, 2012), and is indicated on [Figure 5.2d](#). After  $C^*$  (which occurred at a differential stress of about 103 MPa in the experiment of [Figure 5.2d](#)), the differential stress plateaus at around 120 MPa. During compactant deformation there is not a distinct acceleration in the AE rate, rather—and as shown in [Figure 5.2d](#)—there is a relatively steady and progressive accumulation of damage throughout the experiment. Notably, the cumulative AE energy is over an order of magnitude higher than that recorded in the brittle tests (e.g. [Figure 5.2c](#)) indicating that significantly more damage has been accu-

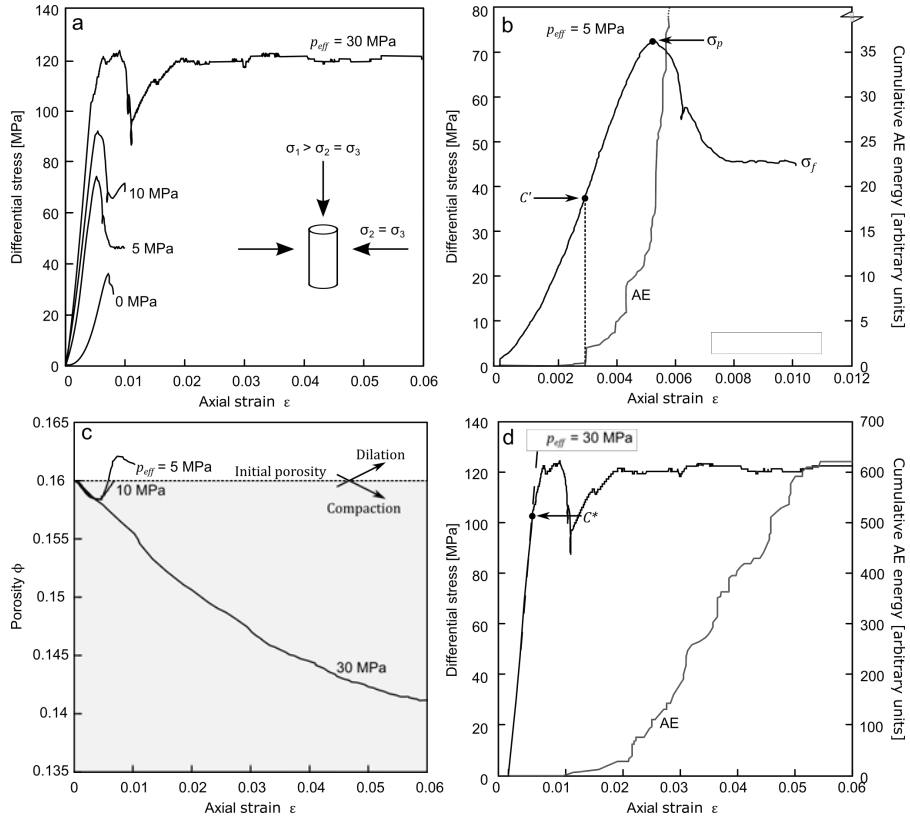


Figure 5.2: Mechanical data for andesites from Volcán de Colima deformed under a constant strain rate. Stress as a function of axial strain for all tests is shown in a). b) shows the change in porosity during deformation for each sample from an initial value of  $\phi = 0.16$  (except the uniaxial test, where this change cannot be monitored). c) gives an example of a test where failure is in the dilatant regime, in a sample deformed at an effective pressure of 5 MPa. Peak stress ( $\sigma_p$ ) and residual post-failure stress ( $\sigma_f$ ) are indicated, as is  $C'$  (the onset of microcracking). Cumulative acoustic emission (AE) data are also shown, plotted in arbitrary units (refer to text for explanation). Note that the onset of AE in c) corresponds with  $C'$ . Equivalent data are shown in d) for a sample which failed through compaction (at an effective pressure of 30 MPa). In this case, failure is marked by  $C^*$  (the onset of shear-enhanced compaction), the point where the stress-strain curve deviates from linear behaviour. This point is also associated with the onset of AE activity.

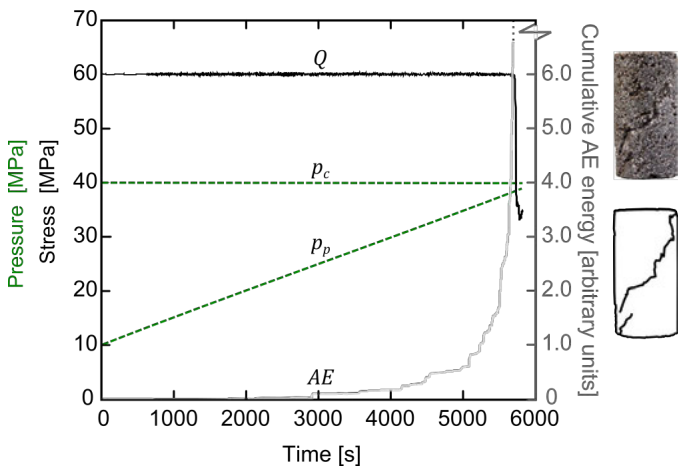


Figure 5.3: Example of a sample under a constant differential stress where pore pressure was increased monotonously until failure. Time represents the time elapsed since the initiation of pore pressure increase. Pore pressure is increased (in this case, at a rate of  $5.0 \times 10^{-3}$  MPa s $^{-1}$ ) from 10 MPa towards 40 MPa (the confining pressure, maintained constant throughout). Failure is manifested by the drop in differential stress, and a rapid acceleration in cumulative AE. The sample (post-failure) is shown, along with an interpretive sketch of the fault.  $p_p$  = pore pressure,  $p_c$  = confining pressure,  $p_{eff}$  = effective pressure, and  $Q$  = differential stress.

mulated by the sample, in agreement with previous studies on porous rocks (Wong et al., 1997).

#### 5.4.2 Increasing pore pressure under constant differential stress

During periods of volcanic unrest and magma ascent in an open system, intact rock in the edifice will likely be subjected to positive excursions in pore pressure (e.g. Heiken et al., 1988; Day, 1996). The second suite of tests therefore explores the effect of increasing pore pressure whilst maintaining a constant differential stress and confining pressure (comparable to the lithostatic pressure) on the sample (see Figure 5.3 for an example). In each of these tests, despite the order of magnitude differences in pore pressure increase rate (pore pressure was increased at servo-controlled rates of  $5.0 \times 10^{-1}$ ,  $5.0 \times 10^{-2}$ ,  $5.0 \times 10^{-3}$ , or  $5.0 \times 10^{-4}$  MPa s $^{-1}$ ), increasing pore pressure ultimately culminated in shear fracturing. A photograph (and interpretative sketch) of one of the fractured samples is provided in Figure 5.3. Notably, these faults are characteristically identical to those resulting from the conventional compressive tests under a constant strain rate (the tests of the preceding section).

Dilatant failure was achieved on the order of 1, 10, 100, and 1000 minutes, at effective pressures of 0.4, 1.0, 1.3, and 4.9 MPa, accord-

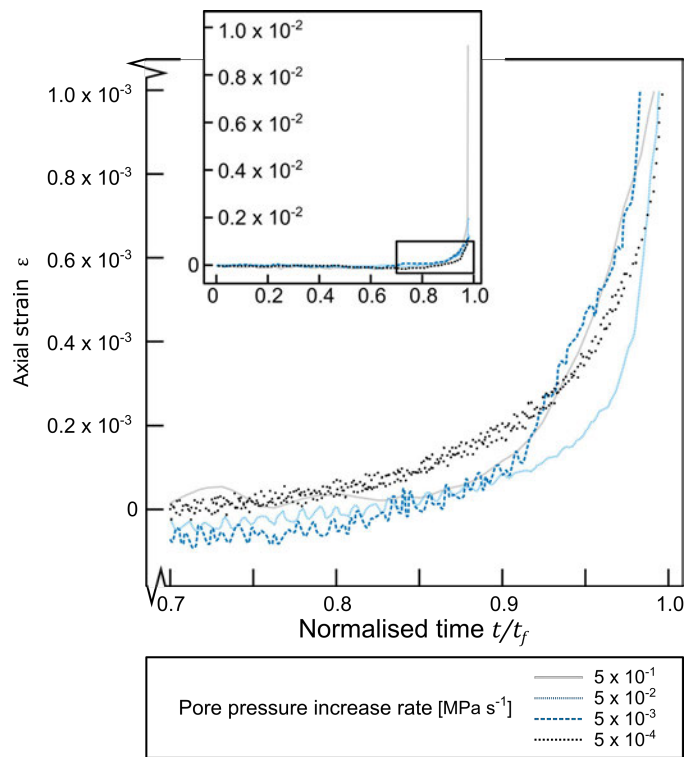


Figure 5.4: Inelastic strain as a function of normalised time (time as a proportion of time-to-failure) for four samples where pore pressure was increased at the set rates ( $\dot{p}_p = 5.0 \times 10^{-1}$ ,  $5.0 \times 10^{-2}$ ,  $5.0 \times 10^{-3}$ , and  $5.0 \times 10^{-4}$  MPa s $^{-1}$ ). The main figure shows the accelerating portion of the strain-time curve. The full curves are shown in the inset.

ing to the pore pressure increase rates of  $5.0 \times 10^{-1}$ ,  $5.0 \times 10^{-2}$ ,  $5.0 \times 10^{-3}$ , and  $5.0 \times 10^{-4}$  MPa s $^{-1}$ , respectively (Table 5.1). In each case, failure (defined by the large stress drop) was precursed by an acceleration of the AE energy rate, an example of which is provided in Figure 5.3, and is comparable—both in terms of shape and magnitude—to the AE activity observed during the dilatant (brittle) constant strain rate tests (Figure 5.2c). Despite the large variation (four orders of magnitude) in pore pressure increase rate, when the time is normalised to the time-to-failure, as in Figure 5.4, the acceleration behaviour in strain observed prior to failure is essentially the same.

#### 5.4.3 Pore pressure oscillation under constant differential stress

Positive pore pressure excursions within a volcanic system may not always culminate in the generation of macroscopic fractures but can increase the level of damage within the edifice. To assess this concept, a further test was performed where a sample was held under a constant confining pressure and differential stress and the pore pressure was oscillated at regular intervals. Starting with confining and pore

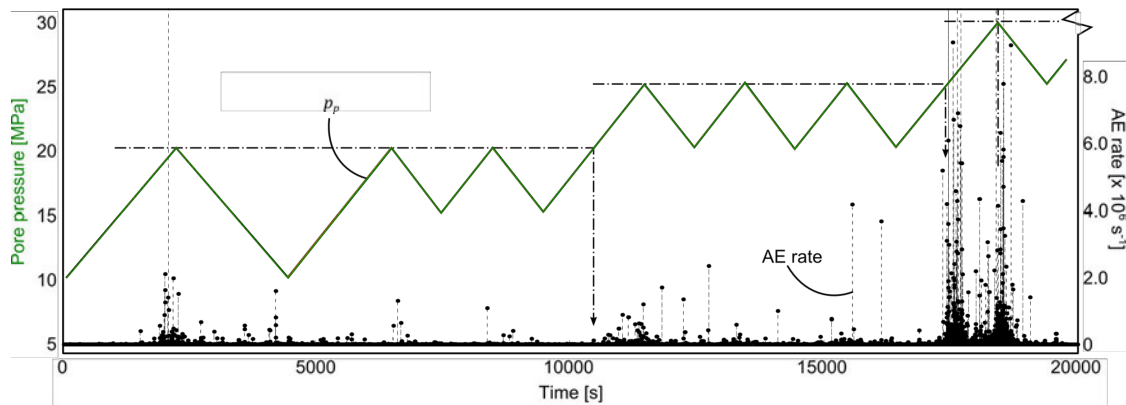


Figure 5.5: Pore pressure and AE rate for a sample where pore pressure was oscillated throughout the test. Peaks in the pore pressure cycling are associated with rapid increases in the AE rate. Brittle failure occurs as the pore pressure is increased from 25 to 30 MPa. Dashed lines and arrows indicate where surges in AE rate are observed when pore pressure is increased to a previously-unseen level. Refer to text for discussion.

pressures of 40 and 10 MPa, respectively, pore pressure was increased at a rate of  $5.0 \times 10^{-2}$  MPa s $^{-1}$  until 20 MPa, then decreased back to 10 MPa at the same rate. This process was iterated three times whilst AE was monitored, before increasing the pore pressure to 25 MPa and repeating the process. Finally, pore pressure was increased to 30 MPa, after which the sample failed via a shear fracture. Figure 5.5 shows the imposed pore pressures for this test, and the accompanying acoustic emission data, given here as the AE rate. Peaks in pore pressure are associated with increases in the rate of acoustic emissions. In detail, large increases in the rate of AE activity correspond to the point at which the pore pressure is increased to a value higher than that previously applied to the rock (marked by the arrows on Figure 5.5). In contrast to the experiments of the previous section where pore pressure was achieved at relatively low effective pressures (<5 MPa), this sample failed at an effective pressure of approximately 12.4 MPa.

#### 5.4.4 Pore pressure increase during constant strain rate deformation

Whereas the experiments in the two preceding sections are analogous to the impact of the infiltration of pore fluids into otherwise intact rock at a constant stress, this following section addresses positive pore fluid excursions in concert with ongoing compactive deformation. This scenario was imposed on a sample by deforming at an effective pressure of 30 MPa ( $p_c = 40$  MPa and  $p_p = 10$  MPa) and a strain rate of  $10^{-5}$  s $^{-1}$ , conditions that were maintained until the sample reached an axial strain of 0.035. At this point, pore pressure was increased at a rate of  $5.0 \times 10^{-2}$  MPa s $^{-1}$  to 35 MPa (i.e.  $p_{eff}$

$= 5$  MPa) as axial deformation was allowed to continue. Deformation was arrested at an axial strain of 0.05. The goal here was to instigate brittle deformation in a sample deforming in the compactant regime. The mechanical data for this experiment indicate that, after  $C^*$ , the sample underwent shear-enhanced compaction, and deformation followed a similar path to the compactant experiment shown in [Figure 5.2d](#). During this period, porosity decreased consistently with increased axial strain (monitored using the pore pressure intensifier).

The imposed increase in pore pressure propagated a dilatant shear fracture, accompanied by a significant stress drop (to a level comparable to the post-failure residual stress  $\sigma_f$  of [Figure 5.2b](#):  $p_{eff} = 5$  MPa). Beyond 0.035 axial strain, there is a brief period where the induced volumetric strain was negligible. However, very quickly following the initiation of pore pressure increase, the compactant behaviour occurring due to the constant strain rate deformation was overcome by the dilatant behaviour induced by the increasing pore fluid pressure. Once the pore pressure had reached 35 MPa it was maintained at this level, during which time the sample continued to dilate. The response of the confining pressure pump affirms that by the end of the experiment, the sample had gained volume (i.e. porosity) relative to its initial condition. Thus, the sample underwent both compactant and dilatant (brittle) deformation, manifest by barrelling of the sample overprinted by a shear fracture (as shown in the photograph and interpretative sketch in [Figure 5.6](#)).

## 5.5 DISCUSSION

### 5.5.1 *The road to failure: stress paths and failure modes of edifice-forming andesite*

Data have been plotted in order to map the failure envelope for andesites from Volcán de Colima, on axes of differential stress  $Q$  and effective mean stress  $P$ , defined in the preceding chapter. The failure envelope, shown in [Figure 5.7a](#), is defined in the brittle field by differential stress at failure, i.e. the peak stress ( $\sigma_p$ ); in the compactant field, failure (yield) is defined at the threshold  $C^*$ , the onset of shear-enhanced compaction ([Table 5.1](#)). A further margin can be delineated by differential stress at  $C'$ , the onset of dilatant microcracking. The failure envelope therefore defines the conditions in  $P$ - $Q$  stress space whereat these andesites are inelastically deformed or otherwise (Wong et al., 1997), for a strain rate of  $10^{-5}$  s $^{-1}$ . At stresses outside the failure envelope, the rock will have undergone mechanical failure. Between the brittle envelope and that defined by the onset of microcracking, samples are damaged but have not undergone macroscopic failure. Finally, the portion of the graph described by the damage

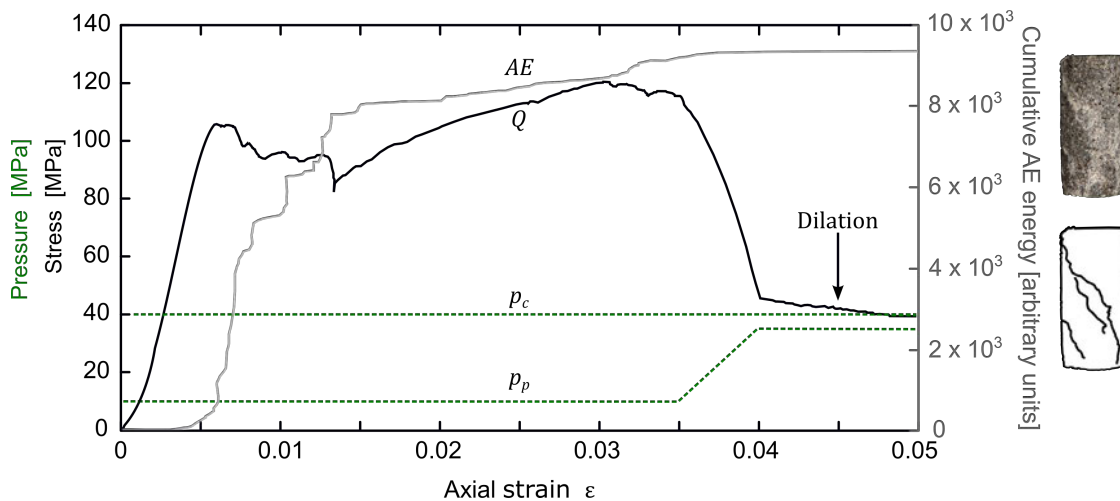


Figure 5.6: Pore pressure increase under constant strain rate deformation.

The stress–strain curve shows that the sample failed in a compactive manner (as in Figure 5.2a, d). The strain rate of  $10^{-5} \text{ s}^{-1}$  was maintained, and after the sample had been subject to 0.035 axial strain, the pore pressure was increased from 10 to 35 MPa. The photograph shows the sample post-failure, with an interpretive sketch illustrating the fault. The sample has undergone both barrelling (compaction) and shear fracture (dilation). Acoustic emission (AE) data are also shown: while the pore pressure is maintained at 35 MPa, there is a negligible amount of AE accumulated.

envelope and the compactive failure envelope are conditions under which the rocks are intact, whereby any deformation imposed on the sample is nominally elastic (recoverable).

The brittle envelope shows that differential stress at failure is a linear function of the effective mean stress, in agreement with the Mohr–Coulomb failure criterion. A previous study on the failure modes of porous andesite (Heap et al., 2015a) suggests that the yield cap is similarly close to linear in the compactant regime, due to the combination of microcracks and pores comprising the total porosity (Heap et al., 2015a; also discussed in Zhu et al., 2010 for limestones containing micro- and macroporosity). This is contrast to typical yield caps for porous sandstones, for example, which tend to be elliptical (e.g. Wong and Baud, 2012).

Figure 5.7b - d show the stress paths of samples for the three types of experiment in which the pore pressure was increased until brittle failure, as discussed in the three preceding sections. The trajectory of each stress path is simply the differential stress and calculated effective mean stress for each timestep during the corresponding experiments. In each case, the initial stress path (shown by the dotted line) begins at a differential stress of zero ( $Q = 0$ ) and an effective mean stress determined by the initial pore and confining pressures

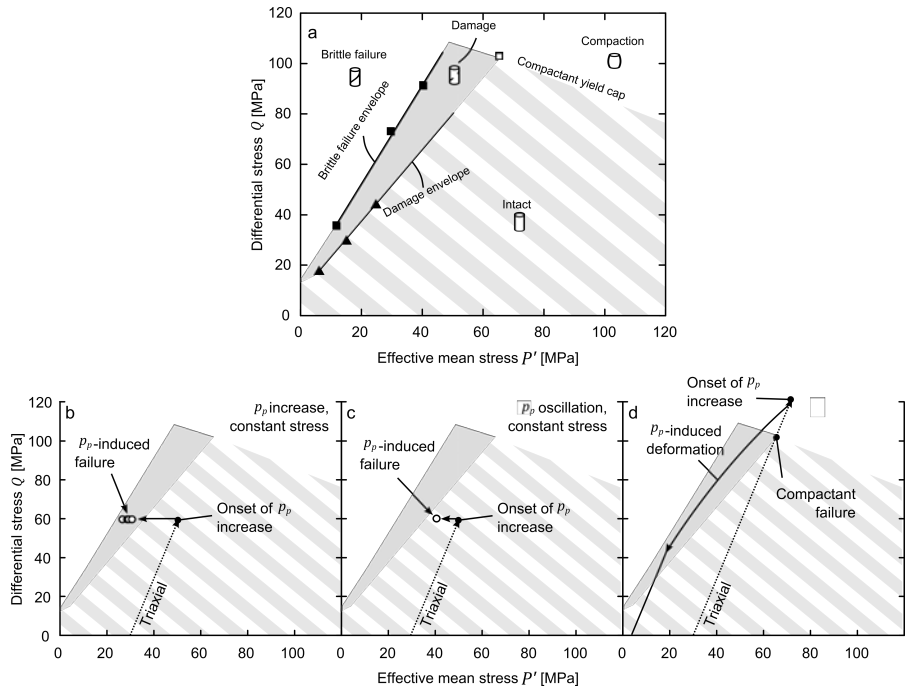


Figure 5.7: Stress paths of deformation experiments. a) shows compiled experimental data from this study in the stress space (differential stress  $Q$  as a function of effective mean stress  $P$ ). Closed symbols indicate brittle experiments ( $p_{eff}$  of 10 or lower), open symbols show compactant experiments. The mode of failure one would observe in each regime of the diagram are illustrated by the cartoons: cracking and brittle failure, compaction, and intact rock (no failure). The slopes of the brittle failure and damage envelopes are described by  $Q = 1.9614P + 13.207$  and  $Q = 1.3992P + 9.4652$ , respectively. b) to d) show the pore pressure-embrittled samples in the context of this envelope (symbols are omitted for clarity). In each case, the dotted line represents the initial triaxial loading of the sample, to the point in the experiment when the pore pressure was increased. The subsequent stress path is shown by the solid line. In b), samples were brought to failure by increasing the pore pressure monotonously at different rates ( $\dot{p}_p = 5.0 \times 10^{-1}, 5.0 \times 10^{-2}, 5.0 \times 10^{-3}, \text{ and } 5.0 \times 10^{-4} \text{ MPa s}^{-1}$ ), under constant differential stress. In these cases, all the samples fail on or near to the brittle failure envelope. In c), the iterative increase of the pore pressure resulted in sample failure well within the failure envelope. Finally, in d), the sample was deformed triaxially at an effective pressure of 30 MPa until it failed in the compactant regime (the point where it crosses the compactant yield cap). The stress path from the onset of pore pressure increase indicates that the sample transited into the brittle regime, generating a shear fault at some (unknown) point on this path.

imposed on the sample. In [Figure 5.7b](#), the path moves from this point to a differential stress of 60 MPa and an effective mean stress of 50 MPa as the samples are deformed triaxially. The differential stress is then maintained constant as pore pressure is increased as described above. In these cases, the stress path (solid line) moves horizontally from an intact condition towards the  $y$ -axis, until failure ([Figure 5.7b](#)). Irrespective of the pore pressure increase rate ( $\dot{p}_p = 5.0 \times 10^{-1}$  to  $5.0 \times 10^{-4}$  MPa s $^{-1}$ ), the samples fail at (or very close to) the brittle failure envelope. This is in agreement with the inelastic strain rate data ([Figure 5.4](#)), from which it can be inferred that, at least on timescales from approximately one minute to one day, the process of embrittlement appears essentially rate-independent. At this scale, any influence of time-dependant processes such as stress corrosion cracking (physico-chemical deformation: see Brantut et al., 2013 for a review) cannot be decoupled from the natural variability of our samples.

In [Figure 5.7c](#), the initial stress path is identical to that in [Figure 5.7b](#). However, in this case, the pore pressure is cycled until sample failure (the experiment of [Figure 5.5](#)). Again, the stress path moves horizontally towards the  $y$ -axis, but sample failure is initiated beneath the brittle envelope. The corresponding cumulative acoustic emission data—a proxy for the amount of damage accumulated by the sample—for the constant differential stress experiments shown in [Figure 5.7b](#) and [5.7c](#) are comparable. This remarkable similarity (shown in [Figure 5.8](#)) indicates that failure will occur when a threshold amount of damage has accumulated, regardless of the rate of pressure increase.

This is a similar observation to those made during experiments designed to investigate the time-dependency of rock deformation (e.g. Kranz and Scholz, 1977; Baud and Meredith, 1997), whereby the final stage of deformation occurs when a critical threshold in event number or energy is surpassed, independent of the stress on the sample (failure is observed in these porous andesites when the cumulative energy under the recorded waveform—in the arbitrary units defined previously—is between  $2 \times 10^1$  and  $2 \times 10^2$ ).

Finally, [Figure 5.7d](#) shows the stress path of the experiment shown in [Figure 5.6](#), in which the pore pressure was increased during constant strain rate deformation. The sample deforms poroelastically before passing  $C^*$  (i.e. the onset of shear-enhanced compaction) during constant strain rate triaxial deformation. Since the sample is deformed to a differential stress higher than  $C^*$ , the sample reaches a stress-state above the compactive yield envelope. Following the onset of pore pressure increase, the stress condition of the sample changes such that it moves along a path towards the brittle envelope (as shown

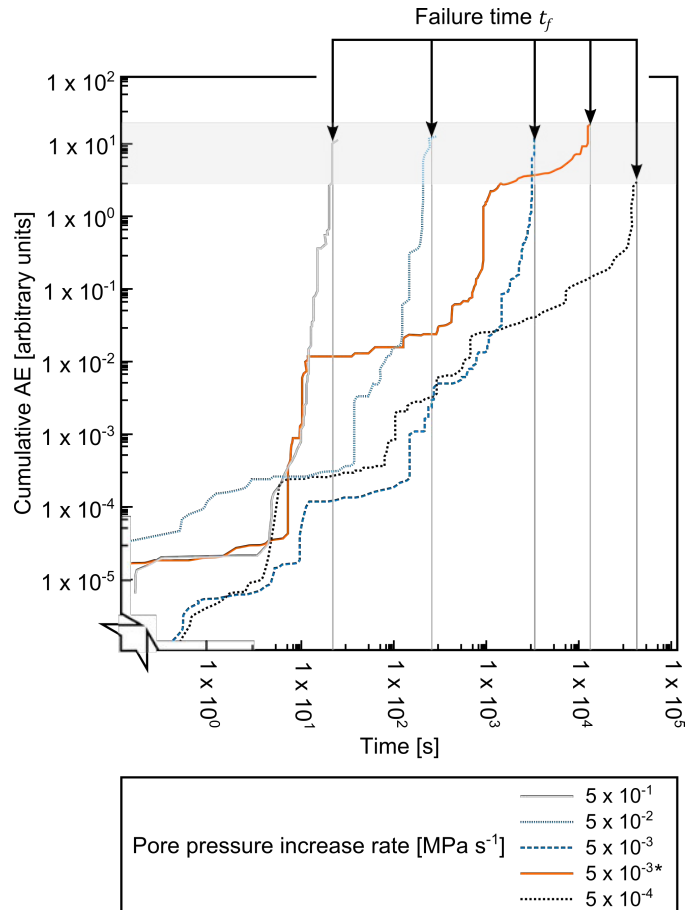


Figure 5.8: Cumulative acoustic energy (cumulative energy under the received waveform, given in arbitrary units) against time, showing the five samples which were brought to failure from an intact stress condition via pore pressure increase: four at different monotonous rates ( $\dot{p}_p = 5.0 \times 10^{-1}, 5.0 \times 10^{-2}, 5.0 \times 10^{-3}, 5.0 \times 10^{-4}$  MPa s $^{-1}$ ), and one by oscillating the pore pressure at  $5.0 \times 10^{-2}$  MPa s $^{-1}$  (marked by an asterisk). Arrows indicate the failure time of each sample. Notably, all samples fail once a given threshold of damage has been accumulated, represented in our experiments by 150 arbitrary units of AE energy.

in [Figure 5.7d](#)); a shear fracture develops as the sample moves along this path (shown in the photograph of [Figure 5.6](#)).

## 5.6 VOLCANIC EDIFICE EMBRITTLEMENT

### 5.6.1 Outgassing and eruptive behaviour

These experiments show that pore pressure increase can cause otherwise intact rock—or rock deforming in a compactant manner—to fail through brittle faulting. The preceding chapter showed that dilatant failure in volcanic rock can bring about increases in permeability of as much as three orders of magnitude. Given the high initial permeability of these San Antonio (C8) andesites ( $\sim 1.08 \times 10^{-12} \text{ m}^2$ : Heap et al., 2014b) it is improbable that permeability will increase by as much as this. Nevertheless, experimental data of Heap and Kennedy (2016) indicate that through-going (tensile) fractures in andesite tend to increase sample permeability to  $\sim 5.0 \times 10^{-11} \text{ m}^2$ , irrespective of the initial sample porosity. Thus, a permeability increase of around a factor of 50 may be expected from inducing dilatant failure in the andesite of this study<sup>1</sup>.

In an open system, pore pressure increases could therefore result in an increase of edifice permeability, due to the embrittlement induced by these positive excursions. Improved open system outgassing associated with increasing permeability can preclude the build-up of pressure in a volcano, fostering effusive—rather than explosive—activity (e.g. Woods and Koyaguchi, 1994; Jaupart, 1998). Hence, the propensity for this method of fracture generation within the edifice may well be an important parameter in limiting explosivity and bridling volcanic hazard at a given site.

[Figure 5.9](#) illustrates potential outgassing mechanisms arising through pore fluid-induced embrittlement. Note that the colour scale is illustrative and arbitrary: any deviation from equilibrium pore pressure—and indeed the equilibrium pressure—rests on several parameters (porosity, temperature, stress regime, and so on) which are poorly constrained within the edifice. Modelling the absolute magnitudes of pore pressure deviations around the conduit is not the focus of this chapter, other than in a qualitative sense. In the first scenario ([Figure 5.9a - c](#)), pore pressure in the edifice host rock is increased due to an ascending point source of thermal or mechanical stress; for example by a migrating magma batch or gas slug ([Figure 5.9a](#)) or a magmatic intrusion ([Figure 5.9b](#)). Close to a conduit

---

<sup>1</sup> Permeability could not be measured post-deformation for these samples as they were deformed without copper jackets; consequently, they often disintegrated when removed from the triaxial deformation rig.

or dyke, where thermal and mechanical stresses are anticipated to be highest, the greatest rates and magnitudes of pore pressure increase are expected (as represented in [Figure 5.9a – c](#)). As a result, and as inferred from these experiments, rock embrittlement (brittle failure) is likely to create a fracture network proximal to the conduit.

In this scenario, in the wake of the ascending body, the process of pore fluid-induced embrittlement would therefore leave a fractured zone or halo surrounding the conduit ([Figure 5.9a - c](#)). If sufficient fractures are generated to constitute a pathway for volatiles, then outgassing can occur (as in [Figure 5.9c](#) and [5.9d](#)), thus mitigating the build-up of pressure beneath a viscous plug or dome, and enhancing lateral outgassing as shown in [Figure 5.9d](#) and [5.9e](#). Indeed, annular outgassing is also predicted for Mono Craters, USA (Rust et al., 2004), Mount St Helens, USA (Gaunt et al., 2014), and observed at Santiaguito volcano, Guatemala (e.g. Lavallée et al., 2013). This fracture-wake process is a highly plausible contender as an explanation for the appearance of new fumaroles during unrest (or renewed outgassing at closed or sealed fumaroles), as inferred from thermal emission data ([Figure 5.9](#)).

As emphasised in [Chapter 4](#), as well as previous experimental studies (e.g. Heap et al., 2015a), it is anticipated that much of the edifice at depth will be undergoing inelastic compaction due to the increased lithostatic pressure of accumulating eruptive products. Compactant deformation may also result from stress perturbations associated with periods of volcanic activity (e.g. Gerst and Savage, 2004; Roman et al., 2004). Significantly, fracture generation in the deep edifice, as a consequence of pore pressure embrittlement, could offset the decrease in permeability associated with deformation in a compactant regime (see [Chapter 4](#)). Thus, transient or sustained pore pressure increases at depth could in fact bring about mechanical behaviour typically expected in the shallower parts of the edifice, effectively transiting the rock from a compactant to a dilatant regime. Shear fault formation in a sample which has already experienced a degree of inelastic compaction (as in the experiment of [Figure 5.6](#)), illustrates that pore fluid-induced embrittlement can encompass all regions in the edifice, even where the lithostatic pressure would otherwise preclude brittle behaviour. Indeed, fluid-induced embrittlement has been posited at even greater depths (of the order of tens of kilometres beneath the surface) in deep magmatic systems (e.g. Power et al., 2004; Sisson and Power, 2013), and subduction environments (e.g. Shiina et al., 2013).

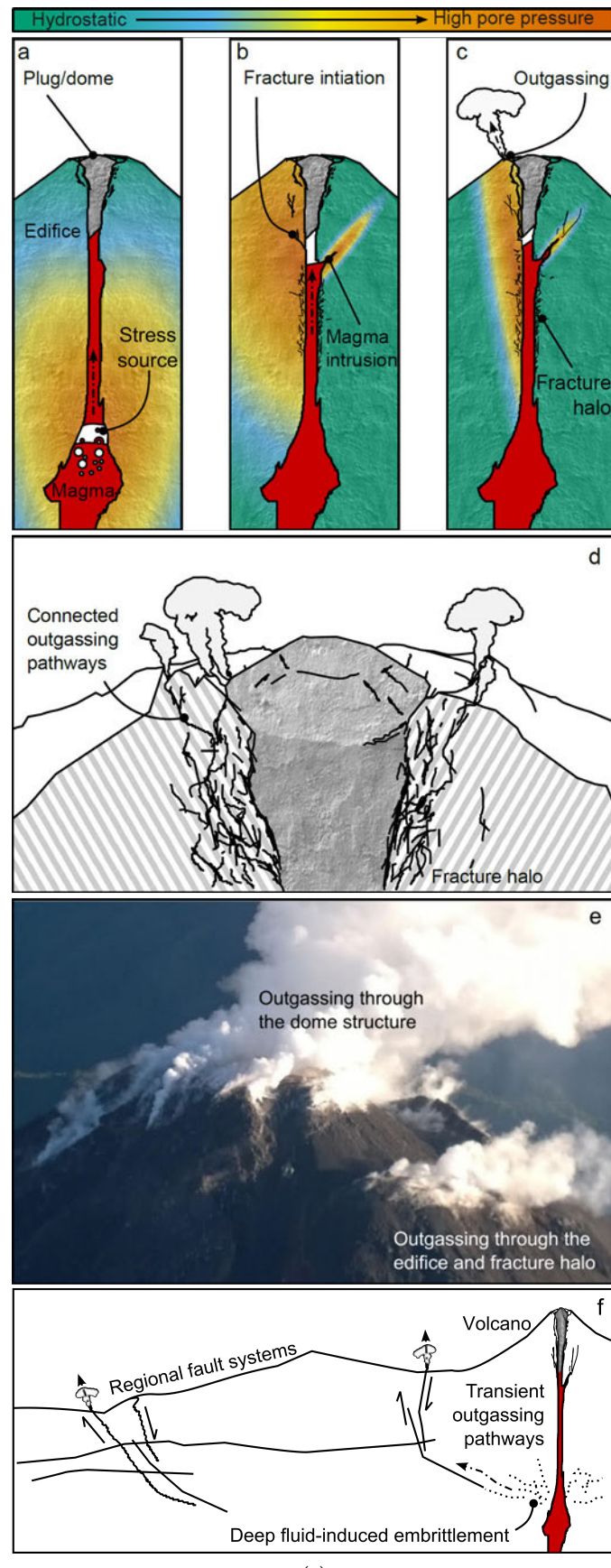
As sketched in [Figure 5.9f](#), the formation of deep pore pressure-induced fractures may serve to forge pathways for exsolved volatiles by connecting the near-conduit fracture network with regional fault

systems. Thus, this deep-edifice embrittlement mechanism could explain anomalous magmatic gas measurements (for example, as observed at Volcán de Colima: Taran et al., 2000; Varley and Taran, 2003), and the ubiquity of LP seismic events recorded at many active volcanoes (e.g. Varley et al., 2010; Jousset et al., 2013; Boué et al., 2015). Outgassing of magmatic volatiles through larger-scale regional fault systems is also supported by field studies of other volcanic systems (e.g. Heiligmann et al., 1997; Giannanco et al., 1998). However, an increase in edifice permeability through deep fracturing is likely to be transient, resting on the initial permeability and porosity of the system, duration and magnitude of pore pressure deviation, and the capacity for fractures to close or heal. Fracture closure can occur simply due to the overlying lithostatic pressure (e.g. Nara et al., 2011), and fracture healing could occur as a result of hydrothermal mineral precipitation (e.g. Edmonds et al., 2003; Ball et al., 2015) or the hot isostatic pressing of fragmented material within fractures (e.g. Kolzenburg et al., 2012).

### 5.6.2 *Edifice stability and seismicity*

Pore pressure fluctuations can directly increase the density of fractures within the edifice, resulting in a subsequent decrease in edifice integrity, particularly if fractures are propagated at or proximal to a structurally critical point (Elsworth et al., 1996; Lagmay et al., 2000; Thomas et al., 2004; Gudmundsson, 2011). In the case where even relatively small overpressures can develop (e.g. when the pore pressure is 0.5 MPa greater than the confining/lithostatic pressure), rock strength has been shown numerically to be reduced by about an order of magnitude (Heap et al., 2015d). Further, decompression events, compromising flank or dome stability (e.g. Collinson and Neuberg, 2012), may be triggered if pore pressure-induced fractures can access overpressurised magma. Indeed, it has been shown experimentally (Lavallée et al., 2011; Benson et al., 2012) that magma fragmentation can be a direct consequence of wall rock failure. In turn, this suggests that positive pore pressure excursions and host rock embrittlement close to the conduit could also bring about decompression and magma fracture. Reduction of structural integrity can give rise to an array of hazards, ranging from relatively harmless rockfalls (e.g. Mueller et al., 2013) to partial flank collapse and the instigation of pyroclastic density currents (Day, 1996; Reid et al., 2000; Watters et al., 2000).

During the pore pressure oscillation experiment, each increase in pore pressure to a previously unseen level is coincident with a surge in AE rate ([Figure 5.5](#)). This is in agreement with the Kaiser "stress-memory" phenomenon, whereby damage (i.e. new microcracking)



(a)

Figure 5.9: Embrittlement in the edifice.  
Caption on opposite page.

Figure 5.9: Embrittlement in the edifice. a) depicts a cartoon of a plugged volcanic system. Note that the colour scale is for illustrative purposes only: these do not correspond to any measured or modelled values. At a given depth, volatiles will exsolve into a discrete gas phase. From a) to b), the gas phase aggregates and ascends, increasing pore fluid pressure within the edifice due to thermal and mechanical stresses. In b), pore pressure-induced fractures initiate in the shallow edifice, creating a fracture network in the wake of the gas slug (equivalently, the ascent of a magmatic body could influence pore fluid pressures in the same manner). Propagation and coalescence of these fractures connect pathways for gases, allowing outgassing around the dome c). d) shows a cross-sectional schematic of the uppermost region of the edifice and dome, illustrating how iterative pore pressure-induced embrittlement could create a pervasively fractured halo around the conduit, comprising many pathways for gas escape. e) shows outgassing through the permeable dome structure at Volcán de Colima, taken in July 2014 (photo credit: Josh Greenwood). Also discernible is outgassing at discrete points in the edifice proximal to the dome. f) illustrates how pore pressure-induced embrittlement in the deeper edifice could permit outgassing, by creating—albeit transiently—pathways from near the volcano and regional fault structures.

only occurs once a threshold level of stress—equivalent to the previous maximum stress imposed on the material—is exceeded (Kaiser, 1953; see also Lavrov, 2003 for a review). This effect has been observed in cyclic stressing experiments on volcanic rock (Heap et al., 2009; Kendrick et al., 2013b). Moreover, a recent study (Heimisson et al., 2015) proves—through the analysis of contemporaneous geodetic and seismic data—the occurrence of the Kaiser effect at the kilometre-scale within the Krafla caldera, Iceland. In the experiments presented here, the observation of this phenomenon indicates that there is also a complex stress memory effect associated with repeated oscillations in pore fluid pressure in the edifice. Eventually, iterative damage of the edifice rock by pore pressure excursions may result in brittle failure due to the cumulative effect of discrete microcracking events over time (as in Figure 5.5 and 5.9). Whether subject to a constant pore pressure increase or iterative transient increases, these data indicate that, for a given porosity, failure and embrittlement of edifice rocks will occur after a threshold amount of damage is accumulated, irrespective of the pore pressure increase rate. This suggests that if the rock has previously accumulated a large amount of damage (i.e. close to the threshold amount) then only a relatively small increase in pore pressure would be necessary to trigger failure.

Further, it is reasonable to assume that pore-fluid induced embrittlement will contribute to the seismic record as suggested by Nishi et al. (1996), evidenced by the AE activity associated with sample dam-

age in our experiments (Figure 5.2, 5.3, 5.5, and 5.8). Recent studies (Palo et al., 2009; Petrosino et al., 2011) identify LP events both in the shallow edifice of Volcán de Colima (i.e. 1 km depth or less) and in deeper edifice regions (up to 4 km), and suggest that these typically arise from a non-repeating source. While this style of seismic activity is often observed to coincide with explosive activity (e.g. Hagerty et al. 2000; Arciniega-Ceballos et al. 2003), this is not always the case (e.g. Kumagai et al., 2002; Petersen et al., 2006). Whether long period seismicity at volcanoes is a result of shear fracturing (e.g. Neuberg et al., 2006; Varley et al., 2010; Thomas and Neuberg, 2012), slow-rupture failure of volcanic materials (e.g. Harrington and Brodsky, 2007; Bean et al., 2014), or the resonance of fluid-filled cracks (e.g. Lahr et al., 1994; Neuberg, 2000; Benson et al., 2008; De Lauro et al., 2012), these interpreted mechanisms are all generally congruent with embrittlement as outlined in this chapter: a seismogenic process which is anticipated to occur throughout the edifice. The coupling of fluid migration and brittle fracturing processes could yield complex seismic signals comprising both short- and long-period frequency elements.

### 5.7 CHAPTER SUMMARY

The effective pressure imposed on a rock, a factor important in dictating its mechanical response and failure mode, can be decreased by an increase in the pore pressure. This process is anticipated throughout volcanic edifices, especially in the thermally and mechanically stressed region proximal to the conduit. Through a suite of triaxial experiments on andesitic rocks—designed to explore the influence of pore pressure excursions on the failure mode of the rocks within a volcanic edifice—it is shown that brittle failure (fracturing) can be induced in an otherwise intact rock by simply increasing the pore pressure. Increasing the pore pressure at different rates, ranging from  $5.0 \times 10^{-1}$  to  $5.0 \times 10^{-4}$  MPa s<sup>-1</sup> yields comparable AE and strain acceleration behaviour relative to time-to-failure, and samples fail at equivalent effective pressures. Over the timescales of these experiments—on the order of one minute to one day—conclusive evidence for time-dependent processes (such as stress corrosion) was not seen.

Cumulative damage due to pore pressure oscillation can cause failure under stress conditions well below the short term strength of the rock, with failure the result of accumulating a threshold amount of damage. As a result, failure occurs at a relatively higher effective pressure in this case. These data further show that pore pressure-induced embrittlement can occur in rock deforming in the compactant regime, indicating that fracture generation can occur in regions of the edifice where brittle deformation would be precluded otherwise. Thus, pore

fluid-induced embrittlement is likely to occur not only in shallow (low confining pressure) regions of the edifice under a constant differential stress, but also in regions that are deeper or closer to the conduit, where the rock is liable to be deforming in a compactant manner. Magma fragmentation, fluid migration, flank destabilisation, and associated seismicity are all potential effects of this process. Nonetheless, by increasing the fracture network throughout the edifice, particularly in the rock surrounding the conduit, pore pressure excursions may serve to locally increase permeability and in turn improve lateral outgassing within volcanic systems, promoting effusive—rather than explosive—activity.



# 6

## THE DEVELOPMENT OF PERMEABILITY ANISOTROPY

---

Now from her bellowing caverns burst away/  
Vast piles of melted rocks, in open day.  
Her shatter'd entrails wide the mountain throws/  
And deep as hell her burning centre glows.

— Virgil, *Aenid*, 19 BCE<sup>1</sup>

*The preceding chapters have been largely focussed on the evolution of permeability of edifice-forming rocks, and how their physical properties may evolve in space and time. However, all volcanic rocks were once magma: what can they tell us about evolution of magma permeability? Volcanic rocks often contain discrete discontinuities providing snapshots of strain localisation processes that occur during magma ascent and extrusion. Whether these features comprise pathways for or barriers to fluid flow is of relevance for volcanic eruption and gas emission modelling, as well as for gaining a fuller understanding of strain localisation at high temperature. This chapter presents a systematic porosity and permeability study of fifty cores obtained from a set of discontinuity-bearing blocks, and a forensic assessment of the genetic processes of each feature is carried by investigating the attendant microstructure. Heterogeneities arising from decompression or shear fracture of magma, strain-induced flow banding, cavitation, and pore infilling are expected to contribute significantly to permeability anisotropy within the conduit and/or dome of a volcanic system. Using an upscaling model, the influence of these features is extrapolated to over different lengthscales.*

This chapter is published as: Farquharson, J. I., M. J. Heap, Y. Lavallée, N. R. Varley, P. Baud. Evidence for the development of permeability anisotropy in lava domes and volcanic conduits. *Journal of Volcanology and Geothermal Research*, 323, pp.163-185.

### 6.1 INTRODUCTION

Magma is inherently heterogeneous. Its physico-chemical properties evolve in time and space due to a host of interrelated processes, such as crystallisation (e.g. Carricchi et al., 2007; Vona et al., 2011; Chevrel et al., 2015), vesiculation (e.g. Bagdassarov and Dingwell, 1992; Burrisser et al., 2010; Okumura et al., 2013), and chemical differentiation

---

<sup>1</sup> Translated from Latin by Christopher Pitt, 1763.

(e.g. Giordano et al., 2008). In turn these processes are affected by variations in shear stress and strain rates across the conduit (Papale, 1999; Gonnerman and Manga, 2003; Caricchi et al., 2007) or during dome extrusion (e.g. Smith et al., 2001; Buisson and Merle, 2002; Cashman et al., 2008). Evidence for this variability is abundant in volcanic environments, where extruded material can show wide ranges in crystal size and assemblage (Cashman, 1992; Blundy et al., 2006) and porosity and pore diameter (Kueppers et al., 2005; Mueller et al., 2005; 2008; Shea et al., 2010; Lavallée et al., 2012; Burgisser et al., 2011; see also [Chapter 3](#)), in turn influencing permeability and strength (e.g. Zhu et al., 2011; Kolzenburg et al., 2012; Kendrick et al., 2013a; Heap et al., 2015a, c; Schaeffer et al., 2015; Lavallée et al., 2016; [Chapter 3, 4](#)). Magmas can also preserve discrete heterogeneities—evidence for strain localisation—in erupted material (e.g. Tuffen and Dingwell, 2005). Strain localisation processes in magma include extensional fracturing (e.g. Heiken et al., 1988; Stasiuk et al., 1996; Tuffen et al., 2003; Tuffen and Dingwell, 2005; Castro et al., 2014), frictional melting (e.g. Kendrick et al., 2014a, b; Plail et al., 2014), brecciation and gouge formation during shear fracturing (e.g. Pallister et al., 2013; Cashman and Cashman 2006; Kennedy and Russell, 2012), cavitation (e.g. Smith et al., 2001), and flow banding (e.g. Gonnerman and Manga, 2003; 2005).

Structural or textural discontinuities in porous media—especially where these heterogeneities are manifest as discrete tabular or (sub) planar features, such as stylolites and compaction bands—have often been observed to comprise conduits for or barriers to fluid flow, or more complex combined architectures (Caine et al., 1996; Baud et al., 2012; Lavallée et al., 2013; Heap et al., 2014d; Gaunt et al., 2014; Deng et al., 2015). The nature of these heterogeneities—their genesis, abundance, size (thickness and lateral extent), and orientation—can have a significant influence on the physical properties of the containing medium. For example, the scale and ratio of strain distribution and strain localisation in crustal fault zones has a marked effect on their permeability, resulting in four end-member regimes: localised conduits, localised barriers, distributed conduits, and combined conduit–barrier systems (e.g. Chester and Logan, 1986; Bruhn et al., 1990; Caine et al., 1996; Schultz and Fossen, 2008; Bense and Person, 2006).

Due to the pre-established importance of fluid transport in volcanic systems, as well as the prevalence of preserved heterogeneities in erupted materials, it is of significance whether discontinuities in magma can in fact act as barriers to or conduits for fluid flow. To date there are few studies that explore the influence of magmatic heterogeneities on permeability, and even fewer that offer laboratory data.

For example, Bouvet de Maisonneuve et al. (2009) present measurements on banded and non-banded pumice, showing that the former tend to be markedly less permeable in their dataset (by over an order of magnitude, depending on orientation). Cabrera et al. (2011), Castro et al. (2012), and Berlo et al. (2013) discuss the permeability of rhyolite containing tuffisite (defined as fractures in magma or rock infilled with transported juvenile clasts and lithic fragments, e.g. Saubin et al., 2016). Kolzenburg et al. (2012), Lavallée et al. (2016), and Kendrick et al. (2016) provide laboratory and field permeability measurements of andesite containing tuffisites and fractures. These studies conclude that the permeability of these features is—at least transiently—higher than that of the host rock mass, implying that they may serve as preferential routes for the outgassing of magmatic volatiles. Similarly, Gaunt et al. (2014) report a strong permeability anisotropy between the central and peripheral conduit of Mount St Helens volcano (USA) due to the juxtaposition of discrete lithofacies: a result of inhomogeneous ascent-driven strain localisation in the magma. Kendrick et al. (2014a) show that pseudotachylites (frictional melts) from Soufrière Hills volcano (Montserrat) are notably less porous and permeable relative to the host rock and therefore may act as barriers to fluid flow in volcanic systems.

This study comprises a systematic examination of the porosity and permeability of discontinuity-bearing andesites to determine whether they comprise effective pathways for—or indeed barriers to—fluid flow in a volcanic system. First, nine andesitic blocks (collected from Volcán de Colima during a recent field campaign) are shown and described, as well as the vast array of microstructure accompanying each feature. Potential mechanisms for their genesis are outlined. The influence of these discontinuities on the physical rock properties is then shown, and the attendant implications for volcanic activity, modelling, and field interpretations are discussed. The dataset of this study complements the large pool of data previously obtained on rocks from Volcán de Colima without discontinuities (e.g. Mueller, 2006; Kolzenburg et al., 2012; Lavallée et al., 2012; Kendrick et al., 2013a; Richard et al., 2013; Heap et al., 2014b; Lavallée et al., 2016; [Chapter 3](#)).

## 6.2 MATERIALS AND METHODS

During the field campaign to Volcán de Colima in May and June 2014, discontinuity-bearing rocks were collected from three sites (shown in [Figure 6.1](#)): two debris-flow tracks on the southwest and southern flanks of the volcano (La Lumbre and Montegrande respectively), and the flanks of the parasitic vent Volcancito. The rocks erupted since 1998 have been remarkably homogeneous in terms of their chemical



Figure 6.1: Google Earth™ satellite image of Volcán de Colima, showing each of the sample sites Volcancito, Montegrande, and La Lumbre (approximately 0.8, 3.5, and 6.7 km from the active vent, respectively). Inset shows the geographic location of Volcán de Colima within the Trans-Mexican Volcanic Belt (TMVB).

composition, being andesitic with a  $\text{SiO}_2$  content typically between 58 and 61 wt.% (e.g. Reubi and Blundy, 2008; Savov et al., 2008). Despite its petrographic constancy, the recent eruptive diversity of Volcán de Colima has given rise to a broad array of erupted material: field studies (Mueller, 2006; Lavallée et al., 2016; Chapter 3) have found porosities of edifice-forming material to range between 0.02 and 0.73. Similarly, the permeability of this material has been observed to differ by up to four orders of magnitude for any given porosity, and almost seven orders of magnitude over the whole dataset (as shown in Chapter 3).

Nine blocks were sampled from the sites shown in Figure 6.1. These blocks were collected so as to represent a variety of observable planar and subplanar heterogeneities (although this range is not necessarily exhaustive with respect to the features discernible in the field). These and other features were commonly observable at each sample site and elsewhere on the volcano, although a quantitative assessment of their abundance is not given here. As the sites shown in Figure 6.1 correspond to the final location of each block after emplacement and potential remobilisation, specific inferences cannot be drawn as to their origin based on the sampling location. Furthermore, this sampling method means that neither the *in situ* orientation of the blocks nor their emplacement conditions—*i.e.* extrusion rate, style of activity etc.—can be assessed. The blocks collected for the purposes of this study were generally smaller than 300 mm in length, but similar discontinuities can be seen on a metre scale. The nine blocks are shown and described in Figure 6.2 and Table 6.1, respectively.

Cylindrical core samples with a diameter of 20 mm were prepared from each block and precision-ground so that their end faces are flat

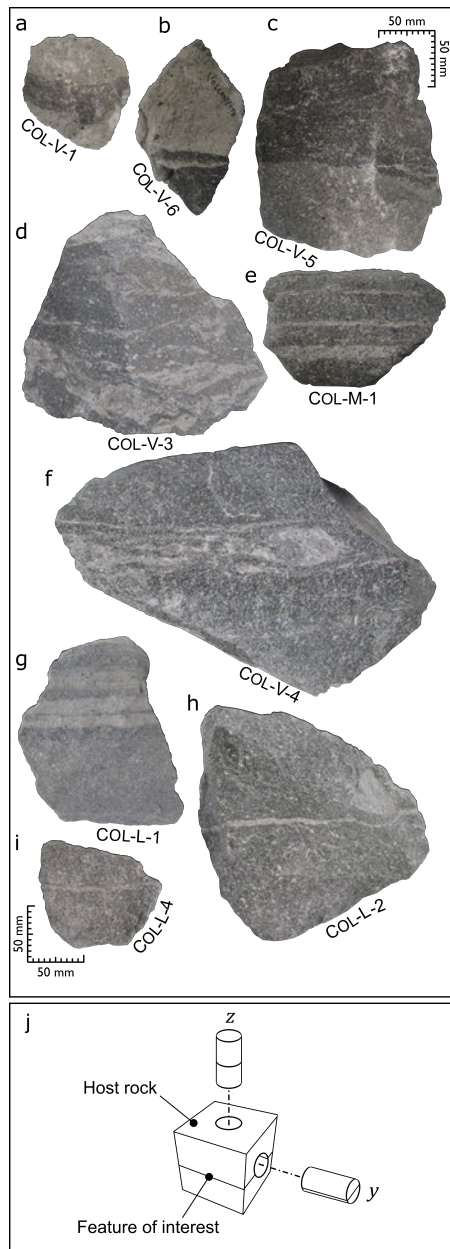


Figure 6.2: Collected discontinuity-bearing andesite blocks are shown in panels a) to i). Scale is the same for all blocks, and images are aligned so that the discontinuity is oriented more-or-less horizontally in each case. V, M, and L in each sample name refer to the sampling sites of Volcancito, Montegrande, and La Lumbre, respectively. Refer to Table 6.1 for detailed description of each block. j) Orthogonal cores are obtained from each block with respect to the plane of the feature of interest.

Table 6.1: Block (hand-sample) descriptions, including reference to the corresponding photographs in [Figure 6.2](#).

Block name	Photograph	Collection location	Description
COL-V-1	<a href="#">Figure 6.2a</a>	Volcancito	Pumiceous clast containing denser, darker grey portions, approximately 40 mm thick.
COL-V-6	<a href="#">Figure 6.2b</a>	Volcancito	Pumiceous clast containing recurring denser, darker grey regions, from 10 to 40 mm thick
COL-V-5	<a href="#">Figure 6.2c</a>	Volcancito	Dense rock displaying two competent portions defined by their difference in colour (a light grey side and a dark grey side). Several small (cm-scale) xenoliths can be observed in the sample.
COL-V-3	<a href="#">Figure 6.2d</a>	Volcancito	Dense, dark grey rock containing variously anastomosed lenses of lighter coloured material, ranging from around 5 to 40 mm in thickness.
COL-M-1	<a href="#">Figure 6.2e</a>	Montegrande	Dark grey clast containing three light grey tabular bands ranging from 5 to 15 mm in thickness.
COL-V-4	<a href="#">Figure 6.2f</a>	Volcancito	Large dense and glassy block, containing numerous anastomosing 1 - 10 mm thick bands of light grey, variably friable material. Some evidence of oxidation can be observed within the bands.
COL-L-1	<a href="#">Figure 6.2g</a>	La Lumbre	Dense rock containing three tabular bands which are light grey in colour. Bands are approximately 5 mm in thickness.
COL-L-2	<a href="#">Figure 6.2h</a>	La Lumbre	Dense glassy block containing a single through-cutting band, approximately 5 - 10 mm thick. The band appears to curve around a xenolith.
COL-L-4	<a href="#">Figure 6.2i</a>	La Lumbre	Dark grey clast containing a tabular band 5 - 10 mm thick. The band is typically light grey, with brick-red oxidation visible.

and parallel. The length of each core (from 25 to 40 mm) was dependent on the initial block size. Where possible, cores were extracted such that the feature of interest was either parallel or perpendicular to the core axis (i.e. in the y and z directions, respectively: [Figure 6.2j](#)). Again where possible, additional cores of the host rock were obtained so as not to include the feature of interest. Altogether, 50 samples were prepared from the nine initial blocks (shown in [Figure 6.3](#)).

Connected gas porosity  $\phi$  and gas permeability  $k$  were determined using the methods described in [Chapter 2](#). While measurements under a low confining pressure may not necessarily represent the in situ conditions, it should be noted that imposing higher pressure requires presupposing a depth of origin for each sample. Similarly, while room-temperature experiments may not capture additional complexities of fluid migration in high-temperature conduit magma, attempting to account for this in the experimental design means presuming a single elevated temperature at which to measure permeability. Importantly, the imposed experimental conditions (fixed pressure and temperature) allow the comparison of permeability of the different samples measured in this study.

Thin sections of all but one of the samples were also prepared in order to explore and analyse the microstructure using a Scanning Electron Microscope (SEM); due to the similarity of the two pumiceous samples, Col-V-1 and Col-V-6 ([Table 6.1](#); [Table 6.2a, b](#)), the microstructure was only examined for the latter (both blocks were collected from the same fall deposit; as such it is probable that the macroscopically similar banding in these samples is characteristic of the same genetic process, rather than two separate mechanisms being coincident in the same deposit). Digital image analysis of photomicrographs was performed in order to estimate 2D porosities both inside and outside of the features using the open-source image-processing program ImageJ (see Schneider et al., 2012). For select samples, X-ray Fluorescence (XRF) was used to assess potential compositional differences.

### 6.3 MICROSTRUCTURAL OBSERVATIONS

This section outlines microtextural and microstructural observations of each sample. Image-derived 2D porosities are also shown in [Table 6.2](#). Inferred genetic processes—based on these observations—are discussed in a later section.

Block Col-V-6 is a pumiceous block made up of distinct dark and light grey portions ([Figure 6.2a](#); [6.4a–c](#)). The 2D porosity is around 0.23 in the dark grey portion, and approximately 0.50 in the lighter coloured regions ([Table 6.2](#)). In the less porous dark grey portions,

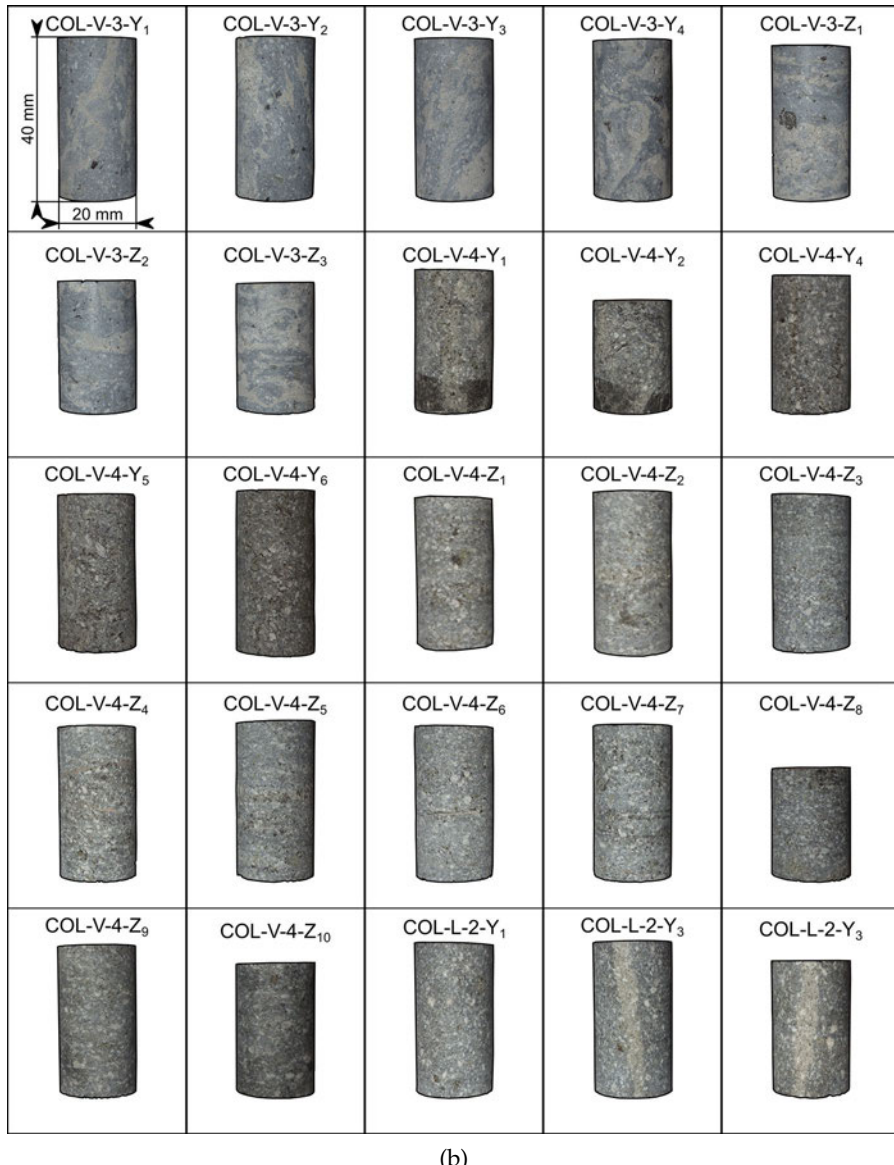
*Scale shown in the top left is the same for each panel.*



(a)

Figure 6.3: Photographs of the core samples measured in this study. Sample names indicate sampling location (V, M, and L refer to Volcanito, Montegrande, La Lumbre, respectively: [Figure 6.1](#)), and coring direction (Y and Z correspond to samples cored parallel and perpendicular to the feature of interest: [Figure 6.2j](#)).

pores are often equant and typically around 50  $\mu\text{m}$  in diameter, but can be 50–100  $\mu\text{m}$  ([Figure 6.4a, b](#)). In the lighter coloured, (i.e. more porous) regions, pore diameters are typically larger—generally around 100  $\mu\text{m}$ , and occasionally up to 500  $\mu\text{m}$ —and are often non-equant ([Figure 6.4c](#)). The long axis of pores in the lighter coloured material is preferentially oriented perpendicular to the interface between the layers, with these pores (the 100  $\mu\text{m}$  range) having an aspect ratio of approximately 2:1. This is in contrast to the pores in the darker coloured portion, which show a preferable orientation parallel to this in-



(b)

Figure 6.3: Continued.

terface (although this tendency is much less pronounced). The boundary between the light grey and dark grey regions is sharp. Occasional jigsaw-fit broken crystals can be discerned ([Figure 6.4b](#)).

Block Col-V-5 ([Figure 6.2c; 6.4d-f](#)) is made up of distinct light grey and dark grey portions. Both regions contain microcracks, and porosity is equivalent in both the lighter and darker coloured parts of the block ( $\phi = 0.09$  in each case: [Table 6.2](#)). In the light grey region, pores are generally from 10 - 100  $\mu\text{m}$  in diameter and are usually rounded ([Figure 6.4e](#)). In contrast, pores in the dark grey region tend to be smaller in size (between 10 and 50  $\mu\text{m}$ ) and amoeboid—rounded but highly irregular—in shape ([Figure 6.4f](#)). This indicates that the differ-

Table 6.2: SEM-derived band and host-rock porosities, including the difference between the two  $\Delta\phi$ .

Sample	Band porosity	Host porosity	$\Delta\phi$
COL-V-6	0.23	0.50	-0.27
COL-V-5	0.09	0.09	0.00
COL-V-3	0.29	0.01	0.28
COL-V-4	0.32	0.06	0.26
COL-M-1	0.20	0.01	0.19
COL-L-1	0.10	0.03	0.07
COL-L-2	0.18	0.01	0.17
COL-L-4	0.03	0.13	-0.10

ence in colour is due to the contrasting pore size and pore size distribution, rather than a significant difference in porosity. The boundary between these two portions is difficult to distinguish on the micro-scale (as evidenced by the low-magnification SEM image shown in [Figure 6.4d](#)). Microstructural examination of the interface indicates that the transition between regions dominated by different pore sizes (and shapes) occurs over  $\sim 2000 \mu\text{m}$ . Approximately cm-size xenoliths can be seen within the sample.

Block Col-V-3 contains tapered bands or lenses ( $\phi = 0.29$ ) up to approximately  $500 \mu\text{m}$  in width within a dense host rock ( $\phi=0.01$ ) ([Figure 6.4g](#) and [6.4h](#)). The dense host rock contains pores, generally less than  $10 \mu\text{m}$  in diameter, and microcracks ([Figure 6.4h](#)). The relatively higher porosity in the bands is responsible for their paler colour relative to the host material. The transition between the host rock and the more porous bands occurs over about  $100 \mu\text{m}$  in each case ([Figure 6.4h](#)). The bands consist of variably sized (from 50 - 100 microns down to less than 10 microns) angular particles with varying sphericity (for example, abundant platy or needle-shaped particles are present). Consequently, the inter-granular porosity is irregularly shaped ([Figure 6.4i](#)). Throughout the host material, micro-scale crystallites can be seen within the glassy groundmass; this texture—the so-called "feathery" texture of Horwell et al. (2012; 2013)—is shown in more detail and discussed in a later section (Evidence for gas transport).

The host rock of block Col-V-4 is glassy and low-porosity ( $\phi \simeq 0.06$ ). As well as microcracks, the porosity of the host rock is made up of subequant pores that tend to be in the region of  $10 - 50 \mu\text{m}$  in diameter ([Figure 6.4j](#)), although some are as large as  $300 \mu\text{m}$ . The host rock contains a number of slightly anastomosing porous bands, from 1 mm

up to 10s of mm in thickness, containing a porosity of around 0.32 ([Table 6.2](#), [Figure 6.4j - l](#)). Thus the relatively higher porosity within the band makes it appear lighter in colour relative to the dense surrounding rock. There is a sharp contact between the host rock and the band, occurring over a few tens of microns. The interior structure of the band ranges from zones of subangular, granular material at the margins (characterised by a particle size rather than a pore size: particles are generally around 20 µm diameter), to more coherent material towards the centre of the band containing rounded, amoeboid pores, which are generally on the order of 10 to 50 µm in diameter ([Figure 6.4k, l](#)). There are also large en échelon tensional fractures (~50 µm wide and ~400 µm in length) which cut through the band, oriented approximately 45° to the band ([Figure 6.4k](#)), and can be seen to skirt around crystal boundaries. Within the granular margins of the band, there are also patches of coherent material, typically adjacent to large phenocrysts ([Figure 6.4k](#)).

Three bands can be discerned in block Col-M-1, each approximately 5 mm in width ([Figure 6.2f](#)), two of which are shown in [Figure 6.4m](#). The heavily microcracked host rock contains a porosity of 0.01, in contrast to the bands which have a porosity of around 0.20. Accordingly, the bands appear paler in colour than the host rock. Feathery groundmass textures (see Horwell et al., 2012; 2013) are also observed in the host rock as well as crystalline silica, darker in colour than the groundmass (discussed further in a later section). Porosity inside the bands tends to be highly irregular in shape ([Figure 6.4n](#)). One population of pores is evident in the range of 10 - 50 µm in diameter, with other, larger pores (100s of µm in diameter) occurring adjacent to large rigid crystals ([Figure 6.4n, o](#)). Despite the bands being very tabular, the transition between each band and the host rock tends to be relatively diffuse, occurring over a distance of approximately 500 µm ([Figure 6.4n, o](#)).

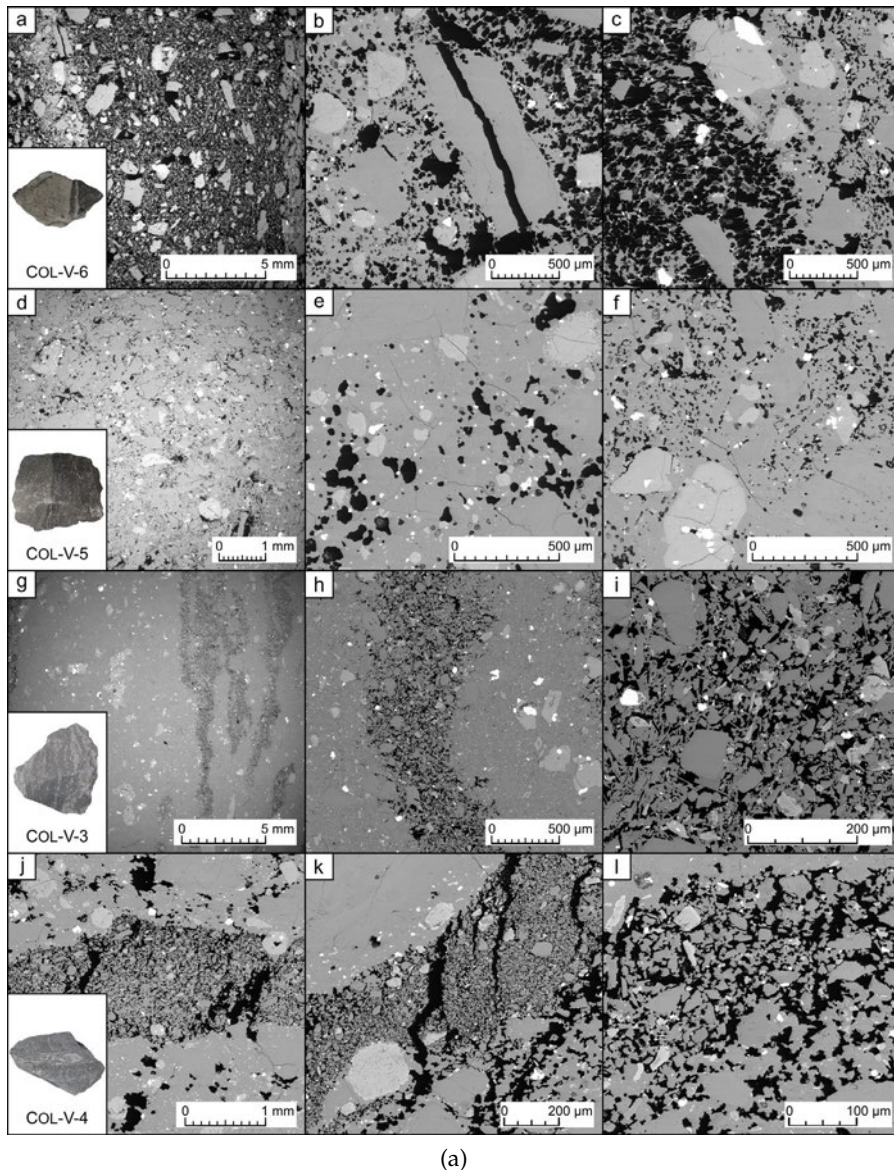
Col-L-1 is a dense glassy block (with a host rock porosity of approximately 0.03) containing tabular bands with relatively higher porosity (around 0.10), manifest in the difference in colour observable in the hand sample. The porosity of the host rock typically comprises small pores (< 20 µm in diameter) and microcracks ([Figure 6.4p - q](#)). The material inside the bands is made up of subangular, prolate fragments with their long axes generally < 50 µm in length, interspersed with relatively large phenocrysts up to 500 µm in diameter ([Figure 6.4q-r](#)). Dark patches of cracked crystalline silica can also be observed. The transition between host and band occurs over a width of up to 1 mm ([Figure 6.4q](#)).

Col-L-2 is another dense, glassy block (with a host rock porosity of approximately 0.01) containing a 3 - 5 mm-thick tabular band containing a porosity around 0.18 ([Figure 6.4s](#)) (the high-porosity band is correspondingly lighter in colour than the rest of the sample). The shape of the intergranular porosity within the band is amoeboid, typically 100 µm or less in diameter, but occasionally up to around 200 µm ([Figure 6.4t - u](#)), whereas the porosity in the host rock consists of equant pores no greater than 100 µm in diameter, and abundant microcracks. Notably, the band appears to deflect around a xenolith in the host material ([Figure 6.4s](#), inset). There is a discrete interface between the host rock and the porous band ([Figure 6.4t-u](#)). Throughout the groundmass, acicular lath-like crystals can be observed, darker than the rest of the groundmass constituents (discussed further in a later section: Evidence for gas transport).

Finally, Col-L-4 is a block with a host rock porosity around 0.13; the porosity of the host rock is made up of irregularly-shaped pores—from around 100 to 1000 µm in diameter—and abundant tortuous microcracks. The band visible in the block ([Figure 6.2i](#), [Figure 6.4v](#) inset) is characterised by a region of relatively lower porosity ( $\phi \simeq 0.03$ ). Much of the band appears reddish in colour at hand-sample scale, as well as in the prepared thin section. The inner walls of the pores at the margins of the low-porosity band are defined by numerous high aspect ratio (platy or needle-like) crystals. Towards the interior of the band, the porosity is characterised by the interparticulate space between this platy or needle-like material ([Figure 6.4w, x](#)), or spherical pores containing variably granular, angular to rounded particles from 10 - 50 µm in diameter ([Figure 6.4w](#)). In the centre of the bands, porosity exists as ~200 µm-diameter patches of subrounded pores that are generally < 20 µm in diameter. The boundary between the host rock and the relatively lower porosity band is very diffuse (the band is difficult to discern on the microscale, [Figure 6.4v](#)), occurring over around 2000 µm in some areas.

#### 6.4 MICROSTRUCTURAL INTERPRETATIONS

The various features described above provide snapshots of a range of interrelated conduit or dome processes. However, the microstructures that develop due to any given process may well overprint earlier textures. To add further complication, the extent of expression of any specific texture is likely to depend heavily on the time allowed for the responsible mechanism to operate. Hereafter, the processes described are inferred to be the most likely genetic for each feature, although it is possible that alternative mechanisms could exist.



Note that the left-most panel of each row is an image of the whole thin section, cropped in order to avoid the visual distortion (i.e. the "fisheye" effect) resulting from the low magnification.

(a)

Figure 6.4: Microstructure of discontinuity-bearing samples.  
(Caption overleaf.)

Note that the left-most panel of each row is an image of the whole thin section, cropped in order to avoid the visual distortion (i.e. the "fisheye" effect) resulting from the low magnification.

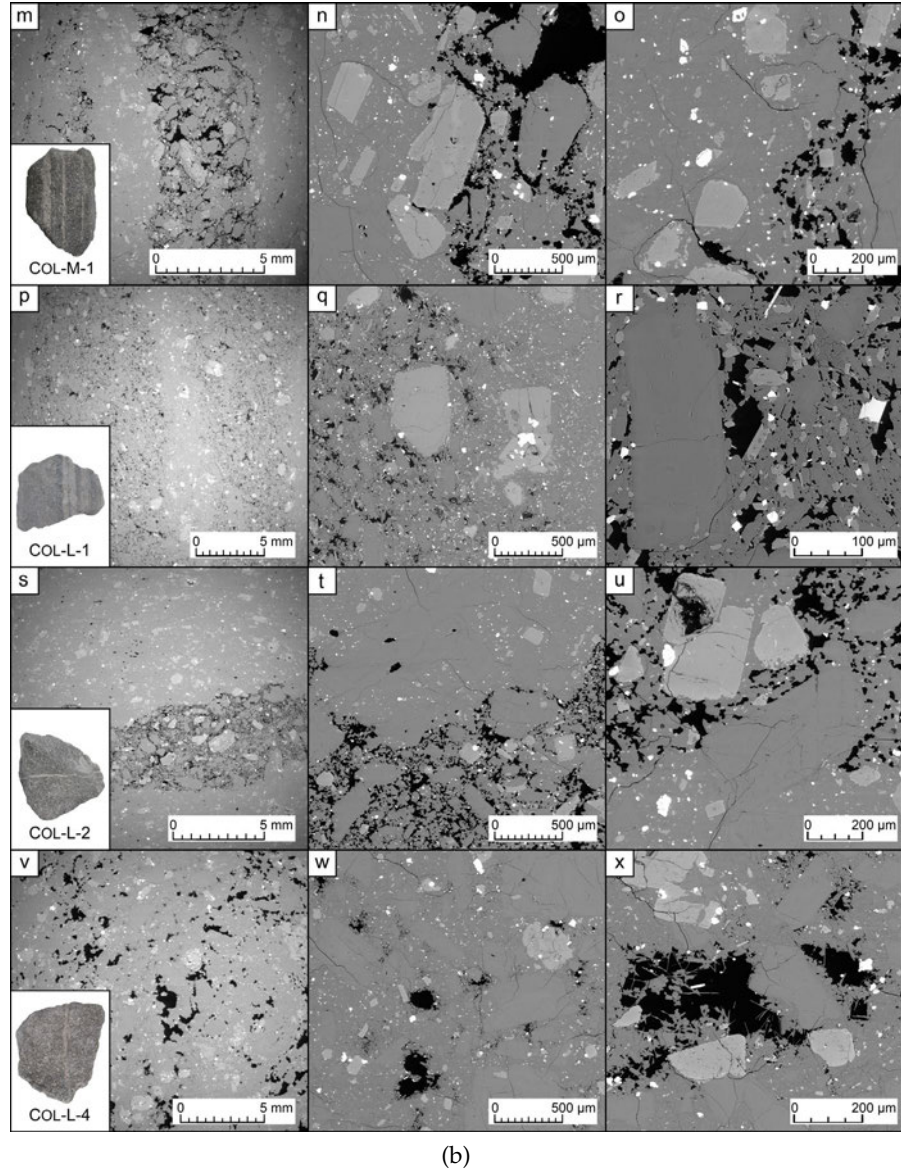


Figure 6.4: Continued. (Caption on opposite page.)

Figure 6.4: Examples of microstructure for eight samples. Each sample is shown inset, with three panels showing microstructure at varying scales. Porosity is shown as black in these and all subsequent SEM images. a) Sample Col-V-6, showing recurring bands of less-porous material within a highly porous sample. b) Large phenocryst in Col-V-6 which has been extensionally fractured and pulled in two by approximately 100 µm. c) The transition from high porosity (left-hand-side) to low porosity (right-hand-side) regions of Col-V-6. Much of the porosity in the left-hand-side appears elongated perpendicular to the band (i.e. elongated horizontally in the image), whereas evidence of band-parallel directionality (vertical elongation in the image) can be seen in the lower-porosity region (right-hand-side). Refer to text for more discussion. d) SEM image of sample Col-V-5. Note that the transition between pale and dense regions appears discrete at hand-sample scale (inset), but is less apparent in the microstructure. e) Typical porosity within the paler part of the block (Col-V-5). It is notably more spherical or amoeboid, as well as typically larger, than the porosity shown in f), which comprises the darker region of the same block. g) The variably anastomosed lenses of higher porosity of Col-V-3. A closer image h) shows that the transition from dense to porous material occurs over a distance on the order of 100 µm. Inside the bands of Col-V-3 i) incipient ("point-to-point") welding, and possible evidence of needle-like vapour-phase crystallisation textures. j) Sample Col-V-4, wherein discrete bands of increased porosity can be easily discerned. Closer images show extensional en échelon porosity k) and variably-sized granular material l). From the edge of the band towards its centre, an evolution from nonwelded fragments towards a partially welded medium can be seen (k, l). m) Sample Col-M-1, wherein two of the three porous bands can be seen (oriented vertically). A closer image of the discontinuity is shown in n), where it can be seen that phenocrysts intrude into the band. In o), "feathery" groundmass textures can be seen, indicative of devitrification within Col-M-1. Panel p) similarly shows the alternating bands of dense and relatively porous material in Col-L-1. The transition between these regions is diffuse, occurring over approximately 500 µm, shown in q). As with sample Col-M-1, panel r) shows that the largest pores in Col-L-1 are associated with phenocrysts. The band in sample Col-L-2 is shown in s). The boundary between the host rock and the fracture is shown in greater detail in t) and u). Notably, the groundmass is entirely interconnected in u), indicating that sintering of transiently granular material is well advanced. In the final sample, Col-L-4, the feature is manifest in a low-porosity band aligned vertically in v) and the hand-sample image, inset. The band is notably diffuse, encompassing the relatively dense patch running more or less vertically through the centre of the image. In w), the progression from relatively spherical or amoeboid pores to almost entirely infilled porosity can be discerned in more detail as one moves from the bottom to the top of the image. Within many of the pores of Col-L-4, variably-sintered material and vapour-phase crystallisation textures can be observed, as shown in x).

#### 6.4.1 Banding in pumiceous samples

XRF analysis of a banded pumiceous block (Col-V-1; [Figure 6.2a](#)) indicates that there is a negligible difference in bulk composition (of the major and trace elements analysed) inside and outside of the bands, suggesting a predominantly physical process in their genesis. This is in contrast to a number of other studies which discuss banding in pumice—for example Vezneky and Rutherford (1997), Hall et al. (1999), and Bouvet de Maisonneuve et al. (2009)—which attribute observed heterogeneities to the intermingling of magma batches of distinct composition or variations in magma differentiation. Burgisser et al. (2010) show macroscopically similar banded pumice collected at Soufrière Hills Volcano (Montserrat) ascribing the heterogeneity of porosity within individual samples to corresponding variations in water content. Based on the porosity data and microstructural observations (notably, band-perpendicular bubble elongation; [Figure 6.4b](#)), the constituent material presumably underwent a certain degree of extension or decompression-driven bubble expansion assisted by viscous deformation (i.e. above its glass transition  $T_g$ ), but not to a degree sufficient to wholly fragment the sample. This process has been observed in shock-tube experiments (e.g. Martel et al., 2000; Namiki and Manga, 2005), which demonstrate that decompression can cause volatile exsolution from a supersaturated liquid, followed by bubble growth and coalescence.

Band-parallel elongation of pores in the denser material ([Figure 6.4b](#)) may be indicative of coincident compression associated with the propagation of a rarefaction wave (i.e. pure-shear flattening of neighbouring bubbles during bubble expansion; Wright and Weinberg, 2009); however one can infer that the process was rapid and predominantly extensional as evidence of crystal parting is observed at the band-host rock interface ([Figure 6.4c](#)). Comparable breakage of crystals was reported by Kennedy et al. (2005), who attribute similar bands in pumice to lateral conduit implosion following the propagation of a fragmentation front through the magmatic column. Such textures could conceivably also arise during magma ascent in the conduit, or during phases of lava dome-extrusion: structures that are inherently prone to collapse and depressurisation (e.g. Fink and Kieffer, 1993; Navon et al., 1998; Voight et al., 2006). Indeed, variably-vesiculated layers of pumice and glass observed at Inyo Dome and Big Glass Mountain, both in the USA, illustrate the complex textural heterogeneities that can develop due to dome depressurisation (Fink and Manley, 1987; Castro et al., 2005).

#### 6.4.2 Shear strain-induced flow banding

The development of laminar flow due to vertical and horizontal gradients in temperature, pressure, and shearing mode or internal friction (e.g. Denlinger and Hoblitt, 1999; Mastin, 2002; Rust and Manga, 2002; Rust et al., 2003; Gonnerman and Manga, 2005; 2007) can ultimately partition magma properties such as crystal content, water content, or porosity, resulting in heterogeneous deformation of the magma even over microscopic scales (e.g. Wright and Weinberg, 2009; Laumonier et al., 2011; Lavallée et al., 2013).

Plug or piston flow within a magma conduit (e.g. Gonnerman and Manga, 2003; Hale and Mülhaus, 2007) dictates that shear strain in magma should be higher at the periphery of the conduit than in the centre (the effect of a variable stress profile across a conduit on a non-Newtonian magma rheology containing crystals and bubbles favours strain localisation, and in particular simple shear, in regions of highest strain rate near the conduit margin; Lavallée et al., 2007; Dingwell et al., 2015). Similarly, large strains—and large gradients thereof—have been estimated from actively extruding domes (e.g. Cashman et al., 2008), and are expected to be prevalent in dome- and spine-building systems (e.g. Griffiths and Fink, 1993; Buisson and Merle, 2004; Hornby et al., 2015). Moreover, additional stresses are likely to be pervasive within an active volcanic system, for example due to cumulative edifice construction and loading of the basement (e.g. van Wyk de Vries and Borgia, 1996; van Wyk de Vries and Merle, 1998; Gerst and Savage, 2004; Roman et al., 2004; Odberth et al., 2015). Deformation induced solely by simple shear (which is to say an isochoric or isovolumetric process) would not result in the creation or destruction of porosity (i.e. dilation or densification of the magma), but in inhomogeneous deformation of the porous melt and modification of the permeability (Wright et al., 2006). This is in line with observations of sample Col-V-5 ([Figure 6.2c](#), [6.4d - f](#)): while the pore size distribution is notably different between the competent light and dark grey regions, the connected porosity is equivalent in both ( $\approx 0.09$ : [Table 6.2](#)). Further, the inclusion of xenoliths in the block may be indicative that energetic shearing has occurred (Rust et al., 2004). This interpretation is given weight by the fact that XRF analysis of this sample yields comparable bulk composition in both the light grey and dark grey portions, suggesting a predominantly physical process rather than a compositional one. Nevertheless, alternative physical mechanisms cannot be discounted. For example, finite element modelling of shallow-vent exogenous dome growth predicts the concurrence of magma batches with contrasting degassing histories, manifest in juxtaposed regions of differing porosity (Massol and Jaupart,

2009).

Purely laminar flow in a conduit is, however, not necessarily the norm (Costa and Macedonio, 2003). Rather, some degree of volumetric change may be associated with shear strain, resulting either in transtension (shear and extension) or transpression (shear and compression). Viscous-to-brittle transtension of fluid—whereby the vapour phase of a liquid is formed due to a local pressure or stress differential—is also termed cavitation (e.g. Gruzdkov and Petrov, 2008), and potential evidence for this process exists in the microstructure of, for example, Col-V-4, Col-M-1, and Col-L-1. Below, some of these characteristic features are described—shown in more detail in [Figure 6.5](#)—analogous to those often observed in material science (such as ceramics studies: Chokshi, 1997), and texturally similar to those described in dacitic dome rocks from Unzen, Yakedake, and Daisen volcanoes (all in Japan) by Smith et al. (2001). For example, en échelon extensional porosity can be seen within some of the porous bands, as shown in [Figure 6.5a](#) (Col-V-4; see also [Figure 6.4j, k](#)). These high aspect ratio pores skirt crystal boundaries, comparable to the "crack-like" porosity of Smith et al. (2001). These features are comparable in form and formation to experimentally-created "tension gashes" in pure melts (A. Kushnir, *pers. comm.*) and extensional fracturing in crystalline magma under uniaxial compression (Lavallée et al., 2013).

Moreover, [Figure 6.5b](#) (Col-M-1) and [Figure 6.5c](#) (Col-V-4) show where porosity has preferentially developed along the borders of large phenocrysts, which can be interpreted as further evidence of cavitational porosity (this can also be observed in sample Col-L-1: see [Figure 6.4q, r](#)). Notably, [Figure 6.5c](#) shows a tail of low-porosity adjacent to a phenocryst. Although the *in situ* stress field cannot be known, this feature is interpreted as an indicator of localised differences in the stress field—i.e. a pressure/stress shadow—which is a prerequisite condition for cavitation.

#### 6.4.3 Magma fracture and sintering

Brittle behaviour in magma is typically ascribed one of two mechanisms: magma fragmentation resulting from a pore overpressure that exceeds the tensile strength of the magma (i.e. a fragmentation threshold: e.g. Alidibirov and Dingwell, 1996; Zhang, 1999; Koyaguchi et al., 2008), or magma failure due to rapid shearing surpassing a critical strain rate in areas of strain localisation (e.g. Woods and Koyaguchi, 1994; Martí et al., 1999; Papale, 1999; Gonnermann and Manga, 2003; Melnik et al., 2005; Lavallée et al., 2008; 2013). The former process is associated with relatively rapid magma decompression or gas waves or slugs fluxing through the magmatic column

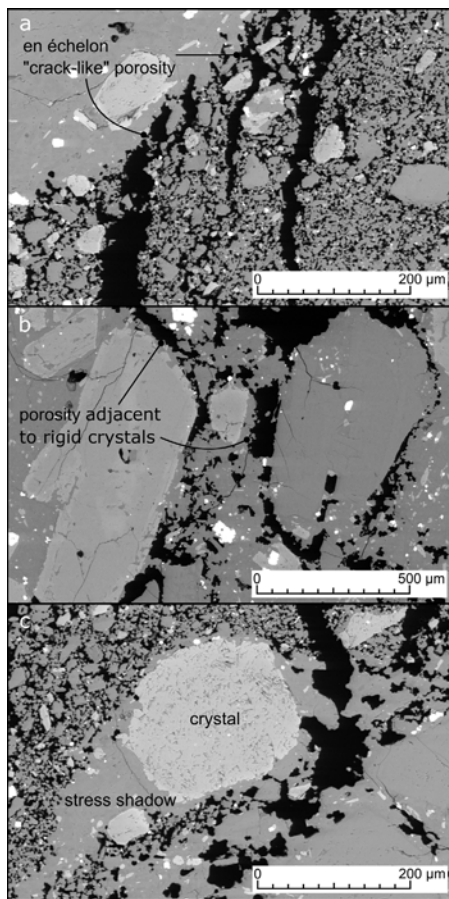


Figure 6.5: Evidence of shear-induced transtension (cavitation) in banded samples. a) High aspect ratio *en échelon* porosity, indicative of extensional shearing in Col-V-4. In b) and c), porosity can be seen preferentially formed around the edge of large phenocrysts (in samples Col-M-1 and Col-V-4, respectively). c) Local differences in stress are evidence by a tail of non-fragmental material, reflecting a stress shadow adjacent to a phenocryst.

(e.g. Michaut et al., 2013). As for the latter, a critical strain rate criterion may be met at any depth in the conduit or within extruding lava domes, resulting in magma fracture (as discussed by, e.g. Dingwell, 1996; Papale, 1999; Tuffen et al., 2003; Edmonds and Herd, 2007; Lavallée et al., 2008; Tuffen et al., 2008; Cordonnier et al., 2012), if the melt viscosity prevents sufficient stress relaxation during rapid magma ascent (Goto, 1999; Papale, 1999; Gonnerman and Manga, 2003).

The sharp transition evident between the host material and the bands present in many of our samples (Col-V-3, Col-L-2, Col-V-4), hints at brittle failure of the magma. Examples of the well-defined contact are shown in Figure 6.6a and 6.6f. In each of these cases, these fractures are also filled with variably granular material, as one may expect if ash-sized material is generated on the fault plane or trans-

ported through the fracture.

Once a fracture is generated in rock or magma, the conditions may exist to allow subsequent viscous sintering or hot pressing of fragmental material within the fracture (e.g. Stasiuk et al., 1996; Tuffen et al., 2003; Kolzenburg et al., 2012; Vasseur et al., 2013; Wadsworth et al., 2014; Heap et al., 2014a; 2015b), either *in situ* or after some degree of transportation (Tuffen and Dingwell, 2005). Viscous sintering—the agglutination of melt particles above  $T_g$ —is common in a range of volcanic environments, examples of which include rhyolitic dykes and conduits (e.g. Tuffen et al., 2003; Tuffen and Dingwell, 2005; Okumura and Sasaki, 2014), welded block-and-ash flow deposits (e.g. Michol et al., 2008; Heap et al., 2014a), lava spatter and spatter ramparts (e.g. Mellors and Sparks, 1991; Sánchez et al., 2012), localised agglutination of scoria (Wadsworth et al., 2015), conduit-filling pyroclastic material (e.g. Kolzenburg and Russell, 2014), and rheomorphic and lava-like ignimbrites (Branney et al., 1992; Lavallée et al., 2015). More specifically, the sintering of "transiently granular" material (Wadsworth et al., 2014) has been described in terms of fracture healing in magma (e.g. Tuffen et al., 2003; Heap et al., 2015b).

Viscous sintering of volcanic material requires the temperature and the timescale of the process to be such that the material remains in a liquid regime (above the glass transition  $T_g$  of its melt phase), whereupon the melt structure can relax and heal particulate material via diffusion (e.g. Vasseur et al., 2013). The process encompasses three separate stages (e.g. Vasseur et al., 2013; Wadsworth et al., 2014):

1. point-to-point connection of melt "necks" between granular materials (*incipient sintering or welding*),
2. a variably porous but melt-dominated medium (*partial sintering or welding*) and,
3. a nonporous melt and crystal phase (i.e. *fully sintered or welded*).

Microstructural evidence of the first two of these stages can be observed in a number of these samples, examples of which are shown in [Figure 6.6](#). Discrete angular granular material is typically observed at the inner margins of fractures ([Figure 6.6c](#), [6.6h](#)). Advancing towards the centre of each sintered band (i.e. from [Figure 6.6c](#) → e and [Figure 6.6h](#) → j), fragments appear progressively more rounded, and often connected by necks of glassy groundmass, indicating melt relaxation associated with *incipient* to *partial* sintering. This process is reflected in increasingly connected groundmass and correspondingly isolated porosity, as the material transitions from fragments within void space to a porous melt wherein the original angular nature of the

fractures cannot be discerned. Pores also appear increasingly spherical or amoeboid within the centre of either band ([Figure 6.6e, 6.6j](#)), illustrative of the relaxation of the internal surface area of the porosity with ongoing sintering (e.g. Mackenzie and Shuttleworth, 1949; Wadsworth et al., 2014). Comparison of samples Col-V-4 and Col-L-2 ([Figure 6.6a - e](#); [Figure 6.6f - j](#)) illustrates that these sintering textures are generally more developed in the latter sample, suggestive of higher temperatures or greater depths (e.g. Wadsworth et al., 2014; Heap et al., 2015b), or longer timescales (Vasseur et al., 2013). Thus one can observe differing degrees of sintering both within a single fracture and between different samples.

#### 6.4.4 Evidence for gas transport

The low-porosity band within the sample Col-L-4 ([Figure 6.2i](#) and [6.4v - x](#)) shows pores partially filled with variably-sintered fragmental material ([Figure 6.7a](#); [Table 6.2](#)). Based on the observations outlined above, a feasible explanation is that the progressive pore infilling is the result of ash deposition from circulating hot ash-laden fluids. The hot and "sticky" ash particles first adhere to and coat the pore walls (as in [Figure 6.7b](#)), subsequently reducing pore throat apertures, which may well encourage further agglutination and filling of the pores ([Figure 6.7c](#)). The originally angular and fragmental ash particles ([Figure 6.7a](#)) gradually lose their shape as surface tension reduces the curvature of the melt/fluid interface, promoting the rounding of particles ([Figure 6.7b, c](#); see Vasseur et al., 2013). Eventually the pore becomes completely filled and the particles continue to densify through sintering. At this stage, the characteristics of the original granular material and the original pore are mostly eradicated; however, relics of the originally granular material are defined by remnant microporous patches ([Figure 6.7d](#), and inset).

Other than in sample Col-L-4, there is no definitive evidence for the transport of fragmented magma or fault gouge—whether juvenile or from previous explosive activity—in our samples. Nevertheless, recent studies (Kolzenburg et al., 2012; Kendrick et al., 2016; Lavallée et al., 2016) suggest that this process may be common at Volcán de Colima in materials derived from either the dome or conduit. However, variable oxidation of the bands in some hand samples (Col-V-4, Col-L-4; see [Table 6.1](#)) indicates through-flow of hot magmatic fluids. This is in agreement with the findings of Plail et al. (2014), who interpreted changes in metal compositions in banded volcanic rock as a result of magmatic gas flow.

Further, textural evidence of silica polymorphs, both within bands and in the host rock groundmass, may point to transport of magmatic

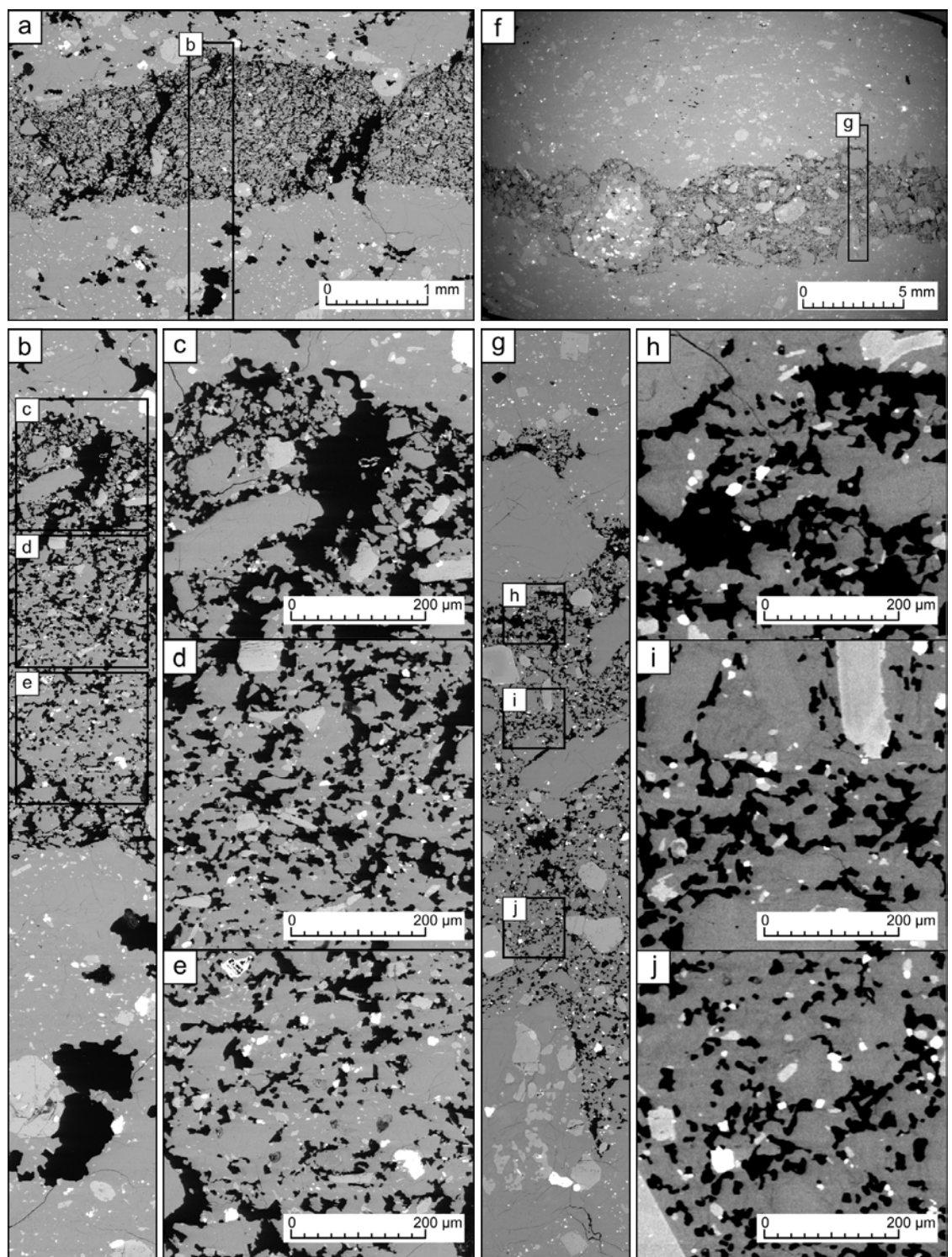


Figure 6.6: The evolution of sintering of granular fracture material.  
(Caption on opposite page)

Figure 6.6: a) Planar fracture in sample Col-V-4. b) Detailed SEM images (c–e) are acquired from the edge and near the centre of the band. c) At the edge of the fracture, discrete ash-sized fragments can be discerned, most of which retain their angular form. For example, a cluster of discrete grains can be seen in the top-left of the panel. d) Some rounding of fragments can be seen, and there is an increased connectivity of the groundmass. Both are indicative of incipient sintering. Characteristic "necks" can be observed forming between some of the formerly angular fragments; i.e. where there is a concave curvature of connecting groundmass between particle bodies, in contrast to the convex curvature of the particle surfaces. e) Closer to the centre of the band, the groundmass is better connected, and porosity is increasingly more isolated relative to c) and d). This is evident throughout the panel, where numerous pores  $< 20 \mu\text{m}$  in diameter can be discerned with little or no connectivity with their neighbouring pores. f) Planar fracture in sample Col-L-2. g) The location of detailed images (h–j) is shown, the first at the edge of the band, the latter two towards the centre. h) As in c), some discrete granular material can be observed within the void space, particularly in the bottom-right of the image. However, rounding of the fragments is more pronounced, suggesting more advanced sintering than their counterparts shown in c). i) Towards the middle of the fracture, the microstructure has transitioned from variably granular material within void space to a competent groundmass with variably connected porosity. Note that the pore shape is generally amoeboid to spherical. Necking textures are pronounced in the centre-right and bottom-left of the image. j) Similar textures to i) are evident, but the image indicates notably poorer connectivity of the pores, suggestive of more advance sintering. Note that the characteristic shapes of the original granular material cannot be discerned.

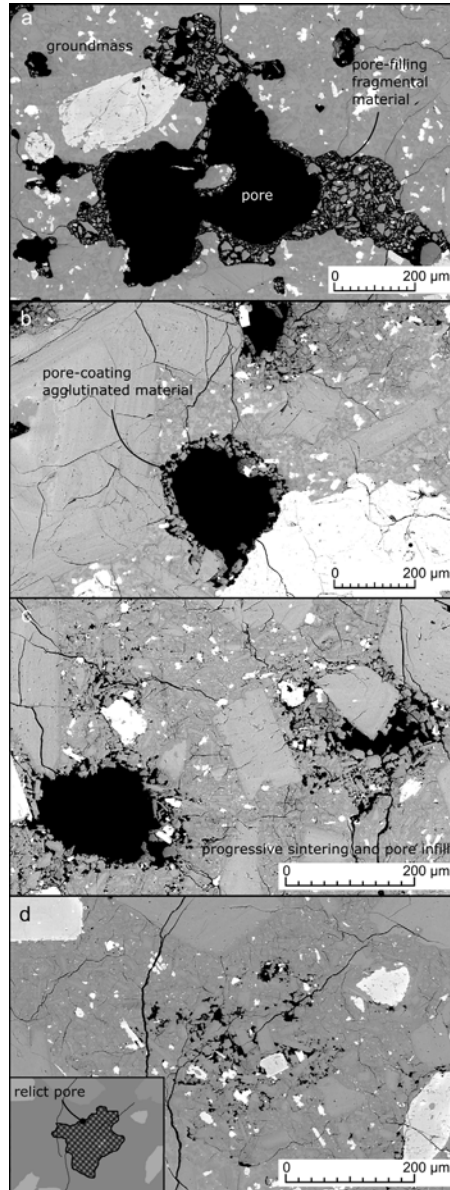


Figure 6.7: Progressive pore occlusion in sample Col-L-4, from near the margin (a) towards the centre (d) of the band. a) A pore, partially infilled with fragmental material. b) Agglutinated material adhering to the pore wall. Textures shown in c) indicate that the infilling material has progressively clogged up pores in this sample. Finally, in d) the pore is almost entirely filled in, and the infilling material is well sintered. The previous extent of the pore is preserved as a patch of microporosity (sketched in inset).

volatiles through porous discontinuities. [Figure 6.8a](#) shows sample Col-M-1, highlighting the darker-coloured crystalline silica. The diagnostic "fish-scale" microcracking texture is indicative of cristobalite having undergone the  $\beta$ - to  $\alpha$ -cristobalite transition (e.g. Damby et al., 2014), often observed in volcanic dome rocks from, for example, Inyo Domes, USA (e.g. Swanson et al., 1989), Mount St Helens, USA (e.g. Blundy and Cashman, 2001), and Gunung Merapi, Indonesia (e.g. Kushnir et al., 2016). In sample Col-L-2 ([Figure 6.8b](#)), lath-like crystals are interpreted to be tridymite (see Blundy and Cashman, 2001).

[Figure 6.8c](#) shows an example of a sample exhibiting a feathery groundmass texture (sample Col-V-3), characterised by microscale crystallites occurring within the groundmass glass. The growth of this texture is thought to represent variable devitrification of the initially glassy groundmass (Horwell et al., 2012; 2013). Needle-like or platy textures within pores and bands of some samples can also be observed, an example of which is shown in [Figure 6.8d](#) (sample Col-L-4). These textures are consistent with prismatic cristobalite growth observed in lavas from the dome of Soufrière Hills volcano by Horwell et al. (2013), both in terms of form and tendency to occur within pores and fractures in the rock. These authors interpret the latter fact as evidence for vapour-phase mineralisation.

Vapour-phase crystallisation of silica polymorphs, namely tridymite and cristobalite, provides strong evidence that transiently connected porosity (e.g. cavities or discrete fractures in magma) does indeed serve as a transport network for element-rich magmatic gases. Tridymite and cristobalite are metastable at high temperatures and low pressures (e.g. Deer et al., 1996; Damby et al., 2014), indicating that the processes involved in forming or infilling these fractures and pores must be occurring in relatively shallow regions of the dome or conduit. This is in agreement with the findings of Ball et al. (2015), who suggest that hydrothermal alteration and precipitation will be preponderant in talus-mantled lava domes, where these processes are enhanced due to favourable heat and permeability conditions.

Similarly, Cashman et al. (2008) show evidence of tridymite in dacite from Mount St Helens (USA), and estimate that its presence necessitates relatively low pressures (between around 5 and 25 MPa). The observation that porosity is created and destroyed by physical and chemical processes in the upper conduit and surficial dome emphasises the importance of understanding localised spatio-temporal variations in permeability.

## 6.5 PERMEABILITY ANISOTROPY

From 2D porosity estimates ([Table 6.2](#)) and an examination of the microstructure, it is clear that the various conduit and dome processes discussed above manifest themselves differently: they may increase or decrease porosity, or porosity can remain effectively constant.

The following section discusses the consequent influence on the permeability of these discontinuity-bearing samples, which can be distinguished into four main categories:

1. an increase in porosity may exert only a negligible influence on permeability,
2. an increase in permeability may arise even when porosity is essentially unchanged,
3. an increase in porosity can be accompanied by an increase in permeability, or
4. a decrease in porosity can yield a decrease in permeability.

In the majority of the collected blocks, porosity within the band or fracture is higher than or equivalent to that of the host rock mass ([Table 6.2](#)). The exceptions are the banded pumiceous samples (Col-V-6 and Col-V-1; [Figure 6.2a](#) and [6.2b](#); [Figure 6.4a](#); [Table 6.2](#)) agree with the connected gas porosity measurements performed on cylindrical cores obtained from each block ([Table 6.3](#)). Gas permeability of all core samples are also given in [Table 6.3](#), as well as whether the heterogeneity—if present—was parallel or perpendicular to the core axis (hence the direction of fluid flow). Permeability as a function of porosity is shown in [Figure 6.9](#). In general, high porosities are associated with high permeabilities, and low porosities with low permeabilities, although the precise relation differs between the high ( $>0.30$ ) and low ( $<0.20$ ) porosities (as described in [Chapter 3](#); see also Heap et al., 2014b; Kushnir et al., 2016).

[Table 6.3](#): Connected gas porosity  $\phi$  and gas permeability  $k$  data for core samples. Table also indicates whether the core was obtained parallel  $\parallel$  or perpendicular  $\perp$  to the feature in the sample, and whether or not the feature was present in the core.

Sample	$\phi$	$k$ [m <sup>2</sup> ]	Core orientation	
			w.r.t flow direction	Feature
COL-V-1-Y	0.35	$7.98 \times 10^{-14}$	$\parallel$	Present
COL-V-1-Z	0.43	$5.44 \times 10^{-14}$	$\perp$	Present

Table 6.3: continued

Sample	$\phi$	$k$ [m <sup>2</sup> ]	Core orientation		Feature
			w.r.t flow direction	Core orientation	
COL-V-6-Z <sub>1</sub>	0.43	$3.42 \times 10^{-13}$	⊥	⊥	Present
COL-V-6-Z <sub>2</sub>	0.44	$3.40 \times 10^{-13}$	⊥	⊥	Present
COL-V-6-Z <sub>3</sub>	0.62	$1.18 \times 10^{-13}$	⊥	⊥	Absent
COL-M-1-Y <sub>1</sub>	0.07	$5.16 \times 10^{-14}$			Present
COL-M-1-Y <sub>2</sub>	0.06	$4.18 \times 10^{-14}$			Present
COL-M-1-Z <sub>1</sub>	0.06	$1.46 \times 10^{-16}$	⊥	⊥	Present
COL-M-1-Z <sub>2</sub>	0.05	$2.40 \times 10^{-16}$	⊥	⊥	Present
COL-L-1-Y <sub>1</sub>	0.08	$2.84 \times 10^{-16}$			Present
COL-L-1-Y <sub>2</sub>	0.03	$1.36 \times 10^{-17}$			Absent
COL-L-1-Z <sub>1</sub>	0.03	$1.29 \times 10^{-18}$	⊥	⊥	Absent
COL-L-1-Z <sub>2</sub>	0.08	$4.24 \times 10^{-16}$	⊥	⊥	Present
COL-V-5-Y <sub>BLACK</sub>	0.13	$1.05 \times 10^{-14}$			Present
COL-V-5-Y <sub>BOTH</sub>	0.11	$3.03 \times 10^{-15}$			Present
COL-V-5-Y <sub>GREY</sub>	0.15	$6.24 \times 10^{-16}$			Absent
COL-V-5-Z <sub>BLACK</sub>	0.15	$1.37 \times 10^{-14}$	⊥	⊥	Present
COL-V-5-Z <sub>GREY</sub>	0.13	$2.90 \times 10^{-16}$	⊥	⊥	Absent
COL-V-5-Z <sub>BOTH</sub>	0.12	$2.48 \times 10^{-16}$	⊥	⊥	Present
COL-L-4-Y <sub>1</sub>	0.13	$2.40 \times 10^{-13}$			Absent
COL-L-4-Y <sub>2</sub>	0.09	$3.18 \times 10^{-14}$			Present
COL-L-4-Z <sub>1</sub>	0.13	$1.11 \times 10^{-14}$	⊥	⊥	Present
COL-L-4-Z <sub>2</sub>	0.15	$3.30 \times 10^{-13}$	⊥	⊥	Absent
COL-L-4-Z <sub>3</sub>	0.14	$6.21 \times 10^{-14}$	⊥	⊥	Present
COL-L-4-Z <sub>4</sub>	0.14	$1.76 \times 10^{-13}$	⊥	⊥	Present
COL-V-3-Y <sub>1</sub>	0.07	$3.45 \times 10^{-16}$			Present
COL-V-3-Y <sub>2</sub>	0.07	$8.03 \times 10^{-16}$			Present
COL-V-3-Y <sub>3</sub>	0.06	$1.56 \times 10^{-16}$			Present
COL-V-3-Y <sub>4</sub>	0.09	$1.22 \times 10^{-15}$			Present
COL-V-3-Z <sub>1</sub>	0.10	$1.41 \times 10^{-16}$	⊥	⊥	Present
COL-V-3-Z <sub>2</sub>	0.08	$4.10 \times 10^{-16}$	⊥	⊥	Present
COL-V-3-Z <sub>3</sub>	0.10	$8.98 \times 10^{-16}$	⊥	⊥	Present

Table 6.3: continued

Sample	$\phi$	$k$ [m <sup>2</sup> ]	Core orientation w.r.t flow direction	Feature
COL-V-4-Y <sub>1</sub>	0.09	$4.23 \times 10^{-14}$		Present
COL-V-4-Y <sub>2</sub>	0.09	$1.56 \times 10^{-14}$		Present
COL-V-4-Y <sub>4</sub>	0.08	$1.78 \times 10^{-14}$		Present
COL-V-4-Y <sub>5</sub>	0.13	$4.70 \times 10^{-14}$		Present
COL-V-4-Y <sub>6</sub>	0.08	$2.41 \times 10^{-14}$		Present
COL-V-4-Z <sub>1</sub>	0.06	$3.00 \times 10^{-16}$	⊥	Absent
COL-V-4-Z <sub>2</sub>	0.08	$2.99 \times 10^{-16}$	⊥	Present
COL-V-4-Z <sub>3</sub>	0.04	$1.29 \times 10^{-16}$	⊥	Absent
COL-V-4-Z <sub>4</sub>	0.08	$2.50 \times 10^{-16}$	⊥	Present
COL-V-4-Z <sub>5</sub>	0.09	$1.70 \times 10^{-16}$	⊥	Present
COL-V-4-Z <sub>6</sub>	0.04	$1.32 \times 10^{-16}$	⊥	Present
COL-V-4-Z <sub>7</sub>	0.07	$2.53 \times 10^{-16}$	⊥	Present
COL-V-4-Z <sub>8</sub>	0.06	$2.83 \times 10^{-16}$	⊥	Present
COL-V-4-Z <sub>9</sub>	0.03	$9.77 \times 10^{-17}$	⊥	Absent
COL-V-4-Z <sub>10</sub>	0.03	$1.05 \times 10^{-16}$	⊥	Absent
COL-L-2-Y <sub>1</sub>	0.01	$1.77 \times 10^{-16}$		Absent
COL-L-2-Y <sub>2</sub>	0.05	$3.09 \times 10^{-14}$		Present
COL-L-2-Y <sub>3</sub>	0.05	$3.30 \times 10^{-14}$		Present

The permeability of a heterogeneous porous medium is termed here the "equivalent" permeability  $k_{eq}$  (see Renard and De Marsily, 1997 for a review). For sample sets where there are at least one core containing a band parallel to the core axis, and at least one band-free core, it is possible to decouple the equivalent permeability in order to estimate the permeability of the band or fracture itself via a simple two-dimensional parallel-plate model. Assuming that the ("intact") host permeability  $k_0$  is that of the feature-free core; thus the permeability of the band or fracture  $k_f$  is calculated as a function of the sample area  $A_s$ , the band area  $A_f$ , and the host and equivalent permeabilities, such that

$$k_f = \frac{k_{eq}A_s - k_0(A_s - A_f)}{A_f}. \quad (6.1)$$

This method has previously been used to calculate the permeability of tensile fractures in variably-porous andesites from Ruapehu (New

Zealand) (Heap and Kennedy, 2016). Note that this model assumes that  $A_f$  is small compared to  $A_s$ . [Table 6.3](#) gives the parameters used, as well as the mean band or fracture permeabilities, for each of the rocks where this calculation was possible. Further, the "relative" permeability  $\lambda k$  between the host rock and the discontinuity, given here by the fractional change in permeability with respect to the host value (as in [Chapter 4](#)):

$$\lambda k = \frac{\log_{10} k_f - \log_{10} k_0}{\log_{10} k_0}, \quad (6.2)$$

where a positive value means that a feature is more permeable than its corresponding host rock, while a negative value indicates the reverse. The data of [Table 6.3](#) and [6.4](#) show that the presence and orientation of a discontinuity has a variable influence on the permeability of these samples: permeability can increase, decrease, or remain roughly constant depending on the properties of the host rock and the feature. These scenarios are discussed below.

First the banded pumice is examined. Data presented in [Figure 6.9b](#) and [Table 6.1](#) show that permeability of pumiceous material (Col-V-1 and Col-V-6) varies by less than an order of magnitude: despite ranging between  $\simeq 0.35$  and  $\simeq 0.65$  porosity, permeability ranges from  $5.44 \times 10^{-14}$  to  $3.42 \times 10^{-13} \text{ m}^2$  in these samples. As observed in [Chapter 3](#) (also Kennedy et al., 2015; Kushnir et al., 2016), the permeability–porosity relationship of porous volcanic rocks can be described by a relatively low power law exponent above a certain threshold in porosity. This is thought to be due to the fact that above this threshold effective fluid pathways (a so-called "backbone" of permeability) must—necessarily—already exist, as expounded on in [Chapter 3](#). Thus, a large increase in porosity by rapid bubble expansion, as inferred for samples Col-V-1 and Col-V-6 (e.g. [Figure 6.4a - c](#)), is likely to be associated with only a marginal increase in permeability. Similarly, one may assume that pure-shear flattening of these bubbles will not significantly decrease permeability until a threshold level of compaction.

Sample Col-V-5 has been interpreted as preserving a simple shearing process. The permeability of the darker coloured side ( $1.37 \times 10^{-14} \text{ m}^2$ ) is measurably higher than that of the lighter coloured portion ( $2.90 - 6.24 \times 10^{-14} \text{ m}^2$ : [Table 6.3](#); [Figure 6.9a](#)). Thus, in samples where the core axis is parallel to the discontinuity, the permeability is controlled by that of the most permeable region (on the order of  $10^{-14} \text{ m}^2$ ). Conversely, when the core axis is perpendicular to the discontinuity, the permeability is comparable to the lower value, on the order of  $10^{-16} \text{ m}^2$  ([Figure 6.9a](#)). As the fraction of connected porosity shows negligible variation, differences in permeability must be driven in this case by some other corresponding parameter. As noted previ-

Table 6.4: Mean permeabilities and dimensions used to calculate the permeability of the feature for five samples. Note that "fracture" permeability is used to refer to the permeability of any of the discussed features, regardless of genesis.  $k_i$  = intact permeability;  $k_{eq}$  = equivalent permeability;

$A_f$  = Fracture area;  $A_f$  = Fracture area;  $k_f$  = fracture permeability;  $\lambda k$  = relative permeability ([Equation 6.2](#)).

Sample	$k_i$ [ $\text{m}^2$ ]	$k_{eq}$ [ $\text{m}^2$ ]	$A_s$ [ $\text{mm}^2$ ]	$A_f$ [ $\text{mm}^2$ ]	$k_f$ [ $\text{m}^2$ ]	$\lambda k$
COL-V-5	$1.37 \times 10^{-16}$	N/A <sup>a</sup>	N/A <sup>b</sup>	N/A <sup>c</sup>	$1.21 \times 10^{-14}$	0.12
COL-V-4	$1.58 \times 10^{-16}$	$2.94 \times 10^{-14}$	312.84	74.1581	$1.04 \times 10^{-13}$ <sup>d</sup>	0.18
COL-L-1	$1.36 \times 10^{-17}$	$2.84 \times 10^{-16}$	312.87	128.23	$3.90 \times 10^{-16}$	0.09
COL-L-2	$1.77 \times 10^{-16}$	$3.19 \times 10^{-14}$	310.92	58.52	$1.37 \times 10^{-13}$ <sup>e</sup>	0.18
COL-L-4	$2.40 \times 10^{-13}$	$3.18 \times 10^{-14}$	308.19	44.80	$6.67 \times 10^{-14}$	-0.04

<sup>a</sup> For Col-V-5 ([Figure 6.2c](#)) it was possible to obtain cores containing only the host material or only the band (see [Table 6.3](#)). Thus there is an independent of the band permeability relative to the initial material, and no calculation is necessary.

<sup>b</sup> See footnote [d](#)

<sup>c</sup> See footnote [d](#)

<sup>d</sup> Value shown is mean value determined from fracture permeabilities of two samples COL-V-4-Y<sub>1</sub>, -Y<sub>2</sub>. Values range from  $1.67 \times 10^{-13}$  –  $4.12 \times 10^{-14}$   $\text{m}^2$ .

<sup>e</sup> Value shown is mean value determined from fracture permeabilities of two samples COL-L-2-Y<sub>1</sub>, -Y<sub>2</sub>. Values range from  $1.32 \times 10^{-13}$  –  $1.42 \times 10^{-13}$   $\text{m}^2$ .

ously, the pore size and pore size distribution differs between the relatively high- and low-permeability regions. In turn this presumably influences the mean aperture of fluid pathways, as well as other factors such as the relative tortuosity of each pathway. Local differences in the stressing history of the magma may therefore provide a partial explanation for the wide variability in volcanic rock permeability observed in nature (e.g. Mueller et al., 2005; 2006; Chapter 3).

Many of the discontinuity-bearing samples discussed herein are considered to represent variably-sintered fractures. For one of these—sample Col-V-4 (Figure 6.4j - l)—fracture permeabilities are obtained on the order of  $1.0 \times 10^{-13} \text{ m}^2$ , approximately three orders of magnitude greater than the mean permeability of non-fractured cores of this sample ( $1.6 \times 10^{-16} \text{ m}^2$ ). It is thus evident that these fractures comprise a highly efficient conduit for fluid flow, despite being partially healed (experiments suggest that the unhealed fracture permeability of a 20 mm-diameter sample containing a single through-going fracture is in the vicinity of  $10^{-11} \text{ m}^2$ : Heap and Kennedy, 2016). This supports the inference of previous authors (e.g. Edmonds and Herd, 2007; Castro et al., 2014), that magma fracture is an effective means of outgassing volatiles from conduit-dwelling magma. However, fractures observed in some of our other samples show evidence of more mature sintering (summarised in Figure 6.6f - j), and are inferred to originate from greater depths or suggest longer healing timescales.

It has been previously suggested through modelling that sintering timescales decrease with depth due to the correspondingly high magmatic (and lithostatic) pressure and low effective viscosity (Russell and Quane, 2005; Quane et al., 2009; Heap et al., 2015b). However, it has been noted that volatile resorption at low pressures may actually serve to accelerate viscous sintering (Sparks et al., 1999) by locally reducing the melt viscosity (Hess and Dingwell, 1996). Viscous sintering results in densification and a reduction of the connectivity of the porous network (e.g. Vasseur et al., 2013), and is commonly recorded in volcanic environments (e.g. Grunder and Russell, 2005; Quane et al., 2009; Kolzenburg and Russell, 2014). This process correspondingly reduces permeability (Heap et al. 2015b; Wadsworth et al., 2016b), ultimately tantamount to the destruction of fluid pathways in magma.

The infilled and relatively low-porosity band of sample Col-L-4 (Figure 6.4v - x; Figure 6.7), yields a fracture permeability of  $6.7 \times 10^{-14} \text{ m}^2$ , approximately an order of magnitude lower than that of the surrounding rock mass ( $2.4 \times 10^{-13} \text{ m}^2$ ); correspondingly the relative permeability  $\lambda k$  is negative (Table 6.4). To preferentially permit

the passage of hot ash-laden fluids (as discussed previously), this now low-porosity band used to be, in all likelihood, a band of higher porosity and permeability than the surrounding host rock. Although the preserved features studied herein only provide snapshots of dynamic processes, this indicates a strong time-dependence of permeability in magma: once fractures generated, fault gouge and preferentially transported fragmental material will quickly sinter due to their small size (e.g. Wadsworth et al., 2014). In turn, permeable fractures, cavities, or bubble networks, may progressively decrease in permeability until they are of comparable or, in some instances, lower permeability than the original magma.

In short, if a feature acts as a conduit for fluid flow, then orientation of the feature parallel to fluid flow typically has a markedly greater influence on permeability than when the feature is normal to fluid flow. On the other hand, a feature acting as a barrier for fluid flow will exert its maximum influence when oriented perpendicular to fluid flow. This is due to the difference between fluid flow in parallel and serial systems. Simply put, when offered the choice of parallel layers, fluid will preferentially flow through the layer that is most permeable, and the overall permeability is thus governed by the most permeable element. Contrastingly, in a serial system, fluids must flow through each and every layer, and permeability is thus controlled by the layer with lowest permeability.

## 6.6 OUTGASSING AND VOLCANIC ACTIVITY

[Figure 6.10](#) summarises the influence of processes discussed in the previous two sections. Magma fracture causes relatively large changes in magma permeability, over relatively small increments in porosity ([Figure 6.10a](#)). Indeed, these data suggest that permeability may increase by three orders of magnitude or more for a change in porosity of only around 0.03 or 0.04 ([Table 6.3](#)). Similarly, shear-induced transtension or cavitation of magma is predicted to yield a local increase in porosity and permeability ([Figure 6.10a](#)); our data for sample Col-M-1, for example, indicates that for comparable porosities (between 0.05 and 0.07), permeability of the magma can be increased by around two orders of magnitude if these porous discontinuities are preferentially oriented ([Table 6.3](#); [Figure 6.9a](#)).

By contrast, densifying processes—e.g. viscous sintering or transgression—result in decreases in both porosity and permeability ([Figure 6.10b](#)). [Figure 6.10a](#) and [6.10b](#) further illustrate the contrasting influences of bubble expansion and the collapse of foaming magma. Because the magma is already highly permeable—due to its high initial porosity—increases or decreases in porosity of tens of percentage

points (e.g. from  $\phi \sim 0.30$  to  $\phi \sim 0.60$ ) are not expected to have a marked influence on the permeability of the magma (less than one order of magnitude difference).

It is important to note that—irrespective of the processes acting on the physical properties of a specific clast or unit of magma (Table 6.3; Figure 6.9)—the permeability–porosity relationship of heterogeneity-bearing rocks (and indeed, the permeability–porosity relationship of the features themselves) appear always to follow a trend remarkably similar to that of andesitic rock free of macroscopic heterogeneities (shown in Figure 6.10c, data from Chapter 3). It follows that at low magma porosities (i.e. lower than around 0.15 or 0.20: see Figure 6.9a), permeability evolution is dominated by the generation and healing of fractures, just as in low-porosity volcanic rocks the permeability evolution is strongly governed by the generation or closure of microcracks (Chapter 4; also Vinciguerra et al., 2005; Nara et al., 2011; Heap et al., 2014b). At higher porosities, the influence of bubble growth, bubble coalescence, and expansion-driven fragmentation become dominant (Figure 6.9b). Thus, dilatant or densifying processes acting on the magma will have a greater marginal influence at low initial porosities than at high initial porosities. In short, these results indicate that an increase or decrease in porosity or permeability will move the magma more-or-less along the paths indicated in panels *a* and *b* of Figure 6.10.

The results of this chapter show that permeability can be increased locally by as much as three orders of magnitude due to dilatant processes (see Figure 6.9, Table 6.3), even if partial sintering has occurred. Such efficient fluid pathways may play an extremely important role in the outgassing of magmatic volatiles, in turn decreasing the propensity for fluid pressurisation and violent explosive behaviour in active volcanic systems. Fracture geometry (i.e. length and aperture) will influence the initial gas volume that can enter and escape through the fracture. If a fracture constitutes a pathway for magmatic fluids to outgas from the system (e.g. into the edifice rock: Heiken et al., 1988; Kolzenburg et al., 2012) then the continuous through-flow of gas has been posited to sustain an open fracture, as long as there exists a persistent supply of gas from beneath which is decoupled from the melt (plus crystal) phase of the magma (e.g. Rust et al., 2004; Plail et al., 2014). Indeed, increased pore fluid pressures are thought to occur, albeit transiently, in particle-filled fractures within magma (e.g. Castro et al., 2014). As such, relatively large volumes of gas can be decoupled from the magma and thus flow through these fractures: a significantly more efficient means of transporting volatiles than bubble migration through a viscous silicate melt, or indeed diffusion-scale processes. Indeed, fractures in magma

could allow outgassing even at very low porosities.

As magma fracturing will preferentially occur where strain rates are thought to be highest (e.g. Papale, 1999; Gonnerman and Manga, 2003; Edmonds and Herd, 2007), permeable fractures are likely to contribute to a "damage halo" zone surrounding the central conduit (e.g. Lavallée et al., 2013; Gaunt et al., 2014; Young and Gottsmann, 2015), as discussed in previous chapters. Microstructural evidence presented here hints that these fractures occur both in shallow regions (textural evidence of silica polymorphs in fractures point to high-temperature, low-pressure conditions) and deeper in the system (advanced sintering textures observed in some samples indicate high-temperature, high-pressure environments), suggesting that this halo may serve to bleed off volatiles from the magma and promote outgassing into the edifice rock or through near-conduit fracture networks along the length of the conduit. Fault gouge and ash entrained in escaping fluids may accelerate sealing or closure of pathways (e.g. Tuffen et al., 2003; Saubin et al., 2016; Kendrick et al., 2016). However, it has been shown experimentally that the relatively slow post-fracture recovery of magma strength may actually promote recrudescent fracture events (Heap et al., 2015b), which in turn may serve to regulate lava dome eruptions (Heap et al., 2015b; Kendrick et al., 2016).

The extraction of magmatic volatiles due to shear strain-induced cavitation (evidence for which process is described above) has similarly been posited to result in premature embrittlement of magma (Smith et al., 2001), assisting the recurrence of fracture events. Repeat faulting events in magma have been proposed as a mechanism for earthquake generation during magma ascent (e.g. Tuffen and Dingwell, 2005; Neuberg et al., 2006; Lavallée et al., 2008; Tuffen et al., 2008; Varley et al. 2010a, b; Kendrick et al., 2014a; Heap et al., 2015b).

In the sample containing a band of lower porosity—characterised by pores that have been variably infilled with ash-sized particles that have sintered to the pore walls—a permeability reduction of an order of magnitude was measured relative to the host material. One inference that may be drawn from this is that barriers to flow (viscous densification, sintering of fractures, and infill of pores with granular material or vapour-phase crystallisation) may trap exsolved volatiles and allow the build-up of pore pressure. Iterative densification events may compartmentalise parcels of magma, create pore overpressures, and result in complex permeability anisotropy within the conduit or the dome. Preferential flow of ash-laden fluid along porous networks—that is, interconnected bubble chains or fractures—will cause a time-dependent permeability anisotropy at the periphery of the con-

duit. The permeability reduction associated with this process (Figure 6.7, Figure 6.9a) means that a pathway that preferentially transmits fluids can consequently evolve into a barrier: the relative permeability  $\lambda k$  (Equation 6.2) will transition from a positive to a negative value). Consequently, fluids will be forced to find another route through the magma.

As previously described, the strain profile across a volcanic conduit or dyke is typically assumed to vary, with strains and strain rates being highest at the margins (e.g. Gonnermann and Manga, 2003). Consequently, fractures in magma may be expected to be oriented subparallel to the direction of magma flow (thus in a traditionally-envisioned volcanic conduit, magma fractures will be predominantly oriented subvertically). As such, permeability-increasing fractures will be preferentially oriented in the conduit to facilitate annular or halo outgassing. However, effective sintering of such fractures could promote a build-up of overpressure, by limiting lateral migration of volatiles from the conduit into the edifice or an intermediate fractured zone. There also exists field evidence for the generation of tensile fractures that propagate laterally into the edifice (see Heiken et al., 1988; Goto et al., 2008). In this case, features acting as pathways for flow will likely improve outgassing into the country rock, whereas barrier-forming features will not majorly influence diffuse edifice outgassing. Similarly, large-scale fractures throughout a lava dome are often oriented vertically to subvertically (e.g. Calder et al., 2015; Walter et al., 2015) and will likely serve to effectively bleed off volatiles.

Due to the inherently fractured nature of many lava domes, low-permeability features resulting from local hydrothermal alteration, mineral precipitation, or ash deposition (e.g. Edmonds et al., 2003; Ball et al., 2015) may not significantly reduce their overall outgassing potential. However, such sealing of permeable pathways may be of great importance in the shallow conduit, where restricting the migration of an exsolved gas phase could rapidly elevate pore pressure in the system, reducing structural integrity and increasing the likelihood of explosive behaviour.

Furthermore, the length of time that features with high relative permeability can act as effective outgassing networks relies on the interplay between the incumbent stress field, the through-flow of gas (e.g. Rust et al., 2004) and effective viscosity- and pressure-dependent densification via compaction or sintering (e.g. Quane et al., 2007; Kolzenburg and Russell, 2014; Vasseur et al. 2013; Heap et al., 2015b) as well as ancillary processes such as the transport of ash and fault gouge (e.g. Tuffen et al., 2003; Kendrick et al., 2015), and hydrothermal mineral precipitation (e.g. Edmonds et al., 2003). Providing

accurate timescales for volcanic processes—even those that are relatively well understood—is inherently problematic due to the lack of knowledge regarding the formation conditions (e.g. depth, temperature, local strain rates) or the state of the initial material (porosity, viscosity, grain size distribution etc.). In reality, all of the processes discussed herein are likely to be concurrent within comparable sub-aerial volcanic systems.

The relative proportion of dilatant versus densifying processes may heavily influence transitions between eruptive regimes and govern, at least partially, repose periods of Vulcanian explosive activity (Quane et al., 2007; Collinson and Neuberg, 2012): dilatational processes should bridle eruptive behaviour and lengthen repose times, while sintering and densification should augment the increase of pore pressure, and decrease repose times. Modelling recurrence intervals during periods of intermittent explosive activity is often fraught with complexity (e.g. Varley et al., 2006), much of which may be attributed to the contrasting influences of dilatant and densifying processes throughout volcanic systems. However, this interplay remains poorly understood, and its description—through systematic sets of controlled experiments—is encouraged.

## 6.7 CONSIDERATIONS FOR SCALING AND MODELLING

The blocks collected for this study were of hand sample size. However, even cursory field observations indicate that variably tabular discontinuities in volcanic material can be seen on much greater lengthscales. Moreover, in the initial stages of their genesis, these features may be orders of magnitude smaller than those discussed herein. Such intra-clast heterogeneity may well be responsible for the large variation in permeabilities measured in volcanic rocks of similar porosities (e.g. Mueller et al., 2005; 2008; Chapter 3). As the permeability of fractured volcanic rocks is greatly scale-dependent (Heap and Kennedy, 2016), it is of importance that the permeable structures discussed in this contribution are discussed in this context.

Although accurate constraints of subsurface volcanic architecture are rare, results from drilling projects suggest that surficial vent and crater systems on the order of 10s or 100s of m in diameter can belie conduits of relatively narrow width (Mastin and Pollard, 1988). For example, Noguchi et al. (2008) describe the dacitic conduit of Mount Unzen (Japan) as ranging from 4 to 40 m in diameter to a depth of 2 km. This is in agreement with studies of exposed feeder dykes (e.g. Keating et al., 2008; Galindo and Gudmundsson, 2012), which show that, deeper than around 50 m, solidified dykes tend to have diameters of only a few m. As a consequence, even relatively small dis-

continuities—such as those described herein—may constitute a non-negligible portion of the conduit width. While the thickness of such features as a proportion of the conduit width will certainly decrease as the conduit widens, in many cases their abundance and longevity will be augmented in shallower systems.

As discussed, the equivalent permeability of each block is dependent on its initial size and the area of the discontinuity and the ratios of their permeabilities, just as [Equation 6.1](#) is strongly influenced by the ratios of  $A_s$  to  $A_f$  and  $k_0$  to  $k_f$ . The partially sintered fracture of Col-V-4, for example, was found to have a permeability of  $1.04 \times 10^{-13} \text{ m}^2$ , yielding an equivalent permeability of  $2.94 \times 10^{-14} \text{ m}^2$  in a core sample of approximately 20 mm diameter ([Table 6.4](#)). To upscale these data, a 1D version of [Equation 6.1](#) was employed, wherein  $A_s$  and  $A_f$  are substituted for  $w_s$  and  $w_f$ : the width of the sample and fracture, respectively (as in Heap and Kennedy, 2016):  $k_f = k_{eq}w_s - k_0(w_s - w_f)/w_f$ . Hence, a fracture of 2.25 mm width in a sample 10 m wide (with the same host permeability:  $1.58 \times 10^{-16} \text{ m}^2$ ) would result in an equivalent permeability of  $1.81 \times 10^{-16} \text{ m}^2$ , not significantly higher than that of the host material. In a sample 1000 m in width, the overall influence of the same fracture would be effectively zero ( $k_{eq} = 1.58 \times 10^{-16} \text{ m}^2$ ).

By contrast, if the fracture width approaches that of the considered lengthscale, then its influence on equivalent permeability will be correspondingly greater. Similarly, an increase in the number of fractures within a given volume of rock or magma will increase the equivalent permeability to a greater or lesser extent, depending on their geometries and fluid transport properties. These concepts are illustrated in [Figure 6.11](#), using the example of Col-V-4 (equally, data from other features—[Table 6.4](#)—could be analysed using this method). The lengthscale refers to the total width of material considered, for example the width of a volcanic conduit at a given depth. For reference, the range of widths measured by Noguchi et al. (2008) is shaded grey in [Figure 6.11](#). Even a single fracture with the thickness and fluid transport properties of that in Col-L-4 can increase the equivalent permeability of a conduit a few m in width (i.e. the intersection of the red line with the shaded region). However, the same fracture in a conduit with a diameter of 40 m has a negligible influence.

In this simplified context, adding new fractures or widening an existing fracture has the same result, namely increasing the "cumulative fracture width". In reality, increasing or decreasing the width of a fracture will introduce complexities associated with non-laminar flow (e.g. Heap and Kennedy, 2016), which are not accounted for in [Figure 6.11](#). Nevertheless, [Figure 6.11](#) demonstrates the significance of

considering upscaling from laboratory samples to outcrop-scale and larger. Accurately incorporating scale effects remains an outstanding challenge in volcanology, especially in transferring experimental data to eruption models and hazard mitigation policies. To advance our understanding of volcanic processes and better predict eruptive scenarios requires the development of models which effectively reproduce eruption characteristics observed in nature (e.g. Melnik, 2000; Burgisser and Garner, 2005; Collombet, 2009), especially the transitions and timescales between explosive and effusive periods (e.g. Jaupart, 1996; Collinson and Neuberg, 2012). Based on this study, it is clear that future models assessing conduit dynamics and permeability evolution should consider the propensity for permeability anisotropy within the magma column and lava dome on multiple lengthscales. Given that such heterogeneities are posited to occur primarily at the conduit margins or in high-strain regions of extruding domes, this could be modelled by stochastic inclusion of transient variations in magma permeability, by a coupling of permeability and shear strain across the width of the conduit, or by the calculation of the (time-dependent) equivalent permeability of fracturing conduit margins (as touched on in [Figure 6.11](#) and the attendant discussion).

## 6.8 FIELD INTERPRETATIONS

In the absence of microstructural examination, interpretation of some textural or structural heterogeneities encountered in volcanic materials can be nontrivial. Despite being visually similar at a hand sample scale, this chapter has shown that such features are not equally efficient at transmitting fluids. Thus it is highly recommended that any interpretation of heterogeneity-bearing volcanic rocks—especially with respect to their influence on permeability and the attendant implications for outgassing—should be buttressed by microstructural description and/or measurements of permeability or porosity.

As a final comment on these data: due to the accretionary growth of stratovolcanoes (e.g. Odber et al., 2015), explosively or effusively erupted lava eventually comprises some portion of the edifice. Thus, if fluid flow pathways or barriers are erupted and preserved—as was the case with our sample set—they may be expected to increase permeability anisotropy and influence fluid partitioning within the edifice. Their presence is anticipated throughout the upper edifice at Volcán de Colima and indeed at other comparable volcanic systems (such discontinuity-bearing rocks can be seen at throughout the Taupō Volcanic Zone in New Zealand for example: see [Figure 6.12](#)). However, a quantitative analysis of their appearance at the surface could be somewhat misleading. For example, it has been noted that features that provide effective outgassing pathways are, by definition, less likely to

be erupted out of the volcano than ineffective (or nonexistent) pathways (Plail et al., 2014). Similarly, Castro et al. (2012) intimates that the pyroclastic origin of tuffisite-bearing bombs indicates that systems containing highly permeable discontinuities can still be subject to significant overpressure development. Further, the preservation of clasts containing fractures may be poor, especially if the fracture is poorly-sintered. Nevertheless, it should be stressed that discontinuity-bearing volcanic materials can provide incredibly informative snapshots of otherwise unobservable magmatic processes, making their continued study a valuable pursuit in volcanology.

### 6.9 CHAPTER SUMMARY

Tabular heterogeneities in andesitic rocks—of both explosive and effusive origin—can be found in abundance at Volcán de Colima (Mexico), providing frozen-in snapshots of magmatic processes. Alongside an examination of their microstructure, a systematic laboratory study of the physical properties of a selection of these heterogeneity-bearing blocks allows important information to be gleaned regarding the likely geneses of these features within a volcanic system, as well as their influence on the physical properties of the magma (at least upon eruption).

Bands were inferred to form in high-porosity pumice blocks ( $\phi$  around 0.30 and higher) due to inhomogeneous bubble expansion in magma. Despite a significant influence on the porosity of these samples, permeabilities of banded and non-banded pumice were found to be comparable (of the order  $10^{-13} \text{ m}^2$ ). This is thought to be due to the pre-established pathways of effectively connected porosity. In lower porosity blocks ( $\phi < 0.20$ ), features are preserved that increase porosity and permeability relative to the surrounding material. These discontinuities may be the frozen relicts of dilatant processes such as viscous cavitation or magma fracturing. These fractures can increase in permeability by about three orders of magnitude relative to the host rock, when they are oriented parallel to fluid flow. Evidence of subsequent fracture healing can also be observed in the microstructure, and the attendant measurements indicate that fracture permeability decreases with more advanced sintering.

Differences in the extent of sintering, and the presence of silica polymorphs in some samples, suggest that these features were likely formed at different depths in the conduit. The evidence therefore suggests that fractures exist—although in some cases, only temporarily—along an extensive portion of the conduit, supporting the concept of a permeable outgassing halo surrounding the conduit. Notably, textures interpreted herein as the infill of pores with transiently granular

material (such as gas-transported volcanic ash) indicates that porous networks may subsequently become barriers to fluid flow over time, especially when oriented normal to fluid flow. This highlights a complex interplay between dilatant and densifying processes in magma, as well as the time-dependent evolution of its physical properties. Evidence has been presented for significant permeability variation within conduit magma and dome at Volcán de Colima, and it is anticipated that the features described here will also exist at similar andesitic stratovolcanoes worldwide, at a range of lengthscales. Localised permeability heterogeneities must be a critical parameter influencing the evolution of pressures within active volcanic systems, and a simple upscaling model illustrates the evolving significance of permeability heterogeneities over different length-scales. It is likely that, in turn, these features will influence the eruptive regime and recurrence intervals of explosions or degassing events at active volcanoes.

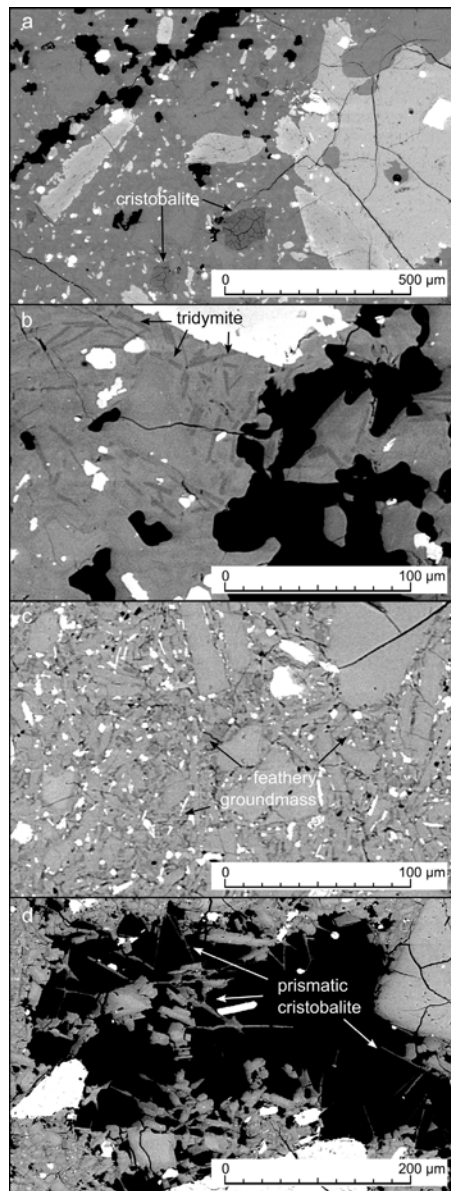


Figure 6.8: Textural evidence for silica polymorphs. a) Dark grey patches are cristobalite crystals, showing characteristic "fish-scale" cracking in sample Col-M-1. b) Dark grey, high aspect ratio crystals are acicular tridymite (sample Col-L-2). c) The groundmass of sample Col-V-3 has a "feathery" texture, indicative of devitrification of the groundmass (see Horwell et al., 2012; 2013). d) High aspect ratio crystals inferred to be prismatic cristobalite are often seen growing into pore spaces (sample Col-L-4).

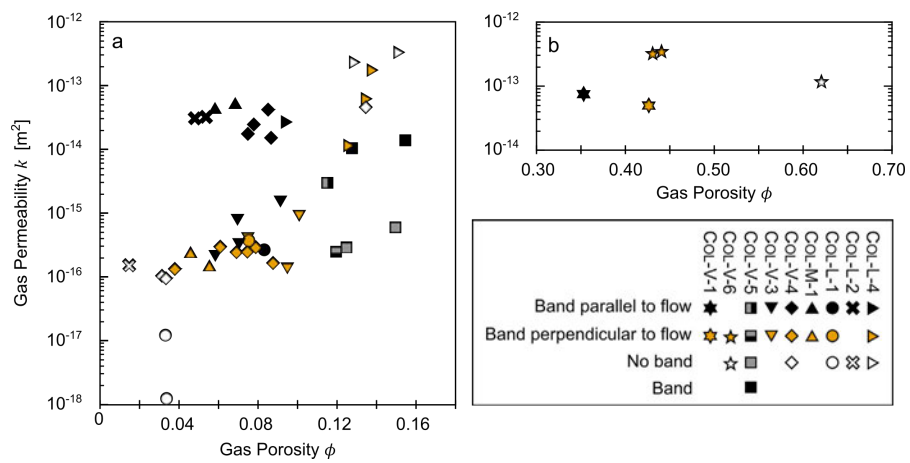


Figure 6.9: Connected gas porosity ( $\phi$ ) and gas permeability ( $k$ ) data for all fifty core samples. a) Low-porosity samples ( $\phi < 20$ ). b) High-porosity samples ( $\phi > 30$ ). Note the difference in scale of the  $x$ -axis between either panel. Different blocks are indicated by different symbols, while the presence or orientation of a feature is given by the symbol colour. Measurement error is less than the symbol size in each case. Refer to text for discussion.

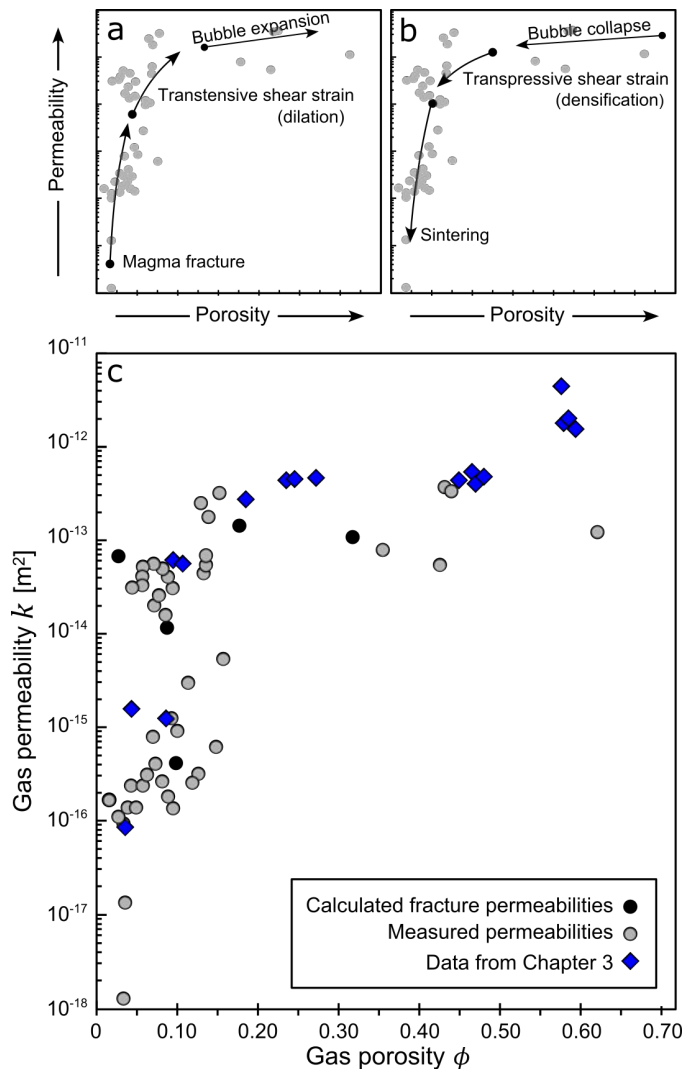


Figure 6.10: The influence of magmatic processes on the development of permeability, as predicted from our microstructural interpretations. a) Dilatant (porosity-increasing) processes, including magma fracture, shear-induced extension, cavitation, and bubble expansion, exhibit a non-linear effect on permeability: at low porosities, large increases in permeability may be observed and vice versa. b) Compactant or densifying processes—such as sintering, pore occlusion, and bubble collapse—similarly exert a large influence when the initial porosity is low, and only a slight influence when the initial porosity and permeability are high. c) Collated permeability and porosity data. Despite the inclusion or orientation of the heterogeneities discussed throughout this study, the permeability–porosity data follow essentially the same trend as that of collected band-free samples (data taken from Chapter 3). Further, the data for the bands themselves (calculated permeability from Equation 6.1 in concert with 2D SEM-derived porosities: from Table 6.2, 6.4) also follow this trend. Measurement error is less than the symbol size in each case.

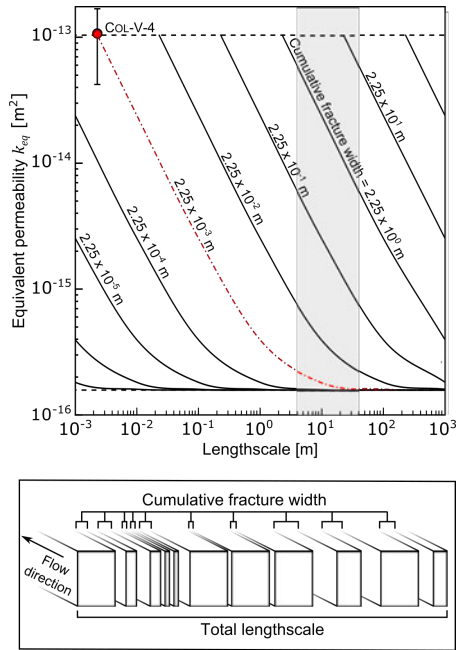


Figure 6.11: The scale-dependence of permeability anisotropy. Equivalent permeability (Equation 6.1) is shown for a fracture or set of fractures within porous magma. As the permeabilities of the fracture and the host material remain constant (defined by the upper and lower dashed lines respectively), equivalent permeability relies on both the considered lengthscale and the cumulative fracture width (i.e. number and width of fractures). Measured value of sample Col-V-4 is shown for reference. Note that  $k_f \geq k_e \geq k_i$ . The shaded area corresponds to the width of a volcanic conduit (see Noguchi et al., 2008); red dashed line describes the influence of a 2.25 mm fracture with the fluid transport properties of that in sample Col-L-4. 1D upscaling model defines flow in parallel cracks, such that the total lengthscale is divided into parallel blocks or plates, shown inset. Refer to text for more discussion.



Figure 6.12: Examples of strain localisation features observed in the Taupō Volcanic Zone (New Zealand). a) Light grey bands (aligned vertically) observed in dense lava. In the background is Mount Ngauruhoe (Orogruin). b) another dense grey block containing tabular light grey bands, much like sample Col-L-1 as discussed in the text. c) Intermediate-porosity block containing lenses of very porous and friable material. The ubiquity of such heterogeneous blocks throughout the Taupō Volcanic Zone, as at Volcán de Colima, suggests that strain localisation mechanisms such as those outlined in this chapter are very common, and as such should be an important consideration when considering evolving volcanic systems.



## SINTERING-DRIVEN EQUIVALENT PERMEABILITY EVOLUTION

---

*It is interesting thus to trace the steps by which a compact granular rock becomes converted into a vesicular, pseudo-porphyritic lava ...*

— Charles Darwin, *Volcanic Islands*, 1844<sup>1</sup>

*The preceding chapters have all discussed the importance of permeability evolution in dictating the explosive style of a volcanic eruption. Indeed, it is generally understood that increasing pore pressure in magma causes overpressures and leads to explosive failure. However, how and when this phenomenon occurs in a given volcanic system remain open questions in volcanology. Chapter 6 presented field evidence for variably-sintered ash-filled fractures, and set the scene for the upscaling of such discrete features to larger scales. Building on this, the following chapter employs a series of numerical models to describe the time-dependent influence of fractures and fracture healing on the permeability of a volcanic system. Importantly, this chapter highlights that different pressurisation behaviours can be expected in different volcanoes as a function of the width and distribution of fractures in the system, the timescales over which they can outgas, and the permeability of the surrounding material. A critical permeability threshold determines whether systems may fracture and outgas efficiently, or if a volcano will be prone to pressure increases, incomplete healing, and explosive failure.*

### 7.1 INTRODUCTION

The ability of a volcanic system to outgas, governed by the permeability of rock and magma, influences eruption explosivity (e.g. Woods and Koyaguchi, 1994). Fractures that form in volcanic environments are often infilled with angular fragments (Figure 7.1; also see Chapter 6) and are expected to play an important role in facilitating outgassing and promoting eruption quiescence (e.g. Tuffen and Dingwell, 2005; Castro et al., 2014; Kendrick et al., 2016; Saubin et al., 2016). However, the lifespan of such fractures is likely transient if the fragments within the fracture can viscously sinter and compact over time (e.g. Wadsworth et al., 2014), thereby reducing the permeability back to the pre-fractured state (Heap et al., 2015b) or lower. Laboratory studies on the permeability of such fractures—often referred to as "tuffisites"—are few (Kolzenburg et al., 2012; Kendrick et al., 2016; also

---

<sup>1</sup> Full title: *Geological Observations on the Volcanic Islands, visited during the Voyage of H.M.S. Beagle*.

[Chapter 6](#)). The paucity of measurements thus impedes the ability to provide estimates for the equivalent permeability of fractured conduit margins and how it may change over time: crucial parameters for models of volcanic outgassing (e.g. Jaupart, 1998; Collinson and Neuberg, 2012).

By coupling permeability reduction timescales of sintering ash-filled fractures from Heap et al. (2015b) with a parallel-layer fluid-flow model, the time-dependent equivalent permeability of a fractured volcanic conduit can be modelled. In this case, the equivalent permeability is that of the edifice rock or magma populated with granular volcanic debris. The constituent model parameters are presented before being applied to two case studies, which form the basis of a discussion on outgassing efficiency and pore-pressure build-up timescales. The model was written in and optimised for MATLAB®, a multi-paradigm numerical computing environment and programming language. The script is appended at the end of this chapter.

## 7.2 GENERAL POROSITY REDUCTION MODEL

Volcanic particles will densify viscously if the temperature  $T$  of the particles remains above the glass transition temperature  $T_g$  (e.g. Wadsworth et al., 2014). Using a semi-empirical compaction model (Russell and Quane, 2005) the time-dependent porosity  $\phi(t)$  can be cast as a simple function of time  $t$ :

$$\phi(t) = \frac{\beta}{\beta - \alpha}; \beta = \ln \left[ \frac{\alpha\sigma}{\eta_0(1 - \phi_i)} t + \exp \left( -\frac{\alpha\phi_i}{1 - \phi_i} \right) \right] \quad (7.1)$$

where  $\eta_0$  is the initial effective viscosity of the melt plus crystal cargo at zero porosity,  $\phi_i$  is the initial porosity, and  $\sigma$  is the overlying lithostatic (or magmastic) stress: the external stress driving compaction. The role of the dimensionless coefficient  $\alpha$  is to scale the dependence of the effective viscosity on  $\phi$  during compaction and therefore encompasses several unconstrained parameters such as the pore size and shape, particle size and shape, and pore and particle size distribution (e.g. Russell and Quane, 2005; Heap et al., 2015b). A constant value of  $\alpha = 2$  is adopted, based on high-temperature (800 - 900 °C) compaction experiments of Heap et al. (2014a). The initial porosity  $\phi_i$  is taken as 0.40 (typical for polydisperse granular materials close to their maximum packing). Lithostatic stress is a function of depth  $z$  such that  $\sigma \propto \rho_b \cdot gz$ , where  $\rho_b$  and  $g$  are the bulk density of the overlying material and acceleration due to gravity, respectively.

The viscosity in [Equation 7.1](#) is a key parameter that can vary orders of magnitude in volcanic liquids or suspensions as a function of temperature, water content, and crystallinity. Herein, two cases are tackled:

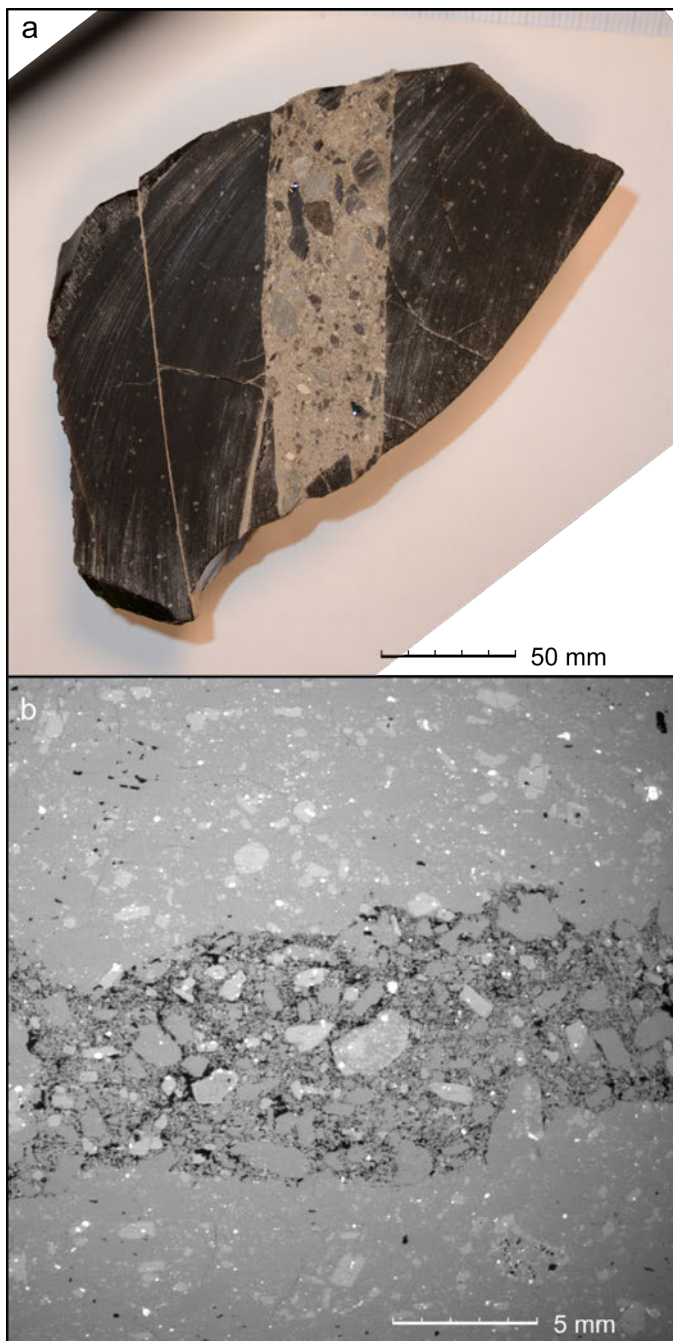


Figure 7.1: Evidence of ash-filled fractures in volcanic environments. a) Sawn block of obsidian containing a large (> 30 mm wide), through-going tuffisite, found at Chaitén volcano, Chile (Castro et al., 2012; 2014; Saubin et al., 2016). b) Scanning Electron Microscope image of fractured andesite collected at Volcán de Colima, Mexico. In both cases, the granular fracture-fill has partially sintered back together into a coherent material, providing snapshots of the healing process.

1. for aphyric magmas where the pure liquid viscosity  $\eta$  replaces  $\eta_0$  in [Equation 7.1](#), and
2. where  $\eta_0$  is the viscosity of a liquid suspending crystals.

Both cases employ the model of Hess and Dingwell (1996) to describe the liquid viscosity:

$$\log_{10}(\eta) = a + \frac{b}{T - c}; \begin{cases} a = a_1 + a_2 \ln(C_{H_2O}) \\ b = b_1 + b_2 \ln(C_{H_2O}) \\ c = c_1 + c_2 \ln(C_{H_2O}) \end{cases} \quad (7.2)$$

for which the temperature  $T$  is in Kelvin and the parameters  $a$ ,  $b$ , and  $c$  depend on the dissolved water content  $C_{H_2O}$  ( $a_1 \dots c_2$  are given in [Table 7.1](#) or in Hess and Dingwell, 1996). In this model,  $10^{12}$  Pa.s is taken as a blunt description of the  $\eta$  at  $T_g$ , and  $\eta$  is cast as a function of the absolute depth of each fracture by assuming a homogeneous upper crustal density (dependent on the case study).

Equilibrium values of  $C_{H_2O}$  are determined using a temperature- and depth-dependent solubility model (Liu et al., 2005):

$$C_{eq} = \frac{s_1 P^{0.5} + s_2 P - s_3 P^{1.5}}{T} + s_4 P^{1.5} \quad (7.3)$$

where  $C_{eq}$  is the equilibrium solubility of  $H_2O$  in rhyolite at temperature  $T$  under pressure  $P$  (coefficients  $s_1 \dots s_4$  are given in [Table 7.1](#) or in Liu et al., 2005).

Assuming the crystals are suspended in the larger volcanic particles such that the viscosity of semi-crystalline particles can be taken as a suspension viscosity, the influence of crystal fraction  $\Phi$  on the initial effective viscosity  $\eta_0$  is given by the model of Mueller et al. (2010) for suspensions of particles in viscous liquids:

$$\eta_0 = \eta \left(1 - \frac{\Phi}{\Phi_m}\right)^{-2} \quad (7.4)$$

where  $\eta$  is the melt viscosity as derived from [Equation 7.2](#) and [7.3](#), and  $\Phi_m$  is the maximum packing of crystals.  $\Phi_m$  is dependent on the shape of the crystals which in turn depends on their aspect ratio  $r_p$ :

$$\Phi_m \approx \Phi_m^* \exp \left[ -\frac{\log_{10} r_p^2}{2\gamma^2} \right] \quad (7.5)$$

where  $\Phi_m^*$  is the maximum packing fraction when  $r_p = 1$  (approximated as 0.656), and  $\gamma$  is an empirical parameter calibrated by Mueller et al. 2010 to be 1.08.

### 7.3 EXTENSION TO A PERMEABILITY REDUCTION MODEL

As described in [Chapter 3](#), porosity and permeability of volcanic materials are often related using one or more power laws (e.g. Klug and Cashman, 1996; Mueller et al., 2005; Kushnir et al., 2016; Wadsworth et al., 2016b). Herein, the two-slope relation of Heap et al. (2015b) is employed, who studied the evolution of permeability at different stages of sintering-driven compaction. The following relationship was found to best describe permeability  $k$  during compaction:

$$k = \begin{cases} A\phi^B & \forall \phi \geq x^* \\ C\phi^D & \forall \phi < x^* \end{cases} \quad (7.6)$$

Experimentally determined values for  $A \dots D$  are given in [Table 7.1](#) or in Heap et al., (2015b). A threshold porosity value  $x^*$  is defined at  $\phi = 0.155$ , whereat the  $k$ - $\phi$  relationship shifts from one power law trend to the other. [Equation 7.6](#) is used in concert with the porosity-reduction timescale ([Equation 7.1](#)) to give a timescale of permeability reduction during sintering-driven compaction of polydisperse materials.

To determine the equivalent permeability  $k_{eq}$  of the considered length of the conduit, a two-dimensional model that considers flow in parallel layers can be used:

$$k_{eq} = \frac{k_0 w_i + \sum_{j=1}^{n_f} (w_{f_j} k_{f_j})}{\ell}; \quad w_i = \ell - \sum_{j=1}^{n_f} w_{f_j} \quad (7.7)$$

where  $k_0$  is the host permeability, and  $\ell$  is the total considered lengthscale (i.e. the length of the conduit, or a fracture "window"). Each fracture has a width  $w_f$  and permeability  $k_f$ , each successive  $w_{f_j} k_{f_j}$  term representing the width and time-dependent permeability of each fracture up to  $n_f$ , the total number of fractures. The intact width  $w_i$  is given by the considered lengthscale minus the sum of all fracture widths.

### 7.4 SCALING PHYSICAL REGIMES

#### 7.4.1 Assessing the calibrated range of the sintering model

[Equation 7.1](#) assumes that the pressure driving compaction is constant across the width of the fracture. To assess this, the compaction length  $\ell_C$  can be calculated, describing the length over which we can expect a significant gradient in porosity to occur during compaction (Kennedy et al., 2016):

$$\ell_C = \sqrt{k_{f_j} \left( \frac{\eta}{v} \right)} \quad (7.8)$$

where  $\nu$  is the pore-fluid viscosity.  $\nu$  is temperature dependent: assuming that the interstitial fluid is air, its viscosity at low pressure across the relevant temperature range (i.e. between around 800 and 1500 K; 526.85 - 1226.85 °C) may be approximated by:

$$\nu \approx \nu_0 \left( \frac{T}{T_0} \right)^{\frac{2}{3}}, \quad (7.9)$$

$\nu_0$  being the viscosity at a reference temperature  $T_0$  (300 K; 26.85 °C). The ratio between fracture width and compaction lengthscale is thus given by  $\delta$ :

$$\delta = \frac{w_{f_J}}{\sqrt{k_{f_J} \left( \frac{\eta}{\nu} \right)}}. \quad (7.10)$$

Compaction can take place if the fracture is sufficiently narrow ( $\delta \ll 1$ ). If  $\delta > 1$ , then gradients of porosity will occur on the scale of the fracture width, meaning that the relatively simple kinetic model of [Equation 7.1](#) would no longer capture the complexities of sintering-driven compaction: in this case the scaling of permeability would be accordingly nontrivial. As such, a first order bound on  $\delta$  of  $10^0$  is imposed in the MATLAB® model, above which [Equation 7.1](#) may not wholly capture the complexities of sintering wide fractures. [Figure 7.2](#) shows  $\delta$  against the ratio of melt viscosity to pore fluid viscosity  $\eta/\nu$  for different fracture widths  $w_{f_J}$ , indicating the regime wherein the model is assumed to be valid. Note that  $\eta/\nu$  is shown rather than either the melt or pore fluid viscosity individually, as the properties exhibit different temperature-dependences ([Equation 7.2](#) and [7.9](#)). It is reliant not only on the fracture width—wider fractures are more likely to exceed the critical width—but also the parameters which affect the viscosities of either the melt or the pore fluid.

#### 7.4.2 A critical permeability threshold for explosive volcanism

As particle-filled fractures compact, it is necessary that the pore fluid phase escapes from the closing pore network. Otherwise, pore pressure will increase within the fracture, inhibiting its healing back to the pre-fracture state. Accordingly, the following section derives a critical compaction time for pore pressure equilibrium. From [Equation 7.1](#), the characteristic compaction timescale may be shown as

$$\lambda_C = \frac{\nu}{\alpha\sigma}. \quad (7.11)$$

From Darcy's law the permeability can be related to the outgassing time  $\lambda_{Da}$ , describing the time it would take an aliquot of fluid to travel

the length of the system and escape under a pressure gradient  $\Delta p$ . In the context of our model, the permeability is that of each fracture  $k_{f_j}$  and the system length corresponds to the vertical distance from the centre of the fracture to its edge.  $\Delta p$  is given by  $\Delta\rho \cdot gz$ , where  $\Delta\rho$  represents the contrast between the bulk density of the granular sintering material and that of the pore fluid which—in concert with gravity and depth—provides the driving force for outgassing. As the pore fluid density can be considered negligible with respect to that of the granular material,  $\Delta\rho$  is equivalent to  $\rho_b$  (making  $\Delta p$  equivalent to  $\sigma$ ):

$$\lambda_{Da} = \frac{v \cdot \left( \frac{w_{f_j}}{2} \right)^2}{k_{f_j} \sigma}. \quad (7.12)$$

Comparing the timescales of compaction (Equation 7.11) and outgassing (Equation 7.12), defines a dimensionless Darcy compaction number  $Da_C$ :

$$Da_C = \frac{\lambda_C}{\lambda_{Da}} = \frac{\eta k_{f_j}}{\alpha v \cdot \left( \frac{w_{f_j}}{2} \right)^2}. \quad (7.13)$$

$Da_C > 1$  implies that the pore pressure can equilibrate during compaction (no pore pressure increase is expected). By contrast, for  $Da_C < 1$ , pore pressure is likely to increase as compaction proceeds. Following this line of reasoning indicates that a critical permeability exists—which will be hereafter termed  $k_{cr}$ —which represents the minimum permeability that will allow pore fluid to migrate and outgas from a fracture:

$$k_{cr} = \frac{\alpha v \cdot \left( \frac{w_{f_j}}{2} \right)^2}{\eta}. \quad (7.14)$$

Significantly, defining this threshold offers a quantitative foundation upon which to base discussion on the propensity for pore pressure to evolve in a given volcanic fracture system. Figure 7.2 plots  $k_{cr}$  against the ratio of melt and pore fluid viscosities, contoured for different fracture widths. If fracture permeability is equal to or less than the critical permeability—for given melt and pore fluid viscosities—interstitial pore pressure is expected to increase, precluding effective sintering of the fracture and pressurising the system, perhaps towards failure. Given the high permeability of a newly generated fracture, the requisite fracture width to allow  $k_{f_j} = k_{cr}$  is impossibly large for relevant viscosities (on the order of hundreds or thousands of m). However, as sintering-driven permeability reduction occurs,

$Da_C$  will tend towards unity and  $k_{f_j}$  will tend towards  $k_{cr}$ . Assuming that the fractured material will always tend to sinter back towards its pre-fracture state, then pore pressure build-up is only precluded in cases where the initial host permeability  $k_0$  is below  $k_{cr}$ .

In concert with knowledge of the typical fracture widths observed in a given system, estimates of pre-eruptive  $\eta_0(T, C_{H_2O}, \Phi)$  and  $v(T)$  can be used to determine the critical permeability threshold for that system. [Figure 7.2](#) shows ranges of  $k_{cr}$  for six different volcanic systems, where the relevant data are available in the literature or can be modelled using the equations above ([Equation 7.2 – 7.5, 7.9](#)).

- For Puyehue–Cordón Caulle (Chile), Schipper et al. (2013) provide estimates of mm- to m-scale fractures in rhyolite, and the attendant rheological data are well constrained by Castro et al. (2013):  

$$\eta_0 = 10^4 - 10^5 \text{ Pa.s.}$$
- For Mount Unzen (Kyūshū, Japan), descriptions of fragment-filled fractures are provided by Goto et al., (2008). Viscosity is determined assuming a pre-eruptive temperature of 900 °C (reasonable for intermediate magmas), a crystal content of ~ 0.15 (Holtz et al., 2005), and an equilibrium water content.
- At the Mule Creek vent (New Mexico, USA), abundant ash-filled fractures were described by Stasiuk et al. (1996). Typical fracture widths range from 10 - 50 mm, and Stasiuk et al. (1996) derive a pre-eruptive temperature range of 700 - 800 °C and water content of between 2.5 and 3.0 wt.% by analysing glass inclusions.
- At Chaitén volcano (Chile), fractures tend to be on average around 1 mm in width. However, preserved specimens such as that in [Figure 7.1a](#) highlight that they may be as wide as 30 mm. A pre-eruptive magma temperature of 825 °C was determined by Castro and Dingwell (2009).
- Berlo et al. (2013) estimate a pre-eruptive temperature of 800 °C and a water content of 0.58 wt.% at Torfajökull (Iceland), and describe volcaniclastic fractures 13 - 15 mm in width.
- Finally, ash-filled fractures have been frequently observed at Volcán de Colima (Mexico), as highlighted in the previous chapter. Kolzenburg et al. (2012), who studied the strength and permeability of tuffisite-bearing andesite, estimating the typical width of such fractures to range between 3 and 50 mm. In a recent study, Kendrick et al. (2016) calculate the relevant viscosity based on a conduit temperature of 940 °C from Reubi et al. (2013) to be in the range  $10^{10.8} - 10^{11.9} \text{ Pa.s.}$

Evidently, different volcanic systems vary greatly in terms of their rheological properties and the typical range of fracture widths observed

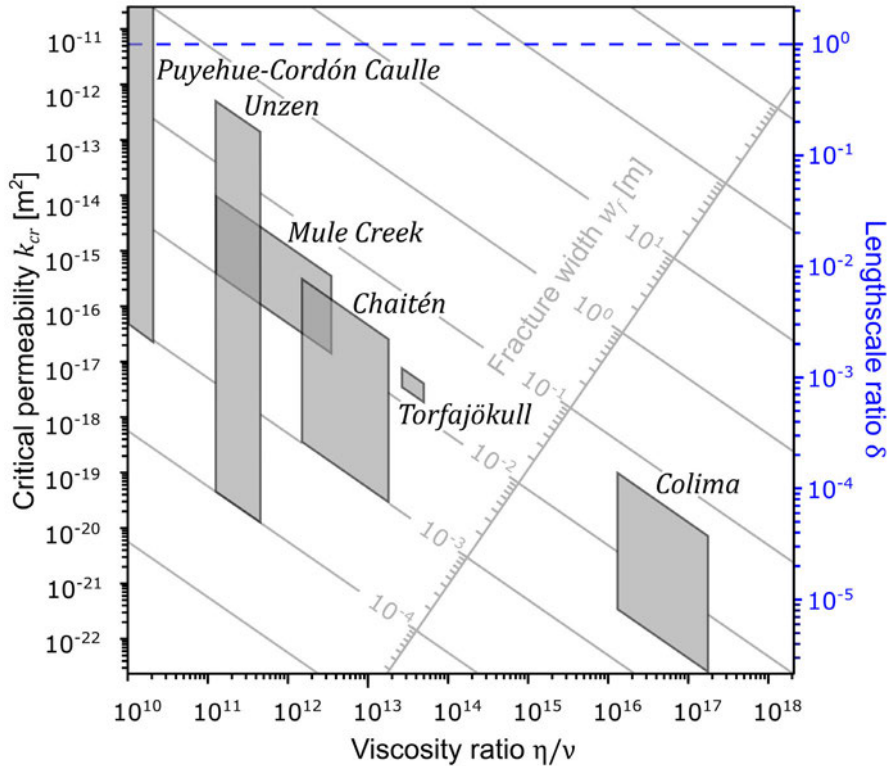


Figure 7.2: Dimensional analysis. The critical permeability  $k_{cr}$  (Equation 7.14) is shown versus the viscosity ratio  $\eta/v$  for different fracture widths  $w_f$ . When a fracture is generated, its permeability will be high. This permeability decreases with time as a consequence of sintering-driven compaction. If, for a given  $w_f$  and a given  $\eta/v$ , the permeability of the fracture  $k_{f_j}$  intersects the critical permeability, then pore pressure will be in disequilibrium. Thus, if the pre-fracture permeability  $k_0$  is lower than the threshold  $k_{cr}$ , pore pressure will increase after a certain degree of compaction. Shaded boxes indicate ranges of  $k_{cr}$  different volcanoes (refer to text). The ratio between the fracture width and compaction lengthscale  $\delta$  (Equation 7.10) shown on the same axes (i.e.  $\eta/v$  for different  $w_f$ ). Dashed line marks the threshold above which the calibrated range of Equation 7.1 is no longer valid.

(Figure 7.2). Consequently, this means that different systems have different propensities for pore pressure augmentation and explosive failure. If  $k_{cr}$  is high (e.g. Puyehue–Cordón Caulle), the likelihood that it exceeds the initial permeability  $k_0$  is also high. Obsidian from Puyehue–Cordón Caulle is often essentially nonporous, meaning that the host permeability  $k_0$  must also be essentially zero (volatiles may only migrate via diffusion), meaning that fracture infill undergoing sintering-driven compaction must achieve the critical threshold  $k_{cr}$  before being able to heal back to the pre-fractured state. Indeed, this tallies with general observations at this system: Schipper et al. (2013) report semi-continuous explosive ash-exhausting events during hybrid explosive-effusive activity at Puyehue–Cordón Caulle between 2011 and 2012. Contrastingly, if the value of  $k_{cr}$  is very low (e.g. Volcán de Colima), there is a strong possibility that the permeability of the host material will be above this threshold. In this case, pore pressure increases are not generally expected. Notably, variably-healed fractures were only observed at Volcán de Colima in dense rocks associated with a low host permeability (Chapter 3, Chapter 6).

Taken together, the ranges of  $k_{cr}$  plotted on Figure 7.2 elucidate which systems are relatively more prone to generating pore overpressures: a key prerequisite for explosive fragmentation. As such, it provides an extremely useful metric by which to categorise the explosive potential of a volcano, based on the physical mechanism of permeability reduction due to fracture healing. (As an additional note, pore pressure is anticipated to increase in the very final stages of compaction, but is thought to be relaxed again by viscous expansion of the isolated pore phase below the percolation threshold: Wadsworth et al., 2016a.) Implications for pressure increase are outlined in the subsequent section.

Table 7.1: Notation used

Symbol	Meaning	Units	Value	Reference
$a$	Limit viscosity at infinite temperature	Pa.s	-	<a href="#">Equation 7.2</a>
$a_1$	Viscosity coefficient	-	3.545	Hess and Dingwell (1996)
$a_2$	Viscosity coefficient	-	0.833	Hess and Dingwell (1996)
$b$	Pseudo-activation energy	J mol <sup>-1</sup>	-	<a href="#">Equation 7.2</a>
$b_1$	Viscosity coefficient	-	9601	Hess and Dingwell (1996)
$b_2$	Viscosity coefficient	-	2368	Hess and Dingwell (1996)
$c$	Vogel-Fulcher-Tamman Temperature	°C; K	-	<a href="#">Equation 7.2</a>
$c_1$	Viscosity coefficient	-	195.7	Hess and Dingwell (1996)
$c_2$	Viscosity coefficient	-	32.25	Hess and Dingwell (1996)
$g$	Acceleration due to gravity	m s <sup>-2</sup>	9.806	
$k$	Permeability	m <sup>2</sup>	-	<a href="#">Equation 7.6</a>
$k_{cr}$	Critical permeability	m <sup>2</sup>	-	<a href="#">Equation 7.14</a>
$k_{f_j}$	Permeability of fracture $j$	m <sup>2</sup>	-	
$k_{eq}$	Equivalent permeability	m <sup>2</sup>	-	<a href="#">Equation 7.7</a>

Table 7.1: Continued

Symbol	Meaning	Units	Value	Reference
$\ell$	Total considered lengthscale	m	-	
$\ell_C$	Compaction lengthscale	m	-	<a href="#">Equation 7.8</a>
$n_f$	Number of fractures	-	-	
$r_p$	Particle aspect ratio	-	1	Mueller et al. (2010)
$s_1$	Solubility law constant	-	354.94	Liu et al. (2005)
$s_2$	Solubility law constant	-	9.623	Liu et al. (2005)
$s_3$	Solubility law constant	-	1.5223	Liu et al. (2005)
$s_4$	Solubility law constant	-	0.00124	Liu et al. (2005)
$t$	Time	s	-	
$w_{f_j}$	Width of fracture $j$	m	-	
$w_i$	Width of intact material	m	-	<a href="#">Equation 7.7</a>
$x^*$	Porosity changepoint	-	0.155	Heap et al. (2015b)
$z$	Depth	m	-	

Table 7.1: Continued

Symbol	Meaning	Units	Value	Reference
$A$	Permeability–porosity prefactor	-	$1.34 \times 10^{-16}$	Heap et al. (2015b)
$B$	Permeability–porosity exponent	-	1.01	Heap et al. (2015b)
$C$	Permeability–porosity prefactor	-	$7.98 \times 10^{-26}$	Heap et al. (2015b)
$D$	Permeability–porosity exponent	-	8.76	Heap et al. (2015b)
$C_{H_2O}$	$H_2O$ content	wt.%	-	<a href="#">Equation 7.3</a>
$C_{eq}$	Equilibrium $H_2O$ content	wt.%	-	<a href="#">Equation 7.3</a>
$Da_C$	Darcy compaction number	-	-	<a href="#">Equation 7.13</a>
$p$	Pressure	MPa	-	
$\Delta p$	Driving pressure gradient	MPa	-	
$T$	Temperature	°C; K	-	
$T_0$	Reference temperature	°C; K	26.85; 300	
$T_g$	Glass transition temperature	°C; K	-	
$\alpha$	Rheological constant	-	2	<a href="#">Equation 7.1</a> ; Russell and Quane (2005)

Table 7.1: Continued

Symbol	Meaning	Units	Value	Reference
$\beta$	Compaction model parameter	-	-	<a href="#">Equation 7.1</a>
$\gamma$	Particle shape parameter	-	1.08	Mueller et al. (2010)
$\delta$	Fracture width ratio	-	-	<a href="#">Equation 7.10</a>
$\eta$	Effective viscosity	Pa.s	-	<a href="#">Equation 7.2</a>
$\eta_0$	Initial viscosity	Pa.s	-	<a href="#">Equation 7.4</a>
$\lambda_C$	Compaction timescale	s	-	<a href="#">Equation 7.11</a>
$\lambda_{Da}$	Darcy outgassing timescale	s	-	<a href="#">Equation 7.12</a>
$\rho_b$	Bulk density	kg m <sup>-3</sup>	-	
$\sigma$	Lithostatic or magmastic stress	MPa	-	
$\nu$	Pore fluid viscosity	Pa.s	-	<a href="#">Equation 7.9</a>
$\nu_0$	Pore fluid viscosity at reference temperature	Pa.s	$1.846 \times 10^{-6}$	
$\phi$	Porosity	-	-	
$\phi_i$	Initial porosity	-	0.40	
$\Phi$	Crystallinity	-	-	

Table 7.1: Continued

Symbol	Meaning	Units	Value	Reference
$\Phi_m$	Maximum packing fraction of crystals	-	-	<a href="#">Equation 7.5</a>
$\Phi_m^*$	Maximum packing when $r_p = 1$	-	0.656	Mueller et al. (2010)

## 7.5 A COMPUTATIONAL TOOL FOR VOLCANOLOGISTS

In [Appendix E](#), a MATLAB® script is presented which combines the series of equations above ([7.1 – 7.12](#)) into a tractable numerical model. The flexible algorithm allows a particular system of interest to be defined in order to predict densification timescales and equivalent permeabilities. Input parameters include a uniform magma temperature, a depth range ("fracture window") of interest, the density and mean width of fractures within the considered depth range, and the crystal cargo of the magma. In actively outgassing fractures, H<sub>2</sub>O content may be below the equilibrium value. As such, the MATLAB® script, includes the option for to use either the equilibrium solubility solution or define a particular  $C_{H_2O}$  value. Given that the precise distribution of fractures within a volcanic system is rarely known, a function is included which randomly positions fractures within the fracture window until the desired fracture density is achieved without overlap. To minimize runtime, the algorithm employs a fixed number of timesteps. Thus, there is a tradeoff between resolution and timescale, which is mitigated by employing a logarithmic time timespan distribution (this means that the first timestep is the smallest, with steps getting progressively larger as the model continues).

### 7.5.1 Case studies: Mount Unzen and Chaitén

A 2004 drilling project recovered cores from the andesitic–dacitic feeder conduit of Mount Unzen, affording an unprecedented description of the subsurface architecture of a polygenetic stratovolcano. Fractures containing variably-sized lithic fragments were observed and quantified radiating laterally from the conduit (Goto et al., 2008). With the fracture density and the mean fracture width (2.2 m<sup>-1</sup> and 0.035 m, respectively) the timescale for which these fractures could provide effective outgassing pathways for magmatic volatiles can be estimated. The generation of these fractures is associated with isolated tremor events, recorded between depths of 500 to 1500 m below the central vent of Mount Unzen and precursing the dome-forming eruptive activity of 1991 - 1995 (Nakada et al., 1999; Goto et al., 2008). Assuming an intermediate initial crystal content ( $\Phi = 0.15$ ; Holtz et al., 2005), a temperature of 900 °C (reasonable for intermediate magmas), a bulk density of 2500 kg m<sup>-3</sup> (Nakada et al., 2005), and an initial host rock permeability of  $2.6 \times 10^{-17}$  m<sup>2</sup> (based on  $\phi = 0.002$  from Nakada et al., 2005), a healing timescale of < 40 min is calculated, with the complete healing of individual fractures taking between 11 and 36 min.

[Figure 7.3a](#) shows that equivalent permeability increases significantly upon fracturing ( $t_0$ ) followed by a sintering-driven permeability reduction. The initial reduction in equivalent permeability is

rapid—over 3 orders of magnitude decrease in under 10 min—after which the rate of permeability reduction diminishes, a function of the two-slope relation of [Equation 7.6](#). After 1 hour, the fractures have entirely healed and the magma has regained its pre-fractured state.

The 2008 eruption of Chaitén volcano (Chile) produced abundant evidence for fractures in which volcanic particles densified either wholly, to be preserved as dense obsidian (Castro et al., 2014), or partially, to be preserved as ash-filled fractures or "tuffisites" (Castro et al., 2012; Saubin et al., 2016; see also [Figure 7.1a](#)). The average pre-eruptive temperature of 825 °C was determined by Castro and Dingwell (2009). Saubin et al. (2016) use microtextures and chemistry of the fracture shown in [Figure 7.1a](#) to show that it was actively transporting gas and ash between 360 and 210 m depth prior to explosive ejection; for our case study we infer a fracture zone from near the surface down to a depth of 500 m.

With a typical fracture width of  $10^{-3}$  m (Berlo et al., 2013), a high fracture density is required in order to be compatible with the results of Castro et al. (2012), who show the requisite fracture spacings requisite to explain measured H<sub>2</sub>O diffusion profiles in a tuffisite-bearing blocks from Chaitén. Results are shown for a fracture density of  $250\text{ m}^{-1}$ , amounting to over  $10^5$  fractures in the shallow conduit with a mean spacing on the order of  $10^{-3}$  m ([Figure 7.3b](#)). In this scenario, the deepest fractures heal in a matter of seconds, while shallow fracture take up to  $\sim 40$  min to heal, with the equivalent permeability of the system dropping accordingly. This is in agreement with the fracture lifespans considered by, among others, Tuffen et al. (2003), Castro et al. (2012), Berlo et al. (2013), and Saubin et al. (2016), who derive timescales ranging from  $\sim 10$  min to 1 day.

Despite exhibiting comparable healing timespans, the model predicts disparate behaviour from the two case study systems—Mount Unzen and Chaitén—arising from different gas evolution mechanisms, with some important distinctions highlighted in [Figure 7.3](#). In [Figure 7.3a](#), a low density of relatively wide fractures transiently increases the equivalent permeability of the system by  $\sim 8$  orders of magnitude. In [Figure 7.3b](#), thin but abundant fractures—representative of a heavily brecciated conduit margin, for example—increases the equivalent permeability of an essentially impermeable host material to almost  $10^{-10}\text{ m}^2$ , constituting extremely effective potential routes for gas and ash escape until the shallowest fractures begin to heal, after which the permeability of the system drops off rapidly, decreasing by  $\sim 8$  orders of magnitude in under 5 min. This rapid permeability shut-off will facilitate pressure increase within densifying magma.

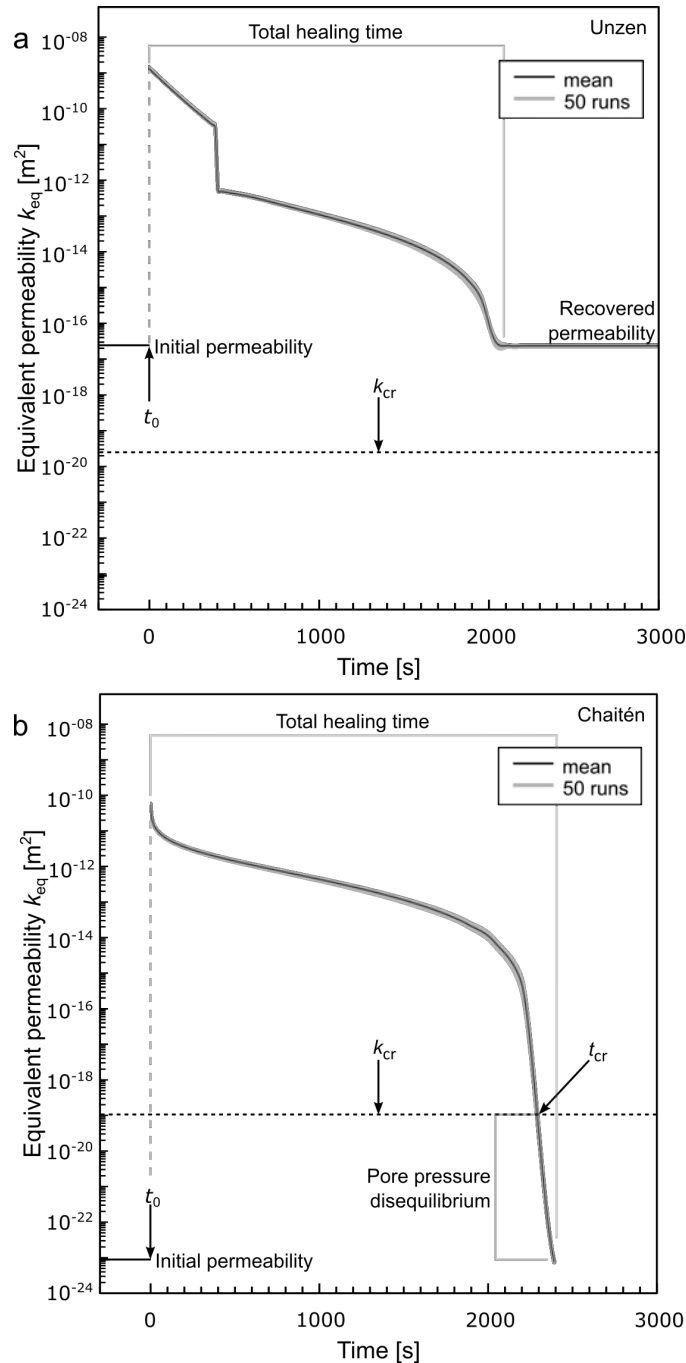


Figure 7.3: Permeability evolution for two case studies. a) Permeability evolution calculated using fracture width data for Mount Unzen (see text for references). Total healing time (the time for  $k_{eq}$  to return to  $k_0$ ) is  $\sim 36$  min. For the given fracture geometry and effective viscosity (refer to text), critical permeability is around  $10^{-20} \text{ m}^2$ , whereas  $k_0$  is greater than  $10^{-17} \text{ m}^2$ . b) Permeability reduction for Chaitén scenario. Total healing time is around 42 min. In this case,  $k_{cr}$  ranges between  $10^{-19}$  and  $10^{-22} \text{ m}^2$ , meaning that this threshold will be achieved before the complete closure of the fracture system ( $t_{cr}$  is less than the total healing time) and overpressure can build.

Pressure build-up is compounded by the evolution of fracture permeabilities relative to the critical permeability. At Mount Unzen ([Figure 7.3a](#)) it is evident that the threshold  $k_{f_j} = k_{cr}$  will not be achieved,  $k_{cr}$  being approximately 3 orders of magnitude lower than the initial permeability. Ultimately, this means that fractures will tend to heal entirely, allowing volatiles to be actively outgassed from magma. In the Chaitén scenario however ([Figure 7.3b](#)), the depth-dependent values of  $k_{cr}$  range from  $1.07 \times 10^{-19}$  to  $8.65 \times 10^{-22} \text{ m}^2$ . During the final stages of sintering, fracture permeabilities in the Chaitén scenario will intersect this value, even when the mean fracture width is very narrow. This will inevitably lead to an increase in pore pressure which may promote additional fracturing—evidence of which has been observed within partially-sintered fractures at Chaitén (Saubin et al. 2016) as well as in other explosive environments (Tuffen et al., 2003)—or may result in more violent explosive failure. Indeed, field and experimental evidence (Saubin et al. 2016) highlights that pressurization can cause tuffisites, nominally effective at venting magmatic volatiles and promoting quiescent behaviour, to be forcibly ejected from depth in Vulcanian explosions.

## 7.6 PERSPECTIVES

A volcano is a capricious mistress, not least due to the potential for rapid and significant evolution of permeability in space and time, as emphasised throughout this thesis. Accounting for permeability variation in the upper conduit and edifice is a fundamental challenge for the development of gas evolution models that more closely reflect nature (e.g. Collombet et al., 2009; Saubin et al., 2016). This chapter outlines a step towards integrating numerical modelling, field observations, and experimental data in a coherent and useful manner. While the relatively simple model presented here cannot fully capture the complexities of outgassing from volcanic conduits, the combination of porosity and permeability reduction timescales with a parallel layer flow model provides a useful a tool with which to estimate the evolution of permeability in volcanic systems over time. With certain caveats, the parallel layer model allows the upscaling of laboratory observations to field-scale, offering information on the expected healing and permeability reduction timescales of zones of fractured magma. Moreover, the determination of a critical permeability threshold—with knowledge of the fracture geometry and the effective viscosity parameters of a given system—affords a diagnostic tool to explain whether or not pore pressures will be prone to increase in a fractured volcanic system, as illustrated in [Figure 7.3](#).

Conceptual work by Neuberg et al. (2006) analysed low-frequency volcanic earthquakes in order to identify a seismogenic fracture zone

at Soufrière Hills Volcano, Montserrat (around 1500 m depth), a critical depth whereat magma fracture is associated with high ascent rates at the conduit wall. As well as scientific drilling and the examination of fracture-bearing ejecta, this method offers a potential avenue by which to incorporate data into models such as that presented here. Similarly, experimental studies of porosity and permeability reduction under volcanically relevant conditions (e.g. Okumura and Sasaki, 2014; Heap et al., 2015b) are fundamental in underpinning the relative evolution of these physical properties during periods of activity and repose. Other promising fields are the combination of permeability evolution models with monitored volumes and timescales of gas emission, which can be used to estimate the bulk system permeability at actively outgassing volcanoes (e.g. Edmonds et al., 2003).

## 7.7 CHAPTER SUMMARY

The efficiency of fracture-assisted outgassing depends on the width and spatial distribution of fractures in a given volcanic system, the timescales over which they are operative, and the permeability of the surrounding material. Significantly, a critical permeability threshold is defined—determined using fracture geometry and effective viscosity parameters—dictating whether or not pore pressure will increase in a given volcanic system.

Literature data pertaining to two case studies, Mount Unzen and Chaitén volcano, show that this model can not only predict timescales over which permeability will evolve, but also—crucially—highlights a fundamental difference in their propensities for pore pressure build-up during fracture-healing cycles. In a permeable system, fractures may provide effective outgassing pathways, which will heal over time until the system retains its original permeability. In a low-permeability system, fractures will similarly yield a highly efficient outgassing mechanism. However, pore pressure will increase as the decreasing fracture permeability intersects the critical permeability (a function of the effective viscosity and the mean fracture width). This means that either a) the system will not achieve its pre-fracture permeability or b) the system will be driven inexorably towards explosive failure. Literature data is used to determine the ranges of this threshold for six silicic volcanoes: Puyehue–Cordón Caulle, Mount Unzen, Mule Creek, Chaitén, Torfajökull, and Volcán de Colima. Notably, the wide span of their critical values reflects the spectrum of eruptive activity observed at these systems.

# 8

## CONCLUSIONS AND PERSPECTIVES

---

*The reticent volcano keeps/ His never slumbering plan;*

*Confided are his projects pink/ To no precarious man.*

— Emily Dickinson, *The reticent volcano keeps*, 1924

### 8.1 CONCLUSIONS

This thesis set out to determine three broad questions:

1. Can the permeability of volcanic edifice material be related to its physical properties, such as porosity?
2. How do porosity and permeability evolve as a consequence of mechanical deformation under volcano-relevant conditions?
3. How do conduit processes influence permeability and permeability anisotropy, and what is the influence of small-scale processes on a volcanic system as a whole?

In this final chapter, these questions shall be addressed in turn as the preceding chapters are summarised.

#### 8.1.1 *Microstructural controls on volcanic rock permeability*

Chapter 3 explored some of the microstructural characteristics controlling volcanic rock permeability. Using the case study of Volcán de Colima, Mexico (regarded as a representative intermediate-composition stratovolcano due to its structural and eruptive traits), Chapter 3 highlighted first of all that the range of porosities and permeabilities of material that makes up the edifice is extraordinarily broad, ranging from essentially nonporous lavas to scoracious ejecta whose volume is composed more of void space than of rock. Correspondingly, permeability was found to vary over seven orders of magnitude across the whole sample set. The analysis of a large, statistically robust dataset allowed the observation of general trends but, just as importantly, emphasised disparities: permeability can vary by as much as four orders of magnitude for any given porosity. Clearly then, the correlation between porosity and permeability of volcanic rocks is complex. Nevertheless, certain tendencies can be gleaned from such a dataset,

augmented by targeted laboratory experiments.

For example, microstructural analysis reveals that low porosity samples are dominated by tortuous microcracks, whereas highly-porous samples contain large interconnected pores. A useful proxy to illustrate this is the ratio of total and unconnected porosity  $\Gamma$ , which—although it does not describe the efficiency of fluid flow through pore networks—highlights a threshold porosity range where the permeability–porosity trend should switch from one regime (partially connected cracks) to another (fully connected cracks and pores). This was borne out by implementing piecewise regression and Bayesian Information Criterion analyses which assume a two-slope power-law relation between permeability and porosity. This model indicates that permeability – porosity data are described by a certain power-law distribution until a particular porosity threshold (changepoint or changezone), whereafter the data are described by a different exponent. This suggests that if porosity is created or destroyed (mechanically or thermo-mechanically) in a natural volcanic system, we need not observe a linear correlation with its permeability.

The field and laboratory data presented in [Chapter 3](#) yielded permeabilities for edifice-forming material ranging from  $10^{-17}$  to  $10^{-11}$  m<sup>2</sup>. Given this range, it is clear that some edifice-forming materials should allow efficient outgassing, whereas others will serve to hinder outgassing. It is important therefore to explore how permeable and impermeable regions of the edifice may evolve in space and time.

### *8.1.2 Exploring the mechanical behaviour of volcanic rock*

Suites of triaxial deformation experiments were carried out on samples of variably porous volcanic rock in order to emulate deformation conditions in a volcanic environment ([Chapter 4](#) and [Chapter 5](#)). In compression, dilatancy (porosity increase) is observed in volcanic rocks with low initial porosities under low effective pressures. Dilatant brittle failure is manifest via macroscopic fault generation as a consequence of the induced growth and coalescence of microcracks. Once a through-running fault is created, dilation may continue with ongoing strain accumulation as the fault planes slide against each other. Despite the generation of fault gouge as fragments from either fracture plane are comminuted and rotated, strain-induced dilatancy almost always led to an increase in sample permeability.

Inelastic compaction (porosity loss) was typically observed when the material had a higher initial permeability or was deformed under a relatively higher effective pressure. The underlying microstructural mechanism driving compaction in these rocks is cataclastic pore

collapse, whereby damage is enhanced concentrically around pores and comminuted fragments of groundmass and crystals subsequently spall into pore space. With increasing strain, this process tends to localise, forming compaction bands oriented sub-perpendicular to the loading direction. Under very high strains, compaction can advance to the point whereat discrete features can no longer be made out; rather, large portions of the sample are completely pulverised. With inelastic compaction, permeability sometimes increases marginally at low strains, with an overarching trend of permeability reduction as strain increases.

By examining the ratio of inelastic porosity change and inelastic strain for deformed samples, it can be seen that all samples tend to approach a threshold where an increase in strain does not yield a change in porosity. Samples at either end of the porosity range studied here ( $\simeq 0.05$  to  $0.22$ ) require a significant amount of strain in order to achieve this limit ( $> 0.10$ , i.e. more than a 10% reduction in sample length). However, samples at intermediate porosities ( $0.10 \leq \phi \leq 0.16$ ) were found to be close to this threshold. Consequently, with increased strain these samples undergo little porosity change: irrespective of the mode of failure (which is strongly dependent on the effective pressure) large changes in permeability can be observed as fault structures or compaction bands increase in size and complexity, but porosity evolution tends to be negligible.

Complex deformation behaviours are also notable at intermediate porosities, including transitions from compactant to dilatant behaviour (a threshold known as  $C^{*I}$ ), or from dilatant to compactant (described here for the first time and termed  $C^{*II}$ ). Significantly, this highlights that the transition from dilatant to compactant behaviour is not only dictated by the initial physical properties of a rock—most importantly, its porosity—and the effective pressure (or depth) at which it is deformed, but can also be a phenomenon governed by the degree of post-failure strain to which the rock is subjected, which may be an important consideration in high-strain volcanic environments.

In Chapter 5, another mechanism of inducing dilatancy was explored, namely embrittlement as a consequence of pore pressure change. Through this process, the effective pressure acting on a rock was altered by increasing or oscillating the pore pressure rather than the confining pressure. Indeed, whilst constant pore pressure tests are important for determining, amongst other things, the failure envelope of a given volcanic rock—elucidating the stress conditions under which the rock will deform elastically or inelastically when subject to an applied stress—experiments which adjust the pore pressure may more accurately reflect active processes arising due to fluid migration

in the edifice.

The primary findings of [Chapter 5](#) are that brittle failure can be induced in otherwise intact rock by increasing the pore pressure, and that cumulative damage due to the oscillation of pore pressure can cause failure under stress conditions far below the short-term strength of the rock, once a threshold amount of damage is accrued. Furthermore, this process can lead to dilatant macroscopic fracture generation in volcanic rock that is undergoing inelastic compaction as a function of the incumbent effective pressure and an applied axial stress. Thus, brittle mechanisms may be at play even in regions of the edifice where the confining pressure would otherwise tend to preclude dilatancy.

#### *8.1.3 Permeability anisotropy: not all outgassing routes are created equal*

Heterogeneities in effusively and explosively erupted volcanic rocks are common, and provide post mortem evidence of magmatic processes. [Chapter 6](#) comprised a forensic assessment of the microstructure and fluid flow properties of a suite of discontinuity-bearing andesites in order to glean evidence of their origins and effects on magma and rock permeability.

In two high-porosity (pumiceous) blocks, bands of low porosity were inferred to be a relic of arrested bubble expansion. Although these features significantly influenced the overall porosity of either block, permeability—which in this case was already high—was largely unaffected. However, in low-porosity materials, strain localisation features such as shear fractures were observed to vastly increase sample permeability relative to the unfractured host, in spite of various degrees of sintering-driven fracture healing.

Differences sintering progression, as well as the presence of silica polymorphs in some of the samples, indicate that these heterogeneities originated at different depths in the conduit, suggesting that these features may exist along the length of the conduit, or at least a significant portion of it.

Notably, other textures were interpreted as a network of pores infilled by transiently granular material. This suggests that a formerly permeable network of pores and cracks eventually transitioned into a low-porosity and low-permeability route. As such, porous networks in rock and magma may subsequently form barriers to fluid flow in a volcanic system over time. This emphasises an intricate interplay between dilatant processes and their porosity-decreasing counterparts. Further textures were interpreted to result from shear strain-

induced flow banding and cavitation.

Given the large (orders of magnitude) differences in permeability that can arise due to strain localisation, localised permeability anisotropy must be a critical parameter controlling the evolution of pore pressures within active volcanoes. Chapter 6 employed a relatively simple upscaling model to illustrate the significance of even very small discontinuities over different lengthscales. It is probable that such features will influence the eruptive regime and recurrence intervals of explosive behaviour at active silicic volcanoes. Indeed, it is generally understood that there is an important interrelation between permeability, outgassing, pore pressure augmentation and explosive failure: can we then delve deeper in order to reveal some of the underlying mechanisms and timescales involved?

#### *8.1.4 Permeability, outgassing, pore pressure and explosive fragmentation*

Previous authors (Russell and Quane, 2005; Hess and Dingwell, 1996; Liu et al., 2005; Mueller et al., 2010; Heap et al., 2015b) present empirical or semi-empirical models that can each be applied to some facet of sintering-driven compaction (and the attendant decrease in permeability) in volcanic environments, a common process interpreted from the microstructural evidence of Chapter 7. By integrating these models with a parallel-layer flow model, Chapter 7 outlined the construction of a multi-step algorithm which computes the time-dependent permeability reduction of a fractured volcanic conduit margin. Testing this algorithm (FRACkR) on two case studies (Mount Unzen and Chaitén volcanoes) highlights that fractures in volcanic systems can provide highly efficient pathways for fluid flow, and can hence enhance outgassing. However, healing timescales tend to be short, especially at high temperatures (low effective viscosity) or at great depths.

Due to this transience, it is critical that interstitial pore fluid in these fractures is able to escape during compaction. A critical permeability threshold has been derived here for the first time, which delineates the point at which pore fluid within healing fractures is no longer in equilibrium (i.e. it can no longer outgas passively). Comparing this threshold (a function of fracture width and the effective viscosity parameters) with the initial host permeability (i.e. the pre-fracture state towards which the system should recover) tells us whether a given system is prone to pore pressure increases—a key precursor to explosive fragmentation—or whether fracture-healing cycles can serve to effectively bleed off pressure and promote effusive or quiescent behaviour. In the two case study scenarios, contrasting gas evolution regimes are predicted: in the Mount Unzen case, no pore pressure increase should occur, whereas at Chaitén the host rock permeab-

ility lies below the critical threshold and the fracture system is anticipated to pressurise towards failure.

From literature data, critical permeability ranges were determined for six volcanic systems: Puyehue–Cordón Caulle, Mule Creek, Torfajökull, and Volcán de Colima, as well as the two mentioned previously. For Volcán de Colima, where there exists a multitude of permeability data (as shown in [Chapter 3](#), [Chapter 6](#)), it can be observed that the majority of host rock material lies above the derived critical permeability threshold range (i.e. host rock permeabilities between  $10^{-17}$  to  $10^{-11} \text{ m}^2$  compared to a critical permeability range around  $10^{-19}$  –  $10^{-23} \text{ m}^2$ ). On the other hand at Puyehue–Cordón Caulle, dense obsidian has zero permeability (Schipper et al., 2013), which is evidently lower than any finite range of critical permeabilities (*a minima*, this value is of the order  $10^{-17} \text{ m}^2$  for fractures described in this system). Thus, this analysis yields a valuable new metric by which to catalogue and compare the explosive potential of different volcanic systems.

## 8.2 PERSPECTIVES

### 8.2.1 Towards a universal model of permeability and porosity

Recent work has significantly advanced the understanding of  $k = f(\phi)$  trends in sintering volcanic materials and sedimentary diagenesis, whereby granular material densifies to become a coherent rock mass. Wadsworth et al. (2016) show that a universal trend can be extracted when the governing microstructural evolution is understood and quantified.

For volcanic rocks wherein the porosity is formed through vesiculation and fracturing of an initial nonporous magma (as with the majority of materials discussed in this thesis), the scaling model of Wadsworth et al. (2016) does not capture the underlying micromechanics determining  $k = f(\phi)$ . Nevertheless, the two-slope regression analysis implemented in [Chapter 3](#) highlights a microstructural change, where volcanic rock permeability presumably transitions from being governed by cracks which are only partially interconnected to a fully connected network of pores and cracks. As such, a promising avenue for determining a universal cross-compositional scaling law for permeability and porosity in volcanic rocks may rest on the incorporation of connectivity ( $\Gamma$ ) defined in this thesis, as well as the ratio of porosity comprising cracks or pores ( $\phi_{\text{cracks}}/\phi_{\text{pores}}$ ) as a function of the overall connected porosity  $\phi$ . Such a model would greatly enhance the prediction of fluid migration during volcanic outgassing,

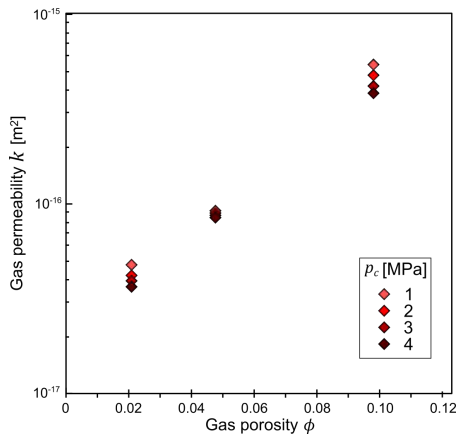


Figure 8.1: Permeability – porosity data for three Ruapehu andesites of varying porosity, measured under four different confining pressures ( $p_c$ ). Permeability can vary by a factor of two depending on small changes in the confining pressure under which the measurement was made.

as well as having numerous ancillary implications and applications.

Such a model may be assisted by compiling and assessing published laboratory data. Permeability is often measured under different experimental conditions at different institutions and in the field; often, different confining pressures are employed between  $\sim 1$  and 5 MPa. As evidenced by previous researchers (e.g. Vinciguerra et al., 2005; Fortin et al., 2011; Faoro et al., 2013), effective pressure can have a notable influence on measured permeability. As shown in Figure 8.1, even relatively small differences in confining pressure during measurement can result in disparity between measured values of permeability on the same sample. Notably, for these samples (Ruapehu andesites of different porosities), the effect of confining pressure does not simply scale with connected porosity; again, this may prove to be a function of the ratio of cracks and pores.

Models that scale permeability with porosity often include a percolation threshold, which indicates a porosity below which there can be no interconnected pores and thus no permeable flow. These models are based on a system of overlapping spheres (e.g. Blower, 2001; Mueller et al., 2005), reflecting the growth and coalescence of bubbles in magma. However, in variably fractured porous rock, the physical meaning of a percolation threshold is less clear. Especially in cases where fluid flow is observed below this theoretical threshold (sometimes predicted to be as high as  $\sim 0.70$ : Gaonac'h et al., 2003), it is likely that the percolation threshold corresponds to the development of a fully interconnected crack network, and that the evolution of permeability is thereafter dependent on the ratio between crack porosity and pore porosity as well as the total void space available

for fluid transport. In the near future, improved methods of fracture density calculation (e.g. through microscopic image analysis) could greatly assist the quantification of this ratio. Moreover, the advent of non-destructive three-dimensional imaging with high-resolution X-ray computed tomography (e.g. Ketcham and Carlson, 2001; Mees et al., 2003; Benson et al., 2007) means that pore and crack networks may be characterised pre-, intra-, and post-deformation, which is key for deriving porosity evolution models in highly heterogeneous volcanic materials.

### 8.2.2 *Other mechanisms of permeability evolution*

[Chapter 7](#) defines the critical permeability threshold that dictates the increase or release of pressure during sintering-driven fracture healing, a common and important process in active volcanic environments. Interestingly, there are other time-dependent permeability reduction mechanisms which could be examined in a similar fashion: for example, the precipitation of hydrothermal minerals (e.g. Edmonds et al., 2003; Ball et al., 2015). Mineral precipitation is expected to clog up permeable networks at rates which are similarly defined by temperature and pressure, as well as the through-flow of magmatic fluids, and experimental affirmation of this may be a fruitful avenue of further research.

Thermal cracking and expansion of edifice rock may well prove to be another mechanism by which permeability can evolve in space and time. Indeed, thermally-induced permeability change is an area of active research: it remains to be seen how the relative contributions of different thermo-mechanical processes compare against each other.

### 8.2.3 *Integrating experimental rock deformation with other data*

Finally, anisotropy at the edifice scale ([Chapter 3](#)) down to the intra-clast scale as a function of low- or high-temperature mechanisms ([Chapter 4 – 6](#)) which, in concert with time-dependent permeability evolution ([Chapter 7](#)), will be reflected in different geochemical and geophysical signals.

As such, in several of these chapters, inferences from experimental data have been extrapolated to larger-scale processes in nature. For example, spatial differences in edifice density determined through gravimetric inversion and other geophysical methods have been related to fracture and compaction observed under different experimental conditions. Further, field measurements of thermal emissions ([Chapter 5](#); also, Spampinato et al., 2011 among others) or gas fluxes monitored at active volcanoes (e.g. Hirabayashi et al., 1995; Delgado-

Granados et al., 2001; Edmonds et al., 2003) have been attributed herein to evolving permeability of the upper plumbing system and edifice.

However, we may go a step further. Numerous sub-disciplines of volcanology and related sciences examine the evolution of the gas fraction in volcanic systems, either directly or indirectly. This thesis has explored many stages of the journey of magmatic volatiles from magma to the edifice and from the edifice to the atmosphere. These results may be complemented by petrological studies of phase equilibria and analysis of melt inclusions or by remotely sensed data on gas species ratios and discharge rate of venting gases, as well as studies of ground deformation and volcano seismology which detect fluid migration and strain changes in volcanic environments. Thus, studies of fluid flow through volcanic environments may be neatly bookended on the one hand by analyses that inform on the volume of dissolved volatiles in the melt and the potential volume of a separated gas fraction, and on the other hand by measurements of the volume and rate at which this gas eventually leaves the system.

An exciting area of research is the cohesive integration of these and other methods: field studies, controlled laboratory experiments and sample characterisation, microstructural observations, remotely-sensed data, and volcano seismology, to name a few. In turn, combined field/ laboratory/ numerical studies can serve to inform a new generation of predictive physical models of volcanic activity, with the ultimate goal of reducing volcanic risk worldwide.



Figure 8.2: Outgassing through a fissure at Cerro Evermann on Isla Socorro (Revillagigedo archipelago, Mexico)

Part II  
APPENDICES



# A

## APPENDIX TO CHAPTER 2: INERTIAL EFFECTS

---

Figure A.1 shows flowrate and pressure data obtained during steady-state permeability measurements on three volcanic samples. For the first example, Figure A.1a - c, flow is laminar, as evident from the linear relation between the volumetric flowrate ( $Q_v$ ) and the driving pressure ( $\nabla p\bar{p}$ ). Accordingly, the reciprocal permeability ( $k_{gas}^{-1}$ ) versus  $Q_v$  is negative and nonlinear, as is the measured permeability  $k_{gas}$  against the reciprocal mean pressure  $\bar{p}^{-1}$ . In the second example, flow is turbulent, and the data in Figure A.1d are nonlinear. Applying the correction derived from Figure A.1e (Equation 2.5) yields Figure A.1f, where the data are randomly distributed about the mean (no Klinkenberg correction is necessary). Finally, the data shown in Figure A.1g - h highlight that a Klinkenberg correction is necessary (Equation 2.6). However, the correction is very slight, as indeed often tends to be the case in volcanic rocks (as opposed to "tight" materials such as granite).

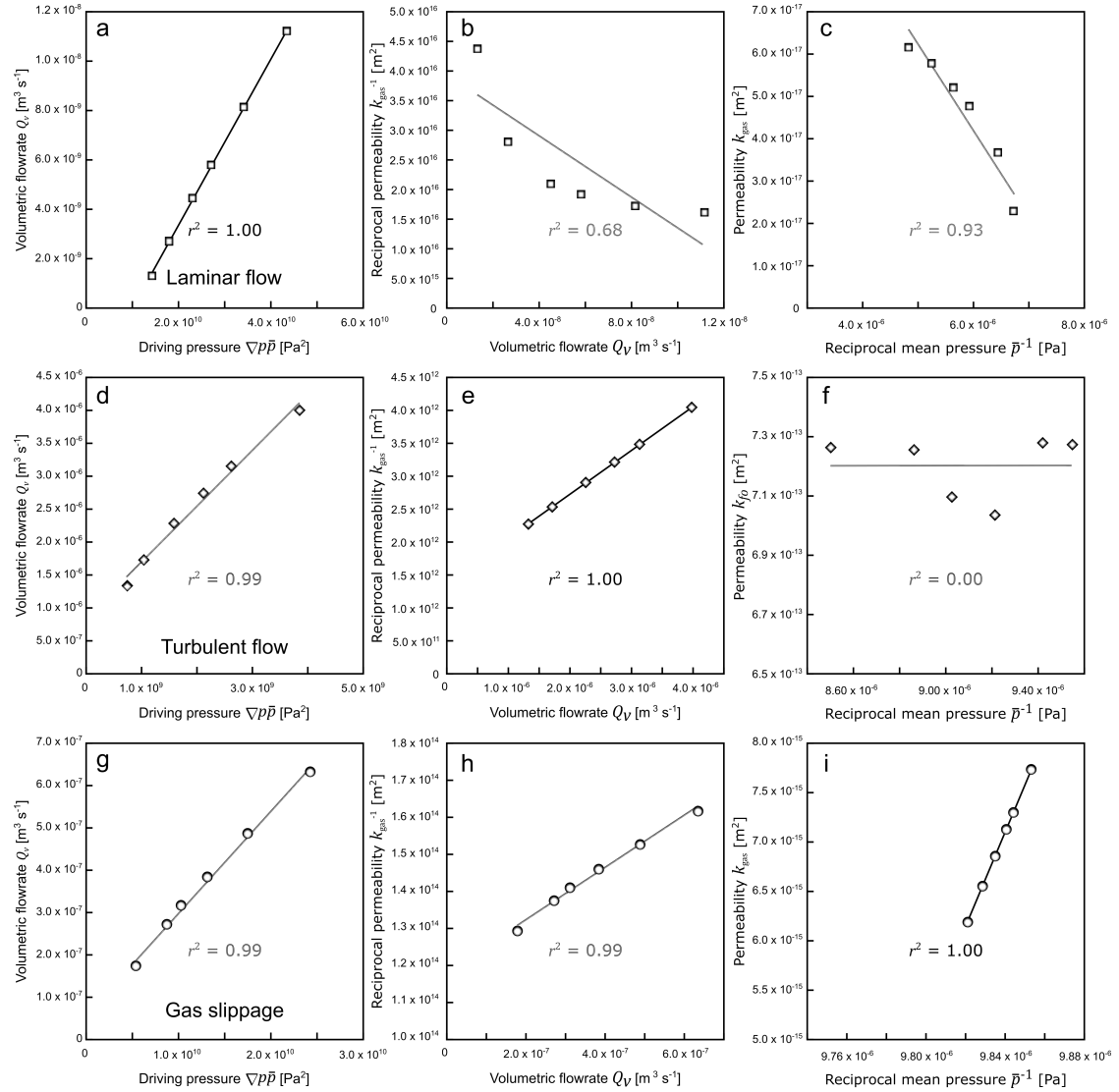


Figure A.1: Data obtained during permeability measurements on three rocks. a) - c) Laminar flow in a sample from Whakaari, New Zealand. d) - f) Turbulent flow, in a sample of Ruapehu andesite. g) - i) A small gas slippage effect in a sample of Açores trachy-andesite.

# B

## APPENDIX TO CHAPTER 3: TINYPERM II: AN ASSESSMENT

---

The field permeameter used in this study was the TinyPerm II, developed by New England Research, Inc. and Vindum Engineering, Inc. The unit comprises a nozzle and chamber attached to a volume syringe with a plunger. An absolute air pressure transducer is housed near the nozzle, and a volume transducer situated within the syringe. To use the permeameter, the nozzle is pressed against a rock surface, then the plunger is depressed, evacuating air from the sample. The sample at ambient pressure is thus subjected to a pressure profile as air is drawn from the rock; this pressure differential returns to ambient after some time interval, dependent on the permeability of the rock. A microcontroller unit is records the absolute pressure at the nozzle–rock interface, as well as monitoring the internal syringe volume and computing the response function of the pressure transient. The underlying semi-empirical theory is described fully in Brown and Smith (2013). Note that this permeameter uses atmospheric air as a permeant, rather than a truly inert fluid as would be used in laboratory measurements. However, as the samples are unconfined, any related effect is probably negligible.

The resultant value, here called  $\dot{k}$ , is displayed onscreen, and corresponds to Darcian permeability such that  $\dot{k} = (-0.8206 \log_{10}(k) + 12.8737)$ . In order to convert  $\dot{k}$  into SI units, this is rearranged such that

$$k = \frac{10^{((\dot{k}-12.8737)/-0.8206)}}{9.869233 \times 10^{10}} \quad (\text{B.1})$$

in  $\text{m}^2$ .

To test the accuracy and repeatability of the field permeameter, a suite of permeability measurements was performed on sedimentary samples for comparison with laboratory-derived permeability measurements. Blocks of eight sedimentary rocks were cored and a cylindrical sample obtained, nominally 40 mm long and 20 mm in diameter. Gas permeability was measured on these cores using the benchtop steady-state gas permeameter described in the main body of the text. TinyPerm measurements were then performed on each of the blocks, parallel to the coring direction. Each block was measured at five or more points, with ten measurements performed at each point.

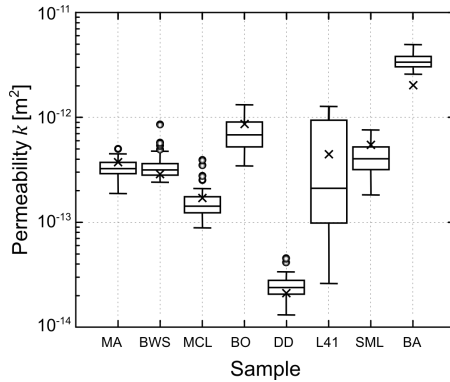


Figure B.1: Box-and-whisker distribution of TinyPerm permeability measurements. Central horizontal line of each box represents the mean measured value. Outliers are shown as circles. Crosses show the results of benchtop steady-state measurements for each sample. The measured rocks were Bentheim Main (MA) and Basis (BA) sandstone, Bleurswiller sandstone (BWS), Monti Climiti limestone (MCL), Boise sandstone (BO), Darley Dale sandstone (DD), Leithakalk calcarenite (L41), and Saint Maximin limestone (SML).

The measured rocks are Bentheim Main (MA) and Basis (BA) sandstone, Bleurswiller sandstone (BWS), Monti Climiti limestone (MCL), Boise sandstone (BO), Darley Dale sandstone (DD), Leithakalk calcarenite (L41), and Saint Maximin limestone (SML); physical properties are given in [Table B.1](#). These materials were chosen for this assessment as they exhibit notable homogeneity in their microstructure and pore size distribution; we can thus be confident that a core sample derived from one of these blocks will represent the physical properties of the block as a whole. Notably, the steady-state method yielded results that were consistently within one standard deviation of the mean TinyPerm value. [Figure B.1](#) compares the steady-state permeability measured on cored cylinders with the range of values determined with the TinyPerm unit.

When obtaining cores from volcanic rocks that are highly heterogeneous in their pore size distribution, the measured porosity (and by extension, permeability) can differ from the bulk clast values, as shown in [Figure B.2](#). Notably, despite these differences, the overall permeability–porosity trend, as discussed in the text, remains the same.

Repeatability of results from the TinyPerm unit was found to be high, measurements on the same point (i.e. A, B, C, D, E) always being within one order of magnitude, and generally less than 20 % either side of mean. Data are given in [Table B.2](#).

Table B.1: Laboratory physical property data (porosity and permeability) for cores of selected sedimentary rocks, alongside TinyPerm results from blocks.  $\phi$  = connected gas porosity;  $k$  = (laboratory) gas permeability;  $\dot{k}$  = TinyPerm permeability;  $SD$  = standard deviation of TinyPerm measurements.

Sample	$\phi$	$k$ [m <sup>2</sup> ]	$\dot{k}$ [m <sup>2</sup> ]	$SD$
MA	0.23	$3.72 \times 10^{-13}$	$3.34 \times 10^{-13}$	$6.65 \times 10^{-14}$
BWS	0.26	$2.85 \times 10^{-13}$	$3.47 \times 10^{-13}$	$1.09 \times 10^{-13}$
MCL	0.29	$1.70 \times 10^{-13}$	$1.58 \times 10^{-13}$	$5.94 \times 10^{-14}$
BO	0.26	$8.65 \times 10^{-13}$	$7.26 \times 10^{-13}$	$2.5 \times 10^{-13}$
DD	0.17	$2.11 \times 10^{-14}$	$2.49 \times 10^{-14}$	$6.78 \times 10^{-15}$
L41	0.24	$4.47 \times 10^{-13}$	$5.01 \times 10^{-13}$	$4.71 \times 10^{-13}$
SML	0.38	$5.50 \times 10^{-13}$	$4.26 \times 10^{-13}$	$1.49 \times 10^{-13}$
BA	0.24	$4.09 \times 10^{-13}$	$3.45 \times 10^{-12}$	$6.02 \times 10^{-13}$

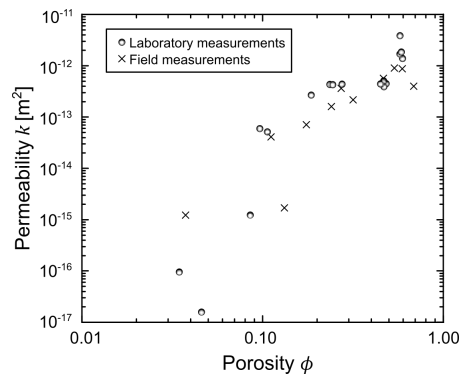


Figure B.2: Comparison of field based whole-clast permeability–porosity measurements and laboratory core measurements).

Two main issues were identified when using the TinyPerm to measure volcanic rock samples. Firstly, obtaining accurate and precise measurements depends on creating an airtight contact between the permeameter nozzle and the sample surface. If the rock surface is non-ideal, then leakage of air into the permeameter chamber can result in over an order of magnitude error in measurements. To preclude this a malleable putty is secured to the end of the nozzle (as suggested by the manufacturer) to seal the nozzle to the sample. With sufficient pressure against the sample, use of the putty seal was effective in preventing the premature decay of the pressure gradient. Secondly, there exists a limit to the maximum  $k$  value observable on the micro-controller ( $\sim 13$ ), corresponding to a  $k$  of  $\sim 6.92 \times 10^{-16} \text{ m}^2$ . Any and all samples with a permeability below this threshold are thus indistinguishable; accordingly, a  $k$  value of 12.99 has been implemented as the limit in this study.

Table B.2: Full table of (transformed) results from permeability measurements on sedimentary blocks. A, B, C, D, and E represent five randomly selected points on the surface of each block, whereat ten repeat measurements were made. MA = Bentheim Main sandstone; BA = Basis sandstone; BWS = Bleurswiller sandstone; MCL = Monte Climiti limestone; BO = Boise sandstone; DD = Darley Dale sandstone; L<sub>41</sub> = Leithakalk calcarenite; SML = Saint Maximin limestone.

Measurement	Rock type							
	MCL	DD	SML	L <sub>41</sub>	MA	BA	BWS	BO
A1	$1.05 \times 10^{-13}$	$4.53 \times 10^{-14}$	$4.04 \times 10^{-13}$	$7.72 \times 10^{-14}$	$2.58 \times 10^{-13}$	$3.71 \times 10^{-12}$	$3.14 \times 10^{-13}$	$6.89 \times 10^{-13}$
A2	$1.35 \times 10^{-13}$	$4.16 \times 10^{-14}$	$3.93 \times 10^{-13}$	$1.84 \times 10^{-13}$	$4.28 \times 10^{-13}$	$3.82 \times 10^{-12}$	$3.14 \times 10^{-13}$	$7.71 \times 10^{-13}$
A3	$1.32 \times 10^{-13}$	$3.33 \times 10^{-14}$	$5.20 \times 10^{-13}$	$2.06 \times 10^{-13}$	$3.05 \times 10^{-13}$	$3.92 \times 10^{-12}$	$2.73 \times 10^{-13}$	$7.71 \times 10^{-13}$
A4	$1.18 \times 10^{-13}$	$2.81 \times 10^{-14}$	$2.81 \times 10^{-13}$	$1.47 \times 10^{-13}$	$3.14 \times 10^{-13}$	$3.82 \times 10^{-12}$	$2.73 \times 10^{-13}$	$8.38 \times 10^{-13}$
A5	$1.43 \times 10^{-13}$	$3.06 \times 10^{-14}$	$4.16 \times 10^{-13}$	$2.81 \times 10^{-13}$	$2.73 \times 10^{-13}$	$4.27 \times 10^{-12}$	$2.81 \times 10^{-13}$	$8.87 \times 10^{-13}$
A6	$1.24 \times 10^{-13}$	$2.44 \times 10^{-14}$	$4.04 \times 10^{-13}$	$2.97 \times 10^{-13}$	$3.61 \times 10^{-13}$	$2.58 \times 10^{-12}$	$2.89 \times 10^{-13}$	$9.12 \times 10^{-13}$
A7	$1.32 \times 10^{-13}$	$3.06 \times 10^{-14}$	$3.32 \times 10^{-13}$	$2.81 \times 10^{-13}$	$3.23 \times 10^{-13}$	$2.65 \times 10^{-12}$	$2.65 \times 10^{-13}$	$5.99 \times 10^{-13}$
A8	$1.32 \times 10^{-13}$	$2.89 \times 10^{-14}$	$4.52 \times 10^{-13}$	$1.90 \times 10^{-13}$	$3.82 \times 10^{-13}$	$2.96 \times 10^{-12}$	$2.44 \times 10^{-13}$	$5.50 \times 10^{-13}$
A9	$1.65 \times 10^{-13}$	$2.58 \times 10^{-14}$	$3.93 \times 10^{-13}$	$2.51 \times 10^{-13}$	$4.04 \times 10^{-13}$	$2.88 \times 10^{-12}$	$2.81 \times 10^{-13}$	$7.09 \times 10^{-13}$
A10	$2.51 \times 10^{-13}$	$4.53 \times 10^{-14}$	$4.52 \times 10^{-13}$	$2.18 \times 10^{-13}$	$3.93 \times 10^{-13}$	$2.96 \times 10^{-12}$	$3.14 \times 10^{-13}$	$6.33 \times 10^{-13}$
B1	$1.24 \times 10^{-13}$	$2.06 \times 10^{-14}$	$3.82 \times 10^{-13}$	$2.58 \times 10^{-14}$	$2.89 \times 10^{-13}$	$4.91 \times 10^{-12}$	$3.14 \times 10^{-13}$	$7.49 \times 10^{-13}$

Table B.2: Continued

Measurement	Rock type							
	MCL	DD	SML	L41	MA	BA	BWS	BO
B2	$3.93 \times 10^{-13}$	$1.47 \times 10^{-14}$	$4.52 \times 10^{-13}$	$4.28 \times 10^{-14}$	$2.89 \times 10^{-13}$	$4.04 \times 10^{-12}$	$2.97 \times 10^{-13}$	$6.70 \times 10^{-13}$
B3	$1.43 \times 10^{-13}$	$1.90 \times 10^{-14}$	$5.20 \times 10^{-13}$	$3.15 \times 10^{-14}$	$3.72 \times 10^{-13}$	$4.51 \times 10^{-12}$	$2.89 \times 10^{-13}$	$8.87 \times 10^{-13}$
B4	$2.06 \times 10^{-13}$	$2.44 \times 10^{-14}$	$3.05 \times 10^{-13}$	$5.21 \times 10^{-14}$	$3.14 \times 10^{-13}$	$4.51 \times 10^{-12}$	$2.81 \times 10^{-13}$	$9.38 \times 10^{-13}$
B5	$1.79 \times 10^{-13}$	$2.18 \times 10^{-14}$	$3.32 \times 10^{-13}$	$5.83 \times 10^{-14}$	$3.32 \times 10^{-13}$	$4.78 \times 10^{-12}$	$2.73 \times 10^{-13}$	$6.89 \times 10^{-13}$
B6	$1.60 \times 10^{-13}$	$2.25 \times 10^{-14}$	$3.72 \times 10^{-13}$	$1.95 \times 10^{-13}$	$2.89 \times 10^{-13}$	$3.82 \times 10^{-12}$	$2.37 \times 10^{-13}$	$7.71 \times 10^{-13}$
B7	$1.95 \times 10^{-13}$	$1.95 \times 10^{-14}$	$3.14 \times 10^{-13}$	$8.88 \times 10^{-14}$	$3.05 \times 10^{-13}$	$3.82 \times 10^{-12}$	$2.73 \times 10^{-13}$	$7.09 \times 10^{-13}$
B8	$1.90 \times 10^{-13}$	$1.90 \times 10^{-14}$	$3.23 \times 10^{-13}$	$5.67 \times 10^{-14}$	$3.23 \times 10^{-13}$	$3.92 \times 10^{-12}$	$2.81 \times 10^{-13}$	$8.62 \times 10^{-13}$
B9	$1.79 \times 10^{-13}$	$1.90 \times 10^{-14}$	$3.42 \times 10^{-13}$	$5.21 \times 10^{-14}$	$3.05 \times 10^{-13}$	$4.04 \times 10^{-12}$	$2.65 \times 10^{-13}$	$9.38 \times 10^{-13}$
B10	$1.74 \times 10^{-13}$	$1.85 \times 10^{-14}$	$3.93 \times 10^{-13}$	$5.67 \times 10^{-14}$	$2.97 \times 10^{-13}$	$4.78 \times 10^{-12}$	$2.89 \times 10^{-13}$	$8.38 \times 10^{-13}$
C1	$1.05 \times 10^{-13}$	$1.32 \times 10^{-14}$	$2.31 \times 10^{-13}$	$1.11 \times 10^{-12}$	$2.97 \times 10^{-13}$	$3.71 \times 10^{-12}$	$3.32 \times 10^{-13}$	$3.93 \times 10^{-13}$
C2	$1.74 \times 10^{-13}$	$1.70 \times 10^{-14}$	$3.05 \times 10^{-13}$	$1.28 \times 10^{-12}$	$3.72 \times 10^{-13}$	$2.96 \times 10^{-12}$	$3.23 \times 10^{-13}$	$3.51 \times 10^{-13}$
C3	$1.74 \times 10^{-13}$	$2.12 \times 10^{-14}$	$3.23 \times 10^{-13}$	$1.28 \times 10^{-12}$	$4.40 \times 10^{-13}$	$2.96 \times 10^{-12}$	$3.32 \times 10^{-13}$	$3.82 \times 10^{-13}$

Table B.2: Continued

Measurement	Rock type							
	MCL	DD	SML	L <sub>41</sub>	MA	BA	BWS	BO
C <sub>4</sub>	$1.35 \times 10^{-13}$	$2.18 \times 10^{-14}$	$3.05 \times 10^{-13}$	$1.28 \times 10^{-12}$	$3.32 \times 10^{-13}$	$3.51 \times 10^{-12}$	$2.51 \times 10^{-13}$	$3.42 \times 10^{-13}$
C <sub>5</sub>	$1.08 \times 10^{-13}$	$2.58 \times 10^{-14}$	$2.81 \times 10^{-13}$	$1.02 \times 10^{-12}$	$2.97 \times 10^{-13}$	$3.41 \times 10^{-12}$	$3.61 \times 10^{-13}$	$3.82 \times 10^{-13}$
C <sub>6</sub>	$1.32 \times 10^{-13}$	$2.44 \times 10^{-14}$	$1.79 \times 10^{-13}$	$9.38 \times 10^{-13}$	$2.65 \times 10^{-13}$	$3.13 \times 10^{-12}$	$3.72 \times 10^{-13}$	$4.16 \times 10^{-13}$
C <sub>7</sub>	$1.43 \times 10^{-13}$	$2.18 \times 10^{-14}$	$2.24 \times 10^{-13}$	$1.21 \times 10^{-12}$	$3.42 \times 10^{-13}$	$3.71 \times 10^{-12}$	$8.62 \times 10^{-13}$	$4.04 \times 10^{-13}$
C <sub>8</sub>	$2.73 \times 10^{-13}$	$2.01 \times 10^{-14}$	$2.31 \times 10^{-13}$	$1.21 \times 10^{-12}$	$3.51 \times 10^{-13}$	$2.65 \times 10^{-12}$	$3.32 \times 10^{-13}$	$4.78 \times 10^{-13}$
C <sub>9</sub>	$1.32 \times 10^{-13}$	$2.18 \times 10^{-14}$	$3.32 \times 10^{-13}$	$1.14 \times 10^{-12}$	$4.40 \times 10^{-13}$	$2.58 \times 10^{-12}$	$3.61 \times 10^{-13}$	$4.28 \times 10^{-13}$
C <sub>10</sub>	$1.05 \times 10^{-13}$	$2.01 \times 10^{-14}$	$5.66 \times 10^{-13}$	$1.17 \times 10^{-12}$	$3.61 \times 10^{-13}$	$3.22 \times 10^{-12}$	$3.51 \times 10^{-13}$	$4.28 \times 10^{-13}$
D <sub>1</sub>	$1.47 \times 10^{-13}$	$2.73 \times 10^{-14}$	$5.99 \times 10^{-13}$	$1.08 \times 10^{-13}$	$3.72 \times 10^{-13}$	$3.32 \times 10^{-12}$	$5.66 \times 10^{-13}$	$1.14 \times 10^{-12}$
D <sub>2</sub>	$1.02 \times 10^{-13}$	$2.31 \times 10^{-14}$	$6.51 \times 10^{-13}$	$1.18 \times 10^{-13}$	$4.16 \times 10^{-13}$	$3.13 \times 10^{-12}$	$5.35 \times 10^{-13}$	$1.08 \times 10^{-12}$
D <sub>3</sub>	$1.39 \times 10^{-13}$	$2.89 \times 10^{-14}$	$5.50 \times 10^{-13}$	$1.35 \times 10^{-13}$	$4.28 \times 10^{-13}$	$3.82 \times 10^{-12}$	$4.40 \times 10^{-13}$	$1.31 \times 10^{-12}$
D <sub>4</sub>	$1.24 \times 10^{-13}$	$3.33 \times 10^{-14}$	$6.16 \times 10^{-13}$	$5.67 \times 10^{-14}$	$5.06 \times 10^{-13}$	$3.13 \times 10^{-12}$	$4.78 \times 10^{-13}$	$1.11 \times 10^{-12}$
D <sub>5</sub>	$1.35 \times 10^{-13}$	$2.81 \times 10^{-14}$	$7.49 \times 10^{-13}$	$1.51 \times 10^{-13}$	$4.28 \times 10^{-13}$	$3.22 \times 10^{-12}$	$4.92 \times 10^{-13}$	$1.08 \times 10^{-12}$

Table B.2: Continued

Measurement	Rock type							
	MCL	DD	SML	L41	MA	BA	BWS	BO
D6	$1.32 \times 10^{-13}$	$1.70 \times 10^{-14}$	$7.09 \times 10^{-13}$	$9.94 \times 10^{-14}$	$3.72 \times 10^{-13}$	$2.80 \times 10^{-12}$	$4.92 \times 10^{-13}$	$1.14 \times 10^{-12}$
D7	$1.56 \times 10^{-13}$	$2.38 \times 10^{-14}$	$7.09 \times 10^{-13}$	$1.18 \times 10^{-13}$	$3.93 \times 10^{-13}$	$2.65 \times 10^{-12}$	$5.35 \times 10^{-13}$	$1.11 \times 10^{-12}$
D8	$1.14 \times 10^{-13}$	$3.06 \times 10^{-14}$	$7.29 \times 10^{-13}$	$1.74 \times 10^{-13}$	$3.32 \times 10^{-13}$	$2.96 \times 10^{-12}$	$2.97 \times 10^{-13}$	$1.02 \times 10^{-12}$
D9	$1.84 \times 10^{-13}$	$3.15 \times 10^{-14}$	$7.09 \times 10^{-13}$	$6.90 \times 10^{-14}$	$3.51 \times 10^{-13}$	$3.13 \times 10^{-12}$	$4.04 \times 10^{-13}$	$1.14 \times 10^{-12}$
D10	$1.69 \times 10^{-13}$	$1.85 \times 10^{-14}$	$5.82 \times 10^{-13}$	$1.84 \times 10^{-13}$	$4.4 \times 10^{-13}$	$3.41 \times 10^{-12}$	$4.16 \times 10^{-13}$	$9.92 \times 10^{-13}$
E1	$8.88 \times 10^{-14}$	$2.31 \times 10^{-14}$	$5.50 \times 10^{-13}$	$1.02 \times 10^{-12}$	$1.84 \times 10^{-13}$	$3.82 \times 10^{-12}$	$3.14 \times 10^{-13}$	$5.20 \times 10^{-13}$
E2	$2.58 \times 10^{-13}$	$2.44 \times 10^{-14}$	$2.44 \times 10^{-13}$	$9.65 \times 10^{-13}$	$2.44 \times 10^{-13}$	$2.96 \times 10^{-12}$	$2.81 \times 10^{-13}$	$5.35 \times 10^{-13}$
E3	$9.94 \times 10^{-14}$	$2.06 \times 10^{-14}$	$2.97 \times 10^{-13}$	$8.87 \times 10^{-13}$	$2.97 \times 10^{-13}$	$2.88 \times 10^{-12}$	$2.97 \times 10^{-13}$	$5.06 \times 10^{-13}$
E4	$1.43 \times 10^{-13}$	$2.81 \times 10^{-14}$	$2.12 \times 10^{-13}$	$9.38 \times 10^{-13}$	$2.51 \times 10^{-13}$	$3.13 \times 10^{-12}$	$3.42 \times 10^{-13}$	$5.66 \times 10^{-13}$
E5	$9.94 \times 10^{-14}$	$3.06 \times 10^{-14}$	$3.72 \times 10^{-13}$	$1.08 \times 10^{-12}$	$2.31 \times 10^{-13}$	$3.61 \times 10^{-12}$	$3.14 \times 10^{-13}$	$5.06 \times 10^{-13}$
E6	$1.51 \times 10^{-13}$	$2.06 \times 10^{-14}$	$4.52 \times 10^{-13}$	$8.38 \times 10^{-13}$	$2.81 \times 10^{-13}$	$3.22 \times 10^{-12}$	$3.23 \times 10^{-13}$	$5.82 \times 10^{-13}$
E7	$1.56 \times 10^{-13}$	$2.51 \times 10^{-14}$	$4.78 \times 10^{-13}$	$9.38 \times 10^{-13}$	$2.18 \times 10^{-13}$	$3.32 \times 10^{-12}$	$3.72 \times 10^{-13}$	$6.16 \times 10^{-13}$

Table B.2: Continued

Measurement	Rock type							
	MCL	DD	SML	L <sub>41</sub>	MA	BA	BWS	BO
E8	$1.21 \times 10^{-13}$	$2.31 \times 10^{-14}$	$4.16 \times 10^{-13}$	$8.62 \times 10^{-13}$	$2.73 \times 10^{-13}$	$3.22 \times 10^{-12}$	$3.51 \times 10^{-13}$	$6.51 \times 10^{-13}$
E9	$1.56 \times 10^{-13}$	$2.38 \times 10^{-14}$	$4.40 \times 10^{-13}$	$9.38 \times 10^{-13}$	$3.05 \times 10^{-13}$	$3.13 \times 10^{-12}$	$2.89 \times 10^{-13}$	$6.16 \times 10^{-13}$
E10	$3.51 \times 10^{-13}$	$2.51 \times 10^{-14}$	$4.65 \times 10^{-13}$	$9.38 \times 10^{-13}$	$3.42 \times 10^{-13}$	$2.96 \times 10^{-12}$	$3.05 \times 10^{-13}$	$6.70 \times 10^{-13}$



# C

## APPENDIX TO CHAPTER 3: TRANSFORMING FIELD DENSITY DATA

---

[Figure C.1](#) shows the densities yielded by two methods performed on the sample suite. The double-weight method is equivalent to that carried out in the field; the second method (the volumetric mass density) is determined by the ratio of the geometric volume and dry mass of a cylindrical sample. Double-weight values are progressively higher than the geometric values at decreasing densities (i.e. higher porosities) ([Figure C.1a](#)). This is a function of the capacity for water imbibition through surface pores over the timescale of each measurement (typically about 5 seconds); incorporating the parameters of the fitted line into further analyses of density data allows this deviation to be accounted for.

Porosity is a direct function of the ratio of bulk and particle densities: the relationship between porosity and volumetric mass density can thus be well constrained, as in [Figure C.1b](#), where the inverse of the absolute value of the slope corresponds to the particle density. The linear correlation between these values attests to a relative lack of variation in bulk composition and thus particle density between samples. The correlations described by [Figure C.1a](#) and [C.1b](#) have been encompassed in an empirical relation ([Figure C.1c](#)), subsequently used to estimate connected porosity from the initial field density data.

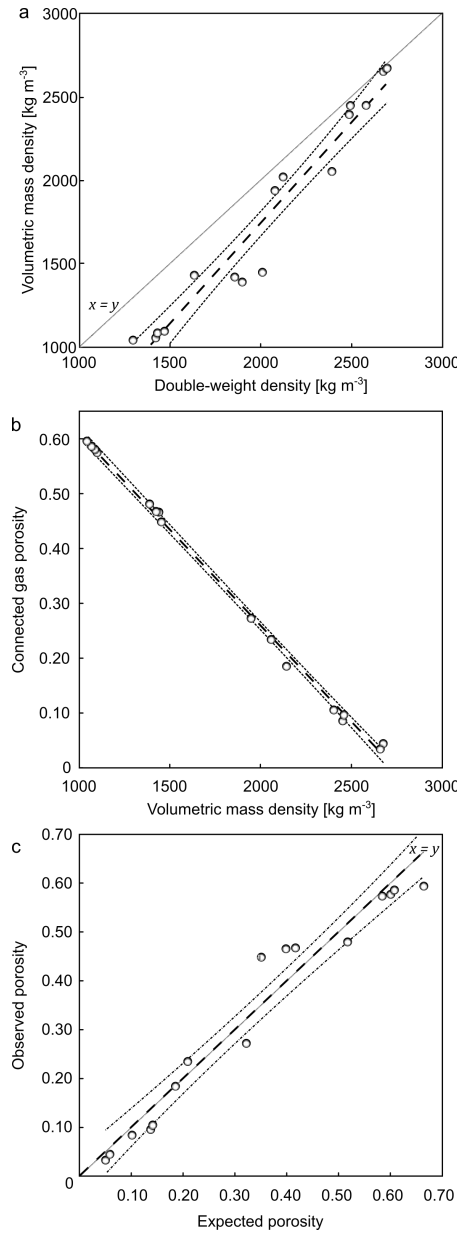


Figure C.1: a) Densities yielded by the double-weight (field) method  $\rho$  and the volumetric mass (laboratory) method  $\rho_b$ . Deviation from  $x = y$  can be described empirically such that  $\rho_b = m_a \rho + c_a$ , [ $r^2 = 0.95$ ]. b) Connected gas porosity  $\phi$  as measured by helium pycnometry is shown against volumetric mass density for andesite cores. The relationship is of the form  $\phi = m_b \rho_b + c_b$ , [ $r^2 = 1.00$ ]. c) Semi-empirical transformation of double-weight core density measurements (Expected) against measured gas porosity (Observed) described by the dashed line [ $r^2 = 0.99$ ]. Transformation is  $\phi = \zeta [m_b(m_a \rho_b + c_a) + c_b]$ , where  $m_a$ ,  $c_a$ ,  $m_b$ , and  $c_b$  are fit components from a) and b). The coefficient  $\zeta$  is an empirical constant close to 1. In each case, thin dashed lines represent the upper and lower 95% confidence intervals (CI) around the fit line (thick dashed line). Grey lines represent  $x = y$ .

# D

## APPENDIX TO CHAPTER 4: IS ROCK STRENGTH COMPOSITION-DEPENDENT?

**Figure D.1** shows compiled data from Heap et al. (2015a) and Zhu et al. (2016) for andesite and basalt failure strength. Heap et al. (2015a) studied variably porous andesite from Volcán de Colima. Selected data are in the porosity range of 0.07 to 0.19, and deformed at effective pressures of 0, 10, 30, and 50 MPa. The strength of these andesites varies between 17.5 and 281.4 MPa (as a function of both porosity and effective pressure). Data presented from Zhu et al. (2016) are Etna basalt samples, similarly deformed at 0, 10, 30, and 50 MPa effective pressure. Porosity varies between 0.05 and 0.11, and strength spans a range from 72.0 to 651.0 MPa. From the trends discernible in **Figure D.1**, it is clear that—for any given  $p_{eff}$ —porosity exerts the major influence on the peak stress  $\sigma_p$ . Nevertheless, sample composition—and related parameters such as pore shape, crystal fraction and so on—may well be important considerations that require systematic experimental study.

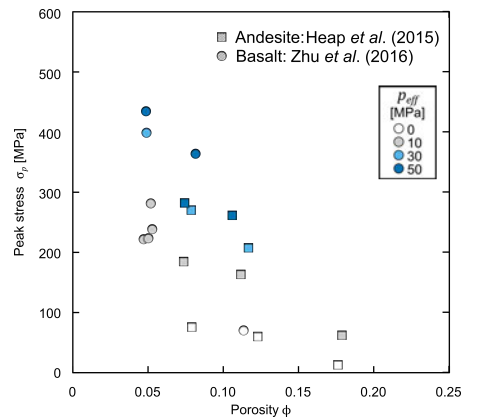


Figure D.1: Compiled strength data against porosity for andesites (Volcán de Colima andesite: Heap et al., 2015a) and basalts (Etna basalt: Zhu et al., 2016). Refer to text for discussion.



# E

## APPENDIX TO CHAPTER 7: FRACTURED CONDUIT PERMEABILITY ( $K$ ) REDUCTION

---

### E.1 MODEL FUNCTIONS

The model `FRACKR.m` is presented hereafter, composed of a series of functions. The constituent models and the parameters therein may be adjusted to reflect new experimental data, for example, or may be substituted should a different model better account for the specific problem parameters of the user. All functions employed by the model are presented below, along with a brief description.

The function `inputs(nt)` allows the user to input values for the timescale to compute, the temperature of the system, the depth range or "window" of interest, the mean fracture width and fracture density, and the crystal cargo of the compacting magma. Embedded in `inputs(nt)` are the following three functions:

```
fracture_width(nf,1);  
fracture_generator(window_min,window_max,nf,mean_wf);  
Crystal().
```

The first of these [`fracture_width(nf,1)`] ensures that the cumulative fracture width is not greater than the overall length of intact material. If this assumption is violated, the user will be prompted to input a smaller value for the mean fracture width.

`fracture_generator(window_min, window_max,nf, mean_wf)` employs a uniform random probability distribution to randomly assign depths to fractures within the depth range imposed by the user, up to the user-defined fracture density. The function will run iteratively until the distance between each fracture is at least half of the mean fracture width, in order to avoid overlap.

The third function [`Crystal()`] ensures that the crystal fraction imposed by the user is between 0 and 1 (i.e. between 0 and 100 vol.%). If the input value is outwith this range, the user will be prompted to re-enter their value.

The initial viscosity is determined by the function `viscosity(T, xc, rho, g, w, sizew)`, which calculates the lithostatic stress driving compaction. The function also allows the user to calculate the equilibrium water content using `equilibrium(T,sigma)`, which employs the solubility law proposed by Liu et al. (2005), or to input their

own value. It then calls the function `HD(T, H2O, xc)`, described below.

`HD(T, H2O, xc)`, is the viscosity model of Hess and Dingwell (1996), developed for hydrous calc-alkaline rhyolites, and allows the non-Arrhenian temperature dependency of melt viscosity to be calculated. To account for the influence of crystal content on rheology, the function `HD(T, H2O, xc)` calls `Xcontent(eta_0, xc, Xm)`, which comprises the particle-suspension model of Mueller et al. (2011).

`timescale(T, mean_wf, A, B, phi_i, eta_0)` calculates the ratio between the mean fracture width and the compaction lengthscale, given by `delta (δ)`. This requires the pore fluid viscosity `nu (ν)` to be known, which is determined by `pore_fluid(T)`. `delta (δ)` is then calculated as described in Chapter 7. A further function [`Darcy_compact_ion(eta_0, A, B, phi_i, alpha, T, mean_wf)`] computes the Darcy compaction number, which delimits whether or not pore pressure can increase within sintering fractures. If this value is less than one, the user is warned that the pore pressure may not be in equilibrium, and given the option on whether they wish to continue with the computation (refer to accompanying article for explanation). This function outputs the critical permeability threshold `k_cr (kcr)`, below which pore pressure will increase.

The final function [`figures(tt, P, time, KK, t, n, ke, w, kk, window_max)`], controls figure formatting and output. The MATLAB<sup>®</sup> script is appended below.

## E.2 MATLAB<sup>®</sup> SCRIPT

```
%%%%%% %%%%%% %%%%%% %%%%%% %%%%%% %%%%%% %%%%%% %%%%%% %%%%%% %%%%%%
%%%%% %%%%%% %%%%%% %%%%%% %%%%%% ~FRACkR~ %%%%%% %%%%%% %%%%%% %%%%%% %%%%%%
%%%%% %%%%%% %%%%%% %%%%%% %%%%%% %%%%%% %%%%%% %%%%%% %%%%%% %%%%%% %%%%%%
5 % The following script allows the calculation of the
% equivalent permeability ke of the wall of a volcanic
% conduit containing multiple fractures. The time-
% dependence of ke is captured by considering depth-
% and temperature- dependent fracture permeability
10 % reduction by viscous sintering.

clearvars; close all; clc

15 %% Create file

%Filename for an the output files, which save equivalent
permeability
```

```

%evolution with time.
xlsFilename = input('Enter the name for the xls file: ', 's');
20
%% Model setup

% Intial time
t0 = 0;
25 % Number of timesteps to compute
nt = 100;

% Call constants function
[alpha, phi_i, rho, g, A, B, C, D, phi_c] = constants();
30
% Call user inputs function
[time, dt, T, window_max, window_min, l, nf, mean_wf, intact,
 spacing, w, sizew, Xc] = inputs(nt);

% Host rock permeabilities [m^2]
35 n = (11:1:22);k0 = 10.^(-n); n = 12;

% Call viscosity functions
[eta_0, sigma] = viscosity(T, Xc, rho, g, w, sizew);

40 % Flag if initial viscosity is greater than viscosity at Tg
if eta_0 > 1e12;
    disp('Fracture material may be below Tg. This may result
          in non-physical values. ');
    choice = questdlg('Fracture material may be below Tg.
                      Would you like to continue?', ...
                      'Continue', ...
                      'Yes','No','No');
45
    % Handle response
    switch choice
        case 'Yes'
            flag = 2;
50        case 'No'
            flag = 1;
        end
    end
%% Preallocate matrices
55
% Creates a matrix to store porosity results
P = NaN(nt,nf);
% Creates a matrix to store time
tt = zeros(nt,nf);
60 % Creates a matrix with host rock permeabilities
kk = repmat(k0,nt,1);
% Creates a matrix to store permeability data
KK = NaN(nt,nf);
% Creates a matrix to store equivalent permeability values
65 ke = NaN(size(kk));

%% Check flags
% This section flags if dimensionless numbers exceed imposed
thresholds

```

```

70 % Determines delta, the ratio between fracture width and
    compaction lengthscale
[delta] = timescale(T, mean_wf, A, B, phi_i, eta_0);
% Determines the Darcy compaction number,
[Dac, kcr, flag] = Darcy_compaction(eta_0, A, B, phi_i, alpha,
T, mean_wf);

75 if any(delta) > 1;
    disp('One or more fractures may be too wide to sinter, or
        may necessitate more complex sintering criteria. This
        may result in non-physical values. ');
choice = questdlg('One or more fractures may be too wide
    to sinter. Would you like to continue?', ...
80     'Continue', ...
     'Yes', 'No', 'No');
% Handle response
switch choice
    case 'Yes'
        flag = 2;
    case 'No'
        flag = 1;
    end
end

90 %% Porosity - permeability evolution over time

% Set time to start time
t = t0;
95 timespan = 10.^linspace(0, log10(time*86400), nt).';

for m = 1:nt

    % porosity starts at initial value of 0.4, a typical
        porosity for polydisperse granular materials close to
        their maximum packing.
100 phi = phi_i;
    % time increases by dt increment each iteration
    phi0 = phi;
    t = timespan(m);

105 for i = 2:nt

        % Porosity evolution with time, after the model of
            Russell and Quane (2005)
        beta = log((alpha.*sigma*t)./(eta_0.*((1 - phi_i))) +
            exp(-alpha*phi_i/(1-phi_i)));
        beta(beta>0) = 0;
    110 phi = beta./(beta-alpha);

        end
    P(m,:)= phi; P(P<0) = 0;

115 % Permeability-porosity model described by two-slope model
        , after Heap et al. (2015).
    if phi>=phi_c

```

```

    k = A*((100*phi).^B);
else k = C*((100*phi).^D);
end
120
% Permeability and time matrices update with each
iteration
k(k < 0) = 0;
KK(m,:) = k;
tt(m,:) = t;
125 end

%% Quit script if user selects not to continue

if flag == 1
130   error('Model quit by user. ')
end
%%
if flag == 0||2

135 %% Equivalent permeability calculation

    % Intact width
    wi =(l - nf*mean_wf);wx = nf*mean_wf;
    % Fracture width times fracture permeability
140    wfkf = wx.*KK; wfkf = sum(wfkf,2); wy = repmat(wfkf,1,n);
    % Intact width for each host rock permeability
    wix = repmat(wi,nt,n);
    % Equivalent permeability for host rock permeability
    ke = ((wix.*kk)+(wy))/l;
145

    %% Assess resolution

    if ke(nt,12)/k0(1,12)>1;
        choice = questdlg('Host material may not have returned
            to pre-fracture permeability. Consider re-running
            model using longer "Timescale to compute".', ...
150        ', ...
        'Continue','Continue');
        % Handle response
        switch choice
            case 'Continue'
155            end
        end
    if ke(nt*0.9,12)/k0(1,12)<1;
        choice = questdlg('For better resolution, consider re-
            running model using shorter "Timescale to compute"
            .', ...
            ', ...
            'Continue','Continue');
160        % Handle response
        switch choice
            case 'Continue'
            end
165    end

    %% Figure plotting

```

```

[hFig] = figures(tt, P, time, KK, t, n, ke, w, kk,
    window_max);
170
%% X = ['Data are saved as ', xlsFilename, '.xls.']; msgbox(X
    );
%% Output file

175 % Saves user inputs on the first sheet, time and
    % equivalent permeability
% (in accordance with the initial host rock permeabilities
    % ) on the second,
% and the randomly generated fracture positions in the
    % third.
rho_frac = nf/l;
User_inputs = {'Max. depth [m]', window_max; 'Min. depth [
    m]', win-dow_min; 'Fracture density [fractures/m]', rho_frac; 'Fracture width [m]', mean_wf; 'Temperature
    [C]', T; 'Crystal content', Xc};
180 header1 = {'User inputs'};
header2 = {'Time [s]', 'Equivalent permeability for host
    permeability of 10^-11[m^2]', '10^-12[m]', '10^-13[m]', '
    10^-14[m]', '10^-15[m]', '10^-16[m]', '10^-17[m]', '
    10^-18[m]', '10^-19[m]', '10^-20[m]', '10^-21[m]', '
    10^-22[m]', {}};
header3 = {'Fracture depths [m]'};
output = [tt(:,1),ke];
185 xlswrite(xlsFilename, header1);
xlswrite(xlsFilename, User_inputs,'Sheet1','A2');
xlswrite(xlsFilename, header2,'Sheet2');
xlswrite(xlsFilename, output,'Sheet2','A2');
xlswrite(xlsFilename, header3,'Sheet3');
xlswrite(xlsFilename, w,'Sheet3','A2');

190 end

%% References
%%
% [1] Russell, J. K., & Quane, S. L. (2005). Rheology of
    welding: inversion of field constraints. Journal of
    Volcanology and Geothermal Research, 142(1), 173–191.
195 %%
% [2] Heap, M. J., Farquharson, J. I., Wadsworth, F. B.,
    Kolzenburg, S., & Russell, J. K. (2015). Timescales for
    permeability reduction and strength recovery in densifying
    magma. Earth and Planetary Science Letters, 429, 223–233.

function [alpha, phi_i, rho, g, A, B, C, D, phi_c] = constants
()
200 %% Imports constants
% Imports constants used in sintering model [1] and
    % permeability model
% [2]. To alter constants, the values below can be changed.

%% Sintering constants
205 alpha = 2;
%empirical coefficient used in porosity reduction model [1]

```

```

phi_i = 0.4;
%initial porosity
rho = 2500;
210 %initial bulk density [kg/m^3]
g = 9.806;
%acceleration due to gravity [m^2/s]

%% Permeability–porosity relation constants
215 A = 7.97686606*10^-26;
% k – phi relation constant [2]
B = 8.76;
% k – phi relation constant [2]
C = 1.335903*10^-16;
220 % k – phi relation constant [2]
D = 1.01;
% k – phi relation constant [2]
phi_c = 0.155;
% changepoint porosity [2]
225 end

%%
% [1] Russell, J. K., & Quane, S. L. (2005). Rheology of
    welding: inversion of field constraints. Journal of
    Volcanology and Geothermal Research, 142(1), 173–191.
%
230 % [2] Heap, M. J., Farquharson, J. I., Wadsworth, F. B.,
    Kolzenburg, S., & Russell, J. K. (2015). Timescales for
    permeability reduction and strength recovery in densifying
    magma. Earth and Planetary Science Letters, 429, 223–233.

function [time, dt, T, window_max, window_min, l, nf, mean_wf,
    intact, spacing, w, sizew, Xc] = inputs(nt)
%% Primary input arguments
235 % Prompted user inputs, which outputs parameters used in
    models.

prompt = 'Timescale to compute [days]? ';
time = input(prompt); dt = (time*86400)./ nt;
T = input('What is the temperature [o C]? ');

240 % Maximum depth of segment of interest
window_max = input('What is the lower limit of the lengthscale
    [m]? ');
% Minimum depth of segment of interest
window_min = input('What is the upper limit of the lengthscale
    [m]? ');
245 % Range of interest
window = window_max - window_min; l = window;
% Fracture density input
rho_frac = input('What is the fracture density [fractures/m]?
    ');
% Calculates total number of fractures
250 nf = rho_frac*window;
% Mean fracture width input
[mean_wf] = fracture_width(nf,l);
% Width of non-fractured lateral [m];

```

```

intact = window - (nf*mean_wf);
255 % Mean spacing in between fractures [m];
spacing = intact/nf;

% Generates fracture depths up to a user-defined density
[w] = fracture_generator(window_min, window_max,nf, mean_wf);
260 % Cumulative fracture width
sizew = size(w,1);

% Call crystal content input
[Xc] = Crystal();
265
end

function [mean_wf] = fracture_width(nf,1)
270 % Ensures that cumulative fracture width is not greater than
      the width of
% intact host material.

mean_wf = input('What is the mean fracture width [m]? ');
while mean_wf*nf >= 1*0.5;
275     disp('Cumulative fracture width cannot be greater than
           intact mate-rial.');
     [mean_wf] = fracture_width(nf,1);
end
end

280
function [w] = fracture_generator(window_min, window_max,nf,
mean_wf)
%% Generates fracture depths up to a given density
% Fractures have a equal likelihood of being generated at any
point
% within the user-specified depth range. If the distance
between two
285 % fractures is less than or equal to the mean fracture width,
the
% function is re-run until this is not the case.
pd = makedist('Uniform', 'lower',window_min,'upper',window_max
);
w = random(pd,nf,1); w = sort(w(:));
diffs = diff(w);
290 if any(diffs)<= (mean_wf/2);
    [w] = fracture_generator(window_min, window_max,nf,
mean_wf);
end
end

295
function [Xc] = Crystal()
%% User-defined fractional crystal content
% Crystal content Xc must be between 0 and 1.
Xc = input('What is the crystal fraction? ');
300 while Xc < 0 || Xc > 1;
    disp('Crystal fraction must be between 0 and 1.');

```

```

    % Recall this function if input crystal content is not
    % between 0 and 100%
    [Xc] = Crystal();
305 end

end

310 function [eta_0, sigma] = viscosity(T, Xc, rho, g, w, sizew)
    %% Incorporates water content into viscosity
    % Allows the user to choose between equilibrium water content
    % or a defined
    % value.
    sigma = rho*g*w;
315     % Calculates magmastic (or lithostatic) stress driving
        densification

    choice = questdlg('Would you like to calculate equilibrium
        H2O content or input value?', ...
        'Continue', ...
        'Manual input','Equilibrium','Manual input');
320     % Handle response
    switch choice
        case 'Equilibrium'

            for i = 1:sizew
325         [H2O] = equilibrium(T,sigma);
            % Runs solubility function

            end
        case 'Manual input'
            [H2O] = input('What is the dissolved water content
                ? ');
330         end
            [eta_0] = HD(T,H2O, Xc);
335         % Runs viscosity function
    end

function [H2O] = equilibrium(T,sigma)
340     %% Pressure dependence of H2O solubility

    % The equilibrium water content is given as a function of
    % pressure and temperature, after Liu et al., 2005 [1].
    % Pressure in MPa
345 P = sigma./1000000;
    % Temperature in Kelvin
    T = T + 273.15;
    s1 = 354.94;
    s2 = 9.623;
350 s3 = 1.5223;
    s4 = 0.0012439;
    %%
    Ceq = (((s1*T.^0.5)+(s2*T)-(s3*T.^1.5))/T)+(s4*T.^1.5);

```

```

H2O = Ceq;
355
end

%%
% [1] Liu, Y., Zhang, Y., and Behrens, H., 2005, Solubility of
    H2O in rhyolitic melts at low pressures and a new
    empirical model for mixed H2O—CO2 solubility in rhyolitic
    melts: Journal of Volcanology and Geothermal Research, v.
    143, no. 1, p. 219–235.

360

function [eta_0] = HD(T,H2O,Xc)

365 %% This viscosity model for calc-alkaline rhyolites is from
    Hess and Dingwell, 1996 [1]

%% Constants

a1 = -3.545;
370 a2 = 0.833;
b1 = 9601;
b2 = -2368;
c1 = 195.7;
c2 = 32.25;

375
%%

a = a1 + (a2*log(H2O));
b = b1 + (b2*log(H2O));
c = c1 + (c2*log(H2O));

380

%% Viscosity calculation

l_eta0 = a+(b./((T+273.15)-c));
385 eta_0 = 10.^l_eta0;

rp = 1;
b = 1.08;

390 Xm_x = 0.656;
Xm = Xm_x*exp(-((log10(rp))^2)/(2*b*b));

%% Call particle suspension function
[eta_0] = Xcontent(eta_0,Xc,Xm);

395
end
%%
% [1] Hess, K. U., and Dingwell, D. B., 1996, Viscosities of
    hydrous leucogranitic melts: A non-Arrhenian model:
    American Mineralogist, v. 81, no. 9–10, p. 1297–1300.

400
function [eta_0] = Xcontent(eta_0,Xc,Xm)

%% Crystal content

```

```

% This function accounts for the influence of suspensions of
% particles on the viscosity of viscous liquids. The model
% is from Mueller et al., 2010 [1];
405
%% Viscosity

eta_0 = eta_0*((1-(Xc/Xm)).^-2);

410 end
%%
% [1] Mueller, S., Llewellyn, E., and Mader, H., 2010, The
% rheology of suspensions of solid particles: Proceedings of
% the Royal Society A: Mathematical, Physical and
% Engineering Science, v. 466, no. 2116, p. 1201–1228.

415 function [delta] = timescale(T, w, A, B, phi_i, eta_0)
%% Delta calculator
% This function computes the value of delta, ratio between
% fracture width and compaction lengthscale

[nu] = pore_fluid(T);
420 % Calculates viscosity of pore fluid at given temperature

%% Constants

kfvj = A*((100*phi_i).^B); % Fracture permeability at intial
% porosity

425 %% Delta calculation

delta = w./((kfvj*(eta_0/nu)).^0.5);

430 end

function [nu] = pore_fluid(T)

435 %% Pore fluid viscosity
% This function calculates the viscosity of air at high
% temperature, representing the interstitial pore fluid
% within ash-laden fractures.

nu_0 = 1.846E-06; % Air viscosity at reference temperature

440 T = T + 273.15; % Temperature in Kelvin
T0 = 300; % Reference temperature in Kelvin

nu = nu_0*((T/T0)^(2/3)); % Pore fluid (air) viscosity at
% temperature

445 end

function [Dac, kcr, flag] = Darcy_compaction(eta_0, A, B,
phi_i, alpha, T, mean_wf)

```

```

450 %% Critical permeability threshold
% This function computes the timescale ratio between
% compaction and pore pressure increase.

flag = 0;

455 % Fracture permeability at initial porosity
kfvj = A*((100*phi_i).^B);
% Call pore fluid viscosity function
[nu] = pore_fluid(T);
% Darcy compaction number
460 Dac = eta_0*kfvj./(alpha*nu*(mean_wf.^2));
%%
% Critical permeability
kcr = (alpha*nu*(mean_wf/2).^2)./eta_0;
%%
465 if Dac < 1e0;
    disp('Pore pressure may not be in equilibrium. This may
        result in non-physical values.');

    choice = questdlg('Would you like to continue?', ...
        '', ...
        'Yes', 'No', 'No');
    % Handle response
    switch choice
        case 'Yes'
            flag = 2;
475        case 'No'
            flag = 1;
        end
    end
end
end
480

function [hFig] = figures(tt, P, time, KK, t, n, ke, w, kk,
window_max)
%% Plots three figures.
% (1): a multipanel figure showing the evolution of fracture
% porosity and permeability over time, the evolution of
% fracture permeability with porosity, and the evolution of
% equivalent permeability over time.
485 % (2): equivalent permeability evolution over time, contoured
% for different host rock permeabilities.
% (3): a schematic representation of the model geometry,
% indicating the randomly positioned fractures in terms of
% their depth.
hFig = figure(1);set(hFig, 'Position', [70 250 700 650]);
%%
% Plots porosity, permeability, equivalent permeability with
% time.
490 subplot (2,3,1);
semilogx((tt./86400),P); xlim([0 time]);
xlabel('Time [days]'), ylabel('Fracture porosity \phi_f');
subplot (2,3,2);
loglog((tt./86400), KK); xlim([0 time]);
495 xlabel('Time [days]'), ylabel('Fracture permeability k_f [m^2]
');

```

```

title({'Permeability and porosity evolution af-ter'};[num2str
    (round(t./86400), n), ' days']));
subplot (2,3,3);
semilogy(P, KK);
xlabel('Fracture porosity \phi_f'), ylabel('Fracture
    permeability k_f [m^2]');
500 subplot (2,3,[4 6]);
semilogy((tt(:,1)./86400),ke); xlim([0 time]); ylim
    ([1*10^(-23) 1*10^(-10)]);
xlabel('Time [days]'), ylabel('Equivalent permeability k_e [m
    ^2]');
505 hFig = figure(2);set(hFig, 'Position', [810 250 700 650]);
%%
% Plots equivalent permeability against time.
semilogy((tt(:,1)./86400), ke, 'k', 'LineWidth',1.1);
x = max((tt(:,1)./86400))*(4.1/5);
510 text(x, 2.5*10^-11, 'k_0 = 10^{-11}'); text(x, 2.5*10^-12, '
    k_0 = 10^{-12}');
text(x, 2.5*10^-13, 'k_0 = 10^{-13}'); text(x, 2.5*10^-14, '
    k_0 = 10^{-14}');
text(x, 2.5*10^-15, 'k_0 = 10^{-15}'); text(x, 2.5*10^-16, '
    k_0 = 10^{-16}');
text(x, 2.5*10^-17, 'k_0 = 10^{-17}'); text(x, 2.5*10^-18, '
    k_0 = 10^{-18}');
text(x, 2.5*10^-19, 'k_0 = 10^{-19}'); text(x, 2.5*10^-20, '
    k_0 = 10^{-20}');
515 text(x, 2.5*10^-21, 'k_0 = 10^{-21}'); text(x, 2.5*10^-22, '
    k_0 = 10^{-22}');
hold on, semilogy((tt(:,1)./86400), kk, 'b:', 'LineWidth',0.5)
;
xlabel('Time [days]'), ylabel('Equivalent permeability k_e [m
    ^2]');
title(['Equivalent permeability evolution after ',num2str(t.
    /86400), ' days']);

520 cond = (tt(:,1)./86400);
fracs = repmat(w,[1,size(cond)]);
limit = 1.2*window_max; con_l = 0.25*max(cond); con_r = 0.5*
    max(cond);

hFig = figure(3); set(hFig, 'Position', [1550 250 300 650]);
525 %%
% Plots model geometry (i.e. fracture positions along conduit/
    dyke)
plot(cond,fracs);
set(gca,'YDir','Reverse'); ylim([0 limit]); set(gca,'xtick'
    ,[]);
ylabel('Depth [m]'); rectangle('Position',[con_l 0 con_r limit
    ],'FaceColor',[1 0 0]);
530 text(0.5, 0.5, 'Conduit/dyke', 'rot',90, 'units','normalized')
    ;
text(0.125, 0.04, 'Host rock', 'rot',90, 'units','normalized')
    ;
text(0.875, 0.04, 'Host rock', 'rot',90, 'units','normalized')
    ;

```

```
title('Fracture positioning');  
535 end
```

**Part III**  
**ANNEXES**



F

FRACTURE AND COMPACTION OF ANDESITE IN A  
VOLCANIC EDIFICE

---

## Fracture and compaction of andesite in a volcanic edifice

M. J. Heap<sup>1</sup> · J. I. Farquharson<sup>1</sup> · P. Baud<sup>1</sup> ·  
Y. Lavallée<sup>2</sup> · T. Reuschlé<sup>1</sup>

Received: 12 October 2014 / Accepted: 21 May 2015 / Published online: 3 June 2015  
© The Author(s) 2015. This article is published with open access at Springerlink.com

**Abstract** The failure mode of lava—dilatant or compactant—depends on the physical attributes of the lava, primarily the porosity and pore size, and the conditions under which it deforms. The failure mode for edifice host rock has attendant implications for the structural stability of the edifice and the efficiency of the sidewall outgassing of the volcanic conduit. In this contribution, we present a systematic experimental study on the failure mode of edifice-forming andesitic rocks (porosity from 7 to 25 %) from Volcán de Colima, Mexico. The experiments show that, at shallow depths (<1 km), both low- and high-porosity lavas dilate and fail by shear fracturing. However, deeper in the edifice (>1 km), while low-porosity (<10 %) lava remains dilatant, the failure of high-porosity lava is compactant and driven by cataclastic pore collapse. Although inelastic compaction is typically characterised by the absence of strain localisation, we observe compactive localisation features in our porous andesite lavas manifest as subplanar surfaces of collapsed pores. In terms of volcano stability, faulting in the upper edifice could destabilise the volcano, leading to an increased risk of flank or large-scale dome collapse, while compactant deformation deeper in the edifice may emerge as a viable mechanism driving volcano subsidence, spreading and destabilisation. The failure mode

influences the evolution of rock physical properties: permeability measurements demonstrate that a throughgoing tensile fracture increases sample permeability (i.e. equivalent permeability) by about a factor of two, and that inelastic compaction to an axial strain of 4.5 % reduces sample permeability by an order of magnitude. The implication of these data is that sidewall outgassing may therefore be efficient in the shallow edifice, where rock can fracture, but may be impeded deeper in the edifice due to compaction. The explosive potential of a volcano may therefore be subject to increase over time if the progressive compaction and permeability reduction in the lower edifice cannot be offset by the formation of permeable fracture pathways in the upper edifice. The mode of failure of the edifice host rock is therefore likely to be an important factor controlling lateral outgassing and thus eruption style (effusive versus explosive) at stratovolcanoes.

**Keywords** Outgassing · Volcán de Colima · Brittle · Inelastic compaction · Pore collapse · Shear fracture · Edifice stability · Permeability · Stratovolcano

### Introduction

Volcanic edifices, products of the accumulation of successive lava and volcaniclastic deposits and endogenous growth (Borgia and Linneman 1990; Kaneko 2002; Biggs et al. 2010), play a central role in governing volcanic hazards (Voight 2000). First, the structural stability of the edifice, and therefore its susceptibility to catastrophic collapse, depends on the integrity of this rapidly emplaced mélange of coherent lava flows and poorly consolidated volcaniclastic deposits (e.g. Gudmundsson 2011). Second, the ease with which exsolving magma can outgas into the country rock (e.g. Jaupart 1998; Collinson and Neuberg 2012), a factor

---

Editorial responsibility: A. Gudmundsson

✉ M. J. Heap  
heap@unistra.fr

<sup>1</sup> Équipe de Géophysique Expérimentale, Institut de Physique de Globe de Strasbourg (UMR 7516 CNRS, Université de Strasbourg/EOST), 5 rue René Descartes, 67084 Strasbourg cedex, France

<sup>2</sup> Earth, Ocean and Ecological Sciences, University of Liverpool, Liverpool L69 3GP, UK

dictating the explosivity of the volcano, relies on the physical state (porosity, permeability) of the edifice host rocks (e.g. Eichelberger et al. 1986; Woods and Koyaguchi 1994; Mueller et al. 2008; Nguyen et al. 2014; Castro et al. 2014; Okumura and Sasaki 2014; Gaunt et al. 2014; Farquharson et al. 2015). Throughout edifice construction, edifice rocks are subject to a multitude of local and regional stresses that persistently alter their physical state, challenging edifice stability and influencing lateral outgassing; for example, local stress fields can rapidly change due to dyke propagation, regional stresses exist in the form of tectonic stresses, and lithostatic stresses build as effusive and explosive products that accumulate over time (e.g. Roman et al. 2004; Gerst and Savage 2004; Gudmundsson 2006). As a result, during the life cycle of a volcano, the initially steep conical structure evolves into a more dispersed and degraded landform (van Wyk de Vries and Borgia 1996; Borgia et al. 2000). Ultimately, this increasingly unstable structure can collapse, evidence of which is exposed in the geological record as sector collapse scars, amphitheatres, craters and calderas (e.g. Guest et al. 1984; Stoops and Sheridan 1992; Hall et al. 1999; Tibaldi 2001). It follows that the mechanical response of the rocks that comprise the edifice to regional and local stresses must represent a fundamental factor in the progressive destabilisation of a volcano and the evolution of outgassing efficiency and thus explosivity.

When exposed to a differential stress, porous rock reacts in one of two ways. The porosity within the rock (a combination of microcracks and pores) will either increase (dilation) or decrease (compaction). The operative micromechanical process, dilatational microcracking or compactive pore collapse/grain crushing, dictates the response of the rock to an applied stress and is dependent on both the initial physical properties of the rock (e.g. porosity, pore size) and the conditions (e.g. pressure, temperature, pore fluid) under which the rock deforms (see the review by Wong and Baud 2012 and references therein). At low confining pressures (shallow depths), both low- and high-porosity rocks will dilate resulting in a dilatant mode of failure, such as axial splitting (at very low confining pressures or depths) or shear failure (e.g. Paterson and Wong 2005). However, as confining pressure (depth) increases, while low-porosity rock will continue to form shear fractures, high-porosity rock will undergo shear-enhanced compaction driven by cataclastic pore collapse and grain crushing (Wong and Baud 2012).

Importantly, the mode of failure will severely impact the evolution of rock physical properties. Laboratory experiments have shown that shear fracturing (and associated dilatancy) is synonymous with an increase in porosity (Read et al. 1995) and a decrease in elastic wave velocity (Aylng et al. 1995). Some experimental data, however, suggest the impact of fracturing on permeability may depend on the initial porosity of the rock. While dilation and the formation of a macroscopic

shear fracture (e.g. Zoback and Byerlee 1975; Mitchell and Faulkner 2008) and tensile (extension) fractures (Nara et al. 2011) have been shown to increase the permeability of low-porosity rock by many orders of magnitude, experiments on high-porosity (>15 %) sandstones have shown that shear fractures can decrease permeability (Zhu et al. 1997a; Ngwenya et al. 2003). Indeed, some field studies on large faults in porous rocks have shown that permeability decreases as the fault is approached (Shipton et al. 2002; Farrell et al. 2014). Similar studies on large faults in low-porosity rock attest to a significant increase in permeability within the adjacent damage zone (Mitchell and Faulkner 2012), although the low permeability of the fault core can impart a permeability anisotropy (Faulkner and Rutter 2001; Wibberley and Shimamoto 2003).

By contrast, inelastic compaction will serve to increase elastic wave velocity (Fortin et al. 2005), decrease porosity (Wong and Baud 2012) and, in all cases, decrease permeability (David et al. 1994; Zhu et al. 1997b; Fortin et al. 2005; Baud et al. 2012). The failure mode also influences the output of acoustic emissions (AE, typically used as a proxy for microcracking) during deformation (Wong et al. 1997). An understanding of the mechanical behaviour and failure modes, and their impact on rock physical properties, of edifice-forming volcanic rocks is therefore of upmost importance. For example, the efficiency of lateral outgassing through the country rock (e.g. Jaupart 1998) is likely aided by a dilatant failure mode and hindered by a compactant failure mode.

Laboratory studies on the mechanical behaviour and failure modes of rock have been biased towards sedimentary rocks (Wong and Baud 2012). Studies on volcanic rocks—rocks with a greater microstructural complexity—are few (e.g. Kennedy et al. 2009; Zhu et al. 2011; Loaiza et al. 2012; Adelinet et al. 2013; Heap et al. 2014a, 2015), but have highlighted that volcanic rock can switch from dilatant to compactive modes of failure as effective pressure (i.e. depth) is increased. High-porosity tuffs (30–50 %) have been shown to switch to inelastic compaction at very low effective pressures ( $P_{eff}=5-10$  MPa;  $P_{eff}=P_c-\alpha P_p$ , where  $P_c$  and  $P_p$  are the confining pressure and pore pressure, respectively, and poroelastic constant  $\alpha$  is assumed to be 1), corresponding to depths of a couple of hundred metres (Zhu et al. 2011; Heap et al. 2014a, 2015). Studies on porous extrusive rocks have shown that inelastic compaction is encountered at much higher effective pressures. An aphanitic basalt from Reykjanes (Iceland) containing a porosity of 8 % switched to compactive behaviour at an effective pressure of 75 MPa (Adelinet et al. 2013), while an aphanitic trachyandesite from the Açores (Portugal) with a porosity of 18 % was compactant at 90 MPa (Loaiza et al. 2012), pressures corresponding to depths greater than 3 km. Kennedy et al. (2009) showed that low-porosity (8 %) dacite from Mount St. Helens (USA) exhibited shear fracturing up to effective pressures of 75 MPa, while the deformation of high-porosity (20–24 %) dacite from

Augustine volcano (USA) was driven by distributed cataclastic flow at pressures of 25 MPa and higher. Despite these studies, the paucity of experimental data on the mechanical behaviour and failure modes of volcanic rock inhibits our understanding, a key element to interpret the evolution of edifice stability and sidewall outgassing. For instance, the rocks comprising a volcanic edifice are known to be variably porous (e.g. Melnik and Sparks 2002; Kueppers et al. 2005; Lavallée et al. 2012; Farquharson et al. 2015). However, little is known about the influence of porosity on the failure mode of representative edifice-forming rocks. To better understand the deformation of edifice-forming rock, we conducted a systematic experimental study on the mechanical behaviour and failure mode of a suite of edifice-forming andesites containing different porosities (7 to 25 %), deformed under volcanologically relevant pressures (corresponding to depths from a couple of hundred metres to about 3 km).

## Case study, materials and methods

### Case study: Volcán de Colima

For the purpose of this study, we selected edifice-forming andesitic rocks from Volcán de Colima (Trans-Mexican Volcanic Belt, Mexico, 19° 30' N, 103° 37' W, Fig. 1). Volcán de Colima was specifically chosen for this study as it is an active and frequently collapsing andesitic stratovolcano, with a construction and eruption history comparable to other active andesitic stratovolcanoes observed worldwide, such as Merapi (Indonesia), Santa María (Guatemala), Tungurahua (Ecuador) and Ruapehu (New Zealand). The volcanic complex comprises the active Fuego de Colima, constructed in the amphitheatre of an earlier collapse structure, and the older and extinct edifice of Nevado de Colima (Fig. 1). The most recent collapse event (2550 BP) was the last of at least five major collapses during the last 18,500 years (Stoops and Sheridan 1992; Cortés et al. 2010). More recent activity has been characterised by lava effusion and Vulcanian explosions sandwiched between Plinian and sub-Plinian eruptions; these major explosive eruptions are thought to occur about every 100 years (Luhr 2002). Present day eruptive activity is extensively monitored through seismicity (Arámbula-Mendoza et al. 2011; Lamb et al. 2014; Lesage et al. 2014), gas geochemistry (Taran et al. 2002; Varley and Taran 2003), thermal infrared imaging (Hutchinson et al. 2013; Stevenson and Varley 2008; Webb et al. 2014), rockfall (Mueller et al. 2013) and deformation (Zobin et al. 2002). Between November 1998 and June 2011, there were five episodes of dome growth. Slow effusion and dome growth occurred in 2001–2003 and 2007–2011, interrupted by much faster episodes in 1998–1999, 2004 and 2005 (Varley et al. 2010). Explosive activity during this time was characterised by small

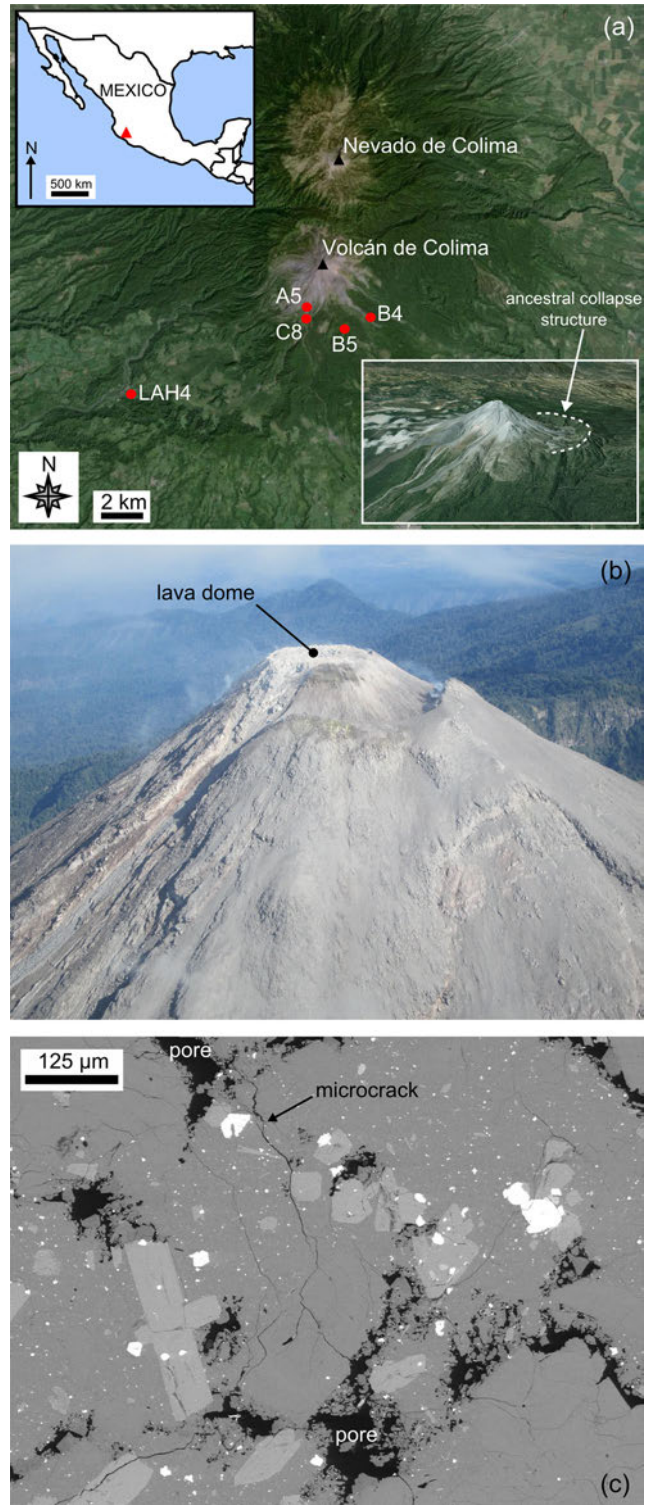


**Fig. 1** **a** Google Earth™ map showing the locations of the sampling sites with respect to Volcán de Colima and Nevado de Colima. Insets show a map of Mexico (the red triangle corresponds to the position of Volcán de Colima) and a Google Earth™ image of Volcán de Colima showing the ancestral collapse structure (dashed white line). **b** Aerial photograph of the dome at Volcán de Colima (May 2014; photo credit: M. Heap). **c** Scanning electron microscope image showing the porosity network with a sample of andesite (B5) from Volcán de Colima. The microstructural elements are identified on the figure

gas-and-ash events and larger dome-disrupting Vulcanian events. The most intense period of activity provided at least 30 explosions, generating pyroclastic flows that reached distances as far as 5.4 km from the active vent (Varley et al. 2010). The most recent eruptive sequence, which started in January 2013, has involved dome growth and lava extrusion punctuated by pyroclastic density currents and Vulcanian explosions. Frequent explosive events were ongoing at the time of writing (i.e. May 2015).

## Experimental materials

We selected four andesitic lava blocks (typically  $30 \times 30 \times 30$  cm) to represent the variation in porosity typically seen within the materials forming the edifice at Volcán de Colima. A recent field-based study at Volcán de Colima (Farquharson et al. 2015) revealed the porosity of the eruptive products to be between 2 and 75 % (based on 542 hand samples). Using the method of Bernard et al. (2015), a weighted abundance analysis of these data shows that the predominant porosity class at Volcán de Colima is between 10 and 25 %. Using a similar field density technique, Mueller et al. (2011) found an average porosity of 16.4 % (based on 299 hand samples; see also Lavallée et al. 2012) and Lavallée et al. (2015) found that the average porosity of 2635 hand samples to be about 20 % (porosity ranged from 8 to 40 %). The range of porosities studied herein (from 7 to 25 %) is therefore representative of the rocks most frequently observed in the field.

The first block, A5, is from the 1998–1999 lava flow in the Cordoban ravine and contains a connected porosity of about 11 %. B5 is from an older lava flow of unknown age and contains a connected porosity of around 8 %. We note that B5 displays a certain degree of high-temperature alteration, as evidenced by the presence of vapour-deposited cristobalite within the pores (Fig. 1c; see Horwell et al. 2013 and Schipper et al. 2015). Block C8 was taken from the 1998–1999 blow-and-ash flow in the San Antonio ravine and contains a connected porosity of about 17 %. Finally, LAH4 is a block of unknown age collected from a lahar deposit on the west flank of the volcano (in the El Zarco river bed near La Becerrera); LAH4 contains a connected porosity of approximately 25 %. The locations of the collection sites are indicated in Fig. 1a. Using the classification scheme of Farquharson et al. (2015), B5 can be classified as “altered lava” and A5, C8 and LAH4 as “lava”. All of the andesite blocks contain a dual porosity: a combination of microcracks and pores (Fig. 1c, Heap et al. 2014b). In detail, the andesites are pervasively microcracked (containing average microcrack densities between 35 and 45 mm<sup>-1</sup>) and contain high pore number densities (between 3.3 and 8.1 mm<sup>-2</sup>) and wide pore size distributions (the pore diameters range between about 0.02 and 2.0 mm; Heap et al. 2014b). The andesites have a porphyritic texture containing a microlitic groundmass (59–68 %)

containing commonly microcracked phenocrysts (<1.5 mm in diameter) of plagioclase (13–25 %), clinopyroxene (3–4 %) and orthopyroxene (2–4 %). All of the andesites contain between 58 and 61 wt% silica (Heap et al. 2014b), compositionally representative of recently erupted materials from Volcán de Colima (Luhr 2002; Savov et al. 2008). Cylindrical core samples, cored in the same orientation to a diameter of 20 mm and precision-ground to a nominal length of 40 mm, were prepared from each of the blocks. The connected water porosities of the samples were measured using the triple weight water-saturation (distilled water) method.

## Experimental methods

All experiments were performed at the Géophysique Expérimentale laboratory at the Institut de Physique du Globe de Strasbourg. Uniaxial compressive strength (UCS;  $\sigma_1 > \sigma_2 = \sigma_3 = 0$ ) experiments were performed on water-saturated samples of each andesite at a constant strain rate of  $10^{-5}$  s<sup>-1</sup> until failure. During uniaxial compression, axial stress was measured using a load cell and axial strain via a displacement transducer. The water-saturated samples were deformed inside a bath of distilled water. Triaxial deformation experiments were performed using a conventional triaxial apparatus ( $\sigma_1 > \sigma_2 = \sigma_3$ ) on water-saturated samples at a constant strain rate of  $10^{-5}$  s<sup>-1</sup>. Our chosen strain rate is the standard for rock deformation experiments in compression, allowing our data to be compared with the wealth of pre-existing data (see review by Wong and Baud 2012). All triaxial experiments were performed under drained conditions. The pore fluid pressure was kept at a constant 10 MPa, and we ran experiments at confining pressures between 15 and 80 MPa (i.e. Peffs between 5 and 70 MPa), equivalent to depths between a couple of a hundred metres to about 3 km. For the purpose of this study, we assume a simple effective pressure (Peff) law such that  $Peff = P_c - \alpha P_p$ , where poroelastic constant  $\alpha$  is assumed to be 1. Prior to deformation, the samples were left at the target effective pressure for at least 12 h to ensure microstructural equilibrium. During experimentation, we measured axial stress via a load cell and axial strain using a displacement transducer located on the top piston. Porosity change was measured using a pore pressure intensifier/volumometer and the output of acoustic emissions (AEs) and AE energy (the area under the received AE waveform) using a piezoelectric crystal attached to the top piston. Hydrostatic experiments—during which the confining pressure acting on a sample is increased while maintaining a constant pore fluid pressure—were also performed on a sample of each andesite. No differential stress is imposed on the sample during these experiments (i.e.  $\sigma_1 = \sigma_2 = \sigma_3$ ). To ensure microstructural equilibration, the samples were first left for at least 12 h under a confining pressure of 12 MPa and a pore pressure of 10 MPa. The confining pressure was increased at a servo-controlled rate of

0.003 MPa s<sup>-1</sup>, and the porosity change was monitored during the experiments using a pore pressure intensifier/volumometer. Details of the triaxial experimental apparatus can be found in a previous contribution (Heap et al. 2014a). All of the experiments reported in this study were performed at room temperature. The focus of this study is to characterise the mechanical behaviour of edifice-forming andesites, which have long since cooled below the glass transition temperature ( $T_g$ ) of their melt phase (~740 °C, Lavallée et al. 2012). While we are confident that viscous deformation will only occur within edifice rock in contact with a heat source (e.g. a dyke), we are aware that elevated temperatures may encourage sub-critical crack growth (Brantut et al. 2013), although we note that increasing the temperature from room temperature to 75 °C did not significantly influence the deformation rate during a long-term triaxial experiment on a basalt from Mt Etna (Brantut et al. 2013). At the strain rates studied herein, we do not expect a temperature-induced change in failure mode at temperatures below  $T_g$ , exemplified by the brittle and dilatant behaviour of basalt and crystallised dacite samples deformed triaxially at high temperature (up to 900 °C; Smith et al. 2011; Violay et al. 2015). In this study, we adopt the convention that compressive stresses and strains are positive. An experimental summary, containing all of the data collected for this study, is given as Table 1.

## Failure mode: dilatant or compactant?

The mechanical behaviour of rock is often classified as brittle or ductile (Rutter 1986; Evans et al. 1990; Paterson and Wong 2005; Wong and Baud 2012). Shear fracturing, a product of the coalescence of (predominately tensile) microcracks, is described as a brittle mode of failure. Ductile behaviour, however, defined simply as the capacity of a material to deform to a substantial strain without the tendency to localise the flow into faults (Rutter 1986), can be the result of a variety of microstructural deformation mechanisms, including microcracking (in the case of cataclastic flow); the description of ductility holds no mechanistic connotation (Rutter 1986). However, due to instances of compaction localisation (e.g. Baud et al. 2004), and because ductile behaviour can be driven by microcracking (i.e. “brittle” on the microscale), we have simplified our classification of the failure mode of rock in this manuscript to “dilatant” and “compactant”.

Stress-strain curves and porosity reduction-strain curves for each of the andesite lavas, for different effective pressures (from 0 to 70 MPa or depths from 0 m to 3.2 km), are shown in Fig. 2. Dilatant behaviour (blue curves) is characterised by strain softening and large stress drops, typically associated with shear fracture formation (Fig. 2). The convex shape of the initial portion of the stress-strain curves (e.g. Fig. 2a) is typically attributed to the closure of microcracks aligned sub-

perpendicular to the loading direction. Indeed, the initial portion of the porosity reduction curves shows that the lava is compacting (e.g. Fig. 2a). The lavas then enter an elastic deformation stage where the stress-strain curve is quasi-linear, followed by a stage where the curves are concave. At the beginning of this latter stage, microcracks nucleate and grow (inelastic deformation). The onset of dilatancy, termed  $C'$  (Wong et al. 1997), is best observed using porosity change measurements (see discussion below) but can usually be observed as the start of an acceleration in AE activity (Fig. 3a), used as a proxy for the nucleation and growth of microcracks (e.g. Lockner 1993). The onset of dilatant microcracking can be observed as a reduction in the rate of porosity decrease in the porosity reduction curves (e.g. Fig. 2a; Wong et al. 1997), and eventually, as the rate of microcracking accelerates, the lava switches from compaction-dominated behaviour to dilation-dominated behaviour. The rate of microcracking, monitored by the output of AE (Fig. 3a), continues to accelerate up to the peak stress ( $\sigma_p$ ). Following the peak stress, there is a strain softening phase before the lava succumbs to macroscopic failure, marked by a large stress drop and a rapid acceleration in AE activity (Fig. 3a). The stress-strain curves for the lavas are typical of those for rock in compression (e.g. Hoek and Bieniawski 1965; Brace et al. 1966; Scholz 1968). We note that, for the dilatant lavas, the peak stress and the strain-at-failure increases, and the magnitude of the stress drop decreases, with increasing effective pressure (see also Paterson and Wong 2005). We also highlight that the porosity reduction curves show that samples deformed at higher effective pressures show less net dilation (e.g. Fig. 2a). Visual inspection of the deformed samples confirmed that the samples contained localised shear fractures typically orientated at about 30° to the maximum principal stress.

Compactant behaviour (red curves) of the andesitic lavas is characterised by the lack of significant strain softening, strain hardening (in some cases) and many small stress drops (of a couple of MPa) (Fig. 2). Similar to the dilatant curves, the compactant curves contain an initial convex portion, associated with the closure of microcracks (the porosity reduction curves show that the lava is compacting; e.g. Fig. 2c, d) and an elastic deformation stage where the stress-strain curve is approximately linear. However, unlike the dilatant curves, there is no switch to dilation dominance. At a critical stress state, termed the onset of shear-enhanced compaction or  $C^*$  (Wong et al. 1997), the rate of compaction increases (e.g. Fig. 2c, d). As for  $C'$ ,  $C^*$  is best observed using porosity change measurements (see discussion below) but also usually marks the position of the onset of significant AE activity (Fig. 3b) whereas the lava begins to deform inelastically. We also note the presence of many small stress drops that are contemporaneous with sudden and temporary increases in the rate of AE output (Fig. 3b); such stress drops and AE bursts have previously been attributed to compaction

**Table 1** Experimental summary of the 39 experiments performed for this study. All experiments were performed at the Géophysique Expérimentale laboratory at the Institut de Physique du Globe de Strasbourg.  $C^*$  - onset of

shear-enhanced compaction;  $P$  - effective mean stress;  $P^*$  - onset of lithostatic inelastic compaction; N/A - not available (sample was too strong to break in our experimental setup under these pressure conditions)

Block	Sample	Connected porosity (%)	Confining pressure (MPa)	Pore pressure (MPa)	Effective pressure (MPa)	Peak differential stress (MPa)	$C^*$ (MPa)	$P$ (MPa)	$P^*$ (MPa)	Notes
B5	4_s1	7.9	0	0 (wet)	0	81.1	—	27.0	—	
B5	8	7.3	15	10	5	136.0	—	50.3	—	
B5	7	7.4	20	10	10	184.9	—	71.6	—	
B5	10	7.9	40	10	30	270.7	—	120.2	—	
B5	11	7.5	60	10	50	281.4	—	143.8	—	
B5	4	7.7	80	10	70	N/A	—	—	—	
B5	2	7.6	Hydro	10	Hydro	—	—	—	—	N/A
B5	3	7.6	Hydro	10	Hydro	—	—	—	—	N/A
A5	7	12.3	0	0 (wet)	0	64.8	—	21.6	—	
A5	17	9.3	15	10	5	128.7	—	47.9	—	
A5	10_s1	11.2	20	10	10	164.2	—	64.7	—	
A5	4_s1	11.7	40	10	30	209.1	—	99.7	—	
A5	14_s1	10.6	60	10	50	261.7	—	137.2	—	
A5	4	11.2	80	10	70	—	290.1	166.7	—	
A5	20	9.8	Hydro	10	Hydro	—	—	—	—	N/A
C8	5_s1	17.6	0	0 (wet)	0	17.5	—	5.8	—	
C8	16	16.2	15	10	5	74.1	—	27.7	—	Microstructure
C8	4_s1	17.9	20	10	10	62.3	—	30.8	—	
C8	19	19.4	40	10	30	—	43.4	44.5	—	
C8	23	18.5	40	10	30	—	48.7	46.2	—	
C8	20	17.6	60	10	50	—	45.3	65.1	—	
C8	8	15.5	60	10	50	—	103.5	84.5	—	$C^*$ (20 % strain)
C8	21	16.5	60	10	50	—	60	70	—	Microstructure; 1.5 % strain
C8	5	16.3	60	10	50	—	78.3	76.1	—	Microstructure; 3 % strain
C8	4	16.4	60	10	50	—	60.3	70.1	—	Microstructure; 6 % strain
C8	26	16.7	60	10	50	—	59.5	69.8	—	Permeability; 1.5 % strain
C8	25	17.2	60	10	50	—	49.4	66.5	—	Permeability; 4.5 % strain
C8	22	19.0	80	10	70	—	26.5	78.8	—	
C8	6	16.7	Hydro	10	Hydro	—	—	—	126.0	
C8	7	16.7	Hydro	10	Hydro	—	—	—	151.7	Microstructure
C8	i	17.2	0	0	0	fractured in tension	—	—	—	Permeability
C8	ii	18.1	0	0	0	fractured in tension	—	—	—	Permeability
LAH4	7	23.8	0	0 (wet)	0	31.3	—	10.4	—	
LAH4	1	24.1	20	10	10	69.5	—	33.2	—	
LAH4	2	24.0	40	10	30	—	92.5	60.8	—	
LAH4	4	24.2	60	10	50	—	72.9	74.3	—	
LAH4	6	24.5	80	10	70	—	56.4	88.8	—	
LAH4	8	23.8	Hydro	10	Hydro	—	—	—	160.6	
LAH4	9	23.8	Hydro	10	Hydro	—	—	—	150.0	

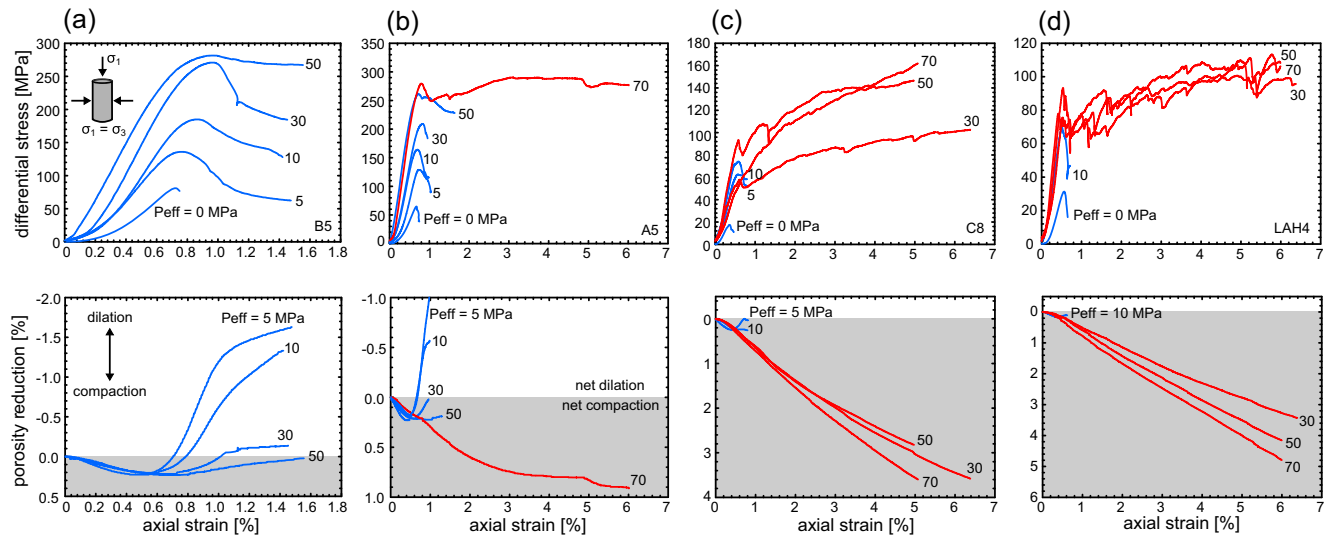


**Fig. 2** Mechanical data. Stress-strain curves and porosity reduction curves for andesitic lava from Volcán de Colima: **a** B5, **b** A5, **c** C8 and **d** LAH4. The effective pressure ( $P_{eff}$ ) of the experiment is shown next to

each curve. Dilatant curves are shown in blue and compactant curves are shown in red. Net compaction in the graphs of porosity reduction is highlighted in grey, net dilation in white

localisation in porous rock (Baud et al. 2004; this is discussed further in the “Operative micromechanical processes” section). Unlike failure in the dilatant regime, the differential stress required for the onset of shear-enhanced compaction decreases with increasing effective pressure. Our experiments highlight that the rate of compaction increases as the effective pressure increases (e.g. Fig. 2d); for example, at 6 % axial strain, LAH4 had lost about 3 and 5 % porosity at effective pressures of 30 and 70 MPa, respectively.

The transition between dilatant and compactant behaviour was observed at effective pressures of 30 MPa and above (equivalent to depths greater than about 1.6 km) for the higher

porosity lavas (C8 and LAH4), while the failure mode of the samples from the blocks containing the lowest porosities (B5 and A5) remained dilatant up to 50 MPa. Above 50 MPa (depth ~2.4 km), A5 switched from a dilatant to a compactive failure mode (B5 was too strong to break in our triaxial press at a  $P_{eff}$  of 70 MPa).

Additional insights into the mechanical behaviour of the andesites can be gleaned by plotting the porosity reduction versus the effective mean stress ( $P$ ), where  $P=((\sigma_1+2\sigma_3)/3)-P_p$ . Such curves highlight the difference between hydrostatic ( $\sigma_1=\sigma_2=\sigma_3$ ) and shear stresses ( $\sigma_1>\sigma_2=\sigma_3$ ) on the evolution of porosity (Fig. 4). In the hydrostatic case, the onset of

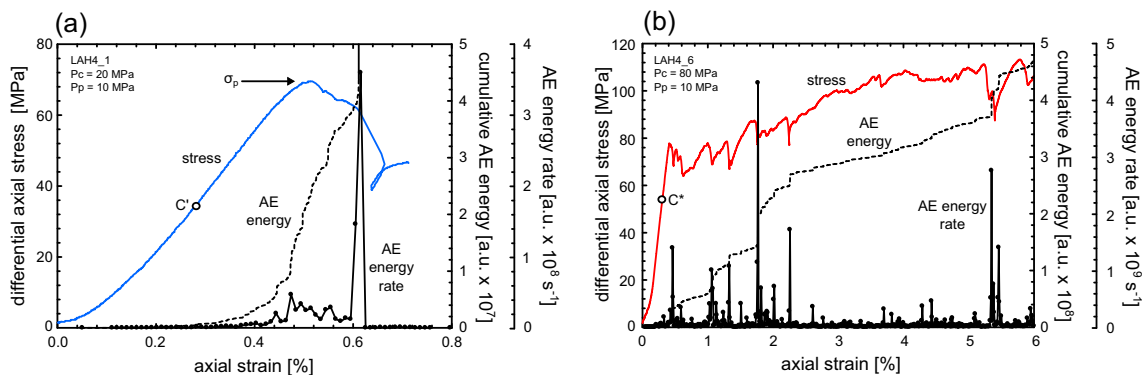


**Fig. 3** Acoustic emission characteristics. Cumulative acoustic emission energy (AE) and AE energy rate (AE energy is given in arbitrary units, a.u.) during **a** a dilatant constant strain rate experiment ( $P_{eff}=10$  MPa) and **b** a compactant constant strain rate experiment ( $P_{eff}=70$  MPa) on porous andesite. The experiments shown here were performed on samples

of LAH4 (the same experiments presented in Fig. 2d). The positions of the onset of dilatational microcracking ( $C'$ ) and the peak stress ( $\sigma_p$ ) are indicated in panel **a**, and the position of the onset of shear-enhanced compaction ( $C^*$ ) is indicated in panel **b**

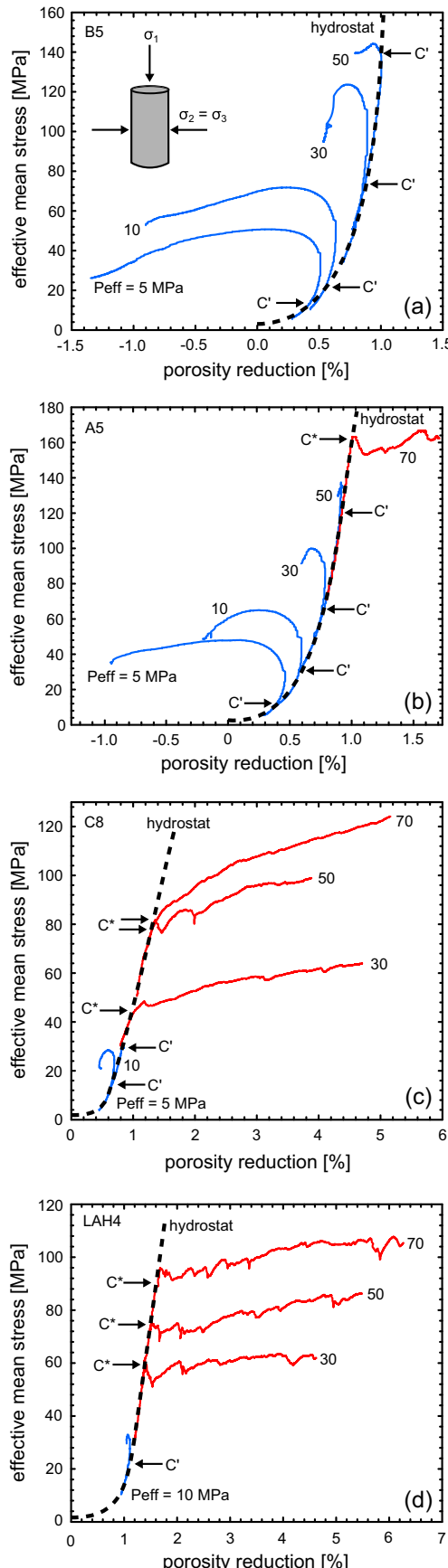


**Fig. 4** Plots of porosity reduction against effective mean stress for andesitic lava from Volcán de Colima (the same experiments presented in Fig. 2): **a** B5, **b** A5, **c** C8 and **d** LAH4. The effective pressure ( $P_{eff}$ ) of the experiment is shown next to each curve. Dilatant curves are shown in blue and compactant curves are shown in red. The positions of the onset of dilatational microcracking ( $C'$ ) and the onset of shear-enhanced compaction ( $C^*$ ) are indicated where appropriate. The hydrostatic curves (“hydrostats”) are given as black dashed lines

inelastic compaction is termed  $P^*$  (Wong et al. 1997; Fig. 4).  $P^*$  was attained for the two most porous samples (C8 and LAH4; see Table 1), but A5 and B5 contain porosities too low to observe  $P^*$  in our experimental setup. We note that, in all cases, an increase in hydrostatic stress resulted in a decrease in porosity. Prior to  $P^*$ , this is attributed to the elastic closure of porosity as pressure is increased; the acceleration in porosity loss following  $P^*$  is attributed to inelastic compaction (Wong et al. 1997). Any deviation from the hydrostatic curve (or “hydrostat”) during a constant strain rate triaxial experiment must therefore be the consequence of differential stress on the porosity evolution. A dilatant mode of failure is characterised by a deviation to the left (porosity increase), marked by  $C'$ , and a compactant mode of failure by a deviation to the right (porosity decrease), marked by  $C^*$  (see Wong et al. 1997).

## Constructing failure envelopes for porous andesite

The data of this study can be used to map failure envelopes for andesite lava containing different porosities (Fig. 5). In the dilatant regime, the peak stress maps the dilatant failure envelope on a plot of differential stress ( $Q$ ) versus effective mean stress. In the compactant regime, it is the stress at the onset of shear-enhanced compaction  $C^*$  that delineates the compactive yield envelope. The positions of  $P^*$ , lithostatic inelastic compaction, plot along the  $x$ -axis ( $Q=0$  MPa). The lava has failed (or yielded) if the stress state plots outside the failure envelope (shear fracture on the left and inelastic compaction on the right; see inset in Fig. 5a). It follows that stronger rocks will therefore be intact over a much larger  $P$ - $Q$  space (i.e. the failure envelope will have a larger amplitude).

The complete failure envelopes are only available for the most porous lavas (C8 and LAH4); the low-porosity lavas (A5 and B5) were dilatant for the majority of the  $P$ - $Q$  space attainable in our apparatus. The dilatant failure envelopes for the andesites highlight that differential stress at failure increases linearly with effective mean stress, in accordance with the Mohr-Coulomb criterion. While it is common for porous sedimentary rocks to have parabolic compactive yield envelopes (Wong and Baud 2012), the andesitic lavas of this study have linear compactive envelopes. This is likely the result of the duality of the porosity (microcracks and pores), as previously suggested by Zhu et al. (2010). As mentioned above, an

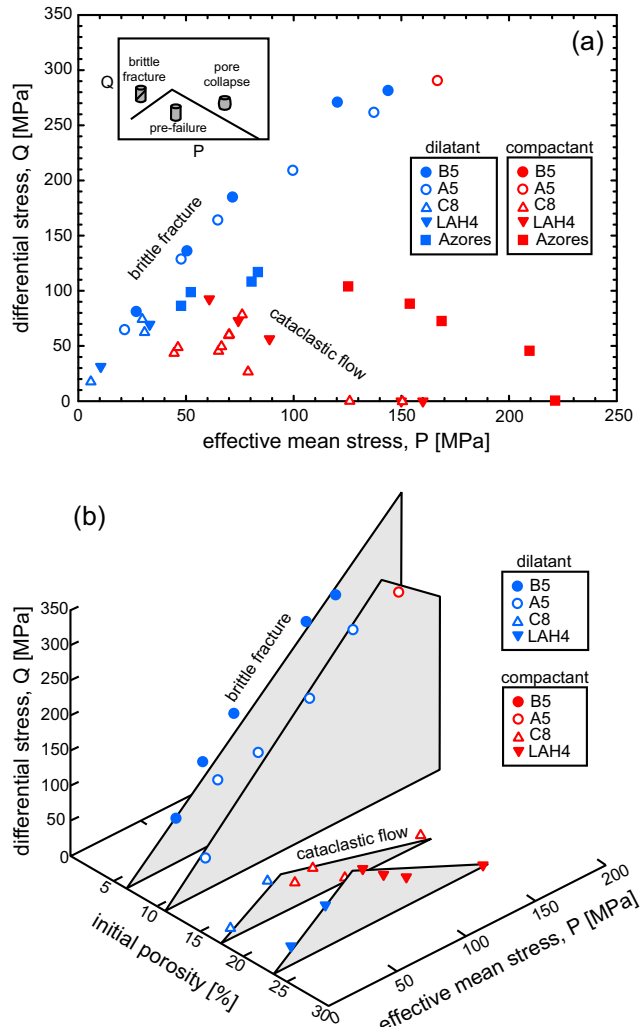


**Fig. 5** Failure envelopes for andesitic lava from Volcán de Colima. **a** The experimental data plotted on differential stress  $Q$  at failure versus effective mean stress  $P$ . **b** A 3D plot of differential stress at failure and effective mean stress plotted alongside the initial connected porosity. Dilatant experiments are shown as blue symbols and compactant experiments as red symbols. Data for Açores trachyandesite (squares) from Loaiza et al. (2012) is also presented in panel **a**

increase in confining pressure on the compactive side of the failure envelope reduces the differential stress required for the onset of shear-enhanced compaction. However, in a rock containing microcracks and pores, an increase in confining pressure must also close a larger proportion of the pre-existing microcracks. Therefore, for the same increase in confining pressure, the decrease in the differential stress required for  $C^*$  may be less for a rock containing microcracks than for an initially microcrack-free rock. The result, in  $P$ - $Q$  space, is a linear compactive envelope. We note that parabolic envelopes were observed for a porous trachyandesite from the Azores (Loaiza et al. 2012; Fig. 5a) and porous tuff (Zhu et al. 2011), both of which contain low initial microcrack densities.

We find, in general, that the amplitude of the failure envelope is lower when the porosity is higher. In other words, lava containing lower porosity is intact (or pre-failure) over a much larger stress space. This is best observed on our 3D plot where the differential stress at failure and the effective mean stress are plotted alongside the initial connected porosity (Fig. 5b). 3D yield caps are typically deployed in soil mechanics, but have also been successfully applied to rocks (see Cuss et al. 2003 and references therein). In these studies, the third axis is the porosity multiplied by the grain size; in our diagram, we have chosen to use initial connected porosity as our third axis, since volcanic rocks cannot be described by a grain size and, while an average pore size could be utilised here, we highlight that the pore size distribution of our rocks varies tremendously (Heap et al. 2014b), raising doubt over the applicability of an average pore size.

Contrary to our expectation, the 3D failure envelopes show that the amplitude of the failure envelope for LAH4 (porosity=25 %) is larger than that of C8 (porosity=18 %) (Fig. 5b). The cause of this discrepancy is likely the result of the difference in pore size distribution and the size of the largest pore between the two andesites. While LAH4 contains a large number of small pores, and few large pores (the largest is about just over 1 mm), C8 contains a much wider pore size distribution, including pores almost 2 mm in diameter (Heap et al. 2014b). The stress intensity is higher at the tips of cracks emanating from larger pores (Sammis and Ashby 1986). A crack will propagate when a critical stress is reached; therefore, the larger the pore, the lower the applied differential stress required for crack propagation (see also Heap et al. 2014c). Therefore, pore size should also be considered important in controlling the mechanical behaviour and failure mode of volcanic rocks, just as grain size is important for sandstones (Wong and Baud 2012). Another noteworthy observation is that the failure envelope for the trachyandesite from the Açores (porosity=18 %, Loaiza et al. 2012) has a much larger amplitude than that of the andesite from Volcán de Colima with a comparable porosity (C8, porosity=17 %; Fig. 5a). While this difference could be explained by the differences in microcrack density and/or the pore size, we highlight a potential role for the presence of phenocrysts. The trachyandesite from the Açores is aphanitic (the crystals are microlites), while the andesites from Volcán de Colima are porphyritic (crystals are as large as a couple of mm). Phenocrysts in volcanic rocks often contain microcracks and other defects (plagioclase can be twinned for example) and could therefore affect their mechanical behaviour, although no firm conclusions can be drawn from the available data.

## Operative micromechanical processes

It is well known that the formation of a shear fracture is the result of the nucleation, growth and coalescence of

microcracks (e.g. Lockner et al. 1991). For porous materials, including rocks, microcracks usually emanate from pre-existing pores (e.g. Sammis and Ashby 1986; Wong and Baud 2012). Figure 6a shows a scanning electron microscope (SEM) image of a sample of andesite (C8) deformed within the dilatant regime ( $P_{eff}=5$  MPa). We clearly see pore-emanated microcracks that are orientated sub-parallel to the maximum principal stress. We note that the microcracks shown in Fig. 6a form part of the macroscopic localised (i.e. the microstructure appears undisturbed outside the fracture) shear fracture.

Microstructurally, the inelastic compaction of porous rocks is typically attributed to cataclastic pore collapse and grain crushing (e.g. Wong and Baud 2012). Although microstructural observations have shown that pore collapse and grain crushing can be distributed throughout the sample (e.g. Menéndez et al. 1996), there are cases of compactive localisation. These features are well documented (in the field and laboratory) in porous sandstones (e.g. Mollema and Antonellini 1996; Baud et al. 2004) and limestones (e.g. Cilona et al. 2014), and are called compaction bands. Compaction bands in sandstones, for example, are subplanar

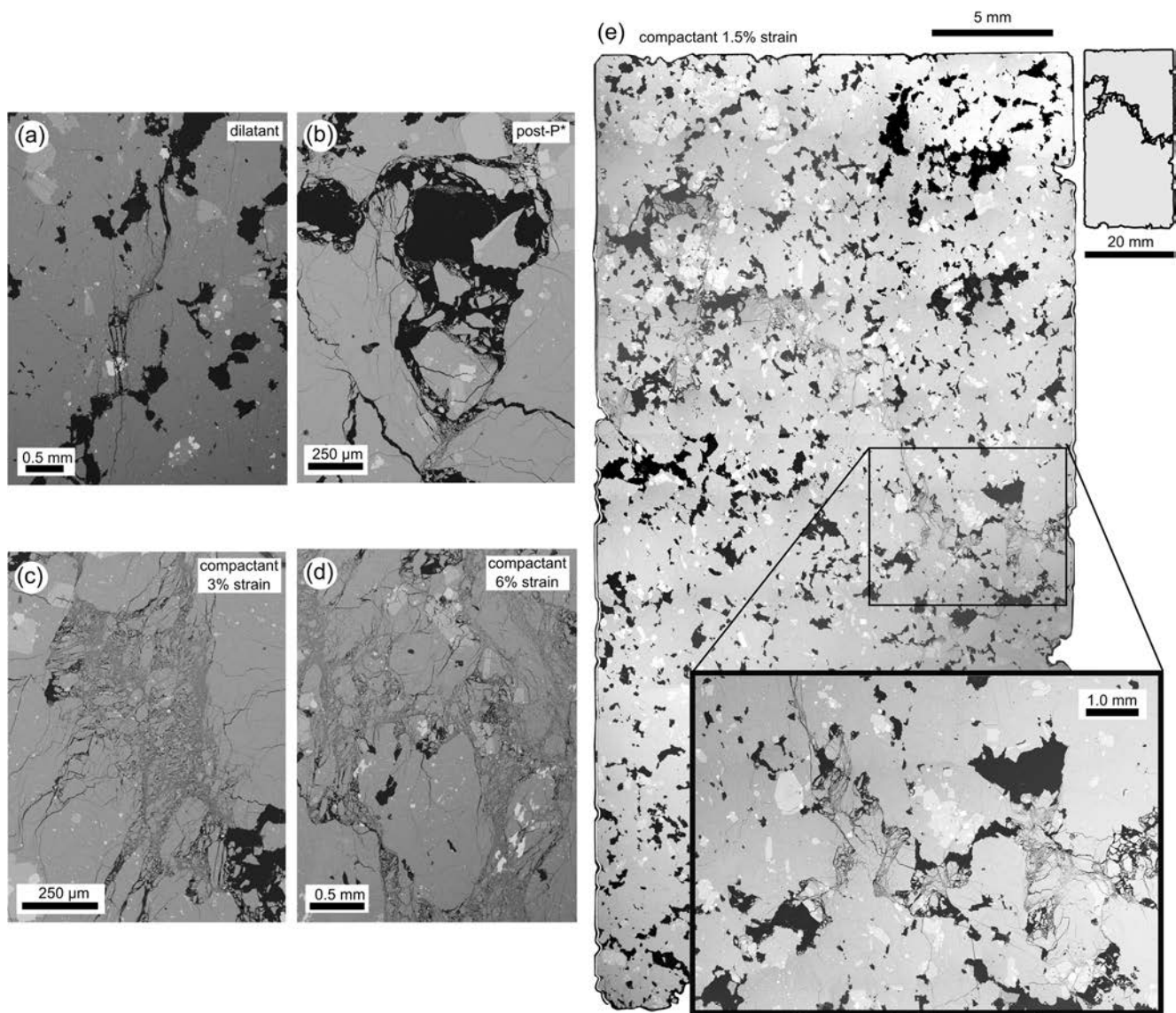


**Fig. 6** Microstructure. **a** Back-scattered scanning electron microscope (SEM) picture of pore-emanating microcracking from a dilatant constant strain rate experiment ( $P_{eff}=5$  MPa) on a sample of C8. **b** SEM picture of cataclastic pore collapse during hydrostatic loading of a sample of C8 beyond the onset of hydrostatic pore collapse ( $P^*$ ). **c** SEM picture of cataclastic pore collapse from a compactant constant strain rate

experiment ( $P_{eff}=50$  MPa) on a sample of C8 taken to 3 % axial strain. **d** SEM picture of cataclastic pore collapse from a compactant constant strain rate experiment ( $P_{eff}=50$  MPa) on a sample of C8 taken to 6 % axial strain. **e** SEM map showing a compaction localisation feature (band of collapsed pores) from a constant strain rate experiment ( $P_{eff}=50$  MPa) on a sample of C8 taken to 1.5 % axial strain

surfaces of localised compaction—typically a few grains thick—orientated perpendicular to the maximum principal stress that show little or no evidence of shear. The porosity within the band is typically much lower than that of the surrounding host rock (e.g. Baud et al. 2006). During laboratory experiments, the appearance of compaction bands in sedimentary rock is typically associated with small stress drops (of a few MPa) and a sudden, temporary increase in the rate of AE activity (Baud et al. 2004, 2006).

Recently, two studies have shown evidence for compaction localisation in porous volcanic rocks (Loaiza et al. 2012; Adelinet et al. 2013). For example, Loaiza et al. (2012) showed that compaction localisation in porous trachyandesite deformed at a confining pressure of 130 MPa is manifest as bands of collapsed pores sub-perpendicular to the maximum principal stress. The structure was approximately 2 mm thick, roughly the average pore diameter. Small stress drops were seen in the stress-strain curves of these experiments, although AEs were not recorded during the experiments. The confining pressures required for the formation of compactive localisation in the trachyandesite were in excess of 95 MPa (i.e. at depths greater than about 4 km; Loaiza et al. 2012), perhaps too deep to be volcanologically relevant. The significance of these features within a volcano is that an experimental study on compactive localisation in sandstones has shown that permeability can be reduced by up to three orders of magnitude (Baud et al. 2012). As discussed above, the permeability of the country rock can impact sidewall outgassing, an important factor governing eruption explosivity (this is discussed further in the “[Impact of failure mode on permeability](#)” section).

To investigate the microstructural progression of our andesite lavas during compactive deformation, and to look for evidence of compaction localisation (as suggested by our mechanical data: we also observe the small stress drops associated with an increase in the rate of AE activity documented by Baud et al. 2004 and Baud et al. 2006), we performed three additional constant strain rate experiments on samples of C8 at an effective pressure of 50 MPa (corresponding to a depth of about 2 km) to axial strains of 1.5, 3 and 6 % (Table 1). As before (Fig. 3b), the stress-strain curves were punctuated by small stress drops associated with bursts of AE activity. We also performed an additional hydrostatic experiment to study the microstructure of a sample deformed beyond  $P^*$  (Table 1). Similarly to previous studies on porous sedimentary rocks (Wong and Baud 2012) and volcanic rocks (Zhu et al. 2011; Loaiza et al. 2012), the acceleration in porosity reduction at  $P^*$  seen here is the result of distributed pore collapse (Fig. 6b). Collapsed pores are partially filled with broken fragments of groundmass and are often bounded by microcracks (Fig. 6b).

An SEM map of the sample deformed to an axial strain of 1.5 %, i.e. immediately following the first stress drop, shows clear evidence of a compactive strain localisation feature (Fig. 6e). The feature, a band of collapsed pores (that have

been infilled or partially filled with broken fragments of groundmass; see inset in Fig. 6e), traverses the diameter of the sample (20 mm) and is the thickness of the collapsed pore through which it passes (typically 0.25–0.5 mm). The band is not perpendicular to the maximum principal stress but is guided through the sample by the distribution of pores. Neighbouring collapsed pores are often connected by microcracks. We note that the pores appear undisturbed outside the band (i.e. the deformation is localised at the millimetre scale). Substantial pore collapse is seen in the samples deformed to 3 and 6 % strain (Fig. 6c, d). Due to the extent of the pore collapse, it is difficult to distinguish discrete bands of compacted pores. The observed deformation is likely the result of the amalgamation of several bands. We highlight that these cataclastic microstructures share similarities with the volcanic breccia found within the conduit zone of Unzen volcano, Japan (Goto et al. 2008).

Since a band is assumed to grow during a discrete stress drop and AE pulse (e.g. Baud et al. 2004), we can estimate (assuming uniaxial strain and that the bands are perpendicular to the maximum principal stress) that the inelastic axial strain associated with band growth is typically between 0.04 and 0.06 % for both C8 and LAH4 (corresponding to an axial shortening of about 20  $\mu\text{m}$ ). Microstructural observations indicate that the localised band has a thickness equal to the collapsed pore through which it passes (typically 0.25–0.5 mm), suggesting that the porosity reduction within the band is on the order of 4 to 8 %. In other words, the porosity is 17 % outside the band and about 10 % within the band. By contrast, the porosity of compaction bands in Bentheim sandstone was estimated to be about 8 %, considerably lower than the initial porosity of 23 % (Baud et al. 2004). These results are discussed further in the section “[Impact of failure mode on permeability](#)”. The ubiquity of cataclastic pore collapse during the deformation of porous volcanic rocks at high confining pressures (Zhu et al. 2011; Loaiza et al. 2012; Adelinet et al. 2013; Heap et al. 2014a, 2015) highlights the universality of pore collapse as the operative micromechanical mechanism driving low-temperature (below  $T_g$ ) compactant deformation in porous volcanic rocks.

Field, experimental and modelling evidence suggest that the development of compaction bands is enhanced in well-sorted sandstones (Wang et al. 2008; Cheung et al. 2012). When the grain size distribution is large, compaction bands do not form because the deformation is accommodated by the smaller grains (Cheung et al. 2012). However, extrusive volcanic rocks cannot be characterised by a grain size. Nevertheless, in a similar manner, could compactive localisation features only occur in volcanic rocks with a homogeneous pore size distribution? It follows that, if the pore size distribution is wide, the deformation may focus on the larger pores (e.g. Heap et al. 2014c), resulting in distributed cataclastic pore collapse (assuming that the large pores are

distributed throughout the sample). Compactive localisation features may therefore develop more easily when the pore size is relatively uniform. The collapse of one pore encourages the collapse of a neighbouring pore, due to the redistribution of stresses, promoting cascading pore collapse across the sample (in a similar way to cascading grain failure in the development of compaction bands in sandstones; Wang et al. 2008). However, we have observed compaction localisation in andesites with an extremely wide pore size distribution (C8; see Heap et al. 2014b; Fig. 6b). Firm conclusions on the favourable rock attributes for compaction localisation in volcanic rocks cannot be provided with currently available data, although we highlight a potentially important role for pore shape, a factor that displays much more variability in volcanic rocks than in sedimentary rocks. In a simplistic scenario where the pore shape is spherical, stresses are likely to focus on the larger pores, allowing the damage to be distributed throughout the sample. However, non-spherical pores may focus the deformation away from the larger pores and permit the formation of compactive localisation features through networks of misshapen pores. This interpretation is supported by the presence of large intact pores in C8 deformed to 1.5 % strain (Fig. 6).

### Impact of failure mode on permeability

Our experimental data demonstrate that edifice-building lavas can either dilate or compact in response to stress, depending on their depth and porosity. To explore permeability evolution as a consequence of dilatant and compactant failure modes, we measured the change in permeability of samples of porous (17 %) andesite (block C8) deformed in both regimes. Two samples (20 mm in diameter and about 20 mm in length) were loaded diametrically in uniaxial compression (at a constant strain rate of  $10^{-5} \text{ s}^{-1}$ ) until tensile failure, and two samples (20 mm in diameter and about 40 mm in length) deformed triaxially at a pore pressure of 10 MPa, a confining pressure of 60 MPa and a constant strain rate of  $10^{-5} \text{ s}^{-1}$  to axial strains of 1.5 and 4.5 %, respectively (Table 1). Gas (nitrogen) permeability was measured before and after deformation at a constant confining pressure of 1 MPa. We found that a tensile fracture—parallel to the imposed flow direction—serves to increase permeability by about a factor of two (permeability increased from  $6.2 \times 10^{-13}$  and  $1.6 \times 10^{-12} \text{ m}^2$  to  $1.0 \times 10^{-12}$  and  $2.8 \times 10^{-12} \text{ m}^2$  for the two samples, respectively). We note that (1) this increase may be reduced at confining pressures higher than 1 MPa (see Nara et al. 2011) and (2) a larger increase may be seen in andesites containing a lower initial porosity. The permeability of the fractured samples can be considered as an equivalent permeability (i.e. equal to the contribution of both the fracture and the host rock). Fracture permeabilities were calculated, using a fracture aperture of ~0.25 mm (determined through microstructural observations),

to be  $3.0 \times 10^{-11}$  and  $9.8 \times 10^{-11} \text{ m}^2$  for the two samples, respectively.

Compaction to 1.5 % strain reduced permeability from  $6.2 \times 10^{-12}$  to  $2.6 \times 10^{-12} \text{ m}^2$  (a decrease by a factor of about two), and compaction to 4.5 % strain reduced permeability from  $3.3 \times 10^{-12}$  to  $3.1 \times 10^{-13} \text{ m}^2$  (a decrease by about an order of magnitude). We highlight that compaction bands in sandstones resulted in a dramatic reduction in sample permeability (by up to three orders of magnitude, Baud et al. 2012). Our data suggest that a single band of collapsed pores—orientated perpendicular to the imposed flow direction—does not significantly reduce permeability and that this may be a result of a combination of their tortuous nature (gaps may exist over the area of the band) and the fact that the estimated porosity reduction within the band (4–8 %) is less than that typically estimated for compaction bands in sandstones (~15 %; Baud et al. 2012).

Taken together, these data suggest that the failure mode of the host rock will play an important role in conduit outgassing and therefore in dictating eruption characteristics: a dilatant failure mode in the upper conduit (<1 km) will assist outgassing, and compaction in the deep edifice (>1 km) will hinder outgassing (this is discussed further in the “Volcanological significance” section).

### Switching failure modes at high strains and the limit of compaction

As previously stated, porosity exerts a crucial role on the failure mode of rock (e.g. Wong and Baud 2012). However, we have also shown that porosity can be severely reduced during compactant deformation (Fig. 2). It follows that, after a certain degree of compaction, the rock may contain a porosity low enough to react to an applied stress in a dilatant manner. In rock mechanics, this strain-dependent switch in mechanical behaviour is referred to as  $C^*$  and has been observed in porous limestones (e.g. Baud et al. 2000) and sandstones (e.g. Schock et al. 1973; Baud et al. 2006).  $C^*$  will also provide us with a measure of the limit of inelastic porosity loss in porous andesitic edifice rocks. Prior to this study, this phenomenon had never been observed in porous extrusive volcanic rocks.

To explore this concept in porous andesite, we performed a constant strain rate experiment on a sample of C8 at an effective pressure of 50 MPa to an axial strain of 20 % (Fig. 7). We find that the switch from compactant to dilatant behaviour,  $C^*$ , occurs at an axial strain of about 13 % and a porosity loss of about 3.6 % (for a sample containing an initial porosity of 15.5 %). In other words, for this sample, the maximum porosity loss as a result of inelastic compaction is 3.6 %, leaving the sample with a porosity of 11.9 %. Considerable porosity destruction may not therefore be obtainable in porous andesitic edifice rocks, although the porosity reduction at  $C^*$  should

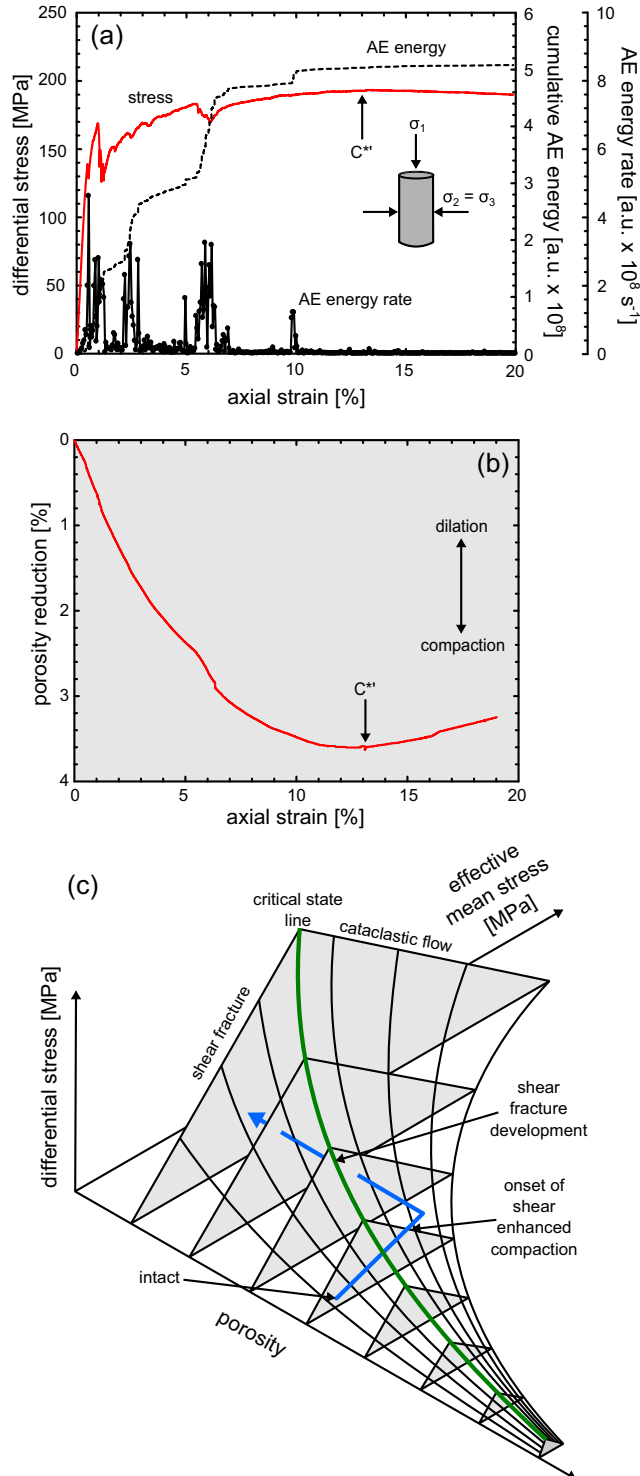


**Fig. 7** The strain-dependent switch to dilatant behaviour in porous andesite. **a** Stress-strain curve and the associated cumulative acoustic emission (AE) energy and AE energy rate (AE energy is given in arbitrary units, a.u.), for a constant strain rate experiment on a sample of C8 ( $P_{eff}=50$  MPa) deformed to an axial strain of 20 %. **b** The porosity reduction with axial strain for the experiment shown in panel **a**. The position of the switch to dilatant behaviour  $C^*$  is indicated on panels **a** and **b**. **c** 3D schematic diagram of differential stress, effective mean stress and initial connected porosity showing the path of a sample (blue solid line) deforming in the compactive regime to high strains. The sample eventually crosses the critical state line (the green solid line, the transition between compactant and dilatant behaviour) as a result of porosity reduction

places, of collapsed pores, intense fracturing and numerous anastomosing shear bands (Fig. 8b) containing fine-grained (from a few microns up to a few tens of microns) pulverised groundmass and crystals (Fig. 8c). Crystals on the boundary of the highly sheared bands have been fractured and the broken fragments have been transported parallel to the direction of shear (Fig. 8d). Outside the shear band, we notice that most of the pores are collapsed; the anastomosing shear bands often overprint evidence of cataclastic pore collapse (Fig. 8e). We again highlight the similarity between these microstructures and those of the volcanic breccia found within the conduit zone of Unzen volcano, Japan (Goto et al. 2008).

The switch in failure mode as porosity is reduced is best depicted on a 3D failure envelope (Fig. 7c). A theoretical “critical state line” can be mapped out schematically in  $P$ - $Q$ -porosity space to delineate the transition between dilatant and compactant behaviour (see Fig. 7c); with progressive compaction (i.e. a reduction on the porosity axis), compactant volcanic materials will migrate towards this line. The switch in failure mode would be observed as the reduction in porosity allows the rock to cross the critical state line, as shown in Fig. 7c. We infer that highly strained rocks (in our experiment,  $C^*$  required an axial strain of 13 %) near the conduit, or deep in the edifice, will be prone to this switch in failure mode (see “Volcanological significance” section). A strain-dependent switch to brittle failure has also been observed in high-temperature (940–945 °C) uniaxial deformation experiments on andesite from Volcán de Colima (Kendrick et al. 2013). However, in magma, the reduction in porosity required for a dilatant response is the consequence of viscous pore rearrangement and closure, rather than cataclastic pore collapse.

## Volcanological significance

Our experimental data help constrain the depth of the transition between a dilatant and compactant failure mode in edifice-forming andesitic lavas. Based on these data, we have constructed a schematic cross section of Volcán de Colima that highlights regions of the volcano that are likely to (1) be intact (any deformation is elastic), (2) fail in a

increase for rocks containing higher initial porosities and at higher pressures (depths) (Baud et al. 2006).

In a sample that has surpassed  $C^*$ , compactive pore collapse should be overprinted by a shear fracture. An SEM map of the deformed sample beyond  $C^*$  is presented as Fig. 8a and shows a well-developed shear zone, up to 10 mm thick in

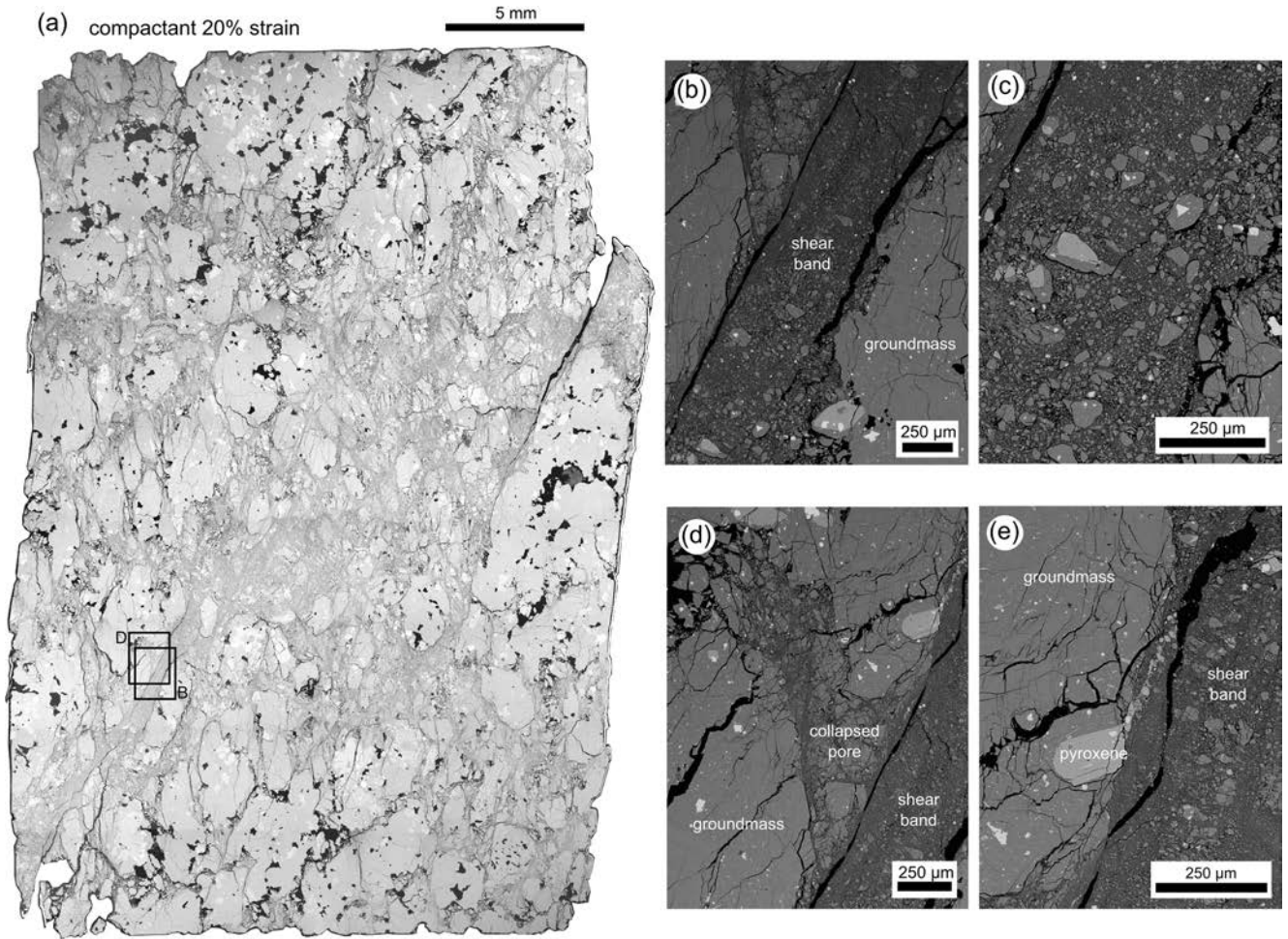


**Fig. 8** Microstructure. **a** Back-scattered scanning electron microscope (SEM) map of a sample of C8 deformed at a constant strain rate ( $P_{eff}= 50$  MPa) to an axial strain of 20 %. **b** SEM picture of one of the anastomosing shear bands. **c** SEM picture showing the crushed

groundmass and crystals within the anastomosing shear band shown in panel **b**. **d** Crosscutting relationships. An anastomosing shear band overprinting a collapsed pore. **e** Crystal fragments entrained by the shear band and transported along the direction of shear

dilatant manner, (3) fail in a compactant manner or, (4) fail via inelastic lithostatic compaction (Fig. 9). We anticipate that differential stress will be higher closer to the central conduit of dykes and that effective pressure will increase with depth. Porous andesites will react to regional and local stresses in a dilatant manner in the shallow edifice (<1 km) and in a compactant manner at depths greater than about 1 km. It is worthwhile noting that the depth of the transition between a dilatant and compactant failure mode is likely reduced for rocks containing higher porosities and increased for rocks containing lower porosities. The strain-dependent switch to dilatant behaviour ( $C^*$ ) is likely to be encountered deeper in the edifice, where older rocks have suffered significant inelastic strain. Inelastic lithostatic compaction ( $P^*$ ) can occur far from the sources of deformation but requires depths of at least 4–5 km (although we note that very porous rocks—such as pumiceous or scoracious rocks (see Farquharson et al. 2015)—may encounter inelastic lithostatic compaction at volcanologically relevant depths).

### Implications for lateral outgassing

The ease with which exsolved gases can escape the conduit can impact the style and intensity of an eruption; generally speaking, efficient outgassing promotes effusive behaviour whereas the retention of gas pressure promotes explosive behaviour (e.g. Eichelberger et al. 1986; Woods and Koyaguchi 1994; Rust et al. 2004; Mueller et al. 2008; Nguyen et al. 2014; Castro et al. 2014; Okumura and Sasaki 2014; Gaunt et al. 2014). The permeability of the edifice host lavas is likely to play an important role in the outgassing of the conduit magma (Jaupart 1998; Collombet 2009; Collinson and Neuberg 2012; Heap et al. 2014b; Farquharson et al. 2015); therefore, high-permeability host rocks may encourage effusive behaviour, and vice versa.

Our experimental data show that a throughgoing tensile fracture can increase sample permeability by a factor of two. Therefore, the dilatant deformation of edifice host rocks in the upper edifice (Fig. 9) may serve to increase permeability and

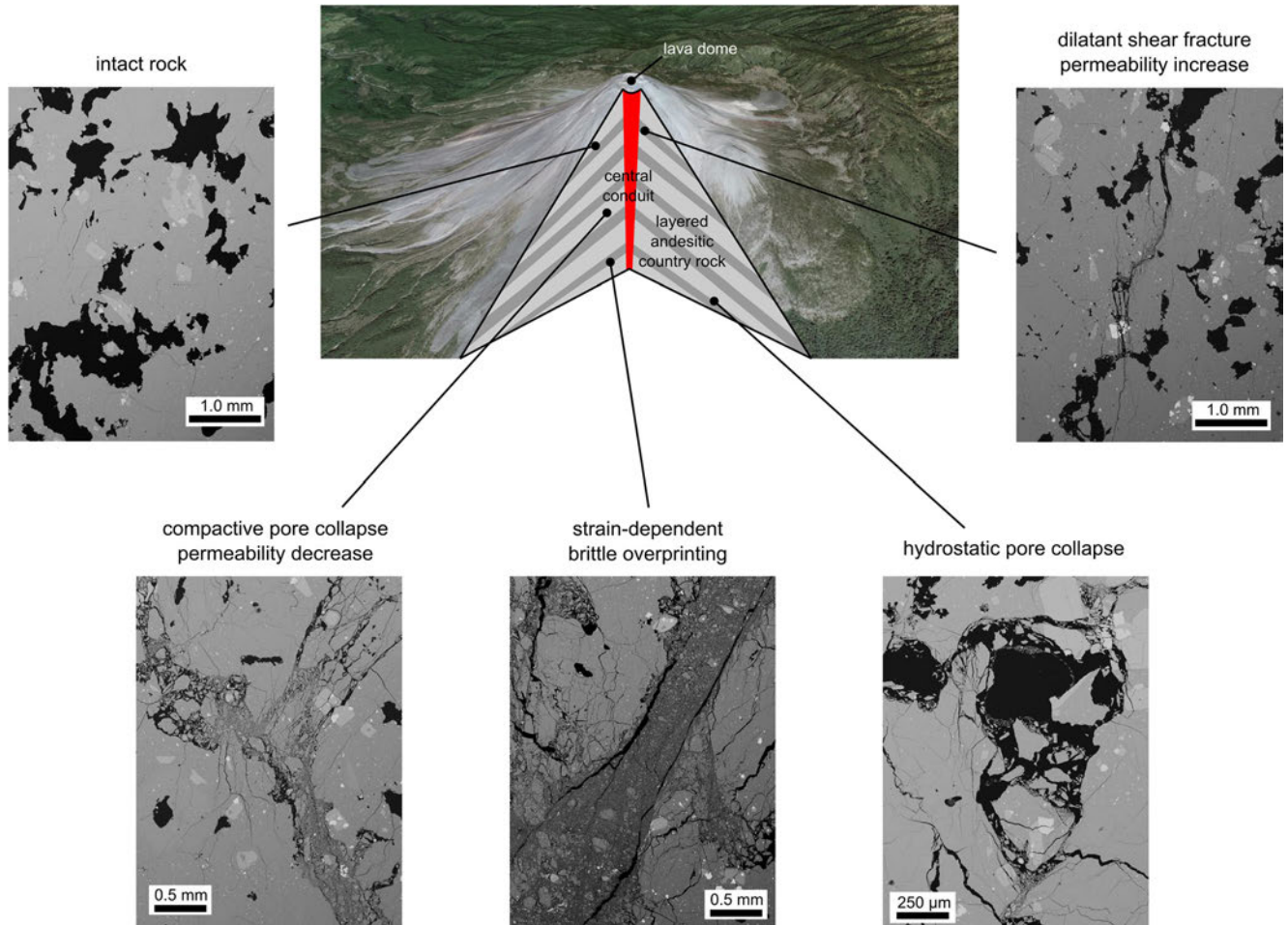


**Fig. 9** Schematic cross section of Volcán de Colima (layered andesitic edifice host rocks with a central conduit of dykes; image taken from Google Earth<sup>TM</sup>) . The cross section is annotated with back-scattered

scanning electron microscope pictures of the intact material and the various deformation microstructures. See text for details

assist the lateral outgassing of the conduit. However, we note that this increase in permeability may be suppressed at pressures high enough to close fluid pathways (e.g. Nara et al. 2011). Recent field evidence has exposed the ubiquitous presence of fractures within the dome, near the dome and on the upper flanks of Volcán de Colima (Kolzenburg et al. 2012; James and Varley 2012; Lavallée et al. 2015). Their presence, anticipated throughout the upper edifice (e.g. Heiken et al. 1988), serves as a testament to the ongoing brittle deformation and outgassing of the shallow edifice. Dilatant failure near the central conduit (the volume inferred to experience higher stresses) may create a permeable halo around the conduit down to a depth of about 1.5 km (i.e. the depth of the dilatant to compactant transition) that provides an efficient outgassing channel (e.g. Rust et al. 2004; Lavallée et al. 2013; Young and Gottsmann 2015). Further, outgassing through large-scale fractures and faults in the edifice is also supported by detailed field studies (e.g. Varley and Taran 2003).

Although edifice rocks are rarely above the temperature of their melt phase, preventing the efficient viscous sintering of

fractures, we highlight that hot pressing (e.g. Kolzenburg et al. 2012) and mineral precipitation (e.g. Taran et al. 2001; Horwell et al. 2013; Schipper et al. 2015) may promote fracture sealing and permeability reduction between periods of unrest activity.

By contrast, rock will deform in a compactant manner deeper in the edifice (Fig. 9). Data from this study show that compaction can decrease permeability significantly (by an order of magnitude at a strain of 4.5 %). Therefore, the compactant deformation of deep edifice host rocks will serve to decrease permeability and impede the lateral outgassing of exsolving magma through the deep conduit wallrock. Evidence for persistent volcano subsidence at Volcán de Colima is provided by both in situ (Murray and Wooller 2002) and passive (Pinel et al. 2011) ground deformation methods. Subsidence rates as high as 93 mm per year (between 1982 and 1999) have been recorded at the edge of the dome, and based on the lack of consistency in horizontal movements, this subsidence has been interpreted as due to the compaction and settling of the edifice (Murray and

Wooller 2002). If the ongoing compaction of Volcán de Colima is the result of compactive deformation, as presented herein, it implies ongoing reduction in the permeability of deep-edifice rocks ( $>1$  km). If faulting within the upper edifice cannot compensate for the continued compaction and permeability reduction of the rocks deeper in the edifice, the potential for explosivity at Volcán de Colima may be subject to increase over time.

Based on our data, we suggest that models of conduit outgassing (e.g. Collombet 2009; Collinson and Neuberg 2012) may be improved by considering permeability of the lower edifice ( $>1$  km) to be lower than that of the upper edifice ( $<1$  km).

### Implications for volcano stability

Fracturing in the upper edifice, as evidenced by the ubiquitous presence of fractures, is likely to reduce the integrity and structural stability of the edifice, leading to an increased risk of flank or large-scale dome collapse. Fault movement can result in bulging, intense fracturing and landsliding within the flanks, greatly destabilising the volcano (Lagmay et al. 2000). Subsequent intrusions of magma preferentially infiltrate heavily faulted domains of the volcano resulting in additional instability (Voight et al. 1983; Lagmay et al. 2000; Donnadieu and Merle 1998). However, we highlight that fracture-induced instability may be offset by the healing of fractures (e.g. Kolzenburg et al. 2012).

Although Volcán de Colima is characterised by persistent edifice subsidence (Murray and Wooller 2002; Pinel et al. 2011), interpreted as due to the compaction and settling of the edifice (Murray and Wooller 2002). There is no clear evidence of volcano spreading at Volcán de Colima (Murray and Wooller 2002), a key contributor to volcano instability (e.g. McGuire 1996; van Wyk de Vries and Francis 1997; Borgia et al. 2000). The lack of definitive evidence for volcano spreading may be explained by the relatively young age of Volcán de Colima (about 4000 years old; Murray and Wooller 2002). Volcanic spreading is one of the final stages of the development of a volcanic structure, preceded by periods of building, compressing, thrusting and intruding (Borgia 1994). Inelastic compaction of the edifice rocks may therefore be one of the principal mechanisms driving the “compressing” stage of the growth of a stratovolcano, representing an early stage in the growth and destruction cycles that have dominated the history of the Colima volcanic complex (Stoopes and Sheridan 1992; Cortés et al. 2010). Volcano growth and destruction cycles at the Colima volcanic complex are exemplified by the fact that Volcán de Colima is constructed within the amphitheatre of an earlier collapse structure (Fig. 1a). We speculate that, later in the life cycle of the volcano, the inelastic compaction of edifice-forming rock may also greatly assist volcano spreading and destabilisation.

The substantial volume and distribution of previous collapses (Stoopes and Sheridan 1992 and references therein) highlight the extreme danger posed by Volcán de Colima.

### Concluding remarks and perspectives

The failure mode of edifice-forming lava depends on the physical attributes of the lava, primarily the porosity and the pore size, and the conditions under which it deforms. At shallow depths ( $<1$  km), both low- and high-porosity lavas dilate and fail by shear fracturing. However, as depth increases, while low-porosity ( $<10\%$ ) lava remains dilatant, the failure of high-porosity lava is compactant and driven, on the micro-scale, by cataclastic pore collapse. Importantly, the choice of failure mode dictates the evolution of key physical properties, such as permeability. Our study has shown that a throughgoing tensile fracture in a sample of porous andesite increases sample permeability by about factor of two and that inelastic compaction can reduce sample permeability by an order of magnitude. The outgassing of volatiles from the conduit may therefore be efficient in the shallow edifice, where rock can fracture, and impeded deeper in the edifice due to compaction. The failure mode of volcanic host rock, and the attendant implications for sidewall outgassing, is thus likely to influence the dominant eruption style: effusive or explosive. If faulting within the shallow edifice cannot compensate for the progressive compaction and permeability reduction of the rocks deeper in the edifice, the explosive potential of a volcano may be subject to increase over time. In terms of volcano stability, fracturing in the upper edifice—which can result in bulging, intense fracturing and landsliding within the flanks—is likely to reduce the integrity of the edifice and lead to an increased risk of flank or large-scale dome collapse. Deeper in the edifice, compactive deformation could explain volcano subsidence and assist in volcano spreading and destabilisation. We highlight that the implications of this study are by no means restricted to Volcán de Colima; due to the comparable construction and eruption histories, and porosity ranges of the edifice host rocks, these implications are likely relevant to similar active andesitic stratovolcanoes, such as Merapi (Indonesia), Santa María (Guatemala), Tungurahua (Ecuador) and Ruapehu (New Zealand).

**Acknowledgments** We would first like to thank Sebastian Mueller and Olivier Spieler for collecting the experimental materials in 2004 (field campaign supported by the R&D Programme GEOTECHNOLOGIEN, funded by the German Ministry of Education and Research (BMBF) and German Research Foundation (DFG), Grant PTJ MGS/03G584A-SUNDAARC-DEVACOM). We would also like to thank Nick Varley, Oliver Lamb, Tom McLaughlin, Graeme Alexander William Sinclair and Josh Greenwood for their help in the field during our May–June 2014 field campaign. We are thankful to Carmel Pinnington for her help operating the SEM at the University of Liverpool, and Gilles Morvan for SEM assistance at Université de Strasbourg. M. J. Heap and Y. Lavallée

acknowledge the support of a Hubert Curien Partnership (PHC) PROCOPPE grant (grant number 27061UE), the Deutscher Akademischer Austauschdienst (DAAD) in Germany and the Ministry of Foreign and European Affairs (MAE) and the Ministry of Higher Education and Research (MESR), both in France. M. J. Heap also acknowledges CNRS INSU grant “*Étude de la stabilité des édifices volcaniques*” and an Initiative d’Excellence (IDEX) Attractivité grant (“VOLPERM”), funded by the University of Strasbourg. J. I. Farquharson acknowledges an IDEX “Contrats doctoraux” grant, and Y. Lavallée acknowledges the ERC starting grant “SLiM” (Strain Localisation in Magmas, project number 306488). This paper benefitted from a conversation with Dan Faulkner and Alain Burgisser. We are appreciative of the constructive comments of Agust Gudmundsson and one anonymous reviewer.

**Open Access** This article is distributed under the terms of the Creative Commons Attribution 4.0 International License (<http://creativecommons.org/licenses/by/4.0/>), which permits unrestricted use, distribution, and reproduction in any medium, provided you give appropriate credit to the original author(s) and the source, provide a link to the Creative Commons license, and indicate if changes were made.

## References

- Adelinet M, Fortin J, Schubnel A, Guéguen Y (2013) Deformation modes in an Icelandic basalt: from brittle failure to localized deformation bands. *J Volcanol Geotherm Res* 255:12–25
- Arámbula-Mendoza R, Lesage P, Valdés-González C, Varley NR, Reyes-Dávila G, Navarro C (2011) Seismic activity that accompanied the effusive and explosive eruptions during the 2004–2005 period at Volcán de Colima, Mexico. *J Volcanol Geotherm Res* 205:30–46
- Ayling MR, Meredith PG, Murrell SAF (1995) Microcracking during triaxial deformation of porous rocks monitored by changes in rock physical properties, I. Elastic-wave propagation measurements on dry rocks. *Tectonophysics* 245:205–221
- Baud P, Schubnel A, Wong T-F (2000) Dilatancy, compaction, and failure mode in Solnhofen limestone. *J Geophys Res* 105(B8):19289–19303
- Baud P, Klein E, Wong T-F (2004) Compaction localization in porous sandstones: spatial evolution of damage and acoustic emission activity. *J Struct Geol* 26:603–624
- Baud P, Vajdova V, Wong T-f (2006) Shear-enhanced compaction and strain localization: inelastic deformation and constitutive modeling of four porous sandstones. *J Geophys Res* 111: B12401. doi: 12410.11029/12005JB004101
- Baud P, Townend E, Meredith PG (2012) Permeability evolution during triaxial compaction of an anisotropic porous sandstone. *J Geophys Res.* doi:10.1029/2012JB009176
- Bernard B, Kueppers U, Ortiz H (2015) Revisiting the statistical analysis of pyroclast density and porosity data. *Solid Earth Discuss* 7:1077–1095
- Biggs J, Mothes P, Ruiz M, Amelung F, Dixon TH, Baker S, Hong S-H (2010) Stratovolcano growth by co-eruptive intrusion: the 2008 eruption of Tungurahua Ecuador. *Geophys Res Lett* 37:21. doi:10.1029/2010GL044942
- Borgia A (1994) Dynamic basis of volcanic spreading. *J Geophys Res* 99: 17791–17804
- Borgia A, Linneman SR (1990) On the mechanisms of lava flow emplacement and volcano growth: Arenal, Costa Rica. *Lava Flows Domes, IAVCEI Proc Volcanol* 2:208–243
- Borgia A, Delaney PT, Denlinger RP (2000) Spreading volcanoes. *Annu Rev Earth Planet Sci* 28:539–570
- Brace WF, Paulting BW, Scholz CH (1966) Dilatancy in the fracture of crystalline rocks. *J Geophys Res* 71:3939–3953
- Brantut N, Heap MJ, Meredith PG, Baud P (2013) Time-dependent cracking and brittle creep in crustal rocks: a review. *J Struct Geol* 52:17–43
- Castro J, Bindeman IN, Tuffen H, Schipper CI (2014) Explosive origin of silicic lava: textural and  $\delta\text{D}-\text{H}_2\text{O}$  evidence for pyroclastic degassing during rhyolite effusion. *Earth Planet Sci Lett* 405:52–61
- Cheung C, Baud P, Wong T-f (2012) Effect of grain size distribution on the development of compaction localization in porous sandstone. *Geophys Res Lett* 39(21). DOI: 10.1029/2012GL053739
- Cilona A, Faulkner DR, Tondi E, Agosta F, Mancini L, Rustichelli A, Baud P, Vinciguerra S (2014) The effects of rock heterogeneity on compaction localization in porous carbonates. *J Struct Geol* 67:75–93
- Collinson ASD, Neuberg J (2012) Gas storage, transport and pressure changes in an evolving permeable volcanic edifice. *J Volcanol Geotherm Res* 243–244:1–13
- Collombet M (2009) Two-dimensional gas loss for silicic magma flows: toward more realistic numerical models. *Geophys J Int* 177:309–318
- Cortés A, Garduño VH, Macías JL, Navarro-Ochoa C, Komorowski JC, Saucedo R, Gavilanes JC (2010) Geologic mapping of the Colima volcanic complex (Mexico) and implications for hazard assessment. *Geol Soc Am Spec Pap* 464:249–264
- Cuss RJ, Rutter E, Holloway RF (2003) The application of critical state soil mechanics to the mechanical behaviour of porous sandstones. *Int J Rock Mech Min Sci* 40:847–862
- David C, Wong T-f, Zhu W, Zhang J (1994) Laboratory measurement of compaction-induced permeability change in porous rocks: implications for the generation and maintenance of pore pressure excess in the crust. *Pure Appl Geophys* 143:425–456
- Donnadieu F, Merle O (1998) Experiments on the indentation process during cryptodome intrusions: new insights into Mount St. Helens deformation. *Geology* 26:79–82
- Eichelberger JC, Carrigan CR, Westrich HR, Price PH (1986) Non-explosive silicic volcanism. *Nature* 323:598–602
- Evans B, Frederich JT, Wong T-F (1990) The brittle-ductile transition in rocks: recent experimental and theoretical progress. In Duba AG, Durham WB, Handin J, Wang HF (eds) *The brittle-ductile transition in rocks. The Heard volume.* pp. 1–20, American Geophysical Union, Geophys Monograph 56, Washington
- Farquharson IJ, Heap MJ, Varley N, Baud P, Reuschlé T (2015) Permeability and porosity relationships of edifice-forming andesites: a combined field and laboratory study. *J Volcanol Geotherm Res* 297:52–68
- Farrell NJC, Healy D, Taylor CW (2014) Anisotropy of permeability in faulted porous sandstones. *J Struct Geol* 63:50–67
- Faulkner DR, Rutter EH (2001) Can the maintenance of overpressured fluids in large strike-slip fault zones explain their apparent weakness? *Geology* 29:503–506
- Fortin J, Schubnel A, Gueguen Y (2005) Elastic wave velocities and permeability evolution during compaction of Bleurswiller sandstone. *Int J Rock Mech Min Sci* 42:873–889
- Gaunt HE, Sammonds PR, Meredith PG, Smith R, Pallister JS (2014) Pathways for degassing during the lava dome eruption of Mount St. Helens 2004–2008. *Geology.* doi:10.1130/G35940.1
- Gerst A, Savage MK (2004) Seismic anisotropy beneath Ruapehu volcano: a possible eruption forecasting tool. *Science* 306:1543–1547
- Goto Y, Nakata S, Kurokawa M, Shimano T, Sugimoto T, Sakuma S, Hoshizumi H, Yoshimoto M, Uto K (2008) Character and origin of lithofacies in the conduit of Unzen volcano, Japan. *Journal of Volcanology and Geothermal Research* 175:45–59
- Gudmundsson A (2006) How local stresses control magma-chamber ruptures, dyke injections, and eruptions in composite volcanoes. *Earth Sci Rev* 79:1–31
- Gudmundsson A (2011) Rock fractures in geological processes. Cambridge University Press, Cambridge

- Guest JE, Chester DK, Duncan AM (1984) The Valle del Bove, Mount Etna: its origin and relation to the stratigraphy and structure of the volcano. *J Volcanol Geotherm Res* 21:1–23
- Hall ML, Robin C, Beate B, Mothes P, Monziger M (1999) Tungurahua Volcano, Ecuador: structure, eruptive history and hazards. *J Volcanol Geotherm Res* 91:1–21
- Heap MJ, Baud P, Meredith PG, Vinciguerra S, Reuschlé T (2014a) The permeability and elastic moduli of tuff from Campi Flegrei, Italy: implications for ground deformation modelling. *Solid Earth* 5:25–44
- Heap MJ, Lavallée Y, Petrakova L, Baud P, Reuschlé T, Varley N, Dingwell DB (2014b) Microstructural controls on the physical and mechanical properties of edifice-forming andesites at Volcán de Colima, Mexico. *J Geophys Res* 119:2925–2963
- Heap MJ, Xu T, Chen C-f (2014c) The influence of porosity and vesicle size on the brittle strength of volcanic rocks and magmas. *Bull Volcanol* 76:856. doi:[10.1007/s00445-014-0856-0](https://doi.org/10.1007/s00445-014-0856-0)
- Heap MJ, Kennedy BM, Pernin N, Jacquemard L, Baud P, Farquharson IJ, Scheu B, Lavallée Y, Gilg HA, Letham-Brake M, Mayer K, Jolly AD, Reuschlé T, Dingwell DB (2015) Mechanical behaviour and failure modes in the Whakaari (White Island volcano) hydrothermal system, New Zealand. *J Volcanol Geotherm Res* 295:26–42
- Heiken G, Wohletz K, Eichelberger JC (1988) Fracture fillings and intrusive pyroclasts, Inyo Domes, California. *J Geophys Res* 93:4335–4350
- Hoek E, Bieniawski ZT (1965) Brittle fracture propagation in rock under compression. *Int J Fract* 1:137–155
- Horwell CJ, Williamson BJ, Llewellyn EW, Damby DE, Le Blond JS (2013) The nature and formation of cristobalite at the Soufrière Hills volcano, Montserrat: implications for the petrology and stability of silicic lava domes. *Bull Volcanol* 75:696. doi:[10.1007/s00445-013-0696-3](https://doi.org/10.1007/s00445-013-0696-3)
- Hutchinson W, Varley N, Pyle DM, Mather TA et al (2013) Airborne thermal remote sensing of the Volcán de Colima (Mexico) lava dome from 2007 to 2010. In: Pyle DL (ed) Remote sensing of volcanoes & volcanic processes: integrating observation & modeling. Geological Society of London, London
- James MR, Varley N (2012) Identification of structural controls in an active lava dome with high resolution DEMs: Volcán de Colima, Mexico. *Geophys Res Lett* 39:22. doi:[10.1029/2012GL054245](https://doi.org/10.1029/2012GL054245)
- Jaupart C (1998) Gas loss from magmas through conduit walls during eruption. *Geol Soc Lond, Spec Publ* 145:73–90
- Kaneko K (2002) Exogenous and endogenous growth of the Unzen lava dome examined by satellite infrared image analysis. *J Volcanol Geotherm Res* 116:151–160
- Kendrick JE, Lavallée Y, Hess K-U, Heap MJ, Gaunt HE, Meredith PG, Dingwell DB (2013) Tracking the permeable porous network during strain-dependent magmatic flow. *J Volcanol Geotherm Res* 260: 117–126
- Kennedy LA, Russell JK, Nelles E (2009) Origins of mount St. Helens cataclasites: experimental insights. *Am Mineral* 94:995–1004
- Kolzenburg S, Heap MJ, Lavallée Y, Russell JKR, Meredith PG, Dingwell DB (2012) Strength and permeability recovery of tuffisite-bearing andesite. *Solid Earth* 3:191–198
- Kueppers U, Scheu B, Spieler O, Dingwell DB (2005) Field-based density measurements as tool to identify pre-eruption dome structure: set-up and first results from Unzen volcano, Japan. *J Volcanol Geotherm Res* 141:65–75
- Lagmay AMF, van Wyk de Vries B, Kerle N, Pyle DM (2000) Volcano instability induced by strike-slip faulting. *Bull Volcanol* 62:331–346
- Lamb OD, Varley NR, Mather TA, Pyle DM, Smith PJ, Liu EJ (2014) Multiple timescales of cyclical behaviour observed at two dome-forming eruptions. *J Volcanol Geotherm Res* 284:106–121
- Lavallée Y, Varley N, Alatorre-Ibargüengoitia MA, Hess K-U, Kueppers U, Mueller S, Richard D, Scheu B, Spieler O, Dingwell DB (2012) Magmatic architecture of dome-building eruptions at Volcán de Colima, Mexico. *Bull Volcanol* 74:249–260
- Lavallée Y, Benson PM, Heap MJ, Hess K-U, Flaws A, Schillinger B, Meredith PG, Dingwell DB (2013) Reconstructing magma failure and the degassing network of dome-building eruptions. *Geology* 41: 515–518
- Lavallée Y, Heap MJ, Kueppers U, Kendrick JE, Dingwell DB (2015) The fragility of Volcán de Colima—a material constraint. In: Varley N, Komorowski JC (eds) Volcán de Colima: managing the threat. Springer, Berlin
- Lesage P, Reyes-Dávila G, Arámbula-Mendoza R (2014) Large tectonic earthquakes induce sharp temporary decreases in seismic velocity in Volcán de Colima, Mexico. *J Geophys Res* 119:4360–4376
- Loaiza S, Fortin J, Schubnel A, Guégan Y, Vinciguerra S, Moreira M (2012) Mechanical behavior and localized failure modes in a porous basalt from the Azores. *Geophys Res Lett* 39. doi: [10.1029/2012GL053218](https://doi.org/10.1029/2012GL053218)
- Lockner D (1993) The role of acoustic emission in the study of rock fracture. *Int J Rock Mech Min Sci Geomech Abstr* 30:883–889
- Lockner D, Byerlee J, Kuksenko V, Ponomarev A, Sidorenko A (1991) Quasi-static fault growth and shear fracture energy in granite. *Nature* 350:39–42
- Luhr JF (2002) Petrology and geochemistry of the 1991 and 1998–1999 lava flows from Volcán de Colima, México: implications for the end of the current eruptive cycle. *J Volcanol Geotherm Res* 117(1–2): 169–194
- McGuire WJ (1996) Volcano instability: a review of contemporary themes. *Geol Soc Lond* 110:1–23
- Melnik O, Sparks RSJ (2002) Dynamics of magma ascent and lava extrusion at Soufrière Hills Volcano, Montserrat. In: Druitt TH, Kokelaar BP (eds) The eruption of Soufrière Hills volcano, Montserrat, from 1995 to 1999. London, Geological Society of London, Memoirs, 21, 153–171
- Menéndez B, Zhu W, Wong T-f (1996) Micromechanics of brittle faulting and cataclastic flow in Berea sandstone. *J Struct Geol* 18:1–16
- Mitchell TM, Faulkner DR (2008) Experimental measurements of permeability evolution during triaxial compression of initially intact crystalline rocks and implications for fluid flow in fault zones. *J Geophys Res* 113:B11. doi:[10.1029/2008JB005588](https://doi.org/10.1029/2008JB005588)
- Mitchell TM, Faulkner DR (2012) Towards quantifying the matrix permeability of fault damage zones in low porosity rocks. *Earth Planet Sci Lett* 339–340:24–31
- Mollema PN, Antonellini MA (1996) Compaction bands: a structural analog for anti-mode I cracks in aeolian sandstone. *Tectonophysics* 267:209–228
- Mueller S, Scheu B, Spieler O, Dingwell DB (2008) Permeability control on magma fragmentation. *Geology* 36:399–402
- Mueller S, Scheu B, Spieler O, Richard D, Dingwell DB (2011) The porosity of pyroclasts as an indicator of volcanic explosivity. *J Volcanol Geotherm Res* 203:168–174
- Mueller SB, Varley NR, Kueppers U, Lesage P, Reyes Davila GÁ, Dingwell DB (2013) Quantification of magma ascent rate through rockfall monitoring at the growing/collapsing lava dome of Volcán de Colima, Mexico. *Solid Earth* 4:201–213
- Murray JB, Wooller LK (2002) Persistent summit subsidence at Volcán de Colima, Mexico, 1982–1999: strong evidence against Mogi deflation. *J Volcanol Geotherm Res* 117:69–78
- Nara Y, Meredith PG, Yoneda T, Kaneko K (2011) Influence of macro-fractures and micro-fractures on permeability and elastic wave velocities in basalt at elevated pressure. *Tectonophysics* 503:52–59
- Nguyen CT, Gonnermann HM, Houghton BF (2014) Explosive to effusive transition during the largest volcanic eruption of the 20th century (Novarupta 1912, Alaska). *Geology*. doi:[10.1130/G35593.1](https://doi.org/10.1130/G35593.1)
- Ngwenya BT, Kwon O, Elphick SC, Main IG (2003) Permeability evolution during progressive development of deformation bands in porous sandstones. *J Geophys Res* 108:B7. doi:[10.1029/2002JB001854](https://doi.org/10.1029/2002JB001854)

- Okumura S, Sasaki O (2014) Permeability reduction of fractured rhyolite in volcanic conduits and its control on eruption cyclicity. *Geology* 42:843–846
- Paterson MS, Wong T-F (2005) Experimental rock deformation—the brittle field. Springer, New York. ISBN 978-3-540-26339-5
- Pinel V, Hooper A, De la Cruz-Reyna S, Reyes-Davila GA, Doin MP, Bascou P (2011) The challenging retrieval of the displacement field from InSAR data for andesitic stratovolcanoes: case study of Popocatepetl and Colima Volcano, Mexico. *J Volcanol Geotherm Res* 200:49–61
- Read MD, Ayling MR, Meredith PG, Murrell SAF (1995) Microcracking during triaxial deformation of porous rocks monitored by changes in rock physical properties, II. Pore volumometry and acoustic emission measurements on water-saturated rocks. *Tectonophysics* 245: 223–235
- Roman DC, Moran SC, Power JA, Cashman KV (2004) Temporal and spatial variation of local stress fields before and after the 1992 eruptions of crater peak vent, Mount Spurr Volcano, Alaska. *Bull Seismol Soc Am* 94:2366–2379
- Rust AC, Cashman KV, Wallace PJ (2004) Magma degassing buffered by vapor flow through brecciated conduit margins. *Geology* 32:349–352
- Rutter E (1986) On the nomenclature of mode of failure transitions in rocks. *Tectonophysics* 122(3–4):381–387
- Sammis CG, Ashby MF (1986). The failure of brittle porous solids under compressive stress states. *Acta Metall* 34: 511–526. doi: 510.1016/0001-6160(1086)90087-90088
- Savov IP, Luhr JF, Navarro-Ochoa C (2008) Petrology and geochemistry of lava and ash erupted from Volcán Colima, Mexico, during 1998–2005. *J Volcanol Geotherm Res* 174:241–256
- Schipper CI, Castro JM, Tuffen H, Wadsworth FB, Chappell D, Pantoja AE, Simpson MP, Le Ru EC (2015) Cristobalite in the 2011–2012 Cordón Caulle eruption (Chile). *Bull Volcanol* 77:34. doi:[10.1007/s00445-015-0925-z](https://doi.org/10.1007/s00445-015-0925-z)
- Schock RN, Heard HC, Stephans DR (1973) Stress-strain behavior of a granodiorite and two graywackes on compression to 20 kilobars. *J Geophys Res* 78:5922–5941
- Scholz CH (1968) Microfracturing and the inelastic deformation of rock in compression. *J Geophys Res* 73:1417–1432
- Shipton ZK, Evans JP, Robeson KR, Forster CB, Snelgrove S (2002) Structural heterogeneity and permeability in faulted eolian sandstone: implications for subsurface modeling of faults. *AAPG Bull* 86:863–883
- Smith R, Sammonds P, Tuffen H, Meredith PG (2011) Evolution of the mechanics of the 2004–2008 Mt. St. Helens lava dome with time and temperature. *Earth Planet Sci Lett* 307:191–200
- Stevenson JA, Varley N (2008) Fumarole monitoring with a handheld infrared camera: Volcán de Colima, Mexico, 2006–2007. *J Volcanol Geotherm Res* 177:911–924
- Stoops GR, Sheridan MF (1992) Giant debris avalanches from the Colima Volcanic Complex, Mexico: implications for long-runout landslides (>100 km) and hazard assessment. *Geology* 20:299–302
- Taran YA, Bernard A, Gavilanes JC, Lunezhava E, Cortés A, Armienta MA (2001) Chemistry and mineralogy of high-temperature gas discharges from Colima volcano, Mexico. Implications for magmatic gas–atmosphere interaction. *J Volcanol Geotherm Res* 108:245–264
- Taran Y, Gavilanes JC, Cortés A (2002) Chemical and isotopic composition of fumarolic gases and the SO<sub>2</sub> flux from Volcán de Colima, Mexico, between the 1994 and 1998 eruptions. *J Volcanol Geotherm Res* 117:105–119
- Tibaldi A (2001) Multiple sector collapses at stromboli volcano, Italy: how they work. *Bull Volcanol* 63:112–125
- van Wyk de Vries B, Borgia A (1996) The role of basement in volcano deformation. *Geol Soc Lond Spec Publ* 110:95–110
- van Wyk de Vries B, Francis PW (1997) Catastrophic collapse at stratovolcanoes induced by gradual volcano spreading. *Nature* 387:387–390
- Varley NR, Taran YA (2003) Degassing processes of Popocatépetl and Volcán de Colima, Mexico. In: Oppenheimer C, Pyle DM, Barclay J (eds) *Volcanic degassing*. Geological Society of London, London, pp 263–280. ISBN 1-86239-136-X
- Varley N, Arámbula-Mendoza R, Reyes-Dávila G, Stevenson J, Harwood R (2010) Long-period seismicity during magma movement at Volcán de Colima. *Bull Volcanol* 72:1093–1107
- Violay M, Gibert B, Mainprice D, Burg J-P (2015) Brittle versus ductile deformation as the main control of the deep fluid circulation in oceanic crust. *Geophys Res Lett.* doi:[10.1002/2015GL063437](https://doi.org/10.1002/2015GL063437)
- Voight B (2000) Structural stability of andesite volcanoes and lava domes, philosophical transactions: mathematical, physical and engineering sciences, 358, No. 1770, causes and consequences of eruptions of andesite volcanoes (May 15, 2000), 1663–1703
- Voight B, Janda RJ, Glicken H, Douglass PM (1983) Nature and mechanics of the Mount St. Helens rockslide avalanche of 18 May. *Geotechnique* 33:243–273
- Wang B, Chen Y, Wong T-f (2008). A discrete element model for the development of compaction localization in granular rock. *J Geophys Res* 113: B03202. doi:03210.01029/02006JB004501
- Webb EB, Varley N, Pyle DM, Mather TA (2014) Thermal imaging and analysis of short-lived Vulcanian explosions at Volcán de Colima, Mexico. *J Volcanol Geotherm Res* 278–279:132–145
- Wibberley CAJ, Shimamoto T (2003) Internal structure and permeability of major strike-slip fault zones: the median tectonic line in Mie Prefecture, southwest Japan. *J Struct Geol* 25:59–78
- Wong T-f, Baud P (2012) The brittle–ductile transition in rocks: a review. *J Struct Geol* 44:25–53
- Wong T-f, David C, Zhu W (1997) The transition from brittle faulting to cataclastic flow in porous sandstones: mechanical deformation. *J Geophys Res* 102(B2):3009–3025
- Woods AW, Koyaguchi T (1994) Transitions between explosive and effusive eruptions of silicic magmas. *Nature* 370:641–644
- Young NK, Gottsmann J (2015) Shallow crustal mechanics from volumetric strain data: insights from Soufrière Hills Volcano, Montserrat. *J Geophys Res* 120:1559–1571
- Zhu W, Wong T-f (1997a) The transition from brittle faulting to cataclastic flow: permeability evolution. *J Geophys Res* 102(B2): 3027–3041
- Zhu W, Montesi LGJ, Wong T-f (1997b) Shear-enhanced compaction and permeability reduction: triaxial extension tests on porous sandstone. *Mech Mater* 25:199–214
- Zhu W, Baud P, Wong T-f (2010) Micromechanics of cataclastic pore collapse in limestone. *J Geophys Res.* doi:[10.1029/2009JB006610](https://doi.org/10.1029/2009JB006610)
- Zhu W, Baud P, Vinciguerra S, Wong T-f (2011). Micromechanics of brittle faulting and cataclastic flow in Alban Hills tuff. *J Geophys Res* 116: B06209. doi:06210.01029/02010JB008046
- Zoback MD, Byerlee JD (1975) The effect of microcrack dilatancy on the permeability of westerly granite. *J Geophys Res* 80:752–755
- Zobin VM, González-Amezcu M, Reyes-Dávila GA (2002) Seismotectonic deformation of the volcanic edifice prior to the 1998 lava eruption of Volcán de Colima, México. *Bull Volcanol* 64:349–355

# G

## RÉSUMÉ DÉTAILLÉ EN FRANÇAIS

---

L'évolution de la perméabilité dans les systèmes volcaniques.

### G.1 CHAPITRE 1: INTRODUCTION

Le volcanisme terrestre est l'expression en surface de la remontée de magmas à travers la croûte. Lors de la progression du magma vers la surface, des processus tels que la décompression (par exemple Proussevitch et Sahagian, 1998; Massol et al., 2001; Cashman 2004; Gonnermann et Manga, 2013) et la vésiculation thermique (Lavallée et al., 2015) forcent une exsolution (dégazage) de volatils magmatiques ( $H_2O$  et  $CO_2$  par exemple). Que ce soit par le biais d'un réseau de bulles interconnectées dans le magma (par exemple Eichelberger et al., 1986; Okumura et al., 2009) ou latéralement à travers l'édifice volcanique (voir par exemple Jaupart et Allègre, 1991; Jaupart, 1998; Collombet, 2009), ou par des réseaux de fractures dans le magma, dans les roches formant l'édifice, et dans les dômes de lave (par exemple Stasiuk et al., 1996; Gonnermann et Manga, 2003; Rust et al., 2004; Edmonds et Herd, 2007; Castro et al., 2012; Cabrera et al., 2011; Lavallée et al., 2013; Pallister et al., 2013; Gaunt et al., 2014), les études antérieures ont montré que la capacité des gaz à migrer dans un système volcanique a une influence fondamentale sur le potentiel explosif d'un volcan. Les modèles prévoient qu'un dégazage efficace diminue ce potentiel explosif en empêchant l'accumulation de surpressions de gaz au sein du magma (par exemple Melnik et al., 2005; Diller et al., 2006). A contrario, l'ascension de magmas mal-dégazés aboutit généralement à des éruptions explosives catastrophiques. La genèse et le maintien de voies de dégazage sont donc les paramètres critiques dictant le comportement éruptif d'un volcan. Même après la mise en place des laves et des dômes, l'existence et l'évolution de chemins d'écoulement pour les gaz restent des facteurs très importants pour la dynamique d'un système volcanique. Evaluer la possibilité d'un dégazage et le cas échéant, comment ce dégazage pourrait se produire est fondamentale pour comprendre le risque potentiel posé par un système volcanique.

Afin de discuter du transport de fluide à travers un système volcanique, nous devons d'abord définir deux concepts (qui sont tous deux des propriétés physiques d'un milieu): la porosité et la perméabilité. La porosité  $\phi$  est la fraction de vide contenu dans un milieu

donné, tel qu'une roche. Dans les roches et le magma, la porosité peut être constituée de pores (vésicules), de fractures ou, fréquemment, une combinaison des deux. La perméabilité  $k$  est la capacité d'écoulement de fluide à travers les matériaux par l'intermédiaire de sa porosité (connectée), et peut varier de plus de douze ordres de grandeur dans les roches naturelles (Guéguen et Palciauskas, 1994).

Au cours des trois dernières décennies, la perméabilité des roches volcaniques est devenue une mesure de plus en plus répandue utilisée pour discuter des mécanismes de dégazage et donc la dynamique des éruptions. Depuis les travaux fondateurs d'Eichelberger et al. (1986), un grand nombre d'études ont examiné la relation entre la perméabilité et la porosité des roches volcaniques. Eichelberger et al. (1986) ont effectué des mesures sur différentes rhyolites de la chaîne Inyo Domes (Californie, USA) et ont utilisé un modèle de mousse perméable pour expliquer le volcanisme silicique non-explosif. Ce travail a été poursuivi par Westrich et Eichelberger (1994). Klug et Cashman (1996), qui ont mesuré la porosité et la perméabilité d'une gamme de dépôts de tephra et de tufs de Crater Lake et de Mt St Helens (USA), en proposant une relation loi de puissance simple entre les deux propriétés.

Une autre contribution notable est celle de Mueller et al. (2005), qui ont effectué des mesures sur des roches poreuses d'origine explosive et des aves extrusives moins poreuses. Mueller et al. (2005) ont combiné un modèle de tube capillaire (pour les matériaux effusifs) et un modèle de percolation basé sur un système de sphères qui se chevauchent (pour les produits explosifs). Mueller et al. (2005), en ont déduit que le volume des pores, mais aussi leur taille et leur forme (et les distributions de ces paramètres) exercent une influence notable sur la perméabilité.

Plusieurs chercheurs ont tenté de déterminer les processus sous-jacents qui contrôlent les microstructures et la perméabilité des roches volcaniques (par exemple Saar et Manga, 1999; Jouniaux et al., 2000; Blower, 2001; Rust et Cashman, 2004; Wright et al., 2006; Bernard et al., 2007; Wright et al., 2009; Yokoyama et Takeuchi, 2009; Rust et Cashman, 2011; Heap et al., 2014a). Ces études mettent l'accent sur l'importance de la connectivité de l'espace des pores, qui n'est pas nécessairement bien décrite par des modèles de perméabilité existants.

En outre, un certain nombre d'auteurs ont mis l'accent sur le développement de d'une anisotropie de l'espace poreux et de son influence sur la perméabilité (par exemple Tait et al., 1998; Wright et al., 2006; Bernard et al., 2007; Degruyter et al., 2010). Tous ces auteurs ont mesuré des différences de perméabilité d'un ordre de grandeur et

plus, résultant d'une élongation préférentielle des vésicules. Des travaux récents ont également cherché à caractériser les propriétés physiques (la porosité, la perméabilité) des discontinuités résultant de la localisation des déformations. Parmi les exemples récents, on peut citer les pseudotachylites (un produit de friction, par exemple Kendrick et al., 2014) et les tuffisites (fractures partiellement suturées, par exemple Kolzenburg et al., 2012; Kendrick et al., 2016).

Les études citées plus haut et d'autres (par exemple Melnik et Sparks, 1999; Klug et al., 2002; Melnik et Sparks, 2002; Dobson et al., 2003; Gonnermann et Manga, 2007; Platz et al., 2007; Nakamura et al., 2008; Yokoyama et Takeuchi, 2009; Bouvet de Maisonneuve et al., 2009; Ball et al., 2013; Heap et al., 2014b, 2015; Mayer et al., 2015) illustrent les variations dans les propriétés physiques des roches qui font écho à la gamme de compositions magmatiques et les styles éruptifs (par exemple Spieler et al., 2004; Burgisser and Gardner, 2005; Mueller et al., 2008). A leur tour, ces études visent généralement à relier ces paramètres à la migration de gaz à travers le système volcanique ou à donner un aperçu de l'histoire de l'activité éruptive.

Toutes ces études donnent une image large et complexe de la perméabilité des matériaux volcaniques. Cependant, les mesures de porosité et de perméabilité ne décrivent évidemment pas toute la dynamique des processus impliqués. Heap et al., (2015b) ont mesuré la perméabilité et la porosité des dépôts pyroclastiques variablement suturées du volcan du Mt Meager (Canada). Leurs résultats mettent en évidence que les propriétés physiques peuvent évoluer pendant et après la mise en place de produits volcaniques. Expérimentalement, Ashwell et Kendrick et al. (2015) ont démontré un phénomène similaire: la perméabilité et la porosité des échantillons rhyolitiques diminuent avec compactage visqueux. En outre, les recherches portant sur la réponse de la perméabilité à une compression hydrostatique (par exemple Vinciguerra et al., 2005; Watanabe et al., 2008; Fortin et al., 2011; Faoro et al., 2013) ou de compression triaxial (Alam et al., 2014) mettent en évidence que son évolution dépend d'une série de paramètres, notamment la géométrie des pores et la pression de confinement.

En combinant des nouvelles données de terrain, des nouvelles données expérimentales et une modélisation numérique, ce travail de thèse explore comment le paramètre fondamental contrôlant la migration des fluides dans les systèmes volcaniques, — i.e. la perméabilité du système — peut évoluer dans l'espace et dans le temps lors des périodes d'activité d'un volcan. Cette étude, divisée en sept parties résumées dans ce qui suit, s'est focalisée sur l'impact de la déformation et du frittage sur les microstructures et les lois de porosité-

perméabilité dans les roches volcaniques.

Ce premier chapitre décrit la formation de la porosité et de la perméabilité dans les volcans, et explique les implications pour l'écoulement de fluide dans les systèmes volcaniques. Ce chapitre présente les résultats existants et les concepts fondamentaux utilisés dans l'ensemble de la thèse.

## G.2 CHAPITRE 2: MÉTHODES

Le deuxième chapitre décrit les méthodes utilisées dans cette thèse. Les échantillons examinés en laboratoire étaient généralement de 40 mm de longueur et 20 mm de diamètre. Dans la plupart des cas, la perméabilité a été mesurée en laboratoire en utilisant la méthode du flux stationnaire («steady-state ») dans un perméamètre modifié. Le gaz (soit de l'argon ou de l'azote) s'écoule à travers un échantillon à différents débits, et le gradient de pression à travers l'échantillon (amont et aval) a été mesuré. En utilisant la loi de Darcy, la perméabilité peut être calculée si les dimensions de l'échantillon et la viscosité du fluide sont connues. Les essais de déformation mécanique ont été réalisés dans une presse triaxiale, dans laquelle la pression de confinement et la pression des pores peuvent être asservies. Un piston axial est utilisé pour appliquer une contrainte différentielle sur l'échantillon. En outre, des images au microscope électronique à balayage (MEB) d'échantillons sélectionnés ont été obtenues et analysées.

## G.3 CHAPITRE 3: IMPACT DE LA MICROSTRUCTURE SUR LA PERMÉABILITÉ DES ROCHES VOLCANIQUES DE COLIMA (MEXIQUE)

Le chapitre 3: présente une série de mesures effectuées sur le terrain, lors d'une mission au Volcán de Colima (Mexique). Des mesures de densité et de perméabilité ont été effectuées sur 572 échantillons d'andésites qui forment l'édifice. Les échantillons de roches ont été pesés dans l'air et en suspension dans l'eau, et à partir du principe d'Archimède, la densité a été calculée. La perméabilité a été mesurée sur le terrain à l'aide d'un perméamètre de type seringue portable (TinyPerm II). La porosité des roches collectées était comprise entre 2,5% et 73% en volume. La densité montre une grande hétérogénéité et une distribution bimodale près du cratère. Ceci traduit un double comportement explosif-effusif, typique des volcans composites actifs. Les perméabilités (également mesurées sur le terrain) sont de l'ordre de  $10^{-16}$  à  $10^{-11} \text{ m}^2$ , une gamme assez large qui comprend des valeurs significativement supérieures à celles généralement considérées par des modèles de transport de fluides dans le magma. Ces nouvelles données soulignent ainsi l'importance de la perméab-

ilité de la roche hôte pour faciliter le dégazage des volatils et ainsi réguler le dynamique des éruptions. Pour une porosité donnée, des variations de perméabilité allant jusqu'à quatre ordres de grandeur ont été observées. Cette variabilité est essentiellement non affectée par les différences méso-échelle dans l'oxydation ou l'altération.

Les données de terrain ont été renforcées par des mesures de laboratoire. L'étude en laboratoire des microstructures des andésites récoltées sur le terrain montre à la fois la complexité et la diversité de ce type de roche. On a noté, par exemple, que les surfaces spécifiques sont anormalement élevées dans les échantillons qui ont une porosité inter-microlites. Cependant, ces «micropores» ne contribuent que très peu à la porosité et à la connectivité des pores, ce qui entraîne une sous-estimation de la tortuosité du réseau poreux, paramètre notamment utilisé dans le modèle de Kozeny–Carman. Ce modèle a été souvent utilisé par les études antérieures pour prédire/interpréter la perméabilité des roches volcaniques. On a ici montré que les valeurs de tortuosité calculées avec ce modèle ne capturent pas la complexité de la microstructure des roches volcaniques de Colima.

Une analyse Bayésienne a permis d'identifier un changement significatif dans l'évolution porosité-perméabilité des roches collectées, à environ 14% de porosité. Ceci suggère que les éléments qui contrôlent l'écoulement du fluide (les fissures ou les pores) ne sont pas les mêmes en dessous et au dessus de cette porosité seuil. L'analyse systématique des microstructures confirme que l'écoulement du fluide dans les andésites de faible porosité (ici <14%) est contrôlé par des microfissures tortueuses, alors dans que dans les échantillons plus poreux (>14%) l'écoulement s'effectue principalement dans un réseau de larges pores interconnectés. Le rapport de la porosité totale et la porosité non connecté ( $\Gamma$ , défini ici pour la première fois) constitue un indicateur utile pour déterminer la connectivité globale d'un échantillon, même s'il ne décrit pas l'efficacité de l'écoulement de fluide à travers des réseaux de pores. Les valeurs de  $\Gamma$  sont notamment différentes au-dessus et en-dessous de ce seuil de porosité (~14%).

Par conséquent, l'évolution porosité-perméabilité pour les roches de Colima peut être décrite de manière satisfaisante à l'aide de deux lois puissance. En outre, les données de perméabilité et de porosité à Colima mesurées par des auteurs précédents (Mueller, 2006; Kolzenburg et al., 2012; Kendrick et al., 2013; Richard et al., 2013; Heap et al., 2014b) sont également bien décrites par ce modèle à deux pentes. De la même manière, ces données prédisent un seuil de porosité similaire d'environ  $\phi \approx 14 - 16\%$ . Ceci signifie qu'au-dessus d'une certaine porosité, l'écoulement de fluide dans l'édifice sera contrôlé par des mécanismes microstructuraux différents que si l'édifice est constitué

de roches plus denses. L'hétérogénéité exceptionnelle des roches qui forment le Volcan de Colima a également des conséquences importantes sur le dégazage latéral, la dynamique des éruptions, ainsi que sur la résistance mécanique de l'édifice et sa stabilité à grande échelle.

#### G.4 CHAPITRE 4: IMPACT DE LA DÉFORMATION SUR LA PERMÉABILITÉ DES ROCHES VOLCANIQUES

La perméabilité d'un édifice volcanique joue un très grand rôle dans les processus de dégazage et le comportement éruptif. La perméabilité dépend d'autres propriétés physiques et mécaniques des roches impliquées, qui est l'objet du chapitre 4. Ces matériaux sont généralement un ensemble de laves, d'éjectas explosifs, et d'autres dépôts volcanoclastiques. Comme les volcans actifs sont par nature des environnements subissant de fortes déformations (voir par exemple, Ōmori, 1920; Mogi, 1958; Dzurisin, 2003), il est important de comprendre l'évolution des propriétés de transport des fluides lors de la déformation inélastique. Dans ce but, des différentes roches volcaniques ( principalement des basaltes et des andésites, de porosités comprises entre 5 et 22%) ont été déformées en compression dans une presse triaxiale. La porosité et la perméabilité ont été mesurées avant et après les expériences, ce qui a permis d'analyser l'influence de l'ampleur de la déformation inélastique sur la perméabilité des roches qui forment l'édifice. Les roches de porosité initiale relativement basse montrent un comportement exclusivement dilatant (une augmentation de la porosité sous l'effet d'une microfissuration). Quand la déformation augmente, la dilatation se poursuit après la rupture macroscopique et elle est plus marquée dans les échantillons initialement moins poreux. Pour les roches les plus poreuses, la rupture est principalement compactante, quelle que soit la pression effective appliquée à l'échantillon. Aux porosités intermédiaires — entre 14 et 16% — on observe relativement peu de changements de porosité, quel que soit le mode de rupture. Dans cette gamme, le mode de rupture est susceptible de varier rapidement avec la pression effective.

De même, les échantillons de faible porosité initiale montrent une augmentation de la perméabilité d'environ trois ordres de grandeur pour des déformations volumiques allant jusqu'à 12%. A contrario, la perméabilité des échantillons plus poreux ( $\simeq 22\%$ ) décroît de façon monotone pour atteindre une décroissance maximum d'environ 1,5 ordres de grandeur. Les échantillons de porosité intermédiaire présentent une évolution plus complexe, parfois contrastée d'un échantillon à l'autre : certains échantillons cassant après une phase de dilatance, pouvant par exemple présenter une réduction de porosité et de perméabilité.

Les échantillons subissant une compaction inélastique peuvent, après avoir accumulé suffisamment de déformation, présenter un comportement dilatant (après une contrainte seuil), comme observé précédemment pour d'autres types roches (grès et carbonates par exemple). Ceci montre que les roches volcaniques ne peuvent se compacter que jusqu'à une certaine limite. La compaction liée à l'effondrement cataclastique des pores peut donc être vue comme un phénomène transitoire, qui précède l'apparition d'une rupture dilatante. Dans certaines conditions de pression effective, une roche volcanique peut toutefois aussi développer une rupture dilatante et ensuite compacter lorsqu'on continue à la déformer.

Une étude systématique de la microstructure des échantillons montre que l'endommagement dans ces roches volcaniques est généralement localisé, dans une bande de cisaillement dilatante ou compactante ou une bande de compaction. Cette localisation pourrait favoriser une anisotropie de perméabilité. En conséquence, les paramètres macroscopiques, comme la déformation inélastique, ne parviennent pas à capturer entièrement l'évolution de la perméabilité. Cette complexité est encore plus importante pour les roches de porosité intermédiaire, pour lesquelles la présence de fissures et de pores rend le matériau plus sensible aux écarts de pressions de confinement ou de pression de pore.

Une analyse du rapport du changement de porosité inélastique et déformation inélastique ( $\delta\phi_i/\varepsilon_i$ ) montre que, à porosité extrême, de grandes variations de porosité (dilatation ou compaction) peuvent être associées à une augmentation de la déformation. Cependant, les échantillons dans une gamme de porosité intermédiaire  $12 \leq \phi \leq 18\%$  se trouvent à proximité du seuil où  $\delta\phi_i/\varepsilon_i = 0$ . Cela implique que lors d'une augmentation de la déformation, ces échantillons présentent peu de variation de porosité. En effet, voici ce que l'on observe: quel que soit le mode de rupture (qui est fortement dépendant de la pression effective) des variations significatives de la perméabilité peuvent être observées lorsque des structures de fractures ou de bandes compactées augmentent en taille et en complexité, mais l'évolution de la porosité tend à être négligeable. Les comportements de déformation complexes sont aussi remarquables à porosité intermédiaire, y compris les transitions de comportement compactant au comportement dilatant (à un seuil de contrainte connu dans la littérature sous le nom  $C^{*'}_i$ ), ou vice versa (qui est ici appelé  $C''_i$ ). La transition entre un comportement dilatant et un comportement compactant est non seulement dictée par les propriétés physiques initiales d'une roche — surtout, sa porosité et de la pression effective (ou profondeur) à laquelle elle est déformée — mais aussi par la quantité de déformation post-rupture que la roche subit. De plus, dans des matériaux

volcaniques, les endommagements tendent à se localiser et il est clair que les variables macroscopiques telles que le changement de porosité inélastique ou la déformation inélastique ne parviennent pas à bien décrire l'évolution de la perméabilité dans les systèmes volcaniques.

On observe fréquemment des variations de la densité de l'édifice, qui pourraient donner lieu à une anisotropie de la perméabilité de l'édifice. Ceci pourrait se manifester, par exemple, par une répartition inégale des fumerolles de dégazage. On doit en outre souligner que l'évolution des modes d'émission de gaz dans les volcans actifs peut refléter l'évolution de la perméabilité, induite par la déformation peu profonde de l'édifice, en particulier autour des marges d'extrusion, des dômes de lave et des épines de lave. Dans un environnement volcanique sans déformation, les régions de l'édifice qui sont composées de roches denses verront généralement moins de dégazage. Cependant, l'augmentation de la perméabilité induite par la dilatation devrait faciliter l'émission de volatiles à travers la roche dense lorsqu'elle subit une déformation. D'autre part, la roche poreuse sera plus efficace pour le dégazage lors des périodes d'inactivité. Cependant, la déformation de ces roches sera préférentiellement compactante et le dégazage pourra devenir moins efficace lors d'une accumulation de contraintes. Ces observations suggèrent que les changements de la localisation et de l'intensité des fumerolles qui dégagent, par exemple, à travers les flancs et le sommet d'un volcan, peuvent refléter une déformation du sous-sol et une activité volcanique renouvelée.

#### G.5 CHAPITRE 5: ENDOMMAGEMENT DES ROCHES SOUS L'EFFET DE VARIATIONS DE LA PRESSION DE PORE

La rupture des roches poreuses en compression est en grande partie régie par la pression de confinement (la pression lithostatique) et par la pression des fluides interstitiels présents au sein de la roche (la pression de pore). Ces deux pressions sont évidemment susceptibles de varier dans l'espace et dans le temps dans un édifice volcanique. Si la pression lithostatique a tendance à augmenter de manière linéaire avec la profondeur, sous l'effet de l'accumulation progressive de matière, les pressions interstitielles peuvent être sujettes à des fluctuations (notamment pendant les périodes de fortes activités volcaniques). Des données de terrain montrant des variations de pression de pores ont été publiées pour de nombreux systèmes volcaniques, par exemple Sigurdsson (1982); Elsworth et Voight (1992), Newhall et al. (2001), Shibata et Akita (2001), et Hurwitz et Johnson (2003). En outre, les données thermiques d'émission du Volcan de Colima — obtenues à l'aide d'une caméra infrarouge — soulignent que la position fumerolle peut migrer au cours des différentes périodes d'activité vol-

canique. Cela suggère que les voies de volatiles magmatiques dans l'édifice supérieur peuvent changer avec l'activité magmatique, qui est également associée à des changements de pression de pore.

A pression lithostatique constante (même profondeur), une augmentation de la pression de pore peut entraîner une rupture fragile (dilatante) de la roche. Ce phénomène a été étudié dans le cinquième chapitre à travers une série d'expériences de compression triaxiale sur des andésites (du Volcán de Colima), typiques de la formation d'un édifice. Des échantillons ont été déformés de manière triaxiale. Contrairement aux expériences du chapitre 4, la contrainte axiale et la pression de confinement ont été maintenues constantes tandis que la pression de pore a été augmentée (ou diminuée) à des taux différents. Ces nouvelles données montrent que l'augmentation de la pression de pore sur des durées comprises entre 1 min et 1 jour peut aboutir à une rupture fragile de la roche. Quelle que soit la vitesse d'augmentation de la pression pore, des accélérations comparables de l'activité acoustique, liée à l'endommagement progressif de la roche, et de la déformation ont été enregistrées avant la rupture macroscopique. L'étude montre en outre que des oscillations de la pression de pore peuvent provoquer une accumulation d'endommagement, entraînant finalement une rupture fragile à des conditions de contrainte moyenne effective relativement faibles. La rupture macroscopique se produit après un seuil critique d'endommagement, ce qui suggère que seulement de petites augmentations de la pression de pores peuvent suffire pour déclencher une rupture dans des roches déjà fragilisées.

Enfin, il est évident qu'en profondeur des fractures liées à ce mécanisme de fragilisation sont susceptibles de s'ajouter à la compaction inélastique des roches volcaniques. La fragilisation induite par des variations de pression de pore pendant l'activité volcanique devrait être plus marquée près du conduit volcanique, et par conséquent peut également contribuer au développement d'une zone fracturée autour de celui-ci. Ce phénomène pourrait expliquer le fait que le dégazage soit plus fréquemment observé près du conduit dans de nombreux volcans actifs. En outre, la fragilisation de la roche en profondeur peut créer des voies de dégazage transitoires en reliant les réseaux de fractures près de l'édifice aux systèmes de fracture régionales à grande échelle. Ces résultats expérimentaux confirment que les fluctuations de pression de fluide interstitiel, associées à l'activité volcanique, peuvent jouer un rôle crucial et même imposer le type d'activité volcanique et son ampleur, en augmentant de manière transitoire la perméabilité du système. Cette hypothèse est corroborée par des données thermiques acquises au Volcán de Colima, qui montrent que

l'intensité du dégazage aux fumerolles sur les flancs du volcan varie avec le degré d'activité au niveau du cratère.

#### G.6 CHAPITRE 6: L'ANISOTROPIE DE LA PERMÉABILITÉ DANS LES DÔMES DE LAVE ET LES CONDUITS VOLCANIQUES

Le sixième chapitre explore le développement de l'anisotropie dans le magma. Les roches volcaniques contiennent souvent des discontinuités discrètes, conséquences des processus de localisation de la déformation qui peuvent se produire durant l'ascension et l'extrusion du magma. Que ces structures localisées soient des conduits ou des barrières à l'écoulement du fluide est donc un élément fondamental pour la modélisation des éruptions volcaniques et des émissions de gaz. Ce dernier chapitre présente des données obtenues sur neuf blocs d'andésite (collectés au Volcán de Colima) contenant de telles discontinuités. Une étude systématique de la porosité et de la perméabilité a été effectuée sur cinquante carottes préparées à partir de ces blocs. Une étude détaillée de la microstructure a également été entreprise pour tenter de comprendre les modes de formation des différentes discontinuités observées.

Les bandes dans les blocs de pierre ponce apparaissent comme des reflets de l'expansion inhomogène des bulles. En dépit de l'augmentation significative de porosité, ces bandes ne modifient pas significativement la perméabilité. D'autres discontinuités dans ces blocs sont interprétées comme des bandes de cisaillement induites par la déformation, de la porosité créée par la cavitation, et/ou par des fractures variablement suturées. Dans chacun de ces cas, une augmentation de la perméabilité (jusqu'à environ trois ordres de grandeur) a été mesurée par rapport aux roches hôtes.

Les différences du degré de frittage, et la présence de polymorphes de silice dans certains échantillons, suggèrent que ces caractéristiques étaient probablement formées à différentes profondeurs dans le conduit. Les données suggèrent donc que les fractures existent — bien que dans certains cas, seulement de façon temporaire — le long d'une partie étendue du conduit, et elles supportent l'idée d'un halo de dégazage perméable qui entoure le conduit.

Un seul échantillon contenait une bande de porosité inférieure à la roche hôte. Cette bande contenait des pores variablement colmatés. Ceci a été interprété comme le remplissage des pores d'un matériau granulaire (par exemple, la cendre volcanique transportée par le gaz) qui se fritte et se densifie à haute température. Dans ce cas, la bande était d'un ordre de grandeur moins perméable que la roche hôte; ainsi, une voie autrefois perméable devient un obstacle à l'écoulement

de fluide.

En raison des grandes différences de perméabilité qui peuvent apparaître du fait de la localisation des déformations (de plusieurs ordres de grandeur), l'anisotropie localisée de la perméabilité doit être un paramètre critique qui contrôle l'évolution des pressions interstitielles au sein des volcans actifs. Le chapitre 6 utilise un modèle relativement simple pour mettre en évidence l'importance même de très petites discontinuités sur différentes longueurs. Il est probable que ces caractéristiques vont influencer l'ampleur et la périodicité du comportement explosif des volcans siliciques actifs. Ceci montre l'interaction complexe entre les processus dilatants et la densification du magma, et met en évidence l'anisotropie de perméabilité importante dans le conduit et/ou dans le dôme d'un système volcanique. Il est probable que l'abondance et la distribution spatiale des structures localisées peuvent donner lieu à une fuite ou à un piégeage de matières volatiles, et donc contrôler l'évolution de la pression interstitielle dans les systèmes volcaniques actifs. En effet, il est généralement admis qu'il existe une relation forte entre la perméabilité, le dégazage, la pression interstitielle et la défaillance explosive: pouvons-nous identifier les mécanismes et les différentes constantes de temps associées?

#### G.7 CHAPITRE 7: L'ÉVOLUTION DE LA PERMÉABILITÉ ÉQUIVALENTE AUTOUR D'UN CONDUIT VOLCANIQUE: DENSIFICATION DES CENDRES VOLCANIQUES CHAUDES DANS LES FRACTURES

Le septième chapitre examine le lien entre la perméabilité et l'augmentation de la pression interstitielle dans les systèmes volcaniques fracturés. Les données de terrain indiquent que les marges des conduits et les dykes volcaniques sont très fracturés. Ceci joue évidemment un rôle fondamental en termes de dégazage et limite l'explosivité des éruptions. Dans ce contexte, les fluides circulent dans un milieu hétérogène composé de la roche hôte et des fractures. La dynamique de ce système va être contrôlée par sa «perméabilité équivalente». Un code MATLAB a donc été développé pour calculer la perméabilité équivalente d'une marge d'un conduit volcanique pour différents niveaux de fracturation et en fonction du temps. Le modèle considère que la diminution de perméabilité est une fonction de la porosité des fractures, qui diminue avec le frittage des cendres (la soudure des particules de cendres au-dessus de la température de transition vitreuse). Ce processus est à son tour une fonction de la profondeur, de la température, de la largeur des fractures, et de la teneur en cristaux et en eau dissoute de chaque fracture.

La diminution de la porosité est modélisée par l'équation de Russell et Quane (2005), qui inclut les effets de la viscosité et la contrainte qui entraîne une densification (qui équivaut à la profondeur dans ce cas). A son tour, la viscosité du magma est une fonction de sa teneur en eau et de la température, déterminées à partir du modèle rhéologique de Hess et Dingwell (1996). La quantité d'eau dissoute dans un magma est également déterminée par sa profondeur, comme indiqué par Liu et al. (2005). En outre, la viscosité du magma est influencée par la teneur en cristaux, ce qui est une approximation du modèle de la suspension de particules de Mueller et al., (2010). La perméabilité lors de la densification est une fonction de la porosité et on peut la calculer avec la relation établie par Heap et al. (2015b). Heap et al. (2015b) ont réalisé des expériences de compactage à haute température en utilisant des matériaux volcaniques. Par la suite, ils emploient une analyse Bayésienne (telle que décrite dans le Chapitre 3) pour modéliser l'évolution de la perméabilité avec deux lois de puissance. Enfin, l'effet d'un nombre « $n_f$  » de fractures est pris en compte par la modification d'un modèle d'écoulement à plaques parallèles, basé sur la conservation de la masse.

L'influence globale des fractures transitoires sur la perméabilité équivalente de la marge du conduit est alors calculée pour des différentes perméabilités de la roche hôte. Cette partie du travail décrit les applications et les implications du modèle. Les résultats du modèle indiquent notamment que la réduction de la perméabilité liée seulement au frittage peut être extrêmement rapide, en particulier à des températures et des pressions élevées (fortes profondeurs). A de plus faibles profondeurs, la durée nécessaire à la saturation des fractures est plus importante qu'à des profondeurs plus élevées. Les fractures peuvent même rester définitivement ouvertes si le matériau de remplissage reste au-dessus de sa température de transition vitreuse. Le décalage entre les délais de dégazage cycliques estimés sur le terrain et les délais de frittage calculés, indique que la fracturation peut être fréquente et récurrente. Ceci suggère que l'écoulement des fluides à travers ces fractures peut servir à les garder ouvertes plus longtemps que prédit par le modèle. Un élément clé du modèle est qu'il permet de calculer un seuil critique pour lequel la pression interstitielle dans les fractures n'est plus en équilibre (la fracture ne peut plus dégazer efficacement).

Ce seuil — une perméabilité critique — est dérivé du rapport de deux échelles de temps. La première est le temps caractéristique de compactage (dérivé à son tour à partir du modèle de réduction de la porosité). La seconde est obtenue par la loi de Darcy, et représente le temps qu'il faudrait pour une aliquote de fluide à traverser une certaine distance (la demi-largeur de la fracture) sous un gradient de

pression. Il à noter que cette perméabilité critique  $k_{cr}$  est déterminée en combinant la géométrie de la fracture au sein d'un système donné avec des paramètres rhéologiques, fournissant ainsi un véritable modèle inter-compositionnelle. Cette analyse est appliquée à six volcans chimiquement distincts: Puyehue–Cordón Caulle (Chili), Mount Unzen (Japon), Mule Creek (USA), Chaitén (Chili), Torfajökull (Islande), et Volcán de Colima (Mexique). Notamment, la large gamme de leurs valeurs critiques ( $k_{cr}$ ) reflète le spectre d'activités éruptives observées dans ces systèmes. Ainsi, on montre que les systèmes volcaniques siliciques et non siliciques existent dans un continuum et peuvent donc être décrits par des modèles holistiques.

Pour Volcán de Colima, où il existe une multitude de données de perméabilité (comme indiqué dans Chapitre 3 et dans Chapitre 6), on peut observer que la majorité des matériaux de roche hôte se trouve au-dessus du seuil de perméabilité critique dérivé (c'est à dire des perméabilités de roche hôte entre  $10^{-17}$  à  $10^{-11} \text{ m}^2$  par rapport à une gamme de perméabilité critique autour  $10^{-19} - 10^{-23} \text{ m}^2$ ). D'autre part, à Puyehue–Cordón Caulle, l'obsidienne dense a une perméabilité nulle (Schipper et al., 2013), ce qui est évidemment plus faible que toute gamme finie de perméabilités critiques (a minima, cette valeur est de l'ordre  $10^{-17} \text{ m}^2$  pour fractures décrites dans ce système). Ainsi, cette analyse donne une nouvelle métrique précieuse permettant de cataloguer et de comparer le potentiel explosif de systèmes volcaniques différents.

L'efficacité du dégazage assisté par des fractures dépend de la répartition spatiale des fractures et de leurs largeurs dans un système volcanique donné, les échelles de temps sur lesquelles ils sont opérationnels, et la perméabilité du matériau environnant. Les données de la littérature concernant les deux études de cas Unzen et Chaitén montrent que ce modèle ne peut pas seulement prévoir des délais sur lesquels la perméabilité va évoluer, mais aussi mettre en évidence des différences fondamentales dans leur capacité à accumuler de la pression de pore pendant les cycles de fracturation et de suturation.

Dans un système perméable, les fractures peuvent fournir des voies de dégazage efficaces, qui se fermeront au fil du temps jusqu'à ce que le système conserve sa perméabilité originale. Dans un système à faible perméabilité, les fractures vont même présenter un mécanisme de dégazage très efficace. Cependant, la pression des pores augmente lorsque la perméabilité de fracture décroît jusqu'à une perméabilité critique. Cela signifie que soit a) le système n'atteindra pas sa perméabilité pré-fractures ou b) le système sera conduit inexorablement vers l'échec explosif. Ceci montre que, dans les dernières étapes de frittage et de densification, les pressions interstitielles doivent aug-

menter et peuvent entraîner un échappement de pression explosif à travers les fractures.

#### 6.8 CHAPITRE 8: CONCLUSIONS

Cette thèse a cherché à répondre à trois grandes questions:

1. La perméabilité du matériau d'édifice volcanique peut-elle être liée à ses propriétés physiques, comme la porosité?
2. Comment porosité et perméabilité évoluent sous l'effet de la contrainte mécanique dans des conditions pertinentes pour les systèmes volcaniques?
3. Comment les processus à hautes températures influencent la perméabilité et son anisotropie, et quelle est l'influence des processus à petite échelle sur un système volcanique dans son ensemble?

Ce dernier chapitre adresse chacune de ces questions en reprenant les éléments de réponse des chapitres précédents.

La perméabilité est une propriété essentielle notamment pour déterminer la nature explosive des volcans, ainsi que pour de nombreuses autres applications scientifiques et industrielles dans les environnements où l'écoulement du fluide est une préoccupation majeure. Combinant des méthodes expérimentales de déformation des roches en laboratoire, des approches de terrain, de la modélisation numérique, et des analyses systématiques de microstructure, ce travail a mis en évidence le caractère complexe de la formation et la destruction des réseaux poreux dans le magma et des roches volcaniques.

Des analyses microstructurales et statistiques révèlent que la roche volcanique de faible porosité est généralement dominée par des microfissures tortueuses, alors que les échantillons à porosité élevée contiennent de grands pores interconnectés. Cette large gamme de propriétés physiques se traduit par une large gamme de comportements mécaniques et de résistances à la rupture. Par ailleurs, le comportement mécanique dépend — entre autres paramètres — de la porosité initiale de la roche. Une transition entre un comportement dilatant et un comportement compactant peut être liée à l'augmentation de la porosité ou de la pression effective. Toutefois, cette transition peut également être induite par une déformation croissante. De même, une faible porosité initiale ou une pression effective basse peut promouvoir un comportement dilatant. Une transition post-rupture d'un comportement dilatant à un comportement compactante peut être induite par la déformation axiale ou en augmentant la pression de pore. Les roches volcaniques peuvent également contenir des hétérogénéités

discrètes, des reliques de processus qui se produisent dans le magma lors de son ascension et après sa mise en place. Ces hétérogénéités peuvent également conduire à une anisotropie significative de la perméabilité. L'anisotropie localisée de la perméabilité est un paramètre critique qui contrôle l'évolution des pressions de fluide de pores au sein des volcans actifs. Il est probable que ces hétérogénéités — telles que les fractures dans le magma — influenceront la récurrence éruptive de comportements explosif dans les volcans actifs. L'influence des fractures dans les systèmes volcaniques n'est que transitoire, car les fractures ferment au fil du temps. Alors qu'elles doivent fournir des voies de dégazage très efficaces pour les gaz volcaniques, leur influence est éphémère. La fermeture de fractures permet d'augmenter la pression, ce qui peut conduire à la fragmentation explosive.

La compétition entre les processus dilatants (qui augmentent la porosité) et compactants (qui la diminuent) exerce une influence sur les propriétés de transport des fluides à la fois dans le magma et dans la roche volcanique solidifiée. Ces processus incluent la vésiculation et la croissance des bulles dans le conduit, la rupture et la compression du magma, la fracturation issue du refroidissement et fracturation induite par le transport, ainsi que la déformation pendant ou après la mise en place des matériaux, et la densification par frittage. Le travail présenté ici pourrait être étendu en utilisant de nouvelles techniques d'imagerie, comme tomodensitométrie rayons X- qui permettrait de connaître la géométrie des pores et des fractures d'un échantillon avant et après sa déformation. Il est probable qu'une grande partie du comportement mécanique observé tout au long de cette thèse ne peut pas être expliqué uniquement par la porosité totale ou la porosité connectée. On pourrait imaginer par exemple, qu'il pourrait être fonction de la proportion de fissures par rapport aux pores. Quantifier ce rapport pores/fissures pourrait être la première étape vers le développement d'une relation universelle entre la porosité et la perméabilité des matériaux volcaniques.



Part IV  
**BIBLIOGRAPHY**



Abdurachman, E.K., Bourdier, J.L. and Voight, B., 2000. Nuées ardentes of 22 November 1994 at Merapi volcano, Java, Indonesia. *Journal of Volcanology and Geothermal Research*, 100(1), pp.345-361.

Adelinet, M., Fortin, J., Schubnel, A. and Guéguen, Y., 2013. Deformation modes in an Icelandic basalt: from brittle failure to localized deformation bands. *Journal of Volcanology and Geothermal Research*, 255, pp.15-25.

Alam, A.B., Niioka, M., Fujii, Y., Fukuda, D. and Kodama, J.I., 2014. Effects of confining pressure on the permeability of three rock types under compression. *International Journal of Rock Mechanics and Mining Sciences*, 65, pp.49-61.

Alidibirov, M. and Dingwell, D.B., 1996. Magma fragmentation by rapid decompression. *Nature*, 380(6570), pp.146-148.

Anderson, K.R., Poland, M.P., Johnson, J.H. and Miklius, A., 2015. Episodic deflation-inflation events at Kīlauea Volcano and implications for the shallow magma system. *Hawaiian Volcanoes: From Source to Surface*, 208, p.229.

Arciniega-Ceballos, A., Chouet, B. and Dawson, P., 2003. Long-period events and tremor at Popocatepetl volcano (1994–2000) and their broadband characteristics. *Bulletin of Volcanology*, 65(2-3), pp.124-135.

Atkinson, B.K. and Meredith, P.G., 1987. The theory of subcritical crack growth with applications to minerals and rocks. *Fracture mechanics of rock*, 2, pp.111-166.

Auker, M.R., Sparks, R.S.J., Siebert, L., Crosweller, H.S. and Ewert, J., 2013. A statistical analysis of the global historical volcanic fatalities record. *Journal of Applied Volcanology*, 2(1), 1 - 24.

Bagdassarov, N.S. and Dingwell, D.B., 1992. A rheological investigation of vesicular rhyolite. *Journal of Volcanology and Geothermal Research*, 50(3), pp.307-322.

Ball, J.L., Stauffer, P.H., Calder, E.S. and Valentine, G.A., 2015. The hydrothermal alteration of cooling lava domes. *Bulletin of Volcanology*, 77(12), pp.1-16.

Balme, M.R., Rocchi, V., Jones, C., Sammonds, P.R., Meredith, P.G. and Boon, S., 2004. Fracture toughness measurements on igneous rocks using a high-pressure, high-temperature rock fracture mechanics cell. *Journal of Volcanology and Geothermal Research*, 132(2), pp.159-172.

Barberi, F., Cassano, E., La Torre, P. and Sbrana, A., 1991. Structural evolution of Campi Flegrei caldera in light of volcanological and geophysical data. *Journal of Volcanology and Geothermal Research*, 48(1-2), pp.33-49.

Baubron, J.C., Allard, P. and Toutain, J.P., 1990. Diffuse volcanic emissions of carbon dioxide from Vulcano Island, Italy. *Nature*, 344(6261), pp.51-53.

Baud P., Zhu W., Wong T.-f., 2000. Failure mode and weakening effect of water on sandstone. *Journal of Geophysical Research*, 105(B7), 16371-16389.

Baud, P., and Meredith, P. G., 1997. Damage accumulation during triaxial creep of Darley Dale sandstone from pore volumometry and acoustic emission. *International Journal of Rock Mechanics and Mining Sciences*, 34(3), 24-e1.

Baud, P., Klein, E. and Wong, T.-f., 2004. Compaction localization in porous sandstones: spatial evolution of damage and acoustic emission activity. *Journal of Structural Geology*, 26(4), pp.603-624.

Baud, P., Meredith, P., and Townend, E., 2012. Permeability evolution during triaxial compaction of an anisotropic porous sandstone. *Journal of Geophysical Research: Solid Earth* (1978–2012), 117(B5).

Baud, P., Reuschlé, T., Ji, Y., Cheung, C.S. and Wong, T.-f., 2015. Mechanical compaction and strain localization in Bleuerswiller sandstone. *Journal of Geophysical Research: Solid Earth*, 120(9), pp.6501-6522.

Bense, V. F., and Person, M. A., 2006. Faults as conduit-barrier systems to fluid flow in siliciclastic sedimentary aquifers. *Water Resources Research*, 42(5).

Benson, P.M., Heap, M.J., Lavallée, Y., Flaws, A., Hess, K.U., Selvadurai, A.P.S., Dingwell, D.B. and Schillinger, B., 2012. Laboratory simulations of tensile fracture development in a volcanic conduit via cyclic magma pressurisation. *Earth and Planetary Science Letters*, 349, pp.231-239.

Benson, P.M., Vinciguerra, S., Meredith, P.G. and Young, R.P., 2008. Laboratory simulation of volcano seismicity. *Science*, 322(5899), pp.249-252.

Benson, P.M., Thompson, B.D., Meredith, P.G., Vinciguerra, S. and Young, R.P., 2007. Imaging slow failure in triaxially deformed Etna basalt using 3D acoustic-emission location and X-ray computed tomography. *Geophysical Research Letters*, 34(3).

Berlo, K., Tuffen, H., Smith, V. C., Castro, J. M., Pyle, D. M., Mather, T. A., and Geraki, K., 2013. Element variations in rhyolitic magma resulting from gas transport. *Geochimica et Cosmochimica Acta*, 121, 436-451.

Bernabe, Y., 1986, June. The effective pressure law for permeability in Chelmsford granite and Barre granite. In *International Journal of Rock Mechanics and Mining Sciences & Geomechanics Abstracts* (Vol. 23, No. 3, pp. 267-275). Pergamon.

Bernabé, Y., Li, M. and Maineult, A., 2010. Permeability and pore connectivity: a new model based on network simulations. *Journal of Geophysical Research: Solid Earth*, 115(B10).

Bernabé, Y., Mok, U. and Evans, B., 2003. Permeability–porosity relationships in rocks subjected to various evolution processes. *Pure and Applied Geophysics*, 160(5–6), pp.937–960.

Bernard, B., Kueppers, U. and Ortiz, H., 2015. Revisiting the statistical analysis of pyroclast density and porosity data. *Solid Earth*, 6(3), p.869.

Berryman, J.G., 1992. Effective stress for transport properties of inhomogeneous porous rock. *Journal of Geophysical Research: Solid Earth*, 97(B12), pp.17409–17424.

Biggs, J., Mothes, P., Ruiz, M., Amelung, F., Dixon, T.H., Baker, S. and Hong, S.H., 2010. Stratovolcano growth by co-eruptive intrusion: The 2008 eruption of Tungurahua Ecuador. *Geophysical Research Letters*, 37(21).

Biot, M. A. (1941). General theory of three-dimensional consolidation. *Journal of Applied Physics*, 12(2), 155–164.

Blower, J., 2001. Factors controlling permeability–porosity relationships in magma. *Bulletin of Volcanology*, 63(7), pp.497–504.

Bonafede, M., 1991. Hot fluid migration: an efficient source of ground deformation: application to the 1982–1985 crisis at Campi Flegrei-Italy. *Journal of Volcanology and Geothermal Research*, 48(1), pp.187–198.

Boué, A., Lesage, P., Cortés, G., Valette, B., and Reyes-Dávila, G., 2015. Real-time eruption forecasting using the material Failure Forecast Method with a Bayesian approach. *Journal of Geophysical Research: Solid Earth*, 120(4), pp.2143–2161.

Bourbie, T. and Zinszner, B., 1985. Hydraulic and acoustic properties as a function of porosity in Fontainebleau sandstone. *Journal of Geophysical Research: Solid Earth*, 90(B13), pp.11524–11532.

Brace, W.F. and Jones, A.H., 1971. Comparison of uniaxial deformation in shock and static loading of three rocks. *Journal of Geophysical Research*, 76(20), pp.4913–4921.

Brace, W.F., Paulding, B.W. and Scholz, C.H., 1966. Dilatancy in the fracture of crystalline rocks. *Journal of Geophysical Research*, 71(16), pp.3939–3953.

Brannen, M.J., Kokelaar, B.P. and McConnell, B.J., 1992. The Bad Step Tuff: a lava-like rheomorphic ignimbrite in a calc-alkaline piece-meal caldera, English Lake District. *Bulletin of Volcanology*, 54(3), pp.187–199.

Brantut, N., Heap, M.J., Meredith, P.G. and Baud, P., 2013. Time-dependent cracking and brittle creep in crustal rocks: A review. *Journal of Structural Geology*, 52, pp.17-43.

Broek, D., 1982. Elementary engineering fracture mechanics. Martin Nijhoff Publishers, The Hague.

Brown, S. and Smith, M., 2013. A transient-flow syringe air permeameter. *Geophysics*, 78(5), pp.D307-D313.

Bruhn, R. L., Yonkee, W. A., and Parry, W. T., 1990. Structural and fluid-chemical properties of seismogenic normal faults. *Tectonophysics*, 175(1), 139-157.

Buisson, C. and Merle, O., 2002. Experiments on internal strain in lava dome cross sections. *Bulletin of Volcanology*, 64(6), pp.363-371.

Bukumirovic, T., Italiano, F. and Nuccio, P.M., 1997. The evolution of a dynamic geological system: the support of a GIS for geochemical measurements at the fumarole field of Vulcano, Italy. *Journal of Volcanology and Geothermal Research*, 79(3), pp.253-263.

Burgisser, A. and Gardner, J.E., 2004. Experimental constraints on degassing and permeability in volcanic conduit flow. *Bulletin of Volcanology*, 67(1), pp.42-56.

Burgisser, A., Arbaret, L., Druitt, T. H., and Giachetti, T., 2011. Pre-explosive conduit conditions of the 1997 Vulcanian explosions at Soufrière Hills Volcano, Montserrat: II. Overpressure and depth distributions. *Journal of Volcanology and Geothermal Research*, 199(3), 193-205.

Burgisser, A., Poussineau, S., Arbaret, L., Druitt, T. H., Giachetti, T., and Bourdier, J. L., 2010. Pre-explosive conduit conditions of the 1997 Vulcanian explosions at Soufrière Hills Volcano, Montserrat: I. Pressure and vesicularity distributions. *Journal of Volcanology and Geothermal Research*, 194(1), 27-41.

Burlini, L. and Di Toro, G., 2008. Volcanic symphony in the lab. *Science*, 322(5899), pp.207-208.

Cabrera, A., Weinberg, R.F. and Wright, H.M., 2015. Magma fracturing and degassing associated with obsidian formation: The explosive-effusive transition. *Journal of Volcanology and Geothermal Research*, 298, pp.71-84.

Cabrera, A., Weinberg, R.F., Wright, H.M., Zlotnik, S. and Cas, R.A., 2011. Melt fracturing and healing: A mechanism for degassing and origin of silicic obsidian. *Geology*, 39(1), pp.67-70.

Cagnoli, B., Barmin, A., Melnik, O., and Sparks, R. S. J., 2002. Depressurization of fine powders in a shock tube and dynamics of fragmented magma in volcanic conduits. *Earth and Planetary Science Letters*, 204(1), 101-113.

Caine, J. S., Evans, J. P., and Forster, C. B., 1996. Fault zone architecture and permeability structure. *Geology*, 24(11), 1025-1028.

Camus, G., Gourgaud, A., Mossand-Berthommier, P.C. and Vincent, P.M., 2000. Merapi (Central Java, Indonesia): an outline of the structural and magmatological evolution, with a special emphasis to the major pyroclastic events. *Journal of Volcanology and Geothermal Research*, 100(1), pp.139-163.

Caricchi, L., Burlini, L., Ulmer, P., Gerya, T., Vassalli, M. and Papale, P., 2007. Non-Newtonian rheology of crystal-bearing magmas and implications for magma ascent dynamics. *Earth and Planetary Science Letters*, 264(3), pp.402-419.

Caricchi, L., Pommier, A., Pistone, M., Castro, J., Burgisser, A. and Perugini, D., 2011. Strain-induced magma degassing: insights from simple-shear experiments on bubble bearing melts. *Bulletin of Volcanology*, 73(9), pp.1245-1257.

Carman, P.C., 1937. Fluid flow through granular beds. *Transactions-Institution of Chemical Engineers*, 15, pp.150-166.

Carrasco-Nuñez, G., 2000. Structure and proximal stratigraphy of Citlaltepetl volcano (Pica de Orizaba), Mexico. Cenozoic tectonics and volcanism of Mexico, 334, p.247.

Cashman, K.V., Thornber, C. R., and Pallister, J. S., 2008. From dome to dust: Shallow crystallization and fragmentation of conduit magma during the 2004-2006 dome extrusion of Mount St. Helens, Washington. US Geological Survey professional paper, 1750, 387-413.

Cashman, K.V. and Hoblitt, R.P., 2004. Magmatic precursors to the 18 May 1980 eruption of Mount St. Helens, USA. *Geology*, 32(2), pp.141-144.

Cashman, K.V., 1992. Groundmass crystallization of Mount St. Helens dacite, 1980-1986: a tool for interpreting shallow magmatic processes. *Contributions to Mineralogy and Petrology*, 109(4), pp.431-449.

Cashman, K.V., 2004. Volatile controls on magma ascent and eruption. *The State of the Planet: Frontiers and Challenges in Geophysics*, pp.109-124.

Cashman, K.V., Mangan, M.T. and Newman, S., 1994. Surface degassing and modifications to vesicle size distributions in active basalt flows. *Journal of Volcanology and Geothermal Research*, 61(1), pp.45-68.

Cashman, S. M., and Cashman, K. V., 2006. Cataclastic textures in La Grange fault rocks, Klamath Mountains, California. *Geological Society of America Special Papers*, 410, 433-450.

Castro, J. M., Bindeman, I. N., Tuffen, H., and Schipper, C. I., 2014. Explosive origin of silicic lava: Textural and  $\delta$ D-H<sub>2</sub>O evidence for

pyroclastic degassing during rhyolite effusion. *Earth and Planetary Science Letters*, 405, 52-61.

Castro, J. M., Cordonnier, B., Tuffen, H., Tobin, M. J., Puskar, L., Martin, M. C., and Bechtel, H. A., 2012. The role of melt-fracture degassing in defusing explosive rhyolite eruptions at volcán Chaitén. *Earth and Planetary Science Letters*, 333, 63-69.

Castro, J. M., Manga, M., and Martin, M. C., 2005. Vesiculation rates of obsidian domes inferred from  $H_2O$  concentration profiles. *Geophysical Research Letters*, 32(21).

Castro, J.M. and Dingwell, D.B., 2009. Rapid ascent of rhyolitic magma at Chaitén volcano, Chile. *Nature*, 461(7265), pp.780-783.

Castro, J.M., Schipper, C.I., Mueller, S.P., Militzer, A.S., Amigo, A., Parejas, C.S. and Jacob, D., 2013. Storage and eruption of near-liquidus rhyolite magma at Cordón Caulle, Chile. *Bulletin of Volcanology*, 75(4), pp.1-17.

Chester, F. M., and Logan, J. M., 1986. Implications for mechanical properties of brittle faults from observations of the Punchbowl fault zone, California. *Pure and Applied Geophysics*, 124(1-2), 79-106.

Chevrel, M.O., Cimarelli, C., deBiasi, L., Hanson, J.B., Lavallée, Y., Arzilli, F. and Dingwell, D.B., 2015. Viscosity measurements of crystallizing andesite from Tungurahua volcano (Ecuador). *Geochemistry, Geophysics, Geosystems*, 16(3), pp.870-889.

Chevrel, M.O., Platz, T., Hauber, E., Baratoux, D., Lavallée, Y. and Dingwell, D.B., 2013. Lava flow rheology: A comparison of morphological and petrological methods. *Earth and Planetary Science Letters*, 384, pp.109-120.

Chokshi, A. H., 1997. A comparative examination of superplastic flow and fracture in metals and ceramics. *Materials Science and Engineering: A*, 234, 986-990.

Chouet, B.A., 1996. Long-period volcano seismicity: its source and use in eruption forecasting. *Nature*. 380, 309- 316

Clarke, A. B., Neri, A., Voight, B., Macedonio, G., and Druitt, T. H., 2002a. Computational modelling of the transient dynamics of the August 1997 Vulcanian explosions at Soufriere Hills Volcano, Montserrat: influence of initial conduit conditions on near-vent pyroclastic dispersal. *Memoirs-Geological Society of London*, 21, 319-348.

Clarke, A. B., Voight, B., Neri, A., and Macedonio, G., 2002b. Transient dynamics of vulcanian explosions and column collapse. *Nature*, 415(6874), 897-901.

Clarke, A.B., Stephens, S., Teasdale, R., Sparks, R.S.J. and Diller, K., 2007. Petrologic constraints on the decompression history of magma

prior to Vulcanian explosions at the Soufrière Hills volcano, Montserrat. *Journal of Volcanology and Geothermal Research*, 161(4), pp.261-274.

Clavaud, J. B., Maineult, A., Zamora, M., Rasolofosaon, P., and Schlitter, C. 2008. Permeability anisotropy and its relations with porous medium structure. *Journal of Geophysical Research: Solid Earth* (1978–2012), 113(B1).

Cnudde, V. and Boone, M.N., 2013. High-resolution X-ray computed tomography in geosciences: A review of the current technology and applications. *Earth Science Reviews*, 123, pp.1-17.

Collinson, A.S.D. and Neuberg, J.W., 2012. Gas storage, transport and pressure changes in an evolving permeable volcanic edifice. *Journal of Volcanology and Geothermal Research*, 243, pp.1-13.

Collombet, M., 2009. Two-dimensional gas loss for silicic magma flows: toward more realistic numerical models. *Geophysical Journal International*, 177(1), pp.309-318.

Commer, M., Helwig, S.L., Hördt, A. and Tezkan, B., 2005. Interpretation of long-offset transient electromagnetic data from Mount Merapi, Indonesia, using a three-dimensional optimization approach. *Journal of Geophysical Research: Solid Earth*, 110(B3).

Cordonnier, B., Caricchi, L., Pistone, M., Castro, J., Hess, K. U., Gottschaller, S., Manga, M., Dingwell, D. B., and Burlini, L., 2012. The viscous-brittle transition of crystal-bearing silicic melt: Direct observation of magma rupture and healing. *Geology*, 40(7), 611-614.

Costa, A., 2006. Permeability-porosity relationship: A reexamination of the Kozeny-Carman equation based on a fractal pore-space geometry assumption. *Geophysical research letters*, 33(2).

Costa, A., and Macedonio, G., 2003. Viscous heating in fluids with temperature-dependent viscosity: implications for magma flows. *Non-linear Processes in Geophysics*, 101 - 111.

Costa, A., Melnik, O. and Vedeneeva, E., 2007. Thermal effects during magma ascent in conduits. *Journal of Geophysical Research: Solid Earth*, 112(B12).

Cubellis, E., Ferri, M. and Luongo, G., 1995. Internal structures of the Campi Flegrei caldera by gravimetric data. *Journal of Volcanology and Geothermal Research*, 65(1), pp.147-156.

Damby, D. E., Llewellyn, E. W., Horwell, C. J., Williamson, B. J., Najorka, J., Cressey, G., and Carpenter, M., 2014. The  $\alpha$ - $\beta$  phase transition in volcanic cristobalite. *Journal of Applied Crystallography*, 47(4).

Darcy, H.P.G., 1856. Les Fontaines publiques de la ville de Dijon. Exposition et application des principes à suivre et des formules à employer dans les questions de distribution d'eau. [Exhibition and

implementation of the principles to follow and to formulae employ in the issue of water distribution.] Victor Dalmont, France. (In French).

David, C., Wong, T.F., Zhu, W. and Zhang, J., 1994. Laboratory measurement of compaction-induced permeability change in porous rocks: Implications for the generation and maintenance of pore pressure excess in the crust. *Pure and Applied Geophysics*, 143(1-3), pp.425-456.

Day, S.J., 1996. Hydrothermal pore fluid pressure and the stability of porous, permeable volcanoes. Geological Society, London, Special Publications, 110(1), pp.77-93.

De Lauro, E., De Martino, S., Palo, M. and Ibañez, J.M., 2012. Self-sustained oscillations at Volcán de Colima (México) inferred by independent component analysis. *Bulletin of Volcanology*, 74(1), pp.279-292.

De Maisonneuve, C. B., Bachmann, O., and Burgisser, A., 2009. Characterization of juvenile pyroclasts from the Kos Plateau Tuff (Aegean Arc): insights into the eruptive dynamics of a large rhyolitic eruption. *Bulletin of Volcanology*, 71(6), 643-658.

Deer, W. A., Howie, R. A., and Zussman, J., 1996. An introduction to the rock forming minerals. Longman Scientific and Technical, New York.

de'Michieli Vitturi, M., Clarke, A.B., Neri, A. and Voight, B., 2008. Effects of conduit geometry on magma ascent dynamics in dome-forming eruptions. *Earth and Planetary Science Letters*, 272(3), pp.567-578.

Deng, S., L. Zuo, A. Aydin, J. Dvorkin, and T. Mukerji, 2015. Permeability characterization of natural compaction bands using core flooding experiments and three-dimensional image-based analysis: Comparing and contrasting the results from two different methods. *AAPG Bulletin*, 99, 27-49.

Denlinger, R. P., and Hoblitt, R. P., 1999. Cyclic eruptive behavior of silicic volcanoes. *Geology*, 27(5), 459-462.

Dieterich, J.H., 1988. Growth and persistence of Hawaiian volcanic rift zones. *Journal of Geophysical Research: Solid Earth*, 93(B5), pp.4258-4270.

Diller, K., Clarke, A.B., Voight, B. and Neri, A., 2006. Mechanisms of conduit plug formation: Implications for vulcanian explosions. *Geophysical Research Letters*, 33(20).

Dingwell D.B., Lavallée Y., Hess K.-U., Flaws A., Marti J., Nichols A.R.L., Gilg H.A., Schillinger B., 2015. Eruptive shearing in tube pumice: pure and simple. *Solid Earth Discussion*. 7, 3053-3085.

Dingwell, D.B., 1996. Volcanic dilemma: flow or blow?. *Science*, 273(5278), p.1054.

Domínguez, T., Zobin, V.M. and Reyes-Davila, G.A., 2001. The fracturing in volcanic edifice before an eruption: the June–July 1998 high-frequency earthquake swarm at Volcán de Colima, México. *Journal of Volcanology and Geothermal research*, 105(1), pp.65-75.

Donnadieu, F., Merle, O., and Besson, J.-C., 2001. Volcanic edifice stability and cryptodome intrusion. *Bulletin of Volcanology*, 63, 61 - 72.

Dvorak, J.J., Okamura, A.T., English, T.T., Koyanagi, R.Y., Nakata, J.S., Sako, M.K., Tanigawa, W.T. and Yamashita, K.M., 1986. Mechanical response of the south flank of Kilauea Volcano, Hawaii, to intrusive events along the rift systems. *Tectonophysics*, 124(3-4), pp.193-209.

Dzurisin, D., 2003. A comprehensive approach to monitoring volcano deformation as a window on the eruption cycle. *Reviews of Geophysics*, 41(1).

Edmonds, M. and Herd, R.A., 2007. A volcanic degassing event at the explosive-effusive transition. *Geophysical Research Letters*, 34(21).

Edmonds, M., Oppenheimer, C., Pyle, D.M., Herd, R.A. and Thompson, G., 2003. SO<sub>2</sub> emissions from Soufrière Hills Volcano and their relationship to conduit permeability, hydrothermal interaction and degassing regime. *Journal of Volcanology and Geothermal Research*, 124(1), pp.23-43.

Eichelberger, J. C., Carrigan, C. R., Westrich, H. R., and Price, R. H., 1986. Non-explosive silicic volcanism. *Nature*, 323(6089), 598-602.

Elsworth, D. and Voight, B., 1992. Theory of dike intrusion in a saturated porous solid. *Journal of Geophysical Research: Solid Earth*, 97(B6), pp.9105-9117.

Elsworth, D., Voight, B., Ouyang, Z. and Piggott, A.R., 1996. Poroelastic response resulting from magma intrusion. In *Mechanics of Poroelastic Media* (pp. 215-233). Springer Netherlands.

Engelder, J.T., 1974. Cataclasis and the generation of fault gouge. *Geological Society of America Bulletin*, 85(10), pp.1515-1522.

Faoro, I., Vinciguerra, S., Marone, C., Elsworth, D. and Schubnel, A., 2013. Linking permeability to crack density evolution in thermally stressed rocks under cyclic loading. *Geophysical Research Letters*, 40(11), pp.2590-2595.

Faulkner, D. R., and Rutter, E. H., 2001. Can the maintenance of overpressured fluids in large strike-slip fault zones explain their apparent weakness? *Geology*, 29(6), 503-506.

Fink, J. H., and Kieffer, S. W., 1993. Estimate of pyroclastic flow velocities resulting from explosive decompression of lava domes. *Nature*, 363(6430), 612-615.

Fink, J. H., and Manley, C. R., 1987. Origin of pumiceous and glassy textures in rhyolite flows and domes. *Geological Society of America Special Papers*, 212, 77-88.

Forchheimer, P., 1901. Wasserbewegung durch boden. [Water movement through soil.] *Zeitschrift des Vereines Deutscher Ingenieure*, 45(1782), p.1788. (In German).

Fortin, J., Stanchits, S., Vinciguerra, S. and Guéguen, Y., 2011. Influence of thermal and mechanical cracks on permeability and elastic wave velocities in a basalt from Mt. Etna volcano subjected to elevated pressure. *Tectonophysics*, 503(1), pp.60-74.

Galindo, I., and Gudmundsson, A., 2012. Basaltic feeder dykes in rift zones: geometry, emplacement, and effusion rates. *Natural Hazards and Earth System Sciences*, 12(12), 3683-3700.

Gamble, J.A., Wood, C.P., Price, R.C., Smith, I.E.M., Stewart, R.B. and Waight, T., 1999. A fifty year perspective of magmatic evolution on Ruapehu Volcano, New Zealand: verification of open system behaviour in an arc volcano. *Earth and Planetary Science Letters*, 170(3), pp.301-314.

Gardeweg, M.C., Sparks, R.S.J. and Matthews, S.J., 1998. Evolution of Lascar volcano, northern Chile. *Journal of the Geological Society*, 155(1), pp.89-104.

Gatto, H.G., 1984. The effect of various states of stress on the permeability of Berea sandstone (Doctoral dissertation, Texas A&M University).

Gaunt, H. E., Sammonds, P. R., Meredith, P. G., Smith, R., and Pallister, J. S., 2014. Pathways for degassing during the lava dome eruption of Mount St. Helens 2004–2008. *Geology*, 42(11), 947-950.

Gaylord, D.R. and Neall, V.E., 2012. Subedifice collapse of an andesitic stratovolcano: The Maitahi Formation, Taranaki Peninsula, New Zealand. *Geological Society of America Bulletin*, 124(1-2), pp.181-199.

Gerst, A. and Savage, M.K., 2004. Seismic anisotropy beneath Ruapehu volcano: a possible eruption forecasting tool. *Science*, 306(5701), pp.1543-1547.

Giammanco, S., Gurrieri, S., and Valenza, M., 1998. Anomalous soil CO<sub>2</sub> degassing in relation to faults and eruptive fissures on Mount Etna (Sicily, Italy). *Bulletin of Volcanology*, 60(4), 252-259.

Giordano, D., Russell, J. K., and Dingwell, D. B., 2008. Viscosity of magmatic liquids: a model. *Earth and Planetary Science Letters*, 271(1), 123-134.

Gonnermann, H. M., and Manga, M., 2005. Flow banding in obsidian: A record of evolving textural heterogeneity during magma deformation. *Earth and Planetary Science Letters*, 236(1), 135-147.

Gonnermann, H. M., and Manga, M., 2007. The fluid mechanics inside a volcano. *Annual Review of Fluid Mechanics*. 39, 321-356.

Gonnermann, H.M. and Manga, M., 2003. Explosive volcanism may not be an inevitable consequence of magma fragmentation. *Nature*, 426(6965), pp.432-435.

Gonnermann, H.M. and Manga, M., 2013. Dynamics of magma ascent in the volcanic conduit. *Modeling Volcanic Processes: The physics and mathematics of volcanism*, p.55.

González, M.B., Ramírez, J.J. and Navarro, C., 2002. Summary of the historical eruptive activity of Volcán de Colima, Mexico 1519–2000. *Journal of Volcanology and Geothermal Research*, 117(1), pp.21-46.

Goto, A., 1999. A new model for volcanic earthquake at Unzen Volcano: melt rupture model. *Geophysical Research Letters*, 26(16), 2541-2544.

Goto, Y., Nakada, S., Kurokawa, M., Shimano, T., Sugimoto, T., Sakuma, S., Hoshizumi, H., Yoshimoto, M. and Uto, K., 2008. Character and origin of lithofacies in the conduit of Unzen volcano, Japan. *Journal of Volcanology and Geothermal Research*, 175(1), pp.45-59.

Gottsmann, J., Camacho, A.G., Martí, J., Wooller, L., Fernández, J., Garcia, A. and Rymer, H., 2008. Shallow structure beneath the Central Volcanic Complex of Tenerife from new gravity data: Implications for its evolution and recent reactivation. *Physics of the Earth and Planetary Interiors*, 168(3), pp.212-230.

Grant, M.A., 1982. *Geothermal reservoir engineering*. John Wiley & Sons, Ltd.

Griffiths, R. W., and Fink, J. H., 1993. Effects of surface cooling on the spreading of lava flows and domes. *Journal of Fluid Mechanics*, 252, 667-702.

Gruzdkov, A. A., and Petrov, Y. V., 2008. Cavitation breakup of low- and high-viscosity liquids. *Technical Physics*, 53(3), 291-295.

Gudmundsson, A., 2011. *Rock Fractures in Geological Processes*. Cambridge University Press, UK.

Gudmundsson, A., 2012. Magma chambers: Formation, local stresses, excess pressures, and compartments. *Journal of Volcanology and Geothermal Research*, 237, pp.19-41.

Gudmundsson, A., 2012. Strengths and strain energies of volcanic edifices: implications for eruptions, collapse calderas, and landslides. *Natural Hazards and Earth System Sciences*, 12(7), pp.2241-2258.

Guéguen, Y. and Palciauskas, V., 1994. Introduction to the physics of rocks. Princeton University Press.

Guéguen, Y., and Palciauskas, V., 1994. Introduction to the physics of rocks. Princeton University Press, UK.

Hagerty, M.T., Schwartz, S.Y., Garces, M.A. and Protti, M., 2000. Analysis of seismic and acoustic observations at Arenal Volcano, Costa Rica, 1995–1997. *Journal of Volcanology and Geothermal Research*, 101(1), pp.27-65.

Hale, A. J., and Mülhaus, H. B., 2007. Modelling shear bands in a volcanic conduit: Implications for overpressures and extrusion-rates. *Earth and Planetary Science Letters*, 263(1), 74-87.

Hall, M. L., Robin, C., Beate, B., Mothes, P., and Monzier, M., 1999. Tungurahua Volcano, Ecuador: structure, eruptive history and hazards. *Journal of Volcanology and Geothermal Research*, 91(1), 1-21.

Harris, A.J.L. and Maciejewski, A.J.H., 2000. Thermal surveys of the Vulcano Fossa fumarole field 1994–1999: evidence for fumarole migration and sealing. *Journal of Volcanology and Geothermal Research*, 102(1), pp.119-147.

Hatton, C.G., Main, I.G. and Meredith, P.G., 1994. Non-universal scaling of fracture length and opening displacement. *Nature*, 367(6459), pp.160-162.

Heap, M. J., Farquharson, J. I., Baud, P., Lavallée, Y., and Reuschlé, T., 2015a. Fracture and compaction of andesite in a volcanic edifice. *Bulletin of Volcanology*, 77(6), pp.1-19.

Heap, M. J., Farquharson, J. I., Wadsworth, F. B., Kolzenburg, S., and Russell, J. K., 2015b. Timescales for permeability reduction and strength recovery in densifying magma. *Earth and Planetary Science Letters*, 429, 223-233.

Heap, M. J., Kennedy, B. M., Pernin, N., Jacquemard, L., Baud, P., Farquharson, J. I., and Dingwell, D. B., 2015c. Mechanical behaviour and failure modes in the Whakaari (White Island volcano) hydrothermal system, New Zealand. *Journal of Volcanology and Geothermal Research*, 295, 26-42.

Heap, M. J., Kolzenburg, S., Russell, J. K., Campbell, M. E., Welles, J., Farquharson, J. I., and Ryan, A., 2014a. Conditions and timescales for welding block-and-ash flow deposits. *Journal of Volcanology and Geothermal Research*, 289, 202-209.

Heap, M. J., Lavallée, Y., Petrakova, L., Baud, P., Reuschle, T., Varley, N. R., and Dingwell, D. B., 2014b. Microstructural controls on the physical and mechanical properties of edifice-forming andesites at Volcán de Colima, Mexico. *Journal of Geophysical Research: Solid Earth*, 119(4), 2925-2963.

Heap, M. J., Xu, T., Kushnir, A. R. L., Kennedy, B. M., and Chen, C. F., 2015d. Fracture of magma containing overpressurised pores. *Journal of Volcanology and Geothermal Research*, 301, pp.180-190

Heap, M.J. and Kennedy, B.M., 2016. Exploring the scale-dependent permeability of fractured andesite. *Earth and Planetary Science Letters*, 447, pp.139-150.

Heap, M.J., Baud, P., Meredith, P.G., Vinciguerra, S. and Reuschlé, T., 2014c. The permeability and elastic moduli of tuff from Campi Flegrei, Italy: implications for ground deformation modelling. *Solid Earth*, 5(1), p.25.

Heap, M.J., Baud, P., Meredith, P.G., Vinciguerra, S., Bell, A.F. and Main, I.G., 2011. Brittle creep in basalt and its application to time-dependent volcano deformation. *Earth and Planetary Science Letters*, 307(1), pp.71-82.

Heap, M.J., Baud, P., Reuschlé, T. and Meredith, P.G., 2014d. Styolites in limestones: Barriers to fluid flow?. *Geology*, 42(1), pp.51-54.

Heap, M.J., Baud, P., Meredith, P. G., Bell, A. F., and Main, I. G., 2009. Time-dependent brittle creep in Darley Dale sandstone. *Journal of Geophysical Research: Solid Earth* (1978–2012), 114(B7).

Heap, M.J. and Wadsworth, F.B., 2016. Closing an open system: Pore pressure changes in permeable edifice rock at high strain rates. *Journal of Volcanology and Geothermal Research*, 315, pp.40-50.

Heap, M.J., Brantut, N., Baud, P. and Meredith, P.G., 2015e. Time-dependent compaction band formation in sandstone. *Journal of Geophysical Research: Solid Earth*, 120(7), pp.4808-4830.

Heiken, G., Wohletz, K., and Eichelberger, J., 1988. Fracture fillings and intrusive pyroclasts, Inyo Domes, California. *Journal of Geophysical Research: Solid Earth*, 93(B5), 4335-4350.

Heiland, J., 2003. Permeability of triaxially compressed sandstone: Influence of deformation and strain-rate on permeability. In *Thermo-Hydro-Mechanical Coupling in Fractured Rock* (pp. 889-908). Birkhäuser Basel.

Heiligmann, M., Stix, J., Williams-Jones, G., Lollar, B. S., and Garzón, V. G., 1997. Distal degassing of radon and carbon dioxide on Galeras volcano, Colombia. *Journal of Volcanology and Geothermal Research*, 77(1), 267-283.

Heilprin, A., 1903. The Ascending Obelisk of the Montagne Pelée. *Science*, pp.184-185.

Heimisson, E. R., Einarsson, P., Sigmundsson, F., and Brandsdóttir, B., 2015. Kilometer-scale Kaiser effect identified in Krafla volcano, Iceland. *Geophysical Research Letters*, 42(19), pp.7958-7965

Hess, K.U. and Dingwell, D.D., 1996. Viscosities of hydrous leucogranitic melts: A non-Arrhenian model. *American Mineralogist*, 81(9-10), pp.1297-1300.

Hoek, E. and Bieniawski, Z.T., 1965. Brittle fracture propagation in rock under compression. *International Journal of Fracture Mechanics*, 1(3), pp.137-155.

Holtz, F., Sato, H., Lewis, J., Behrens, H. and Nakada, S., 2005. Experimental petrology of the 1991–1995 Unzen dacite, Japan. Part I: phase relations, phase composition and pre-eruptive conditions. *Journal of Petrology*, 46(2), pp.319-337.

Hooper, A., Zebker, H., Segall, P. and Kampes, B., 2004. A new method for measuring deformation on volcanoes and other natural terrains using InSAR persistent scatterers. *Geophysical research letters*, 31(23).

Hornby, A.J., Kendrick, J.E., Lamb, O.D., Hirose, T., De Angelis, S., Aulock, F.W., Umakoshi, K., Miwa, T., Henton De Angelis, S., Wadsworth, F.B. and Hess, K.U., 2015. Spine growth and seismogenic faulting at Mt. Unzen, Japan. *Journal of Geophysical Research: Solid Earth*, 120(6), pp.4034-4054.

Houghton, B.F., Latter, J.H. and Hackett, W.R., 1987. Volcanic hazard assessment for Ruapehu composite volcano, Taupo volcanic zone, New Zealand. *Bulletin of Volcanology*, 49(6), pp.737-751.

Hubbert, M.K. and Rubey, W.W., 1959. Role of fluid pressure in mechanics of overthrust faulting I. Mechanics of fluid-filled porous solids and its application to overthrust faulting. *Geological Society of America Bulletin*, 70(2), pp.115-166

Hurwitz, S., and Johnston, M. J., 2003. Groundwater level changes in a deep well in response to a magma intrusion event on Kilauea Volcano, Hawai'i. *Geophysical research letters*, 30(22).

Hurwitz, S., Kipp, K.L., Ingebritsen, S.E. and Reid, M.E., 2003. Groundwater flow, heat transport, and water table position within volcanic edifices: Implications for volcanic processes in the Cascade Range. *Journal of Geophysical Research: Solid Earth*, 108(B12).

Hutchison, W., Varley, N., Pyle, D.M. and Mather, T.A., 2013. Airborne Thermal Remote Sensing of the Volcán de Colima (Mexico) Lava Dome from 2007 to 2010 In: D.L. Pyle and T.A. Mather (Editors), *Remote sensing of volcanoes & volcanic processes: integrating observation & modelling*. Geological Society, London, pp. 203-228.

Invernizzi, C., Pierantoni, P. P., Chiodi, A., Maffucci, R., Corrado, S., Baez, W., and Viramonte, J. (2014). Preliminary assessment of the geothermal potential of Rosario de la Frontera area (Salta, NW Argentina): Insight from hydro-geological, hydro-geochemical and structural investigations. *Journal of South American Earth Sciences*, 54, 20-36. doi:10.1016/j.jsames.2014.04.003

Iverson, R.M., Dzurisin, D., Gardner, C.A., Gerlach, T.M., LaHusen, R.G., Lisowski, M., Major, J.J., Malone, S.D., Messerich, J.A., Moran, S.C. and Pallister, J.S., 2006. Dynamics of seismogenic volcanic extrusion at Mount St Helens in 2004–05. *Nature*, 444(7118), pp.439-443.

Jaeger, J. C., Cook, N. G., and Zimmerman, R., 2009. Fundamentals of rock mechanics. John Wiley & Sons.

James, M.R. and Varley, N., 2012. Identification of structural controls in an active lava dome with high resolution DEMs: Volcán de Colima, Mexico. *Geophysical Research Letters*, 39(22).

James, M.R., Lane, S.J., Chouet, B. and Gilbert, J.S., 2004. Pressure changes associated with the ascent and bursting of gas slugs in liquid-filled vertical and inclined conduits. *Journal of Volcanology and Geothermal Research*, 129(1), pp.61-82.

Jaupart, C. and Allègre, C.J., 1991. Gas content, eruption rate and instabilities of eruption regime in silicic volcanoes. *Earth and Planetary Science Letters*, 102(3), pp.413-429.

Jaupart, C., 1998. Gas loss from magmas through conduit walls during eruption. *Geological Society, London, Special Publications*, 145(1), pp.73-90.

Jeong, H.S., Kang, S.S. and Obara, Y., 2007. Influence of surrounding environments and strain rates on the strength of rocks subjected to uniaxial compression. *International Journal of Rock Mechanics and Mining Sciences*, 44(3), pp.321-331.

John, D.A., Sisson, T.W., Breit, G.N., Rye, R.O. and Vallance, J.W., 2008. Characteristics, extent and origin of hydrothermal alteration at Mount Rainier Volcano, Cascades Arc, USA: Implications for debris-flow hazards and mineral deposits. *Journal of Volcanology and Geothermal Research*, 175(3), pp.289-314.

Johnson, J.B. and Lees, J.M., 2000. Plugs and chugs—seismic and acoustic observations of degassing explosions at Karymsky, Russia and Sangay, Ecuador. *Journal of Volcanology and Geothermal Research*, 101(1), pp.67-82.

Johnson, P.A. and McEvilly, T.V., 1995. Parkfield seismicity: Fluid-driven?. *Journal of Geophysical Research: Solid Earth*, 100(B7), pp.12937-12950.

Jousset, P., Budi-Santoso, A., Jolly, A.D., Boichu, M., Dwiyono, S., Sumarti, S., Hidayati, S. and Thierry, P., 2013. Signs of magma ascent in LP and VLP seismic events and link to degassing: An example from the 2010 explosive eruption at Merapi volcano, Indonesia. *Journal of Volcanology and Geothermal Research*, 261, pp.171-192.

Kaiser, J., 1953. Erkenntnisse und Folgerungen aus der Messung von Geräuschen bei Zugbeanspruchung von metallischen Werkstoff-

fen. [Findings and conclusions from the measurement of noise in tension of metallic materials.] Verlag Stahleisen. (In German).

Keaney, G.M.J., Meredith, P.G. and Murrell, S.A.F., 1998, January. Laboratory Study of Permeability Evolution in a Tight Sandstone under Non-Hydrostatic Stress Conditions. In SPE/ISRM Rock Mechanics in Petroleum Engineering. Society of Petroleum Engineers.

Keating, G.N., Valentine, G.A., Krier, D.J. and Perry, F.V., 2008. Shallow plumbing systems for small-volume basaltic volcanoes. *Bulletin of Volcanology*, 70(5), pp.563-582.

Kempter, K.A., Benner, S.G. and Williams, S.N., 1996. Rincón de la Vieja volcano, Guanacaste province, Costa Rica: geology of the southwestern flank and hazards implications. *Journal of Volcanology and Geothermal research*, 71(2), pp.109-127.

Kendrick, J. E., Lavallée, Y., Ferk, A., Perugini, D., Leonhardt, R., and Dingwell, D. B., 2012. Extreme frictional processes in the volcanic conduit of Mount St. Helens (USA) during the 2004–2008 eruption. *Journal of Structural Geology*, 38, 61-76.

Kendrick, J. E., Lavallée, Y., Hess, K. U., De Angelis, S., Ferk, A., Gaunt, H. E., Meredith, P. G., Dingwell, D. B. and Leonhardt, R., 2014b. Seismogenic frictional melting in the magmatic column. *Solid Earth*, 5(1), 199-208.

Kendrick, J. E., Lavallée, Y., Hess, K. U., Heap, M. J., Gaunt, H. E., Meredith, P. G., and Dingwell, D. B., 2013a. Tracking the permeable porous network during strain-dependent magmatic flow. *Journal of Volcanology and Geothermal Research*, 260, 117-126.

Kendrick, J. E., Lavallée, Y., Hirose, T., Di Toro, G., Hornby, A. J., De Angelis, S., and Dingwell, D. B., 2014a. Volcanic drumbeat seismicity caused by stick-slip motion and magmatic frictional melting. *Nature Geoscience*, 7(6), 438-442.

Kendrick, J. E., Smith, R., Sammonds, P., Meredith, P. G., Dainty, M., and Pallister, J. S., 2013b. The influence of thermal and cyclic stressing on the strength of rocks from Mount St. Helens, Washington. *Bulletin of Volcanology*, 75(7), 1-12.

Kendrick, J.E., Lavallée, Y., Varley, N., Wadsworth, F.B., Lamb, O.D. and Vasseur, J., 2016. Blowing off steam: Tuffisite formation as a regulator for lava dome eruptions. *Frontiers in Earth Science*, 4, p.41.

Kennedy, B. M., Spieler, O., Scheu, B., Kueppers, U., Taddeucci, J., and Dingwell, D. B., 2005. Conduit implosion during Vulcanian eruptions. *Geology*, 33(7), 581-584.

Kennedy, B. M., Wadsworth, F. B., Schipper, C. I., Jellinek, M., Vasseur, J., von Aulock, F. W., Hess, K.-U., Russell, K., Lavallée, Y., Nichols, A. R. L., and Dingwell, D. B., 2015. Surface tension densifies

magma but maintains permeability. *Earth and Planetary Science Letters*, 433, 116-124.

Kennedy, L.A. and Russell, J.K., 2012. Cataclastic production of volcanic ash at Mount Saint Helens. *Physics and Chemistry of the Earth, Parts A/B/C*, 45, pp.40-49.

Kennedy, L.A., Russell, J.K., and Nelles, E., 2009. Origins of mount St. Helens cataclasites: Experimental insights, *American Mineralogist*, 94, 995-1004.

Kiyama, T., Kita, H., Ishijima, Y., Yanagidani, T., Aoki, K. and Sato, T., 1996, January. Permeability in anisotropic granite under hydrostatic compression and triaxial compression including post-failure region. In 2nd North American Rock Mechanics Symposium. American Rock Mechanics Association.

Klein, E. and Reuschlé, T., 2003. A model for the mechanical behaviour of Bentheim sandstone in the brittle regime. In *Thermo-Hydro-Mechanical Coupling in Fractured Rock* (pp. 833-849). Birkhäuser Basel.

Klinkenberg, L.J., 1941. The permeability of porous media to liquids and gases. Drilling and production practice. American Petroleum Institute.

Klug, C. and Cashman, K.V., 1996. Permeability development in vesiculating magmas: implications for fragmentation. *Bulletin of Volcanology*, 58(2-3), pp.87-100.

Klug, C., Cashman, K., and Bacon, C., 2002. Structure and physical characteristics of pumice from the climactic eruption of Mount Mazama (Crater Lake), Oregon. *Bulletin of Volcanology*, 64(7), 486-501.

Knapp, R. B., and Knight, J. E., 1977. Differential thermal expansion of pore fluids: Fracture propagation and microearthquake production in hot pluton environments. *Journal of Geophysical Research*, 82(17), 2515-2522.

Kolzenburg, S., Heap, M.J., Lavallée, Y., Russell, J.K., Meredith, P.G. and Dingwell, D.B., 2012. Strength and permeability recovery of tuffisite-bearing andesite. *Solid Earth*, 3(2), p.191.

Kovari, K., Tisa, A., Einstein, H.H. and Franklin, J.A., 1983. Suggested methods for determining the strength of rock materials in triaxial compression: revised version. *International Journal of Rock Mechanics and Mining Sciences*, 20(6), pp.283-290.

Koyaguchi, T., Scheu, B., Mitani, N.K. and Melnik, O., 2008. A fragmentation criterion for highly viscous bubbly magmas estimated from shock tube experiments. *Journal of Volcanology and Geothermal Research*, 178(1), pp.58-71.

Kozeny, J. (1927). Über kapillare Leitung des Wassers im Boden: (Aufstieg, Versickerung und Anwendung auf die Bewässerung). [On capillary transport of water in soil: (Ascent, infiltration and application to irrigation)]. Hölder-Pichler-Tempsky. (In German).

Kranz, R. L., and Scholz, C. H., 1977. Critical dilatant volume of rocks at the onset of tertiary creep. *Journal of Geophysical Research*, 82(30), 4893-4898.

Kueppers, U., Putz, C., Spieler, O. and Dingwell, D.B., 2012. Abrasion in pyroclastic density currents: insights from tumbling experiments. *Physics and Chemistry of the Earth, Parts A/B/C*, 45, pp.33-39.

Kueppers, U., Scheu, B., Spieler, O. and Dingwell, D.B., 2005. Field-based density measurements as tool to identify preeruption dome structure: set-up and first results from Unzen volcano, Japan. *Journal of Volcanology and Geothermal Research*, 141(1), pp.65-75.

Kumagai, H., Chouet, B.A. and Nakano, M., 2002. Temporal evolution of a hydrothermal system in Kusatsu-Shirane Volcano, Japan, inferred from the complex frequencies of long-period events. *Journal of Geophysical Research: Solid Earth*, 107(B10).

Kushnir, A.R., Martel, C., Bourdier, J.L., Heap, M.J., Reuschlé, T., Erdmann, S., Komorowski, J.C. and Cholik, N., 2016. Probing permeability and microstructure: Unravelling the role of a low-permeability dome on the explosivity of Merapi (Indonesia). *Journal of Volcanology and Geothermal Research*, 316, pp.56-71.

Lacey, A., Ockendon, J. R., and Turcotte, D. L., 1981. On the geometrical form of volcanoes. *Earth and Planetary Science Letters*, 54(1), 139-143.

Lahr, J.C., Chouet, B.A., Stephens, C.D., Power, J.A. and Page, R.A., 1994. Earthquake classification, location, and error analysis in a volcanic environment: Implications for the magmatic system of the 1989–1990 eruptions at Redoubt Volcano, Alaska. *Journal of Volcanology and Geothermal Research*, 62(1), pp.137-151.

Laumonier, M., Arbaret, L., Burgisser, A., and Champallier, R., 2011. Porosity redistribution enhanced by strain localization in crystal-rich magmas. *Geology*, 39(8), 715-718.

Lavallée Y., Wadsworth F.B., Vasseur J., Russell J.K., Andrews G.D.M., Hess K.-U., Aulock F., Kendrick J.E., Tuffen H., Biggin A.J., Dingwell D.B., 2015. Eruption and emplacement time-scales of ignimbrite super-eruptions from thermo-kinetics of glass shards. *Frontiers in Earth Sciences*, 3,2.

Lavallée, Y., Benson, P. M., Heap, M. J., Hess, K. U., Flaws, A., Schillinger, B., and Dingwell, D. B., 2013. Reconstructing magma failure and the degassing network of dome-building eruptions. *Geology*, 41(4), 515-518.

Lavallée, Y., Benson, P.M., Heap, M.J., Flaws, A., Hess, K.U. and Dingwell, D.B., 2012. Volcanic conduit failure as a trigger to magma fragmentation. *Bulletin of Volcanology*, 74(1), pp.11-13.

Lavallée, Y., Dingwell, D.B., Johnson, J.B., Cimarelli, C., Hornby, A.J., Kendrick, J.E., von Aulock, F.W., Kennedy, B.M., Andrews, B.J., Wadsworth, F.B. and Rhodes, E., 2015. Thermal vesiculation during volcanic eruptions. *Nature*, 528(7583), pp.544-547.

Lavallée, Y., Heap, M.J., Kueppers, U., Kendrick, J. and Dingwell, D.B., 2016. The Fragility of Volcán de Colima- a material constraint. In: Varley, N. and Komorowski, J-C., eds *Volcán de Colima: Managing the threat. Active Volcanoes of the World*. Springer, New York. ISBN 978-3-642-25910-4 (In Press)

Lavallée, Y., Hess, K. U., Cordonnier, B., and Dingwell, D. B., 2007. Non-Newtonian rheological law for highly crystalline dome lavas. *Geology*, 35(9), 843-846.

Lavallée, Y., Meredith, P. G., Dingwell, D. B., Hess, K. U., Wassermann, J., Cordonnier, B., and Kruhl, J. H., 2008. Seismogenic lavas and explosive eruption forecasting. *Nature*, 453(7194), 507-510.

Lavallée, Y., Varley, N.R., Alatorre-Ibargüengoitia, M.A., Hess, K.U., Kueppers, U., Mueller, S., Richard, D., Scheu, B., Spieler, O. and Dingwell, D.B., 2012. Magmatic architecture of dome-building eruptions at Volcán de Colima, Mexico. *Bulletin of Volcanology*, 74(1), pp.249-260.

Lavrov, A., 2003. The Kaiser effect in rocks: principles and stress estimation techniques. *International Journal of Rock Mechanics and Mining Sciences*, 40(2), pp.151-171.

Le Cloarec, M.F. and Gauthier, P.J., 2003. Merapi Volcano, Central Java, Indonesia: A case study of radionuclide behavior in volcanic gases and its implications for magma dynamics at andesitic volcanoes. *Journal of Geophysical Research: Solid Earth*, 108(B5).

Le Pennec, J.L., Hermitte, D., Dana, I., Pezard, P., Coulon, C., Cochemé, J.J., Mulyadi, E., Ollagnier, F. and Revest, C., 2001. Electrical conductivity and pore-space topology of Merapi lavas: implications for the degassing of porphyritic andesite magmas. *Geophysical Research Letters*, 28(22), pp.4283-4286.

Lensky, N.G., Navon, O. and Lyakhovsky, V., 2004. Bubble growth during decompression of magma: experimental and theoretical investigation. *Journal of Volcanology and Geothermal Research*, 129(1), pp.7-22.

Liu, Y., Zhang, Y. and Behrens, H., 2005. Solubility of H<sub>2</sub>O in rhyolitic melts at low pressures and a new empirical model for mixed H<sub>2</sub>O-CO<sub>2</sub> solubility in rhyolitic melts. *Journal of Volcanology and Geothermal Research*, 143(1), pp.219-235.

- Loaiza, S., Fortin, J., Schubnel, A., Gueguen, Y., Vinciguerra, S. and Moreira, M., 2012. Mechanical behavior and localized failure modes in a porous basalt from the Azores. *Geophysical Research Letters*, 39(19).
- Lockner, D., 1993. The role of acoustic emission in the study of rock fracture. *International Journal of Rock Mechanics and Mining Sciences* 30, 883 - 899.
- Luhr, J.F., 2002. Petrology and geochemistry of the 1991 and 1998–1999 lava flows from Volcán de Colima, México: implications for the end of the current eruptive cycle. *Journal of Volcanology and Geothermal Research*, 117(1), pp.169-194.
- Ma, J., 2015. Review of permeability evolution model for fractured porous media. *Journal of Rock Mechanics and Geotechnical Engineering*, 7(3), pp.351-357.
- Mackenzie, J.K. and Shuttleworth, R., 1949. A phenomenological theory of sintering. *Proceedings of the Physical Society. Section B*, 62(12), p.833.
- Main, I.G., Leonard, T., Papasouliotis, O., Hatton, C.G. and Meredith, P.G., 1999. One slope or two? Detecting statistically significant breaks of slope in geophysical data, with application to fracture scaling relationships. *Geophysical Research Letters*, 26(18), pp.2801-2804.
- Maksimov, S.O. and Sakhno, V.G., 2011, First data on U-Pb SHRIMP-II isotopic dating based on zircons of ash sediments from Cenozoic depressions in Southwest of Primorie. In *Doklady Earth Sciences* (Vol. 439, No. 1, pp. 919-925). SP MAIK Nauka/Interperiodica.
- Manga, M., Patel, A. and Dufek, J., 2011. Rounding of pumice clasts during transport: field measurements and laboratory studies. *Bulletin of Volcanology*, 73(3), pp.321-333.
- Martel, C. and Iacono-Marziano, G., 2015. Timescales of bubble coalescence, outgassing, and foam collapse in decompressed rhyolitic melts. *Earth and Planetary Science Letters*, 412, pp.173-185.
- Martel, C., Dingwell, D.B., Spieler, O., Pichavant, M. and Wilke, M., 2000. Fragmentation of foamed silicic melts: an experimental study. *Earth and Planetary Science Letters*, 178(1), pp.47-58.
- Marti, J., Soriano, C. and Dingwell, D.B., 1999. Tube pumices as strain markers of the ductile–brittle transition during magma fragmentation. *Nature*, 6402(6762), pp.650-653.
- Massol, H., and Jaupart, C., 2009. Dynamics of magma flow near the vent: Implications for dome eruptions. *Earth and Planetary Science Letters*, 279(3), 185-196.
- Massol, H., Jaupart, C. and Pepper, D., 2001. Ascent and decompression of viscous vesicular magma in a volcanic conduit. *Journal of Geophysical Research-Solid Earth*, 106(B8), p.16223.

Mastin, L. G., 2002. Insights into volcanic conduit flow from an open-source numerical model. *Geochemistry, Geophysics, Geosystems*, 3(7), 1-18.

Mastin, L. G., and Pollard, D. D., 1988. Surface deformation and shallow dike intrusion processes at Inyo Craters, Long Valley, California. *Journal of Geophysical Research: Solid Earth*, 93(B11), 13221-13235.

McPhee, C.A. and Arthur, K.G., 1991. Klinkenberg permeability measurements: problems and practical solutions. In *Advances in Core Evaluation IL Reservoir Appraisal. Proceedings of the 2nd Society of Core Analysts European Core Analysis Symposium*. Gordon & Breach Science Publishers, Philadelphia (pp. 371-391).

Mees, F., Swennen, R., Van Geet, M. and Jacobs, P., 2003. Applications of X-ray computed tomography in the geosciences. *Geological Society, London, Special Publications*, 215(1), pp.1-6.

Mellors, R.A. and Sparks, R.S.J., 1991. Spatter-rich pyroclastic flow deposits on Santorini, Greece. *Bulletin of Volcanology*, 53(5), pp.327-342.

Melnik, O. and Sparks, R.S.J., 1999. Nonlinear dynamics of lava dome extrusion. *Nature*, 402(6757), pp.37-41.

Melnik, O. and Sparks, R.S.J., 2005. Controls on conduit magma flow dynamics during lava dome building eruptions. *Journal of Geophysical Research: Solid Earth*, 110(B2).

Melnik, O., 2000. Dynamics of two-phase conduit flow of high-viscosity gas-saturated magma: large variations of sustained explosive eruption intensity. *Bulletin of Volcanology*, 62(3), pp.153-170.

Melnik, O., and Sparks, R. S. J., 2002. Dynamics of magma ascent and lava extrusion at Soufrière Hills Volcano, Montserrat. *Geological Society, London, Memoirs*, 21(1), 153-171.

Melnik, O., Barmin, A. A., and Sparks, R. S. J., 2005. Dynamics of magma flow inside volcanic conduits with bubble overpressure buildup and gas loss through permeable magma. *Journal of Volcanology and Geothermal Research*, 143(1), 53-68.

Meredith, P.G. and Atkinson, B.K., 1985. Fracture toughness and subcritical crack growth during high-temperature tensile deformation of Westerly granite and Black gabbro. *Physics of the Earth and Planetary Interiors*, 39(1), pp.33-51.

Meredith, P.G., Main, I.G. and Jones, C., 1990. Temporal variations in seismicity during quasi-static and dynamic rock failure. *Tectonophysics*, 175(1-3), pp.249-268.

Michaut, C., Ricard, Y., Bercovici, D., and Sparks, R. S. J., 2013. Eruption cyclicity at silicic volcanoes potentially caused by magmatic gas waves. *Nature Geoscience*, 6(10), 856-860.

Michol, K.A., Russell, J.K. and Andrews, G.D.M., 2008. Welded block and ash flow deposits from Mount Meager, British Columbia, Canada. *Journal of Volcanology and Geothermal Research*, 169(3), 121-144.

Mitchell, T.M. and Faulkner, D.R., 2008. Experimental measurements of permeability evolution during triaxial compression of initially intact crystalline rocks and implications for fluid flow in fault zones. *Journal of Geophysical Research: Solid Earth*, 113(B11).

Mogi, K. 1958. Relations between the eruptions of various volcanoes and the deformation of the ground surfaces around them. *Bulletin of the Earthquake Research Institute*, 36, pp. 99-134

Mora, J.C., Macias, J.L., Saucedo, R., Orlando, A., Manetti, P. and Vaselli, O., 2002. Petrology of the 1998–2000 products of Volcán de Colima, México. *Journal of Volcanology and Geothermal Research*, 117(1), pp.195-212.

Mordecai, M., Morris, L.H. and Eng, C., 1970. An investigation into the changes of permeability occurring in a sandstone when failed under triaxial stress conditions. In The 12th US Symposium on Rock Mechanics (USRMS). American Rock Mechanics Association.

Mueller S., Melnik O., Spieler O., Scheu B., Dingwell D.B., 2005. Permeability and degassing of dome lavas undergoing rapid decompression: An experimental determination: *Bulletin of Volcanology*, 67, p. 526– 538.

Mueller, S., Llewellyn, E., and Mader, H., 2010. The rheology of suspensions of solid particles. *Proceedings of the Royal Society of London A: Mathematical, Physical and Engineering Sciences*, 466, (2116) 1201-1228.

Mueller, S., Melnik, O., Spieler, O., Scheu, B. and Dingwell, D.B., 2005. Permeability and degassing of dome lavas undergoing rapid decompression: an experimental determination. *Bulletin of Volcanology*, 67(6), pp.526-538.

Mueller, S., Scheu, B., Kueppers, U., Spieler, O., Richard, D. and Dingwell, D.B., 2011. The porosity of pyroclasts as an indicator of volcanic explosivity. *Journal of Volcanology and Geothermal Research*, 203(3), pp.168-174.

Mueller, S., Scheu, B., Spieler, O. and Dingwell, D.B., 2008. Permeability control on magma fragmentation. *Geology*, 36(5), pp.399-402.

Mueller, S.B., Varley, N.R., Kueppers, U., Lesage, P., Davila, G.Á.R. and Dingwell, D.B., 2013. Quantification of magma ascent rate through rockfall monitoring at the growing/collapsing lava dome of Volcán de Colima, Mexico. *Solid Earth*, 4(2), p.201.

- Mueller, S.P., 2006. Permeability and porosity as constraints on the explosive eruption of magma: laboratory experiments and field investigations. (PhD Thesis). University of Munich, Munich, Germany.
- Mukhopadhyay, S. and Sahimi, M., 1994. Scaling behavior of permeability and conductivity anisotropy near the percolation threshold. *Journal of Statistical Physics*, 74(5-6), pp.1301-1308.
- Nakada, S., Shimizu, H. and Ohta, K., 1999. Overview of the 1990–1995 eruption at Unzen Volcano. *Journal of Volcanology and Geothermal Research*, 89(1), pp.1-22.
- Nakada, S., Uto, K., Sakuma, S., Eichelberger, J.C. and Shimizu, H., 2005. Scientific results of conduit drilling in the Unzen Scientific Drilling Project (USDP). *Scientific drilling*, 1(2005), 18-22.
- Namiki, A., and Manga, M., 2005. Response of a bubble bearing viscoelastic fluid to rapid decompression: implications for explosive volcanic eruptions. *Earth and Planetary Science Letters*, 236(1), 269-284.
- Nara, Y., Meredith, P.G., Yoneda, T. and Kaneko, K., 2011. Influence of macro-fractures and micro-fractures on permeability and elastic wave velocities in basalt at elevated pressure. *Tectonophysics*, 503(1), pp.52-59.
- Navon, O., Chekhmir, A., and Lyakhovsky, V., 1998. Bubble growth in highly viscous melts: theory, experiments, and autoexplosivity of dome lavas. *Earth and Planetary Science Letters*, 160(3), 763-776.
- Neuberg, J., 2000. Characteristics and causes of shallow seismicity in andesite volcanoes. *Philosophical Transactions of the Royal Society of London. Series A: Mathematical, Physical and Engineering Sciences*, 358(1770), 1533-1546
- Neuberg, J.W., Tuffen, H., Collier, L., Green, D., Powell, T. and Dingwell, D., 2006. The trigger mechanism of low-frequency earthquakes on Montserrat. *Journal of Volcanology and Geothermal Research*, 153(1), pp.37-50.
- Newhall, C. G., Albano, S. E., Matsumoto, N., and Sandoval, T., 2001. Roles of groundwater in volcanic unrest. *Journal of the Geological Society of the Philippines*, 56, 69-84.
- Nguyen, C. T., Gonnermann, H. M., and Houghton, B. F., 2014. Explosive to effusive transition during the largest volcanic eruption of the 20th century (Novarupta 1912, Alaska). *Geology*, 42(8), 703-706.
- Nicholson, E. J., Mather, T. A., Pyle, D. M., Odber, H. M., and Christopher, T., 2013. Cyclical patterns in volcanic degassing revealed by SO<sub>2</sub> flux time-series analysis: An application to Soufrière Hills Volcano, Montserrat. *Earth and Planetary Science Letters*, 375, 209-221.

Nishi, Y., Sherburn, S., Scott, B.J. and Sugihara, M., 1996. High-frequency earthquakes at White Island volcano, New Zealand: insights into the shallow structure of a volcano-hydrothermal system. *Journal of Volcanology and Geothermal Research*, 72(3), pp.183-197.

Noguchi, S., Toramaru, A. and Nakada, S., 2008. Groundmass crystallization in dacite dykes taken in Unzen Scientific Drilling Project (USDP-4). *Journal of Volcanology and Geothermal Research*, 175(1), pp.71-81.

Norini, G., Capra, L., Groppelli, G., Agliardi, F., Pola, A. and Cortes, A., 2010. Structural architecture of the Colima Volcanic Complex. *Journal of Geophysical Research: Solid Earth*, 115(B12).

Odbert, H., Taisne, B., and Gottsmann, J., 2015. Deposit loading and its effect on co-eruptive volcano deformation. *Earth and Planetary Science Letters*, 413, 186-196.

Okumura, S., and Sasaki, O., 2014. Permeability reduction of fractured rhyolite in volcanic conduits and its control on eruption cyclicity. *Geology*, 42(10), 843-846.

Okumura, S., Nakamura, M., Takeuchi, S., Tsuchiyama, A., Nakano, T. and Uesugi, K., 2009. Magma deformation may induce non-explosive volcanism via degassing through bubble networks. *Earth and Planetary Science Letters*, 281(3), pp.267-274.

Okumura, S., Nakamura, M., Uesugi, K., Nakano, T. and Fujioka, T., 2013. Coupled effect of magma degassing and rheology on silicic volcanism. *Earth and Planetary Science Letters*, 362, pp.163-170.

Ōmori, F., 1920. Seismographical Observations of the Fore-shocks, After-shocks, and After-outbursts of the Great Sakurajima Eruption of 1914. *Bulletin of the Imperial Earthquake Investigation Committee*, 8(5), pp.353-377.

Oppenheimer, C., Rothery, D.A. and Francis, P.W., 1993. Thermal distributions at fumarole fields: implications for infrared remote sensing of active volcanoes. *Journal of Volcanology and Geothermal Research*, 55(1-2), pp.97-115.

Ougier-Simonin, A. and Zhu, W., 2013. Effects of pore fluid pressure on slip behaviors: An experimental study. *Geophysical Research Letters*, 40(11), pp.2619-2624.

Pallister, J.S., Cashman, K.V., Hagstrum, J.T., Beeler, N.M., Moran, S.C. and Denlinger, R.P., 2013. Faulting within the Mount St. Helens conduit and implications for volcanic earthquakes. *Geological Society of America Bulletin*, 125(3-4), pp.359-376.

Palo, M., Ibañez, J.M., Cisneros, M., Bretón, M., Del Pezzo, E., Ocana, E., Orozco-Rojas, J. and Posadas, A.M., 2009. Analysis of the seismic

wavefield properties of volcanic explosions at Volcan de Colima, Mexico: insights into the source mechanism. *Geophysical Journal International*, 177(3), pp.1383-1398

Papale, P., 1999. Strain-induced magma fragmentation in explosive eruptions. *Nature*, 397(6718), pp.425-428.

Paterson, M. S., and T.-f. Wong, 2005. *Experimental Rock Deformation—The Brittle Field*, 2nd ed., Springer, New York.

Peach, C.J. and Spiers, C.J., 1996. Influence of crystal plastic deformation on dilatancy and permeability development in synthetic salt rock. *Tectonophysics*, 256(1), pp.101-128.

Petersen, T., Caplan-Auerbach, J. and McNutt, S.R., 2006. Sustained long-period seismicity at Shishaldin Volcano, Alaska. *Journal of Volcanology and Geothermal Research*, 151(4), pp.365-381.

Petrosino, S., Cusano, P., La Rocca, M., Galluzzo, D., Orozco-Rojas, J., Bretón, M., Ibáñez, J. and Del Pezzo, E., 2011. Source location of long period seismicity at Volcán de Colima, México. *Bulletin of Volcanology*, 73(7), pp.887-898.

Plail, M., Edmonds, M., Humphreys, M. C., Barclay, J., and Herd, R. A., 2014. Geochemical evidence for relict degassing pathways preserved in andesite. *Earth and Planetary Science Letters*, 386, 21-33.

Possemiers, M., Huysmans, M., Peeters, L., Batelaan, O. and Dassargues, A., 2012. Relationship between sedimentary features and permeability at different scales in the Brussels Sands. *Geologica Belgica*, 15(3), pp.156-164.

Power, J. A., Stihler, S. D., White, R. A., and Moran, S. C., 2004. Observations of deep long-period (DLP) seismic events beneath Aleutian arc volcanoes; 1989–2002. *Journal of Volcanology and Geothermal Research*, 138(3), 243-266.

Proussevitch, A.A. and Sahagian, D.L., 1998. Dynamics and energetics of bubble growth in magmas: analytical formulation and numerical modeling. *Journal of Geophysical Research: Solid Earth*, 103(B8), pp.18223-18251.

Quane, S.L., Russell, J.K. and Friedlander, E.A., 2009. Time scales of compaction in volcanic systems. *Geology*, 37(5), pp.471-474.

Rabbani, A. and Jamshidi, S., 2014. Specific surface and porosity relationship for sandstones for prediction of permeability. *International Journal of Rock Mechanics and Mining Sciences*, 71, pp.25-32.

Ramsey, M.S. and Harris, A.J., 2013. Volcanology 2020: How will thermal remote sensing of volcanic surface activity evolve over the next decade?. *Journal of Volcanology and Geothermal research*, 249, pp.217-233.

Reid, M.E., 2004. Massive collapse of volcano edifices triggered by hydrothermal pressurization. *Geology*, 32(5), pp.373-376.

Reid, M.E., Christian, S.B. and Brien, D.L., 2000. Gravitational stability of three-dimensional stratovolcano edifices. *Journal of Geophysical Research: Solid Earth*, 105(B3), pp.6043-6056.

Renard, P., and De Marsily, G., 1997. Calculating equivalent permeability: a review. *Advances in Water Resources*, 20(5), 253-278.

Reubi, O., and Blundy, J., 2008. Assimilation of plutonic roots, formation of high-K 'exotic' melt inclusions and genesis of andesitic magmas at Volcán de Colima, Mexico. *Journal of Petrology*, 49(12), 2221-2243.

Richard, D., Scheu, B., Mueller, S.P., Spieler, O. and Dingwell, D.B., 2013. Outgassing: Influence on speed of magma fragmentation. *Journal of Geophysical Research: Solid Earth*, 118(3), pp.862-877.

Robin, C., Camus, G., and Gourgaud, A., 1991. Eruptive and magmatic cycles at Fuego de Colima volcano (Mexico). *Journal of Volcanology and Geothermal Research*, 45(3), 209-225.

Rodríguez-Elizarrarás, S. R., 1995. Estratigrafía y estructura del Volcán de Colima, México. [Stratigraphy and structure of Colima volcano, Mexico] *Revista Mexicana de Ciencias Geológicas* 12, 22 - 46. (In Spanish).

Roman, D. C., S. C. Moran, J. A. Power, and Cashman, K. V., 2004. Temporal and Spatial Variation of Local Stress Fields before and after the 1992 Eruptions of Crater Peak Vent, Mount Spurr Volcano, Alaska, *Bulletin of the Seismological Society of America*, 94, 2366-2379.

Roman, D.C., Power, J.A., Moran, S.C., Cashman, K.V., Doukas, M.P., Neal, C.A. and Gerlach, T.M., 2004. Evidence for dike emplacement beneath Iliamna Volcano, Alaska in 1996. *Journal of Volcanology and Geothermal Research*, 130(3), pp.265-284.

Rose Jr, W. I., Grant, N. K., Hahn, G. A., Lange, I. M., Powell, J. L., Easter, J., and Degriff, J. M., 1977. The evolution of Santa María volcano, Guatemala. *The Journal of Geology*, 63-87.

Rubey, W.W. and Hubbert, M.K., 1959. Role of fluid pressure in mechanics of overthrust faulting II. Overthrust belt in geosynclinal area of western Wyoming in light of fluid-pressure hypothesis. *Geological Society of America Bulletin*, 70(2), pp.167-206

Rudnicki, J.W. and Rice, J.R., 2006. Effective normal stress alteration due to pore pressure changes induced by dynamic slip propagation on a plane between dissimilar materials. *Journal of Geophysical Research: Solid Earth*, 111(B10).

Russell, J.K., and Quane, S.L., 2005. Rheology of welding: inversion of field constraints. *Journal of Volcanology and Geothermal Research*, 142, 173-191.

Rust, A. C., Cashman, K. V., and Wallace, P. J., 2004. Magma degassing buffered by vapor flow through brecciated conduit margins. *Geology*, 32(4), 349-352.

Rust, A.C., Manga, M. and Cashman, K.V., 2003. Determining flow type, shear rate and shear stress in magmas from bubble shapes and orientations. *Journal of Volcanology and Geothermal Research*, 122(1), pp.111-132.

Saar, M. O., and Manga, M., 1999. Permeability-porosity relationship in vesicular basalts. *Geophysical Research Letters*, 26(1), 111-114.

Sahimi, M., 1994. Applications of percolation theory. Taylor Francis, London, UK.

Sahimi, M., 2012. Flow and transport in porous media and fractured rock: from classical methods to modern approaches. John Wiley and Sons.

Sakhno, V.G., Polin, V.F., Akinin, V.V., Sergeev, S.A., Alenicheva, A.A., Tikhomirov, P.L. and Moll-Stalcup, E.J., 2010, September. The diachronous formation of the Enmyvaam and Amguema-Kanchalan volcanic fields in the Okhotsk-Chukotka volcanic belt (NE Russia): Evidence from isotopic data. In *Doklady Earth Sciences* (Vol. 434, No. 1, pp. 1172-1178). MAIK Nauka/Interperiodica

Sakuma, S., Kajiwara, T., Nakada, S., Uto, K. and Shimizu, H., 2008. Drilling and logging results of USDP-4—Penetration into the volcanic conduit of Unzen Volcano, Japan. *Journal of Volcanology and Geothermal Research*, 175(1), pp.1-12.

Sánchez, M. C., Sarriónandia, F., Arostegui, J., Eguiluz, L., and Ibar-guchi, J. G., 2012. The transition of spatter to lava-like body in lava fountain deposits: features and examples from the Cabezo Segura volcano (Calatrava, Spain). *Journal of Volcanology and Geothermal Research*, 227, 1-14.

Saubin, E., Tuffen, H., Gurioli, L., Owen, J., Castro, J.M., Berlo, K., McGowan, E., Schipper, C.I. and Wehbe, K., 2016. Conduit Dynamics in Transitional Rhyolitic Activity Recorded by Tuffisite Vein Textures from the 2008–2009 Chaitén Eruption. *Frontiers in Earth Science*, 4.

Savov, I.P., Luhr, J.F. and Navarro-Ochoa, C., 2008. Petrology and geochemistry of lava and ash erupted from Volcán Colima, Mexico, during 1998–2005. *Journal of Volcanology and Geothermal Research*, 174(4), pp.241-256.

Schaefer, L. N., Kendrick, J. E., Lavallée, Y., Oommen, T., and Chigna, G., 2015. Geomechanical rock properties of a basaltic volcano. *Frontiers in Earth Science*, 3, 29.

Schipper, C.I., Castro, J.M., Tuffen, H., James, M.R. and How, P., 2013. Shallow vent architecture during hybrid explosive–effusive activ-

ity at Cordón Caulle (Chile, 2011–12): evidence from direct observations and pyroclast textures. *Journal of Volcanology and Geothermal Research*, 262, pp.25-37.

Schneider, C.A., Rasband, W.S. and Eliceiri, K.W., 2012. NIH Image to ImageJ: 25 years of image analysis. *Nature Methods*, 9(7), pp.671-675.

Scholz, C.H., 1968. Experimental study of the fracturing process in brittle rock. *Journal of Geophysical Research*, 73(4), pp.1447-1454.

Schultz, R. A., and Fossen, H., 2008. Terminology for structural discontinuities. *AAPG Bulletin*, 92(7), 853-867.

Sepúlveda, F., Lahsen, A., Bonvalot, S., Cembrano, J., Alvarado, A. and Letelier, P., 2005. Morphostructural evolution of the Cordón Caulle geothermal region, Southern Volcanic Zone, Chile: Insights from gravity and  $^{40}\text{Ar}/^{39}\text{Ar}$  dating. *Journal of Volcanology and Geothermal Research*, 148(1), pp.165-189.

Shibata, T., and Akita, F., 2001. Precursory changes in well water level prior to the March, 2000 eruption of Usu volcano, Japan. *Geophysical Research Letters*, 28(9), 1799-1802.

Shimada, M., Ito, K. and Cho, A., 1989. Ductile behavior of a fine-grained porous basalt at room temperature and pressures to 3 GPa. *Physics of the Earth and Planetary Interiors*, 55(3-4), pp.361-373.

Shields, J.K., Mader, H.M., Pistone, M., Caricchi, L., Floess, D. and Putlitz, B., 2014. Strain-induced outgassing of three-phase magmas during simple shear. *Journal of Geophysical Research: Solid Earth*, 119(9), pp.6936-6957.

Shiina, T., Nakajima, J., and Matsuzawa, T., 2013. Seismic evidence for high pore pressures in the oceanic crust: Implications for fluid-related embrittlement. *Geophysical Research Letters*, 40(10), 2006-2010.

Shteynberg, G.S. and Solov'yev, T., 1976. The shape of volcanoes and the position of subordinate vents. *Izvestia Earth Phys*, 5, pp.83-84.

Sigmundsson, F., Pinel, V., Lund, B., Albino, F., Pagli, C., Geirsson, H. and Sturkell, E., 2010. Climate effects on volcanism: influence on magmatic systems of loading and unloading from ice mass variations, with examples from Iceland. *Philosophical Transactions of the Royal Society of London A: Mathematical, Physical and Engineering Sciences*, 368(1919), pp.2519-2534.

Sigurdsson, O., 1982. Analysis of pressure pulses resulting from volcanic activity in the vicinity of a well, M.S. Thesis, 75 pp., University of Oklahoma, Norman, Oklahoma.

Sisson, T. W., and Bacon, C. R., 1999. Gas-driven filter pressing in magmas. *Geology*, 27(7), 613-616

Sisson, T.W., and Power, J.A., 2013. Deep-crustal seismicity in volcanic regions by fluid-enhanced wallrock embrittlement. American Geophysical Union, Fall Meeting 2013, abstract #V13B-2616.

Smith, J. V., Miyake, Y., and Oikawa, T., 2001. Interpretation of porosity in dacite lava domes as ductile–brittle failure textures. *Journal of Volcanology and Geothermal Research*, 112(1), 25-35.

Smyth, H., Hall, R., Hamilton, J., and Kinny, P., 2005. East Java: Cenozoic basins, volcanoes and ancient basement. Indonesian Petroleum Association, Proceedings 30th Annual Convention, 251-266.

Smyth, J.R., 1982. Zeolite stability constraints on radioactive waste isolation in zeolite-bearing volcanic rocks. *The Journal of Geology*, pp.195-202.

Sousa, L.L., Souza, A.D., Fernandes, L., Arantes, V.L. and Salomão, R., 2015. Development of densification-resistant castable porous structures from in situ mullite. *Ceramics International*, 41(8), pp.9443-9454.

Spampinato, L., Calvari, S., Oppenheimer, C. and Boschi, E., 2011. Volcano surveillance using infrared cameras. *Earth-Science Reviews*, 106(1), pp.63-91.

Sparks, R.S.J., 1978. The dynamics of bubble formation and growth in magmas: a review and analysis. *Journal of Volcanology and Geothermal Research*, 3(1-2), pp.1-37.

Sparks, R.S.J., 1997. Causes and consequences of pressurisation in lava dome eruptions: *Earth and Planetary Science Letters*, 150, 177-189.

Sparks, R.S.J., Tait, S.R. and Yanev, Y., 1999. Dense welding caused by volatile resorption. *Journal of the Geological Society*, 156(2), pp.217-225.

Spieler, O., Kennedy, B., Kueppers, U., Dingwell, D. B., Scheu, B., and Taddeucci, J., 2004. The fragmentation threshold of pyroclastic rocks. *Earth and Planetary Science Letters*, 226(1), 139-148.

Sruoga, P., Rubinstein, N., and Hinterwimmer, G., 2004. Porosity and permeability in volcanic rocks: a case study on the Serie Tobífera, South Patagonia, Argentina. *Journal of Volcanology and Geothermal Research*, 132(1), 31-43.

Stanchits, S., Vinciguerra, S. and Dresen, G., 2006. Ultrasonic velocities, acoustic emission characteristics and crack damage of basalt and granite. *Pure and Applied Geophysics*, 163(5-6), pp.975-994.

Stasiuk, M.V., Barclay, J., Carroll, M.R., Jaupart, C., Ratté, J.C., Sparks, R.S.J. and Tait, S.R., 1996. Degassing during magma ascent in the Mule Creek vent (USA). *Bulletin of Volcanology*, 58(2-3), pp.117-130.

Stevenson, J.A. and Varley, N., 2008. Fumarole monitoring with a handheld infrared camera: Volcán de Colima, Mexico, 2006-2007. *Journal of Volcanology and Geothermal Research*, 177(4): 911-924.

Stormont, J.C. and Daemen, J.J.K., 1992, July. Laboratory study of gas permeability changes in rock salt during deformation. In *International journal of rock mechanics and mining sciences & geomechanics abstracts* (Vol. 29, No. 4, pp. 325-342). Pergamon.

Strehlow, K., Gottsmann, J.H. and Rust, A.C., 2015. Poroelastic responses of confined aquifers to subsurface strain changes and their use for volcano monitoring. *Solid Earth Discuss*, 7, pp.1673-1729.

Taisne, B., and Jaupart, C., 2008. Magma degassing and intermittent lava dome growth. *Geophysical Research Letters*, 35(20).

Tait, S., Thomas, R., Gardner, J. and Jaupart, C., 1998. Constraints on cooling rates and permeabilities of pumice in an explosive eruption jet from colour and magnetic mineralogy. *Journal of Volcanology and Geothermal Research*, 86(1), 79-91.

Taran , Y., Gavilanes, J.C., Cortés, A., and Armienta, M.A. (2000). Chemical precursors to the 1998-1999 eruption of Colima volcano, Mexico. *Revista Mexicana de Ciencias Geológicas*, 17(2), 111-124.

Taylor, B.E., Eichelberger, J.C., and Westrich, H.R., 1983. Hydrogen isotopic evidence of rhyolitic magma outgassing during shallow intrusion and eruption. *Nature*. 306, 541 - 545.

Terzaghi, K. V. 1923. Die Berechnung der Durchlässigkeitssziffer des Tones aus dem Verlauf der hydrodynamischen Spannungsscheinungen. [The calculation of the permeability coefficient of clay from the variation of hydrodynamic stress phenomena]. *Sitzungsberichte der Akademie der Wissenschaften in Wien, Mathematisch-Naturwissenschaftliche Klasse, Abteilung IIa*, 132, 125-138. (In German).

Tiede, C., Camacho, A.G., Gerstenecker, C., Fernández, J. and Suyanto, I., 2005. Modeling the density at Merapi volcano area, Indonesia, via the inverse gravimetric problem. *Geochemistry, Geophysics, Geosystems*, 6(9).

Tuffen, H. and Dingwell, D., 2005. Fault textures in volcanic conduits: evidence for seismic trigger mechanisms during silicic eruptions. *Bulletin of Volcanology*, 67(4), pp.370-387.

Tuffen, H., Dingwell, D. B., and Pinkerton, H., 2003. Repeated fracture and healing of silicic magma generate flow banding and earthquakes? *Geology*, 31(12), 1089-1092.

Tuffen, H., Smith, R. and Sammonds, P.R., 2008. Evidence for seismogenic fracture of silicic magma. *Nature*, 453(7194), pp.511-514.

Ulusay, R. and Hudson, J.A., 2007. The complete ISRM suggested methods for rock characterization, testing and monitoring: 1974-2006.

Commission on testing methods. International Society of Rock Mechanics. Compilation arranged by the ISRM Turkish National Group, Ankara, Turkey, 628.

Vajdova, V., Baud, P. and Wong, T.-f., 2004. Permeability evolution during localized deformation in Bentheim sandstone. *Journal of Geophysical Research: Solid Earth*, 109(B10).

Valdez-Moreno, G., Schaaf, P., Macías, J. L., and Kusakabe, M., 2006. New Sr-Nd-Pb-O isotope data for Colima volcano and evidence for the nature of the local basement. *Geological Society of America Special Papers*, 402, 45-63.

van Wyk De Vries, B., and Merle, O., 1998. Extension induced by volcanic loading in regional strike-slip zones. *Geology*, 26(11), 983-986.

van Wyk de Vries, B., Kerle, N. and Petley, D., 2000. Sector collapse forming at Casita volcano, Nicaragua. *Geology*, 28(2), pp.167-170.

van Wyk de Vries, B.V.W. and Borgia, A., 1996. The role of basement in volcano deformation. *Geological Society, London, Special Publications*, 110(1), pp.95-110.

van Wyk de Vries, B.V.W. and Matela, R., 1998. Styles of volcano-induced deformation: numerical models of substratum flexure, spreading and extrusion. *Journal of Volcanology and Geothermal Research*, 81(1), pp.1-18.

Varley, N. R., and Taran, Y., 2003. Degassing processes of Popocatépetl and Volcán de Colima, Mexico. *Geological Society, London, Special Publications*, 213(1), 263-280.

Varley, N. R., Arámbula-Mendoza, R., Reyes-Dávila, G., Sanderson, R., and Stevenson, J., 2010b. Generation of Vulcanian activity and long-period seismicity at Volcán de Colima, Mexico. *Journal of Volcanology and Geothermal Research*, 198(1), 45-56.

Varley, N. R., Arámbula-Mendoza, R., Reyes-Dávila, G., Stevenson, J., and Harwood, R., 2010a. Long-period seismicity during magma movement at Volcán de Colima. *Bulletin of Volcanology*, 72(9), 1093-1107.

Varley, N. R., Johnson, J., Ruiz, M., Reyes-Dávila, G. A. and Martin, K., 2006. Applying statistical analysis to understanding the dynamics of volcanic explosions. In: H.M. Mader, S.G. Coles, C.B. Connor and L.J. Connor (Editors), *Statistics in Volcanology*. Special publication of IAVCEI, pp. 57-76.

Vaselli, O., Tassi, F., Minissale, A., Montegrossi, G., Duarte, E., Fernández, E. and Bergamaschi, F., 2003. Fumarole migration and fluid geochemistry at Poás volcano (Costa Rica) from 1998 to 2001. *Geological Society, London, Special Publications*, 213(1), pp.247-262.

- Vasseur, J., Wadsworth, F. B., Lavallée, Y., Hess, K. U., and Dingwell, D. B., 2013. Volcanic sintering: Timescales of viscous densification and strength recovery. *Geophysical Research Letters*, 40(21), 5658-5664.
- Venezky, D. Y., and Rutherford, M. J., 1997. Preeruption conditions and timing of dacite-andesite magma mixing in the 2.2 ka eruption at Mount Rainier. *Journal of Geophysical Research: Solid Earth (1978–2012)*, 102(B9), 20069-20086.
- Vignaroli, G., Aldega, L., Balsamo, F., Billi, A., De Benedetti, A. A., De Filippis, L., and Rossetti, F., 2014. A way to hydrothermal paroxysm, Colli Albani volcano, Italy. *Geological Society of America Bulletin*, B31139-1.
- Vinciguerra, S., Meredith, P.G. and Hazzard, J., 2004. Experimental and modeling study of fluid pressure-driven fractures in Darley Dale sandstone. *Geophysical Research Letters*, 31(9).
- Vinciguerra, S., Trovato, C., Meredith, P.G. and Benson, P.M., 2005. Relating seismic velocities, thermal cracking and permeability in Mt. Etna and Iceland basalts. *International Journal of Rock Mechanics and Mining Sciences*, 42(7), pp.900-910.
- Violay, M., Gibert, B., Mainprice, D. and Burg, J.P., 2015. Brittle versus ductile deformation as the main control of the deep fluid circulation in oceanic crust. *Geophysical Research Letters*, 42(8), pp.2767-2773.
- Voight B, Sparks RJS, Miller AD, Stewart RC, Hoblitt RP, Clarke A, Ewart J, Aspinall WP, Baptie B, Calder ES, Cole P, Druitt TH, Hartford C, Herd RA, Jackson P, Lejeune AM, Lockhart AB, Loughlin SC, Luckett R, Lynch L, Norton GE, Robertson R, Watson IM, Watts R, Young SR (1999) Magma Flow Instability and Cyclic Activity at Soufriere Hills Volcano, Montserrat, British West Indies. *Science*. 283: 1138 - 1142. doi: 10.1126/science.283.5405.1138.
- Voight, B. and Elsworth, D., 1997. Failure of volcano slopes. *Geotechnique*, 47(1), pp.1-31.
- Voight, B., Hoblitt, R.P., Clarke, A.B., Lockhart, A.B., Miller, A., Lynch, L. and McMahon, J., 1998. Remarkable cyclic ground deformation monitored in real-time on Montserrat, and its use in eruption forecasting. *Geophysical Research Letters*, 25(18), pp.3405-3408.
- Voight, B., Linde, A.T., Sacks, I.S., Mattioli, G.S., Sparks, R.S.J., Elsworth, D., Hidayat, D., Malin, P.E., Shalev, E., Widijayanti, C. and Young, S.R., 2006. Unprecedented pressure increase in deep magma reservoir triggered by lava-dome collapse. *Geophysical Research Letters*, 33(3).
- Voight, B., Sparks, R.S.J., Miller, A.D., Stewart, R.C., Hoblitt, R.P., Clarke, A., Ewart, J., Aspinall, W.P., Baptie, B., Calder, E.S. and Cole,

P., 1999. Magma flow instability and cyclic activity at Soufrière Hills Volcano, Montserrat, British West Indies. *Science*, 283(5405), pp.1138-1142.

Vona, A., Romano, C., Dingwell, D. B., and Giordano, D., 2011. The rheology of crystal-bearing basaltic magmas from Stromboli and Etna. *Geochimica et Cosmochimica Acta*, 75(11), 3214-3236.

Wadge, G., Mattioli, G.S. and Herd, R.A., 2006. Ground deformation at Soufrière Hills Volcano, Montserrat during 1998–2000 measured by radar interferometry and GPS. *Journal of Volcanology and Geothermal Research*, 152(1), pp.157-173.

Wadsworth, F.B., Kennedy, B.M., Branney, M.J., von Aulock, F.W., Lavallée, Y. and Menendez, A., 2015. Exhumed conduit records magma ascent and drain-back during a Strombolian eruption at Tongariro volcano, New Zealand. *Bulletin of Volcanology*, 77(9), pp.1-10.

Wadsworth, F.B., Vasseur, J., Aulock, F.W., Hess, K.U., Scheu, B., Lavallée, Y. and Dingwell, D.B., 2014. Nonisothermal viscous sintering of volcanic ash. *Journal of Geophysical Research: Solid Earth*, 119(12), pp.8792-8804.

Wadsworth, F.B., Vasseur, J., Llewellyn, E.W., Schauroth, J., Dobson, K.J., Scheu, B. and Dingwell, D.B., 2016a. Sintering of viscous droplets under surface tension. *Proceedings of the Royal Society of London A*. 472 (2188).

Wadsworth, F.B., Vasseur, J., Scheu, B., Kendrick, J.E., Lavallée, Y. and Dingwell, D.B., 201b6. Universal scaling of fluid permeability during volcanic welding and sediment diagenesis. *Geology*, 44(3), pp.219-222.

Walter, T.R., Subandriyo, J., Kirbani, S., Bathke, H., Suryanto, W., Aisyah, N., Darmawan, H., Jousset, P., Luehr, B.G. and Dahm, T., 2015. Volcano-tectonic control of Merapi's lava dome splitting: The November 2013 fracture observed from high resolution TerraSAR-X data. *Tectonophysics*, 639, pp.23-33.

Wang, H. F. 2000. *Theory of Linear Poroelasticity With Applications to Geomechanics and Hydrogeology*, Princeton Univ. Press, Princeton, N. J.

Watanabe, T., Shimizu, Y., Noguchi, S. and Nakada, S., 2008. Permeability measurements on rock samples from Unzen scientific drilling project drill hole 4 (USDP-4). *Journal of Volcanology and Geothermal Research*, 175(1), pp.82-90.

Watson, I.M., Oppenheimer, C., Voight, B., Francis, P.W., Clarke, A., Stix, J., Miller, A., Pyle, D.M., Burton, M.R., Young, S.R. and Norton, G., 2000. The relationship between degassing and ground deformation at Soufrière Hills Volcano, Montserrat. *Journal of Volcanology and Geothermal Research*, 98(1), pp.117-126.

Watters, R.J., Zimbelman, D.R., Bowman, S.D. and Crowley, J.K., 2000. Rock mass strength assessment and significance to edifice stability, Mount Rainier and Mount Hood, Cascade Range volcanoes. *Pure and Applied Geophysics*, 157(6-8), pp.957-976.

Wong, T.-f., and Baud, P., 2012. The brittle-ductile transition in porous rock: A review. *Journal of Structural Geology*, 44, pp.25-53.

Wong, T.-f., Baud, P. and Klein, E., 2001. Localized failure modes in a compactant porous rock. *Geophysical Research Letters*, 28(13), pp.2521-2524.

Wong, T.-f., David, C. and Zhu, W., 1997. The transition from brittle faulting to cataclastic flow in porous sandstones: Mechanical deformation. *Journal of Geophysical Research: Solid Earth*, 102(B2), pp.3009-3025.

Woods, A. W., and Koyaguchi, T., 1994. Transitions between explosive and effusive eruptions of silicic magmas. *Nature*, 370(6491), 641-644.

Wright, H. M., and Weinberg, R. F., 2009. Strain localization in vesicular magma: Implications for rheology and fragmentation. *Geology*, 37(11), 1023-1026.

Wright, H., Roberts, J.J. and Cashman, K.V., 2006. Permeability of anisotropic tube pumice: model calculations and measurements. *Geophysical Research Letters*, 33(17).

Wright, H.M., Cashman, K.V., Gottesfeld, E.H. and Roberts, J.J., 2009. Pore structure of volcanic clasts: measurements of permeability and electrical conductivity. *Earth and Planetary Science Letters*, 280(1), pp.93-104.

Xiaochun, L., Manabu, T., Zhishen, W., Hitoshi, K. and Takashi, O., 2003. Faulting-induced permeability change in Shirahama sandstone and implication for CO<sub>2</sub> aquifer storage. *Chinese Journal of Rock Mechanics and Engineering* (岩石力学与工程学报) 22(6), pp.995-1001.

Yokoo, A., Iguchi, M., Tameguri, T., and Yamamoto, K. (2013). Processes prior to outbursts of vulcanian eruption at Showa crater of Sakurajima volcano. *Bulletin of the Volcanological Society of Japan*, 58, 163-181.

Yokoyama, T. and Takeuchi, S., 2009. Porosimetry of vesicular volcanic products by a water-expulsion method and the relationship of pore characteristics to permeability. *Journal of Geophysical Research: Solid Earth*, 114(B2).

Zhang, S., Paterson, M.S. and Cox, S.F., 1994. Porosity and permeability evolution during hot isostatic pressing of calcite aggregates. *Journal of Geophysical Research: Solid Earth*, 99(B8), pp.15741-15760.

- Zhang, Y., 1999. A criterion for the fragmentation of bubbly magma based on brittle failure theory. *Nature*, 402(6762), pp.648-650.
- Zhu, W. and Wong, T.-f., 1996. Permeability reduction in a dilating rock: Network modeling of damage and tortuosity. *Geophysical Research Letters*, 23(22), pp.3099-3102.
- Zhu, W. and Wong, T.-f., 1997. The transition from brittle faulting to cataclastic flow: Permeability evolution. *Journal of Geophysical Research: Solid Earth*, 102(B2), pp.3027-3041.
- Zhu, W. and Wong, T.-f., 1999. Network modeling of the evolution of permeability and dilatancy in compact rock. *Journal of Geophysical Research: Solid Earth*, 104(B2), pp.2963-2971.
- Zhu, W., Baud, P. and Wong, T.-f., 2010. Micromechanics of cataclastic pore collapse in limestone. *Journal of Geophysical Research: Solid Earth*, 115(B4).
- Zhu, W., Baud, P., Vinciguerra, S. and Wong, T.-f., 2011. Micromechanics of brittle faulting and cataclastic flow in Alban Hills tuff. *Journal of Geophysical Research: Solid Earth*, 116(B6).
- Zhu, W., Baud, P., Vinciguerra, S. and Wong, T.-f., 2016. Micromechanics of brittle faulting and cataclastic flow in Mount Etna basalt. *Journal of Geophysical Research: Solid Earth*.
- Zoback, M.D. and Byerlee, J.D., 1975. The effect of microcrack dilatancy on the permeability of Westerly granite. *Journal of Geophysical Research*, 80 (5), pp.752-755.
- Zobin, V.M., Luhr, J.F., Taran, Y.A., Bretón, M., Cortés, A., De La Cruz-Reyna, S., Dominguez, T., Galindo, I., Gavilanes, J.C., Muniz, J.J. and Navarro, C., 2002. Overview of the 1997–2000 activity of Volcán de Colima, Mexico. *Journal of Volcanology and Geothermal Research*, 117(1), pp.1-19.
- Zou, C., 2013. Volcanic reservoirs in petroleum exploration. Newnes.
- Zucca, J.J., Hill, D.P. and Kovach, R.L., 1982. Crustal structure of Mauna Loa volcano, Hawaii, from seismic refraction and gravity data. *Bulletin of the Seismological Society of America*, 72(5), pp.1535-1550.



## COLOPHON

This document was typeset by the author using  $\text{\LaTeX}\ 2\varepsilon$  in the  $\text{\TeX}{}works$  working environment. The typesetting style was inspired by the typographical look-and-feel `classicthesis` developed by André Miede, in turn inspired by Robert Bringhurst's seminal book on typography "*The Elements of Typographic Style*".

James FARQUHARSON

PERMEABILITY EVOLUTION IN VOLCANIC SYSTEMS:  
*Field, Laboratory, and Numerical Investigations*

RÉSUMÉ

La perméabilité est une propriété essentielle notamment pour déterminer la nature explosive des volcans, ainsi que pour de nombreuses autres applications scientifiques et industrielles dans les environnements où l'écoulement du fluide est une préoccupation majeure. Combinant des méthodes expérimentales de déformation des roches en laboratoire, des approches de terrain, de la modélisation numérique, et des analyses systématiques de microstructure, ce travail a mis en évidence le caractère complexe de la formation et la destruction des réseaux poreux dans le magma et des roches volcaniques. La compétition entre les processus dilatants (qui augmentent la porosité) et compactants (qui la diminuent) exerce une influence sur les propriétés de transport des fluides à la fois dans le magma et dans la roche volcanique solidifiée. Ces processus incluent la vésiculation et la croissance des bulles dans le conduit, la rupture et la compression du magma, la fracturation issue du refroidissement et fracturation induite par le transport, ainsi que la déformation pendant ou après la mise en place des matériaux, et la densification par frittage.

Mots clés: *Perméabilité, porosité, volcanologie, déformation des roches, dégazage, les éruptions volcaniques*

RÉSUMÉ EN ANGLAIS

The permeability of various volcanic materials is an essential parameter governing the explosive behaviour of volcanic systems, as well as being important in many other scientific and industrial applications in environments where fluid flow is a major concern. Combining experimental rock deformation methods with field measurements, numerical modelling, and systematic analyses of rock microstructure, this work explores the complexities involved in the formation and destruction of porous networks in magma and volcanic rocks, addressing how permeability can evolve in volcanic systems. Competition between dilatant processes (which increase porosity) and compactant processes (which decrease porosity) influences the fluid transport properties both in the conduit-dwelling magma and in solidified edifice rock. These processes include (but are not limited to) vesiculation and bubble growth in the conduit, fracture and compaction of magma, post-emplacement thermal or mechanical fracturing, strain-induced deformation, and viscous sintering.

Keywords: *Permeability, porosity, volcanology, rock deformation, outgassing, volcanic eruptions*